

3.01

Finite Element Methods for Linear Elastic Fracture Mechanics

A. R. INGRAFFEA

Cornell University, Ithaca, New York, USA

and

P. A. WAWRZYNEK

Fracture Analysis Consultants, Inc., Ithaca, New York, USA

3.01.1 INTRODUCTION	2
3.01.2 SINGULAR FINITE ELEMENTS	3
3.01.2.1 Isoparametric, Quadratic Singular Elements	3
3.01.2.2 1D Quarter-point Elements	3
3.01.2.2.1 Isoparametric, cubic-order singular elements	4
3.01.2.2.2 Hierarchical singular elements	5
3.01.2.3 2D Quarter-point Elements	6
3.01.2.4 3D Quarter-point Elements	7
3.01.2.5 Summary	9
3.01.3 EXTRACTING STRESS INTENSITY FACTORS AND ENERGY RELEASE RATES FROM FE RESULTS	9
3.01.3.1 Displacement Correlation Methods	9
3.01.3.2 Virtual Crack Extension Methods	10
3.01.3.3 Modified Crack Closure Integral	11
3.01.3.4 The J-Integral (2D)	12
3.01.3.4.1 J-Integral mode separation	14
3.01.3.5 The J-Integral (3D)	14
3.01.3.6 Numerical Examples	16
3.01.3.7 Considerations for Orthotropic Materials	18
3.01.3.8 Considerations for Plate and Shell FEs	21
3.01.3.9 Summary	24
3.01.4 PREDICTING CRACK TRAJECTORY AND ITS STABILITY	25
3.01.4.1 Linear Elastic Crack Kinking due to Mixed-mode Loading without T-stress: First-order Kinking Theory	25
3.01.4.2 Linear Elastic Crack Path Stability in a T-stress Environment: First-order Crack-path Instability Theory	26
3.01.4.3 Fracture Resistance Orthotropy in 2D	28
3.01.4.4 Fracture Resistance Orthotropy in 3D	29
3.01.4.5 Crack-turning Theories with Process Zone Effects and Fracture Resistance Orthotropy	31
3.01.4.5.1 Representation of a curvilinear crack by a series of segments	31
3.01.4.5.2 Second-order, linear elastic, isotropic maximum stress kinking theory	32
3.01.4.5.3 The characteristic length, r_c , of the second-order maximum tangential stress theory	33
3.01.4.5.4 Second-order maximum tangential stress theory for materials with fracture resistance orthotropy (mode I dominated)	34
3.01.4.5.5 Second-order maximum shear stress theory with fracture orthotropy (mode II dominated)	35
3.01.4.5.6 Second-order linear elastic virtual kink theory	35

3.01.4.6 Calculation of the T-stress	39
3.01.4.6.1 Contour integral methods	39
3.01.4.6.2 Error correction scheme	41
3.01.4.6.3 High-accuracy reference solutions	42
3.01.4.6.4 Calibration of the rosette geometry	42
3.01.4.6.5 Other details of potential significance with regard to T-stress calculation	44
3.01.4.7 Summary	44
3.01.5 RATES OF ENERGY RELEASE RATE AND STABILITY OF 2D CRACK SYSTEMS	44
3.01.5.1 Formulation	45
3.01.5.1.1 General formulation for rates of energy release rate for multiply cracked systems	45
3.01.5.1.2 Additional considerations for crack-face, thermal and body force loading	47
3.01.5.1.3 Perturbation of nonsingular elements layers	48
3.01.5.1.4 Formulation for mixed-mode fracture problem	49
3.01.5.1.5 Formulation for axisymmetric problem	50
3.01.5.1.6 Derivations for the second-order derivative of energy release rate	52
3.01.5.2 Numerical Examples	53
3.01.5.2.1 Example 1: a pressurized mode-I crack in an infinite plate	53
3.01.5.2.2 Example 2: a center-cracked infinite plate subjected to a uniform remote tensile stress	53
3.01.5.2.3 Example 3: a circular crack under two symmetric point loads in an infinite space	56
3.01.5.2.4 Example 4: a system of interacting parallel equidistant cracks in a semi-infinite plane	57
3.01.5.3 Summary	59
3.01.6 RATES OF ENERGY RELEASE RATE FOR AND STABILITY OF A 3D PLANAR CRACK OF ARBITRARY SHAPE	59
3.01.6.1 Formulation	60
3.01.6.1.1 First-order derivatives of energy release rates for a crack with arbitrarily curved front	63
3.01.6.1.2 Derivations of stiffness derivatives for 3D FEs	63
3.01.6.1.3 Crack-face, thermal and body-force loadings in 3D	66
3.01.6.1.4 Mixed-mode fracture problem	66
3.01.6.2 Numerical Examples	67
3.01.6.2.1 Example 5: embedded penny-shaped crack in a large cylinder under a remote uniform tensile loading normal to the crack plane	67
3.01.6.2.2 Example 6: semi-circular surface crack in a half-cylinder under a remote uniform tensile loading normal to the crack plane	69
3.01.6.2.3 Example 7: a center-cracked plate subjected to a remote uniform tensile loading normal to the crack plane	69
3.01.6.2.4 Summary	70
3.01.7 PRACTICAL APPLICATIONS OF THE FE METHOD FOR LEFM	71
3.01.7.1 Computing Stress Intensity Factor Histories in a Lug	71
3.01.7.2 Predicting Fatigue Crack Life and Trajectory in an Aircraft Fuselage Section	74
3.01.7.2.1 Description of experiment	75
3.01.7.2.2 Numerical model	76
3.01.7.2.3 Fracture parameter evaluation	77
3.01.7.2.4 Results of crack growth simulation	78
3.01.7.3 Predicting Evolution of 3D Crack Shape in a Spiral Bevel Gear	80
3.01.7.3.1 Modeling of moving tooth loads	81
3.01.7.3.2 Parallel FE analyses	81
3.01.7.3.3 Determining new crack front	83
3.01.7.3.4 Results of crack growth simulation	84
3.01.8 REFERENCES	84

3.01.1 INTRODUCTION

Many issues of structural integrity can be cast as problems of linear elastic fracture mechanics (LEFM). These can include fatigue crack propagation and life prediction, other types of sub-critical crack growth, residual strength estimation, and brittle fracture. In these and other related problems, it is essential to be able to predict the onset of crack growth, and its rate, shape, and stability. The finite element method (FEM), as performed within modern high-performance and low-cost computing environments, is a

natural tool for attacking such LEFM problems. Therefore, this chapter has two purposes. The first is to show how the FEM can be formulated and used to calculate the parameters needed by LEFM. The chapter describes:

- (i) Representation of the elastic crack front singularity, Section 3.01.2;
- (ii) Calculation of stress intensity factors (SIF) and energy release rates for two dimensional (2D), 3D, and plate and shell idealizations, Section 3.01.3;
- (iii) Prediction of crack trajectory and its stability, Section 3.01.4;

(iv) Calculation of rates of energy release rates and growth instability of 2D crack systems, Section 3.01.5; and

(v) Calculation of rates of energy release rates for 3D planar cracks, Section 3.01.6.

The second purpose is to demonstrate how the FEM can be used to simulate the process of crack growth under LEFM conditions on example problems of practical scope, Section 3.01.7. All of the necessary background theory for LEFM can be found in Chapter 2.03. This chapter concentrates on developing the mathematical formulations of that theory that are in the context of the FEM and readily accessible by modern FEM codes.

3.01.2 SINGULAR FINITE ELEMENTS

3.01.2.1 Isoparametric, Quadratic Singular Elements

A fundamental difficulty when modeling LEFM problems using the FEM is that the polynomial basis functions used for most conventional elements cannot represent the singular crack-tip stress and strain fields predicted by the theory. This means that as the mesh is refined, the finite element (FE) solution will initially begin to converge to the theoretical solution, but eventually will diverge. This difficulty was recognized and demonstrated relatively early in the development of the FEM (Chan *et al.*, 1970). A number of researchers investigated special FE formulations that incorporate singular basis functions or stress intensity factors as nodal variables (e.g., Byskov, 1970; Tracey, 1971; Tong *et al.*, 1973; Papaioannou *et al.*, 1974; Atluri *et al.*, 1975; and Benzley, 1974). Whilst successful, these special purpose elements are not available in most general-purpose FE programs and thus are used very infrequently.

A significant advancement in the use of the FEM for LEFM problems was the simultaneous, and independent, development of “quarter-point” elements by Henshell and Shaw (1975) and Barsoum (1976). These researchers showed that the proper crack-tip displacement, stress, and strain fields are modeled by standard quadratic order isoparametric FEs if one simply moves the element’s mid-side node to the position one quarter of the way from the crack tip to the far end of the element. This procedure introduces a singularity into the mapping between the element’s parametric coordinate space and Cartesian space.

Henshell and Shaw described a quadrilateral quarter-point element, illustrated in Figure 1(a). Barsoum proposed collapsing one edge

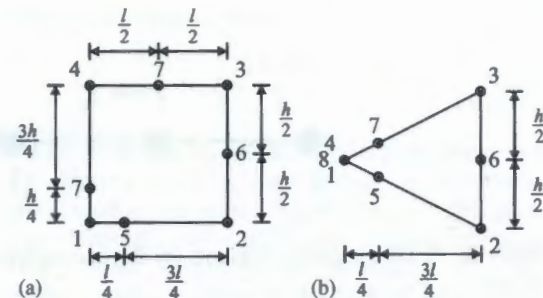


Figure 1 Quadrilateral (a) and collapsed quadrilateral (b) quarter-point elements.

of the element at the crack tip. This is shown in Figure 1(b), where the crack-tip nodes (1, 4, 8) are constrained to move together. The discovery of quarter-point elements was a significant milestone in the development of FE procedures for LEFM. With these elements standard and widely available, FE programs can be used to model crack-tip fields accurately with only minimal preprocessing required. The remainder of this section will focus exclusively on quarter-point elements in their various forms.

3.01.2.2 1D Quarter-point Elements

The effect of moving the side node of a quadratic element to the quarter-point position can be best illustrated with a 1D element. Although these elements are not practically very useful, the algebra is much simpler than with 2D and 3D elements, and is the same in principle for the higher dimensionality elements. A 1D quadratic order element is illustrated in Figure 2. Figure 2(a) shows the parametric space of the element. Figure 2(b) shows the element in the Cartesian space, with the location of the center node controlled by the value of the parameter α , and the “crack tip” is located at $r=0$.

The displacement, u , at any point within the element is determined by interpolating the nodal displacements, u_i , using the standard Lagrange second-order shape functions,

$$u = \sum_{i=1}^3 N_i u_i \\ = \frac{1}{2}\xi(\xi-1)u_1 + (1-\xi^2)u_2 + \frac{1}{2}\xi(\xi+1)u_3 \quad (1)$$

or, regrouping in powers of ξ ,

$$u = u_2 + \frac{1}{2}(u_3 - u_1)\xi + (\frac{1}{2}(u_1 + u_3) - u_2)\xi^2 \quad (2)$$

Using an isoparametric formulation, the same shape functions are used to interpolate the

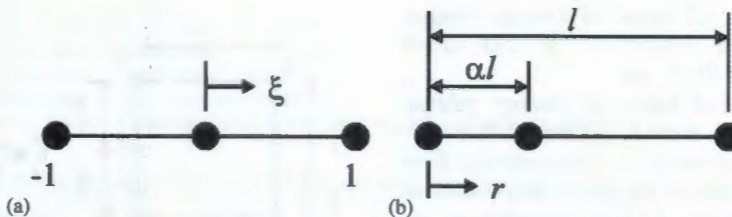


Figure 2 A 1D quadratic element: (a) the parametric space of the element and (b) the Cartesian space of the element.

geometry of the element:

$$r = \sum_{i=1}^3 N_i r_i = \alpha l + \frac{1}{2} \xi + l \left(\frac{1}{2} - \alpha \right) \xi^2 \quad (3)$$

First consider the case where the center node is located at the midpoint of the element. That is, $\alpha = 1/2$, and $\xi = 2r/l - 1$. Substituting this expression for ξ into Equation (2) yields the expected quadratic expression in r for the displacements:

$$u = u_1 + (-3u_1 + 4u_2 - u_3) \frac{r}{l} + 2(u_1 - 2u_2 + u_3) \frac{r^2}{l^2} \quad (4)$$

Differentiating this expression yields the expected linear expression in r for the strains in the element:

$$\epsilon = \frac{du}{dr} = (-3u_1 + 4u_2 - u_3) \frac{1}{l} + 4(u_1 - 2u_2 + u_3) \frac{r}{l^2} \quad (5)$$

Under linear elastic conditions, the stresses are linearly related to the strains so the stress distribution will be linear in r also.

Now consider the case where the middle node is moved to the quarter-point position. For this case $\alpha = 1/4$ and $\xi = 2\sqrt{l}r/l - 1$. Substituting this expression for ξ into Equation (2) and differentiating yields the following expressions for the displacements and strains in the element:

$$u = u_1 + 2(u_1 - 2u_2 + u_3) \frac{r}{l} + (-3u_1 + 4u_2 + u_3) \frac{\sqrt{l}r}{l} \quad (6)$$

$$\epsilon = \frac{du}{dr} = 2(u_1 - 2u_2 + u_3) \frac{1}{l} + \left(-\frac{3}{2}u_1 + 2u_2 - \frac{1}{2}u_3 \right) \frac{1}{\sqrt{l}r} \quad (7)$$

One can clearly see that the three terms in the displacement expression model a constant value, a linear variation in r , and the square

root variation in r . This corresponds to the leading terms in the LEFM expressions for the near crack-tip displacement. The expression for the strains contains a constant term and a singular term that varies as $r^{-1/2}$, the form of lead term in the LEFM stress and strain expansions.

3.01.2.2.1 Isoparametric, cubic-order singular elements

The “quarter-point” singular mapping is not unique to quadratic-order elements. Consider a cubic-order, isoparametric element with Lagrange shape functions. The expression for the displacement in the element is

$$u = \frac{1}{16}(-1 + \xi + 9\xi^2 - 9\xi^3)u_1 + \frac{9}{16}(1 - 3\xi - \xi^2 + 3\xi^3)u_2 + \frac{9}{16}(1 + 3\xi - \xi^2 - 3\xi^3)u_3 + \frac{1}{16}(-1 - \xi + 9\xi^2 + 9\xi^3)u_4 \quad (8)$$

If the locations of the middle nodes are parameterized by α and β , the expression that interpolates geometry within the element is

$$r = \frac{9\alpha l}{16}(1 - 3\xi - \xi^2 + 3\xi^3) + \frac{9\beta l}{16}(1 + 3\xi - \xi^2 - 3\xi^3) + \frac{l}{16}(-1 - \xi + 9\xi^2 + 9\xi^3) \quad (9)$$

If one selects $\alpha = 1/9$ and $\beta = 4/9$ then, similar to the quarter-point quadratic element, $\xi = 2\sqrt{l}r/l - 1$. Substituting this into the displacement expression and differentiating yields

$$u = u_1 + 9(u_1 - \frac{5}{2}u_2 + 2u_3 - \frac{1}{4}u_4) \frac{r}{l} + \left(-\frac{11}{2}u_1 + 9u_2 - \frac{9}{2}u_3 + u_4 \right) \frac{\sqrt{l}r}{l} + \frac{9}{2}(-u_1 + 3u_2 - 3u_3 + u_4) \frac{r\sqrt{l}r}{l^2} \quad (10)$$

and

When element, displacement field, strain field, expression for crack-tip

The stra...
spond to
Additional
modeled
basis fun

3.01.2.2.2

The p...
isoparam...
interest,
used in
practical
basis fun
used with
and Bab

There
formulat...
is to sta...
that in
element's
higher-ord...
grendre
functions
are ass...
not ass...
of any pr...

In ge...
isoparam...
potential...
tions are
geometry...
element.

To de...
we can
function...
quarter-
the elem...
between

and

$$\begin{aligned}\varepsilon &= \frac{du}{dr} \\ &= 9(u_1 - \frac{1}{2}u_2 + 2u_3 - \frac{1}{2}u_4)\frac{1}{l} \\ &\quad + \frac{1}{2}(-\frac{11}{2}u_1 + 9u_2 - \frac{9}{2}u_3 + u_4)\frac{1}{\sqrt{lr}} \\ &\quad + \frac{27}{4}(-u_1 + 3u_2 - 3u_3 + u_4)\frac{r}{l\sqrt{lr}} \quad (11)\end{aligned}$$

When compared to the quadratic-order element, there is an additional $r^{3/2}$ term in the displacement fields and an $r^{1/2}$ term in the strain fields. As discussed in Chapter 2.03, the expression for the series solution for the near crack-tip strain field is

$$\varepsilon = \frac{B_1}{\sqrt{r}} + \sum_{n=1}^{\infty} B_n r^{(n-1)/2} \quad (12)$$

The strain terms in the cubic element correspond to the first three terms in this expansion. Additional terms in the expansion can be modeled by using elements with higher-order basis functions.

3.01.2.2.2 Hierarchical singular elements

The preceding discussion regarding cubic isoparametric elements is largely of academic interest, because cubic elements are not widely used in practice. A related topic of more practical interest is elements with hierarchical basis functions. These elements are typically used with the “p-version” of the FEM (Szabo and Babuška, 1991).

There are a number of different ways to formulate hierarchical FEs. One popular way is to start with linear Lagrange shape functions that interpolate the displacements of the element's corner nodes. To these are added higher-order shape functions based on Legendre polynomials. The higher-order shape functions are “nodeless,” meaning that they are associated with generalized displacements not associated with the physical displacement of any particular location in the element.

In general, hierarchical elements are not isoparametric. That is, different orders, and potentially different families, of basis functions are used for interpolating the element's geometry and the displacements within the element.

To develop a singular hierarchical element we can use second-order Lagrange shape functions with the center node located at the quarter-point to interpolate the geometry of the element. This means that the relationship between the element's parametric space and the

Cartesian space will be

$$\xi = \frac{2\sqrt{lr}}{l} - 1 \quad (13)$$

Other schemes for geometry interpolation can be used providing they result in a similar relationship between the geometry mappings in the element's parametric and Cartesian space (e.g., cubic Lagrange polynomials with the center nodes position at the (1/9)th and (4/9)th positions).

The first-order basis functions for interpolating displacements within the element are

$$u^{h1} = -\frac{1}{2}(\xi - 1)u_1 + \frac{1}{2}(\xi + 1)u_2 \quad (14)$$

The superscript h1 here indicates that this is the first-order hierarchical term. Substituting Equation (13) into Equation (14) gives the following expression for the displacement variation in the element:

$$u^{h1} = u_1 + (-u_1 + u_2)\frac{\sqrt{lr}}{l} \quad (15)$$

The corresponding strain variation is

$$\varepsilon^{h1} = \frac{1}{2}(-u_1 + u_2)\frac{1}{\sqrt{lr}} \quad (16)$$

that is, the first term of Equation (12).

Higher-order elements are developed by adding “nodeless” basis functions based on Legendre polynomials to the linear interpolation. For example, the second- order displacement and strain variations are

$$u^{h2} = u^{h1} + (\xi^2 - 1)a_3 = u^{h1} + 4a_3\left(-\frac{\sqrt{lr}}{l} + \frac{r}{l}\right) \quad (17)$$

and

$$\varepsilon^{h2} = \varepsilon^{h1} + 4a_3\left(-\frac{2}{\sqrt{lr}} + \frac{1}{l}\right) \quad (18)$$

That is, the second-order basis functions generate expressions associated with the first two terms of Equation (12).

The expression for the third-order elements is

$$\begin{aligned}u^{h3} &= u^{h2} + 2(\xi^3 - \xi)a_4 \\ &= u^{h2} + 8a_4\left(\frac{\sqrt{lr}}{l} - 3\frac{r}{l} + 2\frac{r\sqrt{lr}}{l^2}\right) \quad (19)\end{aligned}$$

and

$$\varepsilon^{h3} = \varepsilon^{h2} + 4a_4\left(\frac{1}{\sqrt{lr}} - 6\frac{1}{l} + 4\frac{r}{l\sqrt{lr}}\right) \quad (20)$$

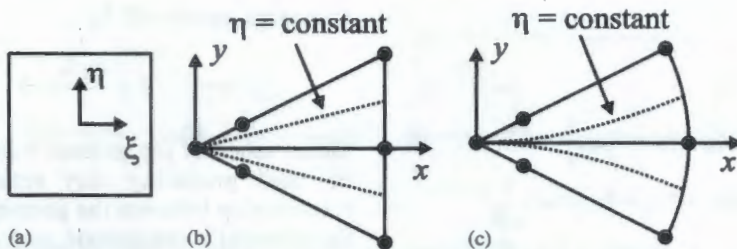


Figure 3 (a) The parametric space of a quadrilateral element; (b) and (c) The mapping of constant η lines in the Cartesian space for different far-side node placements for collapsed quadrilateral quarter-point elements.

that adds terms associated with the first three terms of Equation (12). This pattern continues when higher-order Legendre polynomials are used in the element. For example, the expressions for the fourth-order element are

$$\begin{aligned} u^{h4} &= u^{h3} + \frac{3}{4}(5\xi^4 - 6\xi^2 + 1)a_5 \\ &= u^{h3} + 12a_4\left(\frac{\sqrt{lr}}{l} - 6\frac{r}{l} + 10\frac{r\sqrt{lr}}{l^2} + 5\frac{r^2}{l^2}\right) \quad (21) \end{aligned}$$

and

$$\varepsilon^{h4} = \varepsilon^{h3} + 6a_4\left(\frac{1}{\sqrt{lr}} + 12\frac{1}{l} - 30\frac{r}{l\sqrt{lr}} + 20\frac{r}{l^2}\right) \quad (22)$$

In summary, provided the mapping of geometry in a hierarchical element is similar to that given in Equation (13), as higher polynomial orders are used to interpolate the displacements in the element, higher-order terms in the theoretical crack-tip displacement, stress, and strain fields will be modeled.

3.01.2.3 2D Quarter-point Elements

Expression (7) demonstrates that the quarter-point elements shown in Figure 1 have the desired strain (and stress) singularities along the quarter-point element edges (edges 1-5-2 and 1-7-4). However, this may not necessarily be the case for all rays through the element emanating from the crack tip.

For the collapsed triangular form, Figure 1(b), Barsoum (1977) showed that the proper singular form is obtained along all rays provided that the side node on the edge opposite the crack tip (node 6) is placed at the midpoint between the two corner nodes (nodes 2 and 3). Freese and Tracey (1976) showed that the $r^{-1/2}$ singularity holds along paths of constant parametric coordinate η , (see Figure 3(a)). When the opposite side node is midway between the corner nodes, lines of constant η map into straight rays emanating from the crack tip in the Cartesian space (Figure 3(b)). However, when the node is

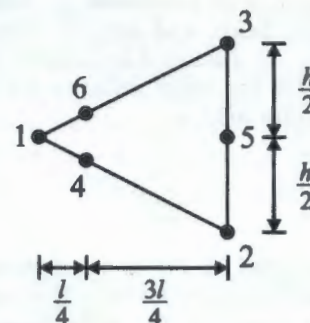


Figure 4 The natural triangle quarter-point element.

moved from the center position, lines of constant η map into quadratic curves in the Cartesian space (Figure 3(c)). The $r^{-1/2}$ singularity holds along these curves but not along straight rays.

Freese and Tracey (1976) have shown that the, so called, natural triangle quarter-point element, Figure 4, reproduces the $r^{-1/2}$ singularity along all rays emanating from the crack tip regardless of the placement of the node opposite the crack front.

Another triangular quarter-point element is a collapsed 9-noded element. Manu (1985) showed that this element produces square root behavior along all rays, provided the far side node is midway between the far corner points and that the central node is also moved to the quarter-point position.

The quadrilateral quarter-point element shown in Figure 1(a) has been used less frequently in practice than the triangular versions. This may be in part because fewer of these elements can be placed conveniently around a crack tip. With fewer elements, the (trigonometric) circumferential variation of the stress and displacement fields about a crack tip may be less accurately represented than in the triangular case where more elements can be used.

The unpopularity may also be due in part to a note published by Hibbit (1977) that claimed that the element's strain energy, and hence

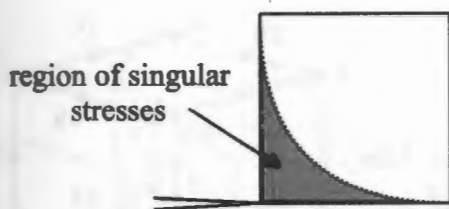


Figure 5 A schematic of the neighborhood where square root singularity is modeled in quadrilateral quarter-point elements.

stiffness, was unbounded. This assertion has since been demonstrated not to be true (Ying, 1982; Banks-Sills and Bortman, 1984).

Banks-Sills and Bortman (1984) demonstrated that this element has a square root singularity along all rays emanating from the crack tip, but only in a small neighborhood near the tip (shown schematically in Figure 5), and only if the element has a rectangular shape (Banks-Sills and Bortman, 1987). Banks-Sills and Einav (1987) show that the region of singular stresses is slightly larger for 9-noded quadrilateral elements providing the central node is suitably positioned (at a location on the diagonal between the crack tip and the far corner, $(11/32)$ nds of the distance from the crack tip).

3.01.2.4 3D Quarter-point Elements

3D quarter-point elements can be created by extruding the 2D forms along the crack front. Barsoum (1976) discussed the use of a collapsed 20-noded brick element as a natural extension of the collapsed 8-noded quadrilateral. He considered straight-sided elements were all three element faces were rectangles.

Hussain *et al.* (1981), Manu (1983), and Koers (1989) considered collapsed 20-noded elements with curved crack fronts. Manu gives constraints on node positioning that must be observed to insure the proper square root singularity on all rays emanating from the crack front. With respect to Figure 6(a), the constraints one might expect are

$$\begin{aligned} x_1 &= x_4 = x_{12} & x_{17} &= x_{20} & x_5 &= x_8 = x_{16} \\ x_{10} &= \frac{1}{2}(x_1 + x_3) & x_{14} &= \frac{1}{2}(x_6 + x_7) \\ x_9 &= \frac{1}{4}(x_1 + x_2) \\ x_{11} &= \frac{1}{4}(x_1 + x_3) & x_{13} &= \frac{1}{4}(x_5 + x_6) \\ x_{15} &= \frac{1}{4}(x_5 + x_7) \end{aligned} \quad (23a)$$

In addition, the less obvious conditions:

$$\begin{aligned} x_{18} &= \frac{1}{2}(-x_1 + x_2 - x_5 + x_6 + 2x_{17}) \\ x_{19} &= \frac{1}{2}(-x_1 + x_3 - x_5 + x_7 + 2x_{17}) \end{aligned} \quad (23b)$$

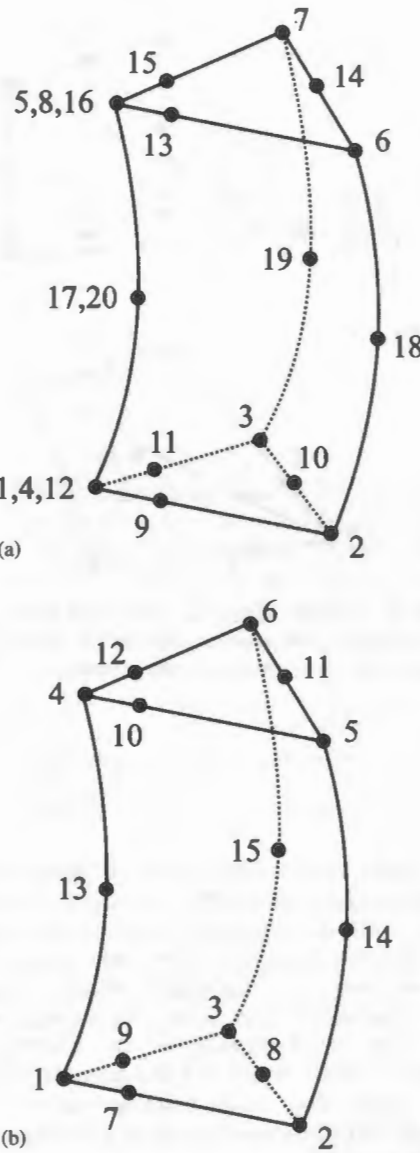


Figure 6 (a) The collapsed, 20-noded brick, quarter-point element and (b) the natural, 15-noded, wedge quarter-point element.

must be enforced. Similar conditions hold for the y and z coordinates of the nodes.

Manu (1985) showed that square root singular behavior holds for 21-noded elements provided node placements similar to those given by Equation (23) are followed. However, this result is primarily of academic interest, as 21-noded elements are used only infrequently in practice.

The 15-noded natural wedge element shown in Figure 6(b) is of practical interest. If the following node placement rules, similar to Equation (23), are observed,

$$\begin{aligned} x_7 &= \frac{1}{4}(x_1 + x_2) & x_9 &= \frac{1}{4}(x_1 + x_3) \\ x_{10} &= \frac{1}{4}(x_4 + x_5) & x_{12} &= \frac{1}{4}(x_4 + x_6) \end{aligned} \quad (24)$$

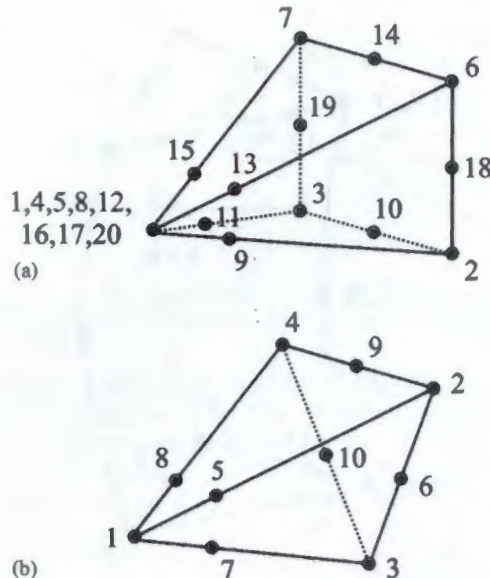


Figure 7 (a) The collapsed, 20-noded brick, pyramid quarter-point element and (b) the natural, 10-noded tetrahedral, quarter-point element.

$$x_{14} = \frac{1}{2}(-x_1 + x_2 - x_4 + x_5 + 2x_{13})$$

$$x_{15} = \frac{1}{2}(-x_1 + x_3 - x_4 + x_6 + 2x_{13})$$

it is easily shown that the determinant of the Jacobian mapping matrix is singular along the crack front, a necessary condition for square root singular behavior. However, the authors are not aware of a published proof of square root singular behavior along all rays emanating from the crack front. Given Freese and Tracey's (1976) results for the natural triangle it is likely that such behavior exists. The authors' experience is that these elements work well in practice.

Koers (1989) showed that if a 20-noded element is further collapsed to a pyramid, Figure 7(a), a square root singularity is found along all rays emanating from the collapse node.

It is relatively straightforward to show that similar behavior is obtained in the quarter-point version of a natural 10-noded tetrahedral element, Figure 7(b). However, the practical use of these element forms is somewhat limited, because the singular behavior is seen at only one point in the element. A potential situation where these elements could be used is modeling a crack front meeting a free surface at a relatively large or relatively small angle.

The behavior of hexahedral crack-front elements has been studied by Banks-Sills (1988) and Banks-Sills and Sherman (1989). They show that for a straight crack front, Figure 8, if the nodes are placed so that the

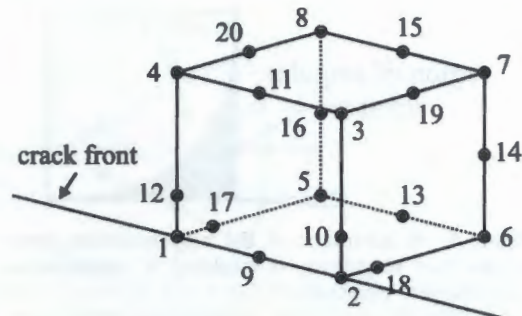


Figure 8 The 20-noded brick quarter-point element.

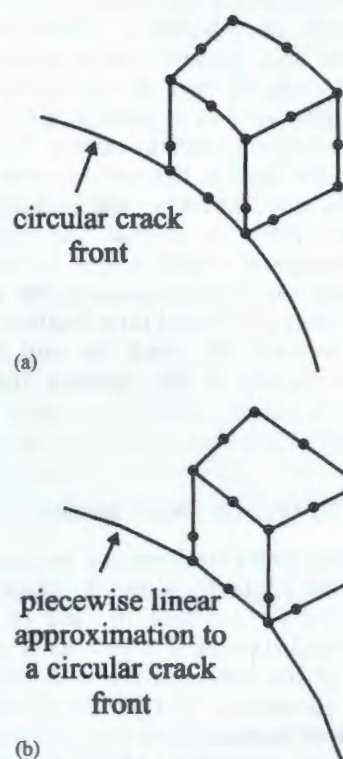


Figure 9 (a) A 20-noded quarter-point element with circular arc edges on and parallel to the crack front and (b) a trapezoidal element that approximates the circular front.

element forms a rectangular parallelepiped, then square root singularity is reproduced on all rays emanating from the crack front in each cross-section perpendicular to the front. The square root behavior is seen in a small neighborhood near the crack front similar to that illustrated in Figure 5.

For circular crack fronts they show that square root behavior is observed in all planes perpendicular to the crack front, provided the element edges on and parallel to the crack front are curved to form an arc of a circle, Figure 9(a). A trapezoidal, straight-sided

Figure
point e

versid
square
faces,
show
side f
norma
square
hyper
front.

As a
front
front
between
elements
would
perform
be acc
the me
an an
shape.

3.01.2

In t
predic
can b
secon
vided
quarte
if the
for h
added
additi
are m
quart

3.01.3

In
LEFI

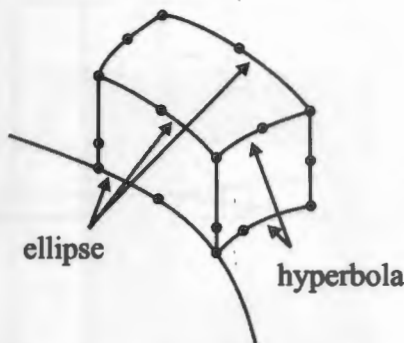


Figure 10 An ellipse/hyperbola, 20-noded quarter-point element for modeling elliptical crack fronts.

version of this element, Figure 9(b), exhibits square root singularity only on the element faces, not on all cross-sections. Similarly, they showed that for elliptical crack fronts, if the side faces form hyperbolic surfaces locally normal to the front, as in Figure 10, then a square root singularity is observed on all hyperbolic surfaces perpendicular to the crack front.

As a practical matter, if the size of the crack front elements is small relative to the crack front curvature, the difference in geometry between the circular and elliptical/hyperbolic elements and the trapezoidal approximation would be small, and one might expect that the performance of the trapezoidal elements would be acceptable. Their use seems reasonable for the more general case where one does not have an analytical description of the crack front shape.

3.01.2.5 Summary

In this section it was shown that the LEFM-predicted stress, strain, and displacement fields can be accurately modeled with standard, second-order, isoparametric elements, provided that the side nodes are moved to the quarter-points. In addition, it was shown that if the quarter-point geometry mapping is used for hierarchical elements, then as terms are added to the polynomial order of the element, additional terms of the LEFM crack-tip fields are modeled. A number of different 2D and 3D quarter-point configurations were presented.

3.01.3 EXTRACTING STRESS INTENSITY FACTORS AND ENERGY RELEASE RATES FROM FE RESULTS

In Chapter 2.03, it was shown that, under LEFM assumptions, the stress, strain, and

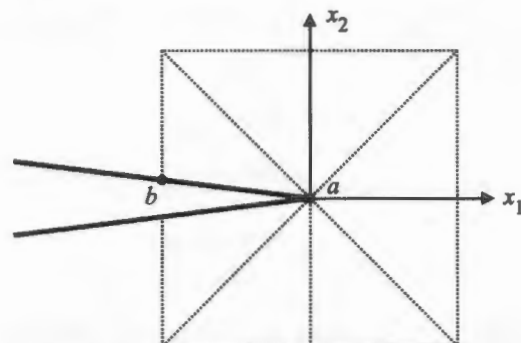


Figure 11 Possible sample point locations for simple displacement correlation.

displacement fields in the near crack-tip region are determined by the stress intensity factors (SIFs). Therefore, fundamental to the use of the FEM for LEFM is the extraction of accurate SIFs from the FE results. A large number of different techniques for extracting SIFs have been presented in the literature. In this section, four techniques are presented: displacement correlation, virtual crack extension, modified crack closure integral, and the J -integral. These were selected for their historical importance, simplicity, or their accuracy.

Techniques for extracting SIFs fall into one of two categories: direct approaches, which correlate the SIFs with FEM results directly; and “energy” approaches, which first compute energy release rates. In general, the energy approaches are more accurate and should be used preferentially. However, the direct approaches have utility and are especially useful as a check on energy approaches, because the expressions are simple enough that they are amenable to hand calculations.

3.01.3.1 Displacement Correlation Methods

Displacement correlation is one of the simplest and historically one of the first techniques used to extract SIFs from FEM results (Chan *et al.*, 1970). It is a direct approach. In its simplest form, the FE displacements for one point in the mesh are substituted directly into the analytical expressions for near-tip displacements, after subtracting the displacements of the crack tip. Usually, the point is selected to be a node on the crack face where the displacements will be greatest, and thus the relative error in the displacements is expected to be smallest. The configuration for this simple approach is shown in Figure 11.

The expressions for the SIFs using plane strain assumptions are

$$\begin{aligned} K_I &= \frac{\mu\sqrt{2\pi}(v_b - v_a)}{\sqrt{r}(2 - 2\nu)} \\ K_{II} &= \frac{\mu\sqrt{2\pi}(u_b - u_a)}{\sqrt{r}(2 - 2\nu)} \\ K_{III} &= \frac{\mu\sqrt{\pi}(w_b - w_a)}{\sqrt{2r}} \end{aligned} \quad (25)$$

where μ is the shear modulus, ν is Poisson's ratio, r is the distance from the crack tip to the correlation point, and u_i, v_i, w_i are the x, y , and z displacements at point i (see Figure 11). The same expressions can be used for plane stress assumptions if ν is replaced with $\nu = \nu/(1 + \nu)$.

Nice features of this technique are its simplicity and inherent separation of the SIFs for the three modes of fracture. Unfortunately, to obtain accurate results using the approach, care must be taken in selecting the correlation point, and usually a highly refined mesh in the crack-tip region is required. The correlation point needs to be selected so that it is clearly in the zone where the K fields dominate. One approach sometimes used with this technique is to compute SIFs for a series of points approaching the crack tip. A curve is then fitted through these results and extrapolated to a SIF value for r equals zero.

The SIFs computed by this approach can be improved if quarter-point crack-tip elements (Section 3.01.2) are used (Shih *et al.*, 1976, Tracey, 1977). In this case the displacements along the crack face for the quarter-point element interpolation are (Figure 12)

$$\begin{aligned} v_{upper} &= v_a + (-3v_a + 4v_b - v_c)\sqrt{\frac{r}{l}} \\ &\quad + (2v_a - 4v_b + 2v_c)\frac{r}{l} \\ v_{lower} &= v_a + (-3v_a + 4v_d - v_e)\sqrt{\frac{r}{l}} \\ &\quad + (2v_a - 4v_d + 2v_e)\frac{r}{l} \end{aligned} \quad (26)$$

The FEM crack opening displacement (COD) is

$$\begin{aligned} v_{upper} - v_{lower} &= [4(v_b - v_d) + v_e - v_c]\sqrt{\frac{r}{l}} \\ &\quad + [4(v_b - v_d) + 2(v_c - v_e)]\frac{r}{l} \end{aligned} \quad (27)$$

The square root term of the FEM COD can then be substituted into the analytical crack-tip displacement field to yield,

$$K_I = \frac{\mu\sqrt{2\pi}}{\sqrt{r}(2 - 2\nu)}[4(v_b - v_d) + v_e - v_c] \quad (28)$$

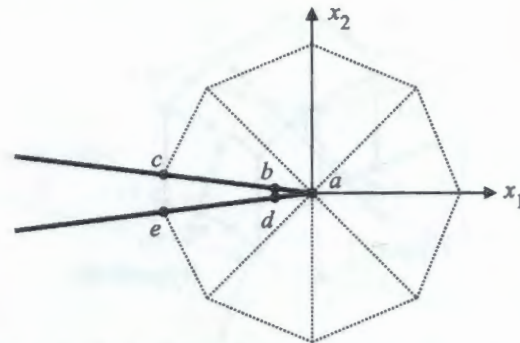


Figure 12 Node labeling for displacement correlation with quarter-point crack-tip elements.

A similar expression,

$$K_{II} = \frac{\mu\sqrt{2\pi}}{\sqrt{r}(2 - 2\nu)}[4(u_b - u_d) + u_e - u_c], \quad (29)$$

is obtained for mode II if the sliding displacements, u , are substituted for the opening displacements. Similar expressions are given by Ingraffea and Manu (1980) for 3D configurations.

3.01.3.2 Virtual Crack Extension Methods

The virtual crack extension method is an energy approach that computes the rate of change in the total potential energy of a system for a small (virtual) extension of the crack. Under LEFM assumptions, this is equal to the energy release rate. This method was first proposed by Parks (1974) and by Hellen (1975).

The total potential energy, Π , of a FE system (in the absence of body forces) is

$$\Pi = \frac{1}{2}\mathbf{u}^T \mathbf{K} \mathbf{u} - \mathbf{u}^T \mathbf{p} \quad (30)$$

where \mathbf{u} is the nodal displacement vector, \mathbf{K} is the stiffness matrix, and \mathbf{p} is the external force vector. The energy release rate for a small (virtual) crack extension is

$$G = \frac{\partial \Pi}{\partial a} = \frac{1}{2}\mathbf{u}^T \frac{\partial \mathbf{K}}{\partial a} \mathbf{u} - \mathbf{u}^T \frac{\partial \mathbf{p}}{\partial a} + \frac{\partial \mathbf{u}^T}{\partial a} [\mathbf{K} \mathbf{u} - \mathbf{p}] \quad (31)$$

The FE procedure makes the bracketed term zero. If one makes the simplifying assumption that the external forces do not change during crack growth, then Equation (31) simplifies to

$$G = \frac{1}{2}\mathbf{u}^T \frac{\partial \mathbf{K}}{\partial a} \mathbf{u} \quad (32)$$

Parks used a finite difference approximation for $\partial \mathbf{K} / \partial a$

$$\frac{\partial \mathbf{K}}{\partial a} \approx \frac{\mathbf{K}_{a+\Delta a} - \mathbf{K}_a}{\Delta a} \quad (33)$$

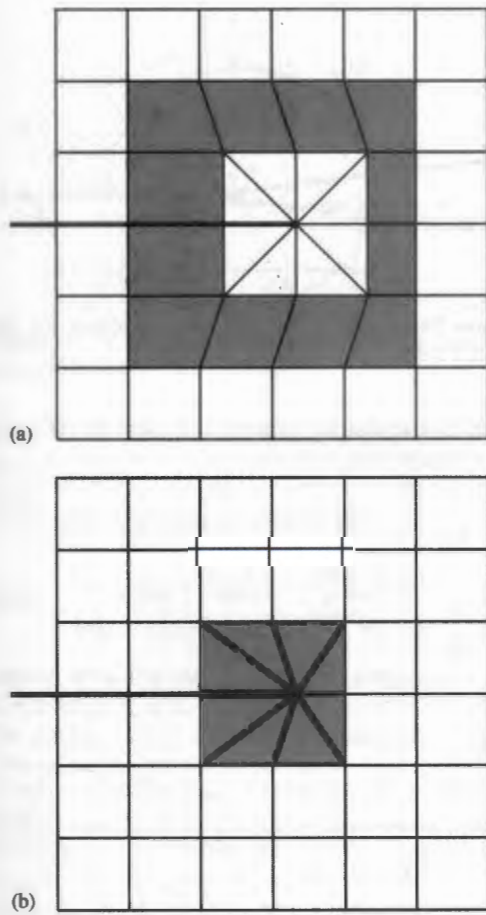


Figure 13 Two of many possible virtual crack extensions: (a) an annular ring of elements around the crack tip and (b) just the crack-tip elements. The shaded area indicates elements that have nonzero contributions to Equation 32.

where only the element stiffness matrices of the elements affected by the virtual crack extension need be considered. Figure 13 shows two possible virtual crack extensions.

In general, the virtual crack extension approach will be more accurate than the displacement correlation approach for a given FE mesh. However, as originally proposed, only a total energy release rate is computed. It is not separated for the three modes of fracture. This shortcoming can be rectified by a decomposition of the displacement fields as described in the *J*-integral section below.

Haber and Koh (1985) substituted an analytical treatment for $\partial K/\partial a$, which substantially improves the fidelity of the method. Banks-Sills and Sherman (1992) showed that the resulting technique is mathematically equivalent to the equivalent domain version of the *J*-integral, discussed below. Another related technique is that due to Lin and Abel (1988), which is discussed in Section 3.01.5,

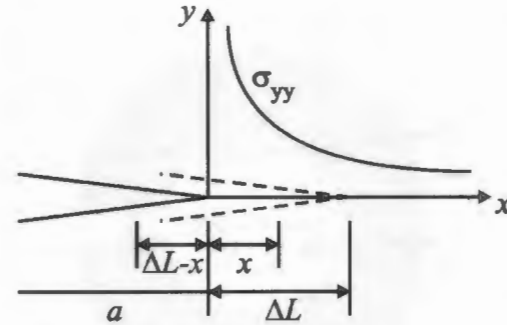


Figure 14 Crack-tip stress and displacement fields used in Irwin's crack closure integral.

below. This approach is particularly useful if derivatives of the energy release rates are required.

3.01.3.3 Modified Crack Closure Integral

The modified crack closure integral (MCCI) technique was originally proposed by Rybicki and Kanninen (1977). They observed that Irwin's crack closure Irwin (1957) could be used as a computational tool. Irwin's integral,

$$\begin{aligned} G_I &= \lim_{\Delta L \rightarrow 0} \frac{1}{2\Delta L} \int_0^{\Delta L} \sigma_{yy}(r = x, \theta = 0) \\ &\quad \times u_y(r = \Delta L - x, \theta = \pi) dr \\ G_{II} &= \lim_{\Delta L \rightarrow 0} \frac{1}{2\Delta L} \int_0^{\Delta L} \tau_{xy}(r = x, \theta = 0) \\ &\quad \times u_x(r = \Delta L - x, \theta = \pi) dr \end{aligned} \quad (34)$$

relates the energy release rate to the crack-tip stress and displacement fields for a small crack increment, Figure 14.

FE equations can be used to relate the crack-tip stresses to the internal FE forces near the crack tip, so that Equation (34) can be expressed directly in terms of nodal forces and displacements, the primary FEM variables. Furthermore, the fracture modes can be easily separated.

Rybicki and Kanninen discussed the case where linear displacement FEs are used. For this case, the expressions for G become very simple. In reference to Figure 15(a), one analysis can be performed to compute the internal nodal force at the crack tip, F^c . The crack is then extended and a second analysis is performed, Figure 15(b), yielding displacements at nodes c and d (u^c and u^d). The nodal force and displacement version of Equation (34) then reduces to

$$\begin{aligned} G_I &= \frac{1}{2\Delta L} F_y^c (u_y^c - u_y^d) \\ G_{II} &= \frac{1}{2\Delta L} F_x^c (u_x^c - u_x^d) \end{aligned} \quad (35)$$

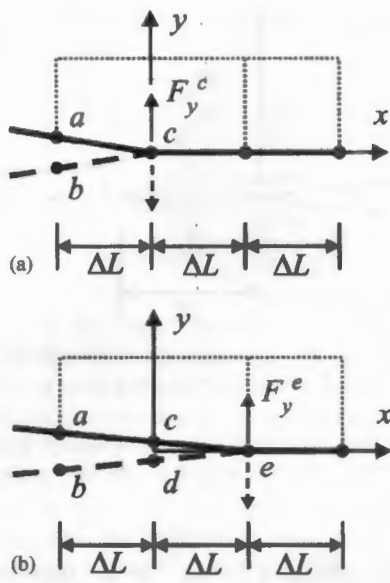


Figure 15 Local mesh configuration used for the MCCI technique: (a) first analysis and (b) second analysis after the crack has been extended.

They further observed that this procedure can be used with only one FEM analysis. If the crack step is small, then the displacements at nodes *c* and *d* in Figure 15(b) can be closely approximated by the displacements at nodes *a* and *b* in Figure 15(a). In this case the expressions for the energy release rates are

$$\begin{aligned} G_I &= \frac{1}{2\Delta L} F_y^c (u_y^a - u_y^b) \\ G_{II} &= \frac{1}{2\Delta L} F_x^c (u_x^a - u_x^b) \end{aligned} \quad (36)$$

The stress intensity factors can then be computed from the simple relations:

$$\begin{aligned} K_I &= \sqrt{G_I E} \quad \text{and} \\ K_{II} &= \sqrt{G_{II} E} \quad \text{for plane stress} \end{aligned} \quad (37a)$$

and

$$\begin{aligned} K_I &= \sqrt{G_I E / (1 - v^2)} \quad \text{and} \\ K_{II} &= \sqrt{G_{II} E / (1 - v^2)} \quad \text{for plane strain} \end{aligned} \quad (37b)$$

The signs of the K_I and K_{II} values must be determined from the crack opening and sliding displacements.

The MCCI procedure has been extended for use with higher-order elements. Of particular interest is its formulation for quarter-point elements due to Ramamurthy *et al.* (1986). They expressed the crack-tip displacement and stress fields in terms of second-order polynomials that were consistent with the quarter-point behavior. After integration of Equation

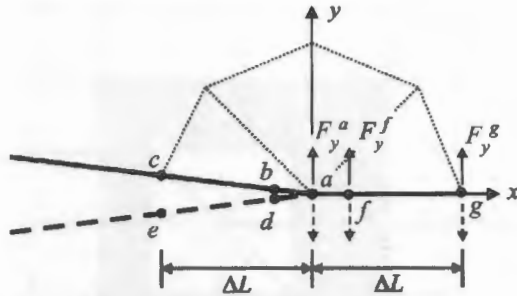


Figure 16 Local mesh and node labeling for the MCCI using quarter-point elements.

(34), the resulting expressions for the G 's are (see Figure 16)

$$\begin{aligned} G_I &= \frac{1}{\Delta L} \left[(C_{11}F_y^a + C_{12}F_y^f + C_{13}F_y^g)(u_y^b - u_y^e) \right. \\ &\quad \left. + (C_{21}F_y^a + C_{22}F_y^f + C_{23}F_y^g)(u_y^f - u_y^d) \right] \end{aligned} \quad (38a)$$

$$\begin{aligned} G_{II} &= \frac{1}{\Delta L} \left[(C_{11}F_x^a + C_{12}F_x^f + C_{13}F_x^g)(u_x^b - u_x^e) \right. \\ &\quad \left. + (C_{21}F_x^a + C_{22}F_x^f + C_{23}F_x^g)(u_x^f - u_x^d) \right] \end{aligned}$$

with

$$\begin{aligned} C_{11} &= \frac{33}{2}\pi - 52 & C_{12} &= 17 - \frac{21}{4}\pi & C_{13} &= \frac{21}{2}\pi - 32 \\ C_{21} &= 14 - \frac{33}{8}\pi & C_{22} &= \frac{21}{6}\pi - \frac{7}{2} & & \\ C_{23} &= 8 - \frac{21}{8}\pi & & & & \end{aligned} \quad (38b)$$

Figure 16 shows triangular quarter-point elements, but the same expressions can be used with rectangular quarter-point elements.

Raju (1987) presents formula for a number of additional element types. The method has been further generalized for arbitrary numerical techniques and field interpolations by Singh *et al.* (1998). In general, for the same mesh, the MCCI technique yields SIFs that are more accurate than the displacement correlation approach, but less accurate than the *J*-integral approach (discussed next). However, it gives surprisingly accurate results for its simplicity and requires nodal forces and displacements only, which are standard outputs from many FE programs. Terms in addition to those presented here are required if crack-face tractions are present.

3.01.3.4 The *J*-Integral (2D)

The *J*-integral is a well known nonlinear fracture mechanics parameter (Rice, 1968; Cherepanov, 1967; Budiansky and Rice, 1973). Under linear elastic material assumptions, the *J*-integral, *J*, can be interpreted as being equivalent to the energy release rate, *G*. In its original formulation, it relates the energy release rate of a two-dimensional body to a

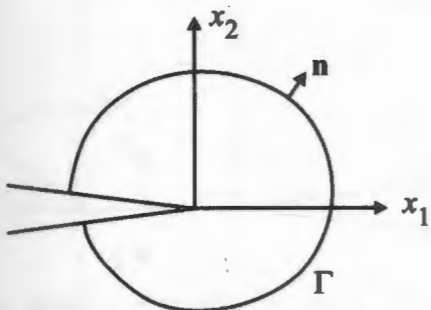


Figure 17 Crack-tip coordinates and contour for the evaluation of the J -integral.

contour integral. Using a crack coordinate system where the x_1 axis is tangential to the crack and the x_2 axis is perpendicular to the crack, the J -integral is defined as

$$J = \lim_{\Gamma \rightarrow 0} \int_{\Gamma} \left[W n_1 - \sigma_{ij} \frac{\partial u_i}{\partial x_j} n_j \right] d\Gamma \quad (39)$$

where W is the strain energy density, σ is the stress tensor, n is the unit outward normal to the contour, and u is the displacement vector (summation convention used over identical indices): see Figure 17. The contour integral in this simple form can be shown to be path-independent providing there are no body forces inside the integration area, there are no tractions on the crack surface, and the material behavior is elastic (linear or nonlinear). Path independence for cases with body forces or crack-face tractions requires additional terms in the integral.

Early use of the J -integral with FEs focused on a direct evaluation of Equation (39) along a contour in the FE mesh. Usually, the contour is selected to pass through element Gauss integration points, where stresses are expected to be most accurately evaluated. Unfortunately, such an implementation rarely exhibits path independence of the integral and *ad hoc* procedures must be adopted to obtain an objective value for J .

Li *et al.* (1985) showed how the contour J -integral can be transformed to an equivalent area integral, which is much simpler to implement in a FE context, and has been shown to be objective with respect to the domain of integration (Banks-Sills and Sherman, 1992). The area form of the integral is:

$$J = \int_A \left[\sigma_{ij} \frac{\partial u_i}{\partial x_j} - W \delta_{ij} \right] \frac{\partial q_j}{\partial x_j} dA \quad (40)$$

where δ is the Kronecker delta and q is a weighting function defined over the domain of integration. Physically, q can be thought of as

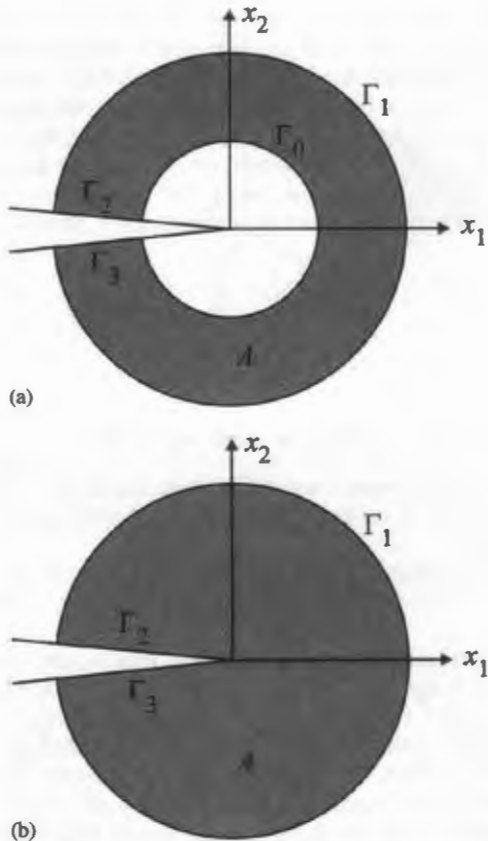


Figure 18 Domains of integration for an equivalent domain evaluation of the J -integral.

the displacement field due to a virtual crack extension.

The domain of integration can be defined in two ways: either an annular region that surrounds the crack tip, Figure 18(a), or the inner contour can be contracted all the way to the crack tip, Figure 18(b). The latter case, where only crack-tip elements are used in the integration, is particularly convenient to implement in a FE program. These cases are conceptually similar to Figure 13 but no actual physical displacements are imposed.

The q function is defined by prescribing nodal values that are interpolated over elements in the domain using the standard shape functions:

$$q = \sum_i N_i q_i \quad \text{and} \quad \frac{\partial q}{\partial x_j} = \sum_i \frac{\partial N_i}{\partial x_j} q_i \quad (41)$$

The other quantities in Equation (40) are easily computed in a FE context ($W = \frac{1}{2} \sigma_{ij} \epsilon_{ij}$).

The q function should have a value of one on the inner contour of the domain, Figure 18(a), or the crack tip, Figure 18(b), and have a value of zero on the outer contour of the domain. A linear spatial variation is usually assumed between the two contours. For example, if

the domain of evolution is the crack-tip elements only, and quarter-point elements are used, then the nodal values for q should be one at the crack-tip node, 0.75 at the quarter-point nodes, and zero at all other element nodes.

If there are tractions on the crack faces, an additional term must be added to the J -integral. For crack face tractions t_i this is

$$J = J_A + J_\Gamma = J_A + \int_{\Gamma_3 \cup \Gamma_4} t_i \frac{\partial u_i}{\partial x_1} q d\Gamma \quad (42)$$

where J_A is given by Equation (40).

3.01.3.4.1 J -Integral mode separation

The J -integral as defined in Equation (40) gives the total energy release rate for the crack, that is:

$$J = G = (K_I^2 + K_{II}^2)/E \quad (\text{plane stress}) \quad (43)$$

For mixed-mode crack growth one would like a technique for separating the SIFs due to the different fracture modes. An effective technique for doing this was introduced by Ishikawa *et al.* (1979, 1980) and independently by Bui (1983). Bui separated the modes by decomposing the near crack-tip displacement fields into one field that is symmetric with respect to the crack and another field that is anti-symmetric with respect to the crack. That is, consider a coordinate system x_1, x_2 , centered at the crack tip, with the crack lying on the negative x_1 axis, Figure 19.

Then the local displacement can be expressed as

$$u = u^I + u^{II} = \frac{1}{2} \begin{Bmatrix} u_1 + \bar{u}_1 \\ u_2 - \bar{u}_2 \end{Bmatrix} + \frac{1}{2} \begin{Bmatrix} u_1 - \bar{u}_1 \\ u_2 + \bar{u}_2 \end{Bmatrix} \quad (44)$$

with

$$\bar{u}(x_1, x_2) = u(x_1, -x_2) \quad (45)$$

A similar decomposition can be used for the stress field:

$$\sigma = \sigma^I + \sigma^{II} = \frac{1}{2} \begin{Bmatrix} \sigma_{11} + \bar{\sigma}_{11} & \sigma_{12} - \bar{\sigma}_{12} \\ \text{sym} & \sigma_{22} + \bar{\sigma}_{22} \end{Bmatrix} + \frac{1}{2} \begin{Bmatrix} \sigma_{11} - \bar{\sigma}_{11} & \sigma_{12} + \bar{\sigma}_{12} \\ \text{sym} & \sigma_{22} - \bar{\sigma}_{22} \end{Bmatrix} \quad (46)$$

The u^I field is symmetric about the crack plane and the u^{II} field is anti-symmetric about this plane.

The mode-separated J -integral values can be computed by evaluating Equation (40) using the decomposed displacements and stresses.

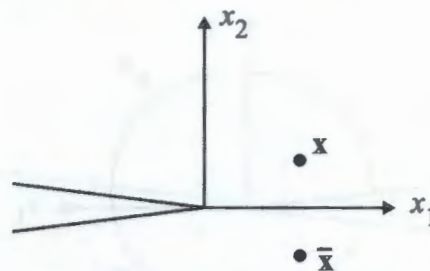


Figure 19 Schematic illustration of points symmetric about the crack plane.

That is,

$$G_I = J_I = J(u^I) \quad \text{and} \quad G_{II} = J_{II} = J(u^{II}) \quad (47)$$

The SIFs can be computed using Equation (37).

This modal decomposition technique is simple to implement if the mesh used in the domain of evaluation is symmetric about the crack plane. However, this is not necessary. Interpolation can be used to find displacements and stresses for non-symmetric meshes (Ceranek and Saouma, 1997). Another technique for modal decomposition of the J -integral based on Betti's reciprocal work theorem was developed by Yau *et al.* (1980). This approach is not discussed here.

3.01.3.5 The J -Integral (3D)

In 3D a *local* value of the J -integral, denoted $J(s)$, at each point s on a crack front is given by

$$J(s) = \lim_{\Gamma \rightarrow 0} \int_{\Gamma} \left[W n_1 - \sigma_{ij} \frac{\partial u_i}{\partial x_1} n_j \right] d\Gamma \quad (48)$$

where Γ lies in the plane normal to the crack front at s , and all quantities are expressed in the local orthogonal coordinate system located at s . Unlike the *global* path independence of the 2D version, Equation (39), the 3D J -integral is only path independent in a *local* sense as $\Gamma \rightarrow 0$ (Moran and Shih, 1987). Again, as in 2D, direct evaluation of Equation (48) within a FE context is difficult because of the need to define a path, Γ , that passes through integration points. Also, the limiting definition of the contour requires a high degree of mesh refinement at the crack front in order to obtain accurate results.

As with 2D, a weighting function can be introduced to transform the 3D J -integral into a volume integral (Nikishkov and Atluri, 1987). For the case of an elastic material with small strain assumptions, and no body forces within the contour, the expression for the

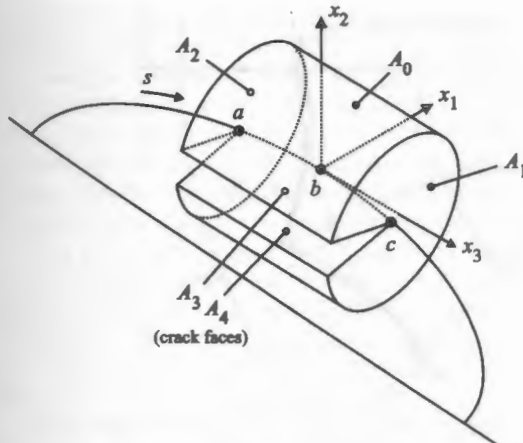


Figure 20 The domain of integration for the 3D equivalent domain formulation of the J -integral.

integral is

$$\begin{aligned} J = & \int_V \left[\sigma_{ij} \frac{\partial u_i}{\partial x_j} - W \delta_{kj} \right] \frac{\partial q_j}{\partial x_k} dV \\ & + \int_{A_3+A_4} t_i \frac{\partial u_i}{\partial x_1} q dA \end{aligned} \quad (49)$$

The domain of integration is illustrated in Figure 20.

The q -function should be defined so that it vanishes on surfaces A_1 , A_2 , and A_3 . The variation in the amplitude of the one possible q -function for the integration domain of Figure 20 is shown in Figure 21. As with 2D, the q -function can be interpreted as virtual displacement of a material point due to the virtual extension of the crack front, $q_t(s)$.

A number of candidate q functions for quadratic-order elements were presented by Nikishkov and Atluri. Banks-Sills and Sherman studied three of these in some detail (1989). They showed that the q functions of Figures 22(a) and (b), which arise naturally from the quadratic-order shape functions, are inferior to the variation shown in Figure 22(c). A similar linear variation of q_t along the crack front can be used for linear-order FEs.

Equation (49) gives the total energy release over the domain of integration for the virtual crack front extension q . An approximate local value, $J(s_b)$, can be obtained by normalizing the integral with respect to the area of the virtual crack extension (Koppenhoefer and Gullerund, 1994). That is,

$$J(s=b) \approx \frac{\int_{s_a}^{s_b} J(s) q_t(s) ds}{\int_{s_a}^{s_b} q_t(s) ds} = \frac{J}{A_q} \quad (50)$$

The modal decomposition approach presented above for 2D can be extended for 3D. In this

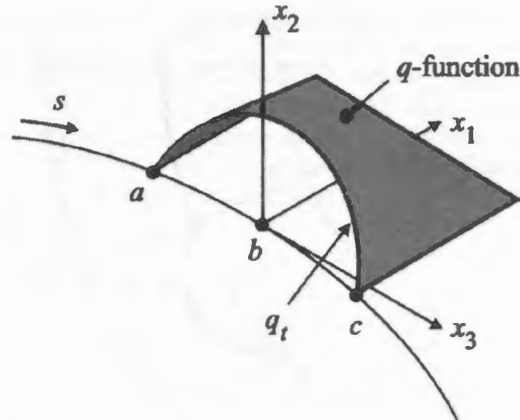


Figure 21 A schematic of the weighting function, q , used with the equivalent domain integration shown in Figure 20.

case the decomposed displacement fields are:

$$\begin{aligned} u = & u^I + u^{II} + u^{III} \\ = & \frac{1}{2} \begin{Bmatrix} u_1 + \bar{u}_1 \\ u_2 - \bar{u}_2 \\ u_3 + \bar{u}_3 \end{Bmatrix} + \frac{1}{2} \begin{Bmatrix} u_1 - \bar{u}_1 \\ u_2 + \bar{u}_2 \\ 0 \end{Bmatrix} + \frac{1}{2} \begin{Bmatrix} 0 \\ 0 \\ u_3 + \bar{u}_3 \end{Bmatrix} \end{aligned} \quad (51)$$

with

$$\bar{u}(x_1, x_2, x_3) = u(x_1, -x_2, x_3) \quad (52)$$

and the corresponding decomposition of the stress field is

$$\begin{aligned} \sigma = & \sigma^I + \sigma^{II} + \sigma^{III} \\ = & \frac{1}{2} \begin{Bmatrix} \sigma_{11} + \bar{\sigma}_{11} \\ \sigma_{22} + \bar{\sigma}_{22} \\ \sigma_{33} + \bar{\sigma}_{33} \\ \sigma_{12} - \bar{\sigma}_{12} \\ \sigma_{23} - \bar{\sigma}_{23} \\ \sigma_{31} - \bar{\sigma}_{31} \end{Bmatrix} + \frac{1}{2} \begin{Bmatrix} \sigma_{11} - \bar{\sigma}_{11} \\ \sigma_{22} - \bar{\sigma}_{22} \\ 0 \\ \sigma_{12} + \bar{\sigma}_{12} \\ 0 \\ 0 \end{Bmatrix} \\ & + \frac{1}{2} \begin{Bmatrix} 0 \\ 0 \\ \sigma_{33} - \bar{\sigma}_{33} \\ 0 \\ \sigma_{23} + \bar{\sigma}_{23} \\ \sigma_{31} + \bar{\sigma}_{31} \end{Bmatrix} \end{aligned} \quad (53)$$

As with 2D, the modal decomposition can be performed easily if the crack-front mesh is symmetric about the crack plane. Unfortunately, this situation may be difficult to achieve. For the general case of an arbitrarily shaped crack in an arbitrarily shaped object, one usually must use a mesh generator that produces an unstructured tetrahedral mesh with no guarantees of symmetry about the

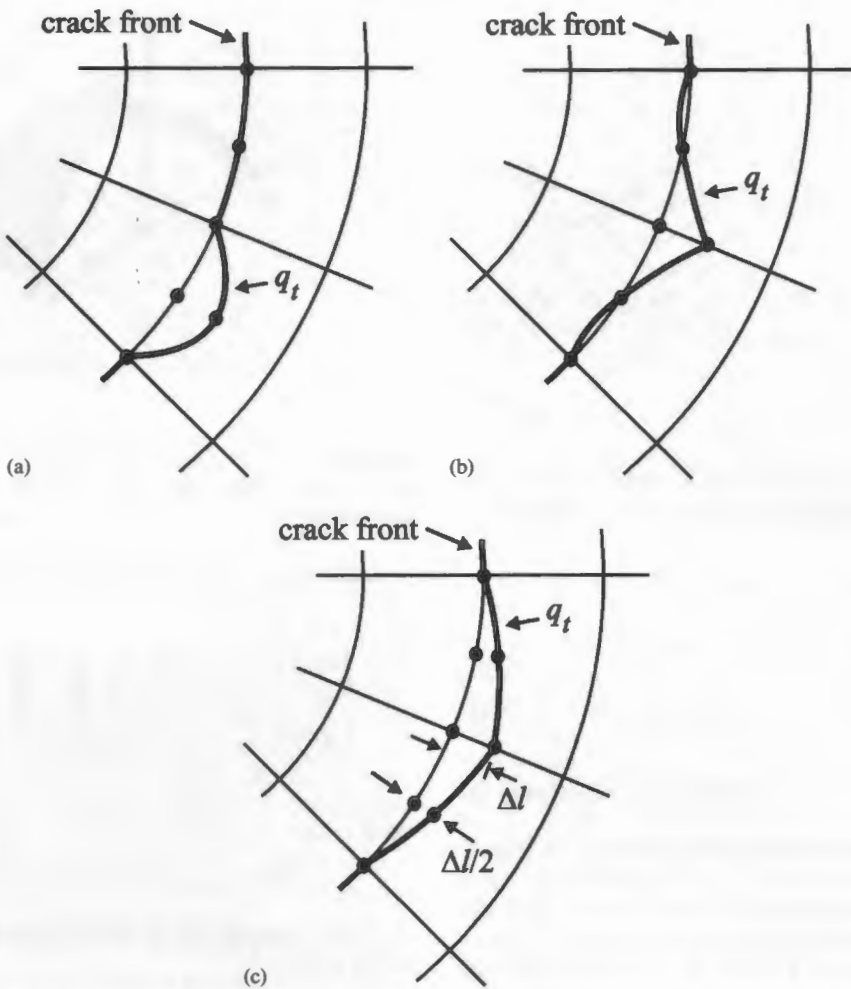


Figure 22 Three potential virtual crack extensions (q functions) for use with the equivalent domain J -integral: (a) and (b) functions derived from quadratic order shape functions; (c) a more accurate linear variation of q_t .

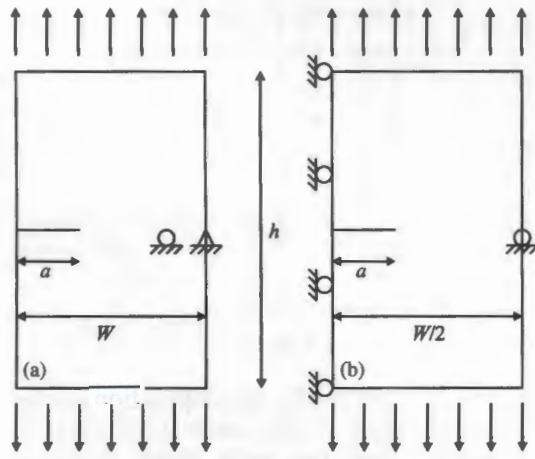


Figure 23 Schematics of the first two numerical studies.

crack plane. Červenka and Saouma (1997) present an approach where Equation (49) is evaluated directly over a cylindrical domain

using cylindrical Gauss integration rules. While the simplicity of such an approach is appealing, it suffers from the fact that stresses and displacement derivatives will likely need to be evaluated at locations that are not the optimal sampling points for the elements. This can be overcome somewhat by evaluating the J -integral using a virtual regular mesh of hexahedral or wedge elements along the crack front. The displacements for the virtual nodes of these elements are found by interpolating nodal displacements from the real, unstructured, tetrahedral mesh. The stresses and displacement derivatives are then found using the derivatives of the shape functions for the virtual elements. These can be sampled at optimal points for these elements.

3.01.3.6 Numerical Examples

In this section, a number of simple numerical studies are presented to illustrate, in 2D, the

relative accuracy and convergence properties of displacement correlation, MCCI, and J -integral techniques. All three cases are for problems with well-known analytical solutions. The first two studies use the same mesh with differing boundary conditions to model an edge crack plate, Figure 23(a), and a center-cracked plate, Figure 23(b). The normalized dimensions used in the study are $W/a = 3$ and $h/a = 10$. Plane stress conditions are assumed. A detail of the mesh in the crack region is shown in Figure 24. Quadratic-order FEs were used throughout, and eight quarter-point elements were used at the crack tip in a symmetric pattern.

Convergence behavior is studied by reducing the size of the crack-tip elements as shown in Figure 25. The results are presented as a function of the ratio of the crack-tip element size to the crack length, L/a . This value is used as a convenience, and the present results should not be interpreted as describing any universal relationship between this ratio and the expected accuracy of these methods. In general, the relationship between crack-tip element size and

accuracy is complicated and depends on more than just the crack-tip mesh (Saouma and Schwemmer, 1984). As with all FE analysis, one can usually only be assured of accurate results if a convergence study is performed.

For the case of an edge cracked plate, Figure 23(a), the analytical expression for the mode I SIF is

$$K_I = F\sigma\sqrt{a}, \quad \text{with}$$

$$F = 1.99 - 0.41\left(\frac{a}{W}\right) + 18.7\left(\frac{a}{W}\right)^2 - 38.48\left(\frac{a}{W}\right)^3 + 53.85\left(\frac{a}{W}\right)^4 \quad (54)$$

The numerical results for four crack-tip element sizes using three different techniques for computing K are shown in Table 1. The table presents SIFs normalized by the analytical values,

$$I = K_{\text{FEM}}/K_{\text{analytical}} \quad (55)$$

One can see from the table that for this case all three methods give accurate SIF values ($< 1\%$ error) even for a relatively coarse mesh with relatively large crack-tip elements. The J -integral values are the most accurate followed by MCCI and then displacement correlation. The convergence behavior of the three methods is interesting. The J -integral approach shows monotonic convergence, while displacement correlation is somewhat more erratic, and MCCI shows nearly uniform values for all mesh sizes.

The stress intensity factor for a center-cracked plate, Figure 23(b), is

$$K_I = \sigma\sqrt{\pi a} \sqrt{\sec \frac{\pi a}{W}} \quad (56)$$

The numerical results for this case are presented in Table 2. One can see that for all three techniques the results are less accurate than those seen in Table 1 (considerably less accurate for displacement correlation). Again, the J -integral results are the most accurate, followed by MCCI and displacement correlation. This time all three methods show monotonic convergence.

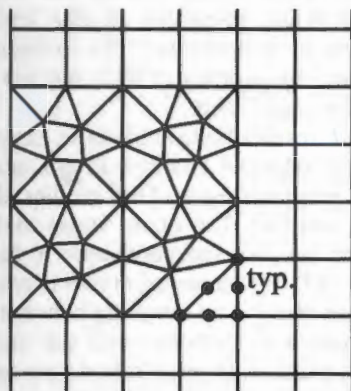


Figure 24 A detail of the mesh used in the crack region for the first two numerical studies.

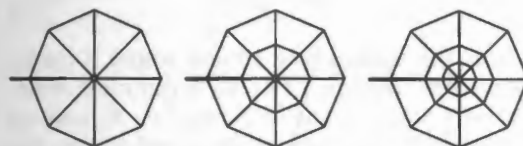


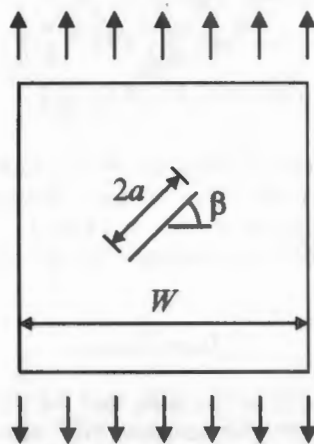
Figure 25 Illustration of the pattern of mesh refinement used in the numerical studies.

Table 1 Normalized SIFs for an edge-cracked plate, Figure 23(a).

L/a	Displacement correlation		MCCI		J -integral	
	I	% error	I	% error	I	% error
0.5	0.992	-0.81	0.994	-0.65	1.003	0.31
0.25	1.000	0.00	0.994	-0.65	1.002	0.15
0.125	0.999	-0.14	0.994	-0.60	1.001	0.13
0.0625	0.999	-0.09	0.994	-0.65	1.001	0.11

Table 2 Normalized SIFs for a center cracked plate, Figure 23(b).

L/a	Displacement correlation		MCCI		J-integral	
	I	% error	I	% error	I	% error
0.5	1.074	7.40	0.986	-1.36	1.005	0.46
0.25	1.038	3.84	0.993	-0.69	1.004	0.43
0.125	1.019	1.87	0.995	-0.47	1.004	0.39
0.0625	1.010	1.02	0.996	-0.43	1.004	0.35

**Figure 26** Schematic illustration of the third numerical study.

In the first two cases only mode I loading is present. The third case involves both modes I and II loading. The problem is a center-cracked plate with the crack oriented at an angle to the horizontal axis. This is shown in Figure 26.

The analytical solution for an angled crack in an infinite plate is

$$\begin{aligned} K_I &= \sigma \sin^2 \beta \sqrt{\pi a} \\ K_{II} &= \sigma \sin \beta \cos \beta \sqrt{\pi a} \end{aligned} \quad (57)$$

To approximate the infinite condition in a finite width model, $W/a = 80$ was used. β was set to 45° . The numerical results are presented in Tables 3 and 4.

In Table 3 one again sees a similar pattern of the relative accuracy among the methods, with all three showing monotonic convergence. The mode II results, Table 4, show a divergence in accuracy for all three methods as the mesh is refined. This implies that a mesh optimized for

accurate K_I values may not be the optimal mesh to use for accurate K_{II} values.

3.01.3.7 Considerations for Orthotropic Materials

Many materials of engineering interest are orthotropic in nature. That is, they are anisotropic with three planes of material symmetry. The stress and displacement fields in the crack-tip region, along with the SIFs and energy release rates, are of interest for fracture mechanics analyses of such materials. Sih *et al.* (1965) developed expressions for these quantities for 2D and some limited 3D configurations. These are presented in this section. A generalization to additional 3D configurations is presented by Hoenig (1982), but his results are not discussed here.

Sih *et al.* restrict their analysis to cases where loads in the plane of analysis do not cause out-of-plane displacements. This implies that the plane of analysis (for plane stress and plane strain) and the plane perpendicular to the crack front (for 3D) are planes of material symmetry. In this case, there is no coupling between the in-plane modes I-II behavior and the anti-plane mode III behavior. In what follows it is assumed (without loss of generality) that the $x-y$ plane is the plane of analysis with the crack lying along the x axis. The generalized Hook's law,

$$\{\sigma\} = [E]\{\epsilon\} \quad (58)$$

relates the stresses and strains within a linear, anisotropic material. For an orthotropic material with principal material axes (x_1 , x_2 , and x_3) aligned with the Cartesian (x , y , and z) axes, this can be expressed in terms of engineering constants as

$$\begin{Bmatrix} \epsilon_x \\ \epsilon_y \\ \epsilon_z \\ \gamma_{xy} \\ \gamma_{yz} \\ \gamma_{zx} \end{Bmatrix} = \begin{bmatrix} 1/E_1 & -v_{21}/E_2 & -v_{31}/E_3 & 0 & 0 & 0 \\ -v_{12}/E_1 & 1/E_2 & -v_{32}/E_3 & 0 & 0 & 0 \\ -v_{13}/E_1 & -v_{23}/E_2 & 1/E_3 & 0 & 0 & 0 \\ 0 & 0 & 0 & 1/G_{12} & 0 & 0 \\ 0 & 0 & 0 & 0 & 1/G_{23} & 0 \\ 0 & 0 & 0 & 0 & 0 & 1/G_{31} \end{bmatrix} \begin{Bmatrix} \sigma_x \\ \sigma_y \\ \sigma_z \\ \tau_{xy} \\ \tau_{yz} \\ \tau_{zx} \end{Bmatrix} \quad (59)$$

If the in-plane material axes are rotated with respect to the Cartesian coordinates, then the generalized Hook's law can be expressed as:

$$\{\varepsilon\} = [T]^T [E] [T] \{\sigma\} = [S] \{\sigma\} \quad (60)$$

or

$$\begin{Bmatrix} \varepsilon_x \\ \varepsilon_y \\ \varepsilon_z \\ \gamma_{xy} \\ \gamma_{yz} \\ \gamma_{zx} \end{Bmatrix} = \begin{Bmatrix} S_{11} & S_{12} & S_{13} & S_{14} & 0 & 0 \\ S_{21} & S_{22} & S_{23} & S_{24} & 0 & 0 \\ S_{31} & S_{32} & S_{33} & S_{34} & 0 & 0 \\ S_{41} & S_{42} & S_{43} & S_{44} & 0 & 0 \\ \text{sym} & & & S_{55} & S_{56} & S_{66} \end{Bmatrix} \begin{Bmatrix} \sigma_x \\ \sigma_y \\ \sigma_z \\ \tau_{xy} \\ \tau_{yz} \\ \tau_{zx} \end{Bmatrix} \quad (61)$$

with

$$[T] = \begin{bmatrix} \cos^2 \beta & \sin^2 \beta & 0 & \cos \beta \sin \beta & 0 & 0 \\ \sin^2 \beta & \cos^2 \beta & 0 & -\cos \beta \sin \beta & 0 & 0 \\ 0 & 0 & 1 & 0 & 0 & 0 \\ -2 \cos \beta \sin \beta & 2 \cos \beta \sin \beta & 0 & \cos^2 \beta - \sin^2 \beta & 0 & 0 \\ 0 & 0 & 0 & 0 & \cos \beta & -\sin \beta \\ 0 & 0 & 0 & 0 & \sin \beta & \cos \beta \end{bmatrix} \quad (62)$$

where β is the angle between the x Cartesian axis and the x_1 material axis. The definitions of the crack tip and material axes are shown in Figure 27.

Equation (61) can be specialized for plane stress ($\sigma_z = \tau_{yz} = \tau_{zx} = 0$) as

$$\begin{Bmatrix} \varepsilon_x \\ \varepsilon_y \\ \gamma_{xy} \end{Bmatrix} = \begin{Bmatrix} S_{11} & S_{12} & S_{14} \\ S_{21} & S_{22} & S_{24} \\ \text{sym} & & S_{44} \end{Bmatrix} \begin{Bmatrix} \sigma_x \\ \sigma_y \\ \tau_{xy} \end{Bmatrix} \quad (63)$$

For plane strain ($\varepsilon_z = \tau_{yz} = \tau_{zx} = 0$) the expression is

$$\begin{Bmatrix} \varepsilon_x \\ \varepsilon_y \\ \gamma_{xy} \end{Bmatrix} = \begin{Bmatrix} S_{11} - \frac{S_{12}S_{13}}{S_{33}} & S_{12}\left(1 - \frac{S_{23}}{S_{33}}\right) & S_{14} - \frac{S_{12}S_{34}}{S_{33}} \\ S_{21}\left(1 - \frac{S_{23}}{S_{33}}\right) & S_{22} - \frac{S_{22}S_{34}}{S_{33}} & S_{24} - \frac{S_{22}S_{34}}{S_{33}} \\ \text{sym} & & S_{44} - \frac{S_{22}S_{34}}{S_{33}} \end{Bmatrix} \begin{Bmatrix} \sigma_x \\ \sigma_y \\ \tau_{xy} \end{Bmatrix} = \begin{Bmatrix} S'_{11} & S'_{12} & S'_{14} \\ S'_{21} & S'_{22} & S'_{24} \\ \text{sym} & & S'_{44} \end{Bmatrix} \begin{Bmatrix} \sigma_x \\ \sigma_y \\ \tau_{xy} \end{Bmatrix} \quad (64)$$

The plane stress and plane strain expressions are structurally similar, the difference being the values of the constitutive coefficients. Therefore, it should be understood that the plane stress development that follows is valid for plane strain analyses if S'_{ij} coefficients are substituted for S_{ij} in all expressions.

From Sih *et al.* the in-plane stress and displacement fields near a crack tip can be expressed in polar coordinates, $r-\theta$ (see Figure 27), as

$$\begin{aligned} \sigma_x &= \frac{K_I}{\sqrt{2\pi r}} \operatorname{Re} \left[\frac{\mu_1 \mu_2}{\mu_1 - \mu_2} \left(\frac{\mu_2}{d_2} - \frac{\mu_1}{d_1} \right) \right. \\ &\quad \left. + \frac{K_{II}}{K_I} \frac{1}{\mu_1 - \mu_2} \left(\frac{\mu_2^2}{d_2} - \frac{\mu_1^2}{d_1} \right) \right] \\ \sigma_y &= \frac{K_I}{\sqrt{2\pi r}} \operatorname{Re} \left[\frac{1}{\mu_1 - \mu_2} \left(\frac{\mu_1}{d_2} - \frac{\mu_2}{d_1} \right) \right. \\ &\quad \left. + \frac{K_{II}}{K_I} \frac{1}{\mu_1 - \mu_2} \left(\frac{1}{d_2} - \frac{1}{d_1} \right) \right] \\ \tau_{xy} &= \frac{K_I}{\sqrt{2\pi r}} \operatorname{Re} \left[\frac{\mu_1 \mu_2}{\mu_1 - \mu_2} \left(\frac{1}{d_1} - \frac{1}{d_2} \right) \right. \\ &\quad \left. + \frac{K_{II}}{K_I} \frac{1}{\mu_1 - \mu_2} \left(\frac{\mu_1}{d_1} - \frac{\mu_2}{d_2} \right) \right] \end{aligned} \quad (65)$$

and

$$\begin{aligned} u &= K_I \sqrt{\frac{2r}{\pi}} \operatorname{Re} \left[\frac{1}{\mu_1 - \mu_2} \left(\mu_1 p_2 d_2 - \mu_2 p_1 d_1 \right. \right. \\ &\quad \left. \left. + \frac{K_{II}}{K_I} [p_2 d_2 - p_1 d_1] \right) \right] \\ v &= K_I \sqrt{\frac{2r}{\pi}} \operatorname{Re} \left[\frac{1}{\mu_1 - \mu_2} \left(\mu_1 q_2 d_2 - \mu_2 q_1 d_1 \right. \right. \\ &\quad \left. \left. + \frac{K_{II}}{K_I} [q_2 d_2 - q_1 d_1] \right) \right] \end{aligned} \quad (66)$$

Table 3 Normalized mode I SIFs for a 45° crack in an "infinite" plate.

L/a	Displacement correlation		MCCI		J-integral	
	I	% error	I	% error	I	% error
0.5	1.066	6.59	0.985	-1.53	1.003	0.27
0.25	1.033	3.30	0.989	-1.11	1.002	0.25
0.125	1.013	1.34	0.992	-0.83	1.002	0.20

Table 4 Normalized mode II SIFs for a 45° crack in an "infinite" plate.

L/a	Displacement correlation		MCCI		J-integral	
	I	% error	I	% error	I	% error
0.5	0.982	-1.77	0.968	-3.17	1.001	0.14
0.25	0.936	-6.43	0.959	-4.08	0.987	-1.26
0.125	0.905	-9.50	0.948	-5.19	0.971	-2.91

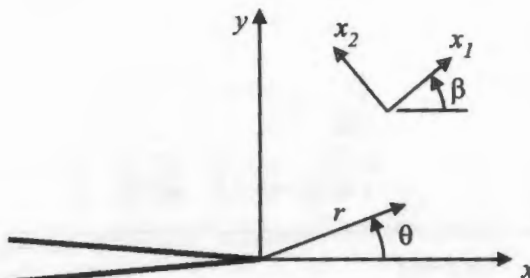


Figure 27 The crack-tip Cartesian and material coordinates.

with

$$\begin{aligned} d_i &= \sqrt{\cos \theta + \mu_i \sin \theta} \\ p_i &= S_{11}\mu_i^2 + S_{12} - S_{14}\mu_i \\ q_i &= S_{12}\mu_i + S_{22}/\mu_i - S_{24} \end{aligned} \quad (67)$$

Irwin's crack-closure integral (Irwin, 1957):

$$G = \lim_{\Delta L \rightarrow 0} \frac{1}{\Delta L} \int_0^{\Delta L} \sigma_{2i}(\Delta L - r, \theta = 0) u_i(r, \theta = \pi) dr, \quad (i = 1, 2) \quad (69)$$

This yields, separated by modes, the following expressions:

$$\begin{aligned} G_I &= -\frac{1}{2} K_I S_{22} \operatorname{Im} \left[\frac{K_I(\mu_1 + \mu_2) + K_{II}}{\mu_1 \mu_2} \right] \\ K_{II} &= \frac{1}{2} K_{II} S_{11} \operatorname{Im} [K_{II}(\mu_1 + \mu_2) + K_I \mu_1 \mu_2] \end{aligned} \quad (70)$$

In a FE context, the energy release rates can be computed with the J-integral approach (Section 3.01.3). Equations (70) can be solved for the SIFs

$$\begin{aligned} K_I &= \pm \frac{A_2 [2G_{II}S_{22}(A_0A_2 - A_1^2) - (G_I S_{11}A_3A_1^2 + G_{II}S_{22}(2A_0A_2 - A_1^2) \pm A_4)]}{A_3 [S_{11}S_{22}A_2(A_0A_2 - A_1^2)(G_I S_{11}A_3A_1^2 + G_{II}S_{22}(2A_0A_2 - A_1^2) \pm A_4)]^{1/2}} \\ K_{II} &= \pm \frac{[S_{11}S_{22}A_2(A_0A_2 - A_1^2)(G_I S_{11}A_3A_1^2 + G_{II}S_{22}(2A_0A_2 - A_1^2) \pm A_4)]^{1/2}}{S_{11}S_{22}A_2(A_0A_2 - A_1^2)} \end{aligned} \quad (71)$$

 μ_1 and μ_2 are the two roots with positive imaginary parts of the equation

$$S_{11}\mu^4 - 2S_{14}\mu^3 + 2(S_{12} + S_{44})\mu^2 - 2S_{24}\mu + S_{22} = 0 \quad (68)$$

(Since this equation has real coefficients, the roots will be two sets of complex conjugates).

Energy release rates for this case can be derived by substituting the stress and displacement expressions of Equations 65 and 66 into

with

$$\begin{aligned} A_0 &= \operatorname{Im}(\mu_1)[\operatorname{Im}(\mu_2)\operatorname{Re}(\mu_2)^2 + \operatorname{Im}(\mu_2)[\operatorname{Im}(\mu_1)\operatorname{Re}(\mu_1)]^2] \\ A_1 &= \operatorname{Re}(\mu_1)\operatorname{Im}(\mu_2) + \operatorname{Im}(\mu_1)\operatorname{Re}(\mu_2) \\ A_2 &= \operatorname{Im}(\mu_1) + \operatorname{Im}(\mu_2) \\ A_3 &= [\operatorname{Re}(\mu_1)\operatorname{Re}(\mu_2)]^2 + [\operatorname{Im}(\mu_1)\operatorname{Im}(\mu_2)]^2 \\ &\quad + [\operatorname{Re}(\mu_1)\operatorname{Im}(\mu_2)]^2 + [\operatorname{Im}(\mu_1)\operatorname{Re}(\mu_2)]^2 \\ A_4 &= A_1 [(G_I S_{11}A_3A_1)^2 + 2G_I G_{II}S_{11}S_{22}(2A_0A_2 - A_1^2) \\ &\quad - A_1^2 A_3] + (G_{II}S_{22}A_1)^2]^{1/2} \end{aligned} \quad (72)$$

The signs used for the full expressions and the A_4 terms of Equation (71) must be determined

Table 5 Signs for the full expression and the A_4 terms based on the signs of the COD and CSD.

		CSD	
		+	-
		full +	full -
COD	+	A_4 -	A_4 -
	-	full +	full -
		A_4 +	A_4 -

from the signs of the COD and crack sliding displacement (CSD). These signs are given in Table 5. For example, if the crack is opening (COD is positive) and the sliding displacement is negative, then negative signs should be used for both the full expressions in Equation (71) and the A_4 terms.

For the pure antiplane shear (mode III) case

$$u = v = 0 \quad w = w(x, y) \quad (73)$$

Hook's law for this case is

$$\begin{cases} \gamma_{yz} \\ \gamma_{zx} \end{cases} = \begin{cases} S_{55} & S_{56} \\ \text{sym} & S_{66} \end{cases} \begin{cases} \tau_{yz} \\ \tau_{zx} \end{cases} \quad \text{or}$$

$$\begin{cases} \tau_{yz} \\ \tau_{zx} \end{cases} = \frac{1}{S_{55}S_{66} - S_{56}^2} \begin{cases} S_{66} & -S_{56} \\ \text{sym} & S_{55} \end{cases} \begin{cases} \gamma_{yz} \\ \gamma_{zx} \end{cases} \quad (74)$$

The stress and displacement fields are

$$\begin{aligned} \tau_{yz} &= \frac{K_{III}}{\sqrt{2\pi r}} \operatorname{Re} \left[\frac{1}{\sqrt{\cos \theta + \mu_3 \sin \theta}} \right] \\ \tau_{zx} &= \frac{K_{III}}{\sqrt{2\pi r}} \operatorname{Re} \left[\frac{\mu_3}{\sqrt{\cos \theta + \mu_3 \sin \theta}} \right] \end{aligned} \quad (75)$$

and

$$w = K_{III} \sqrt{\frac{2r}{\pi}} \operatorname{Re} \left[\frac{(S_{55}S_{66} - S_{56}^2)\sqrt{\cos \theta + \mu_3 \sin \theta}}{\mu_3 S_{66} - S_{56}} \right] \quad (76)$$

where μ_3 is the root of the equation:

$$\frac{S_{66}\mu_3^2 - 2S_{56}\mu_3 + S_{55}}{S_{55}S_{66} - S_{56}^2} = 0 \quad (77)$$

with the positive imaginary part.

Again, using Irwin's crack closure integral, Equation (69), the expression for the energy release rate is:

$$G_{III} = \frac{1}{2} K_{III}^2 \frac{\operatorname{Im}[\mu_3 S_{66} - S_{56}]}{S_{55}S_{66}} \quad (78)$$

that can be solved simply for the stress intensity factor

$$K_{III} = \sqrt{\frac{2G_{III}S_{55}S_{66}}{\operatorname{Im}[\mu_3 S_{66} - S_{56}]}} \quad (79)$$

In summary, Sih, Paris, and Irwin developed expressions for the near-tip stress and displacement fields for cracks in orthotropic materials where one of the planes of material symmetry is perpendicular to the crack front, the plane of analysis (Equations (65) and (66)). Irwin's crack closure integral, Equation (69), can be used to relate the SIFs to the energy release rate, which for an LEFM analysis can be computed using FEs and the J -integral technique (Sections 3.01.3.4 and 3.01.3.5).

3.01.3.8 Considerations for Plate and Shell FEs

There are many practical applications of fracture mechanics to structures that can be idealized as thin plates or shells. For example, a typical narrow body transport aircraft has a fuselage radius of ~ 2 m (79 in). However, the skin thickness is only ~ 1 mm (0.4 in). Clearly, with a radius to thickness ratio of 2,000, thin shell assumptions are valid and economies can be realized in FE analysis if thin shell elements are used rather than modeling the fuselage with 3D elements (Potyondy *et al.*, 1995).

In this section, the SIFs for through cracks in plates that correspond to Kirchhoff and Reissner plate theories are presented. It is argued that the Kirchhoff assumptions are more appropriate for most FE analyses. Expressions for extracting the SIFs using a crack closure approach are then presented. Much of the material presented in this section follows very closely the work of Hui and Zehnder (1993).

A naive fracture analysis approach for plate and shell structures is to assume 2D (plane stress) behavior because the plate is flat or the radius of curvature of the shell is very large. This can lead to highly inaccurate (and usually unconservative) predictions. A 2D analysis ignores out-of-plane bending, which usually is the most flexible mode of deformation. For example, with aircraft fuselages or other pressure vessels, the internal pressure causes the crack faces to "bulge." This bulging behavior, illustrated in Figure 28, significantly increases the SIFs. Furthermore, the bulging effect is nonlinear. For small amounts of bulging the structure is very flexible for out-of-plane bending of the crack flanks. However, as the amount of bulging increases the fibers

parallel to the crack faces "stress stiffen," resisting further bulging.

When structures are idealized as thin plates or shells, it is normal to assume that the overall stresses and displacements are a combination of membrane behavior that is constant through the thickness, and bending behavior that has a through thickness variation. Similarly, membrane and bending fracture modes can be identified. These are shown in Figure 29. The symmetric and anti-symmetric membrane modes correspond to the plane stress modes I and II. The bending behavior can be separated into two modes also, corresponding to symmetric and anti-symmetric bending about the crack.

All plate theories make assumptions about the nature of the stress and displacement variation through the plate thickness. Two different plate theories, Kirchhoff theory (Timoshenko and Woinowsky-Krieger, 1959) and Reissner theory (Reissner, 1947)

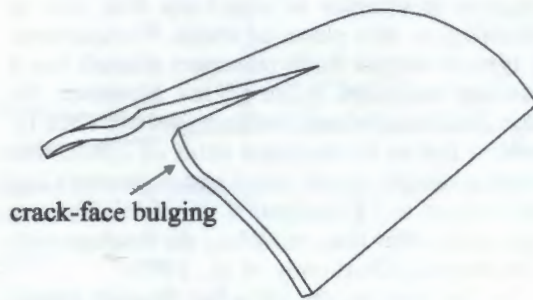


Figure 28 Illustration of crack-face bulging in a thin cylinder.

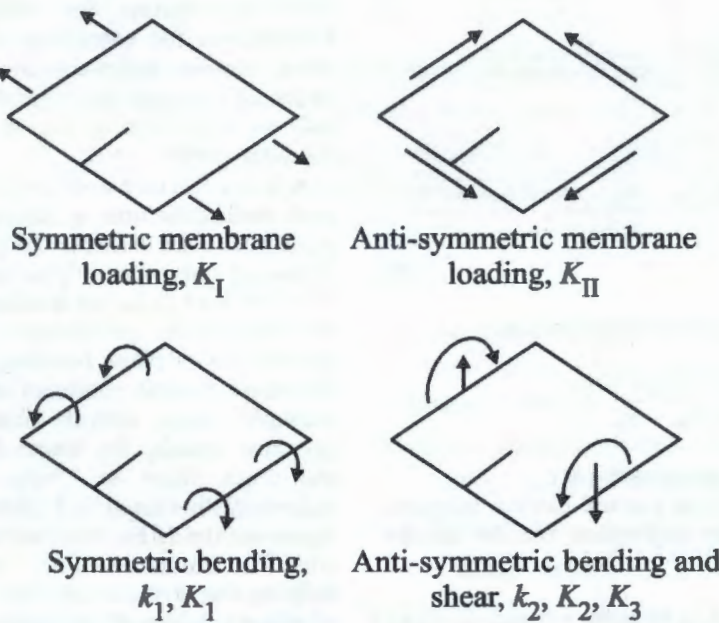


Figure 29 The four basic fracture modes for a thin cracked plate

are considered here. Each results in different bending SIFs. SIFs based on Kirchhoff bending are denoted k_1 and k_2 . SIFs based on Reissner theory are denoted K_1 , K_2 , and K_3 .

The stress field near the tip of a through crack in a thin elastic plate was first obtained by Williams (1961) using Kirchhoff assumptions. With respect to the coordinate system shown in Figure 30, these are

$$\begin{pmatrix} \sigma_{rr} \\ \sigma_{r\theta} \\ \sigma_{\theta\theta} \end{pmatrix} = \frac{k_1}{(3+v)\sqrt{2r}2h} z \times \begin{pmatrix} (3+5v)\cos(\theta/2) - (7+v)\cos(3\theta/2) \\ -(1-v)\sin(\theta/2) + (7+v)\sin(3\theta/2) \\ (5+3v)\cos(\theta/2) + (7+v)\cos(3\theta/2) \end{pmatrix} + \frac{k_2}{(3+v)\sqrt{2r}2h} \times \begin{pmatrix} (3-5v)\sin(\theta/2) + (5+3v)\sin(3\theta/2) \\ -(1-v)\cos(\theta/2) + (5+3v)\cos(3\theta/2) \\ -2(5+3v)\cos(\theta/2)\sin(\theta) \end{pmatrix} \quad (80)$$

$$\begin{pmatrix} \sigma_{rz} \\ \sigma_{\theta z} \end{pmatrix} = \frac{\left[1 - (2z/h)^2\right](h/2)}{(3+v)(2r)^{3/2}} \begin{pmatrix} -k_1\cos(\theta/2) + k_2\sin(\theta/2) \\ -k_1\sin(\theta/2) - k_2\cos(\theta/2) \end{pmatrix} \quad (81)$$

and

$$\sigma_{zz} = 0$$

Figure 3
in a plat

were v
thicknd
stress c
singula
by elas
stressed
Unlikd
of the
ratio. T
between
theory
off the
bounda

The
singula
has led
near-ti
(Know
1968; V
The res

$$\begin{pmatrix} \sigma_{rr} \\ \sigma_{r\theta} \\ \sigma_{\theta\theta} \end{pmatrix}$$

$$+ \frac{K_1}{\sqrt{2r}}$$

$$\begin{pmatrix} \sigma_r \\ \sigma_\theta \end{pmatrix}$$

With t
crack-
predict

With
SIFs a
two q
betwee
priate
and Z
J-integ
demon
ship
indepe
applie

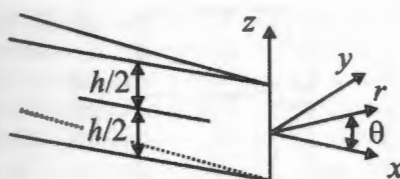


Figure 30 Coordinate system for a through crack in a plate.

were ν is the Poisson's ratio, h is the plate thickness, and k_1, k_2 are the SIFs. The in-plane stress components, $\sigma_{rr}, \sigma_{\theta\theta}, \sigma_{r\theta}$, have an $r^{-1/2}$ singularity, which is the same as predicted by elasticity theory. The out-of-plane shear stresses, σ_{rz} and $\sigma_{\theta z}$, have an $r^{-3/2}$ singularity. Unlike elasticity theory, the angular variation of the stress fields depends on the Poisson's ratio. The discrepancy in the stress singularity between the elasticity theory and the plate theory arises from the inability of the Kirchhoff theory to completely satisfy stress-free boundary conditions along the crack face.

The inconsistency in the order of the singularity for the out-of-plane shear stresses has led a number of authors to investigate the near-tip stress fields using Reissner plate theory (Knowles and Wang, 1960; Hartranft and Sih, 1968; Wang, 1970; Joseph and Erdogan, 1989). The resulting asymptotic crack-tip stress field is

$$\begin{pmatrix} \sigma_{rr} \\ \sigma_{r\theta} \\ \sigma_{\theta\theta} \end{pmatrix} = \frac{K_1}{\sqrt{2r}} \frac{z}{2h} \begin{pmatrix} 5\cos(\theta/2) - \cos(3\theta/2) \\ \sin(\theta/2) + \sin(3\theta/2) \\ 3\cos(\theta/2) + \cos(3\theta/2) \end{pmatrix} + \frac{K_2}{\sqrt{2r}} \frac{z}{2h} \begin{pmatrix} -5\sin(\theta/2) + 3\sin(3\theta/2) \\ \cos(\theta/2) + 3\cos(3\theta/2) \\ -3\sin(\theta/2) - 3\sin(3\theta/2) \end{pmatrix} \quad (82)$$

$$\begin{pmatrix} \sigma_{rz} \\ \sigma_{\theta z} \end{pmatrix} = \frac{K_3}{\sqrt{2r}} \left[1 - \left(\frac{2z}{h} \right)^2 \right] \begin{pmatrix} \sin(\theta/2) \\ \cos(\theta/2) \end{pmatrix} \quad (83)$$

With the exception of the z variation, these crack-tip stress fields are identical to those predicted by elasticity theory.

With two separate sets of relations for the SIFs and near tip stresses for cracks in plates, two questions arise: is there a relationship between them, and which set is more appropriate for use in a FE analysis? Hui and Zehnder (1993) used evaluations of the J -integral for the two crack-tip fields to demonstrate that there is a universal relationship between the two sets of SIFs that is independent of the specimen geometry and applied loading. These relationships are:

$$K_1/k_1 = [(1+\nu)/(3+\nu)]^{1/2} \quad (84)$$

and

$$k_2^2 \frac{1+\nu}{3+\nu} = K_2^2 + K_3^2 \frac{8(1+\nu)}{5} \quad (85)$$

The implication of this relationship is significant. From a FE analysis point of view, the important question is which plate theory should be used. The Reissner theory yields the expected singularity at the crack tip for all stress components. However, Hui and Zehnder argue that the region of dominance of the Reissner K field is $\sim h/10$. This is smaller than the expected plastic zone size for many engineering materials. The region of dominance of the Kirchhoff field is $\sim L/10$, where, similar to plane stress, L is a relevant in-plane dimension, such as crack length. Equations (84) and (85) demonstrate that the SIFs in the Reissner K -dominant zone are uniquely determined by the SIFs in the much larger Kirchhoff zone. This is similar to the concept of small-scale yielding in LEFM, where the size of the plastic zone is small compared to the region of dominance of the elastic K field. The behavior in the small-scale yielding zone is determined by the enclosing K field. This is illustrated schematically in Figure 31.

Therefore, for FE analysis, in most cases the Kirchhoff theory should be preferred, as the size of the region of dominance of this theory is similar to what one would expect for plane stress. This means that one could expect to be able to extract accurate Kirchhoff SIFs using "reasonably"-sized elements relative to the crack length (unlike the Reissner theory, where element sizes on the order of the plate thickness would be required). Furthermore, if needed, the Reissner SIFs can be determined from the Kirchhoff SIFs.

Moreover, both theories assume that the crack front is oriented perpendicular to the

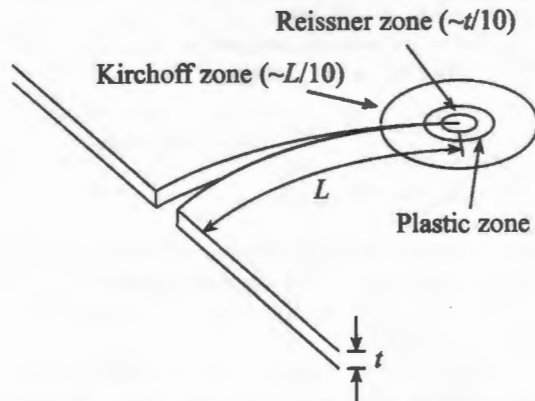


Figure 31 Schematic showing the relative sizes of the zone of dominance of the Kirchhoff and Reissner SIFs.

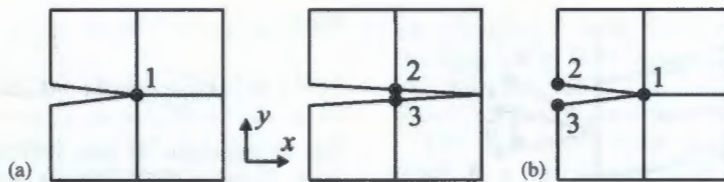


Figure 32 The nodes used for extracting energy release rates: (a) using two analyses and (b) using one analysis.

thickness of the crack. For many materials, metals in particular, this assumption is frequently violated, with "slant cracking" being typical. Obviously, deviation from the crack orientations assumption will have a much larger impact on the Reissner predictions, with a characteristic dimension of the plate thickness, than on the Kirchhoff predictions where the characteristic dimension is much larger, on the order of the crack length.

Among the important interim results in Hui and Zehnder's analysis are expressions for the relationship between the energy release rates and the Kirchhoff SIFs:

$$G_I = \frac{k_1^2 \pi (1 + v)}{3E(3 + v)} \quad \text{and} \quad G_{II} = \frac{k_2^2 \pi (1 + v)}{3E(3 + v)} \quad (86)$$

These can be used in combination with the plane stress expressions,

$$G_I = \frac{K_I^2}{E} \quad \text{and} \quad G_{II} = \frac{K_{II}^2}{E} \quad (87)$$

to extract SIFs from thin shell analyses, provided that the energy release rates can be computed from a FE analysis.

The Modified Crack Closure Integral was presented in Section 3.01.3.3. There it was shown that the energy released during crack growth is equal to the work done by the tractions acting over the area of crack extension. Switching, for the moment, to the notation that $x_1, x_2, x_3 = x, y, z$, for a linear elastic plate of thickness h , the energy release rate for a self-similar extension of a through-crack lying in the $x-z$ plane is (Irwin, 1957)

$$G = \lim_{\Delta L \rightarrow 0} \frac{1}{2h\Delta L} \int_0^{\Delta L} \int_{-h/2}^{+h/2} \sigma_{2i}(x_1, \theta = 0) \Delta u_i \times (\Delta L - x_1, \theta = \pi) dx_3 dx_1 \quad (88)$$

where Δu_i are the components of relative crack tip displacements for a crack extension of ΔL , and the repeated index i implies summation over $i = 1, 2, 3$.

Using the above crack closure integral, but segregating the displacements and stresses associated with each mode of fracture, Viz et al. (1995) developed expressions for the energy release rates in terms of nodal (general-

ized) forces and displacements. This was done for plate and shell FEs with linear shape functions. Figure 32(a) illustrates the procedure using two FE analyses. The forces and moments are extracted at node 1 (the crack tip) from the first analysis. The crack is then extended and the model is reanalyzed. The displacements and rotations are extracted from nodes 2 and 3 of the second analysis. The expressions for the (Kirchhoff) energy release rates are:

$$\begin{aligned} G_I &= \frac{1}{2} [F_y^1(u_y^2 - u_y^3) + M_z^1(\theta_z^2 - \theta_z^3)] \\ G_{II} &= \frac{1}{2} [F_x^1(u_x^2 - u_x^3)] \\ G_I &= \frac{1}{2} [M_x^1(\theta_x^2 - \theta_x^3)] \\ G_{II} &= \frac{1}{2} [F_z^1(u_z^2 - u_z^3) + M_y^1(\theta_y^2 - \theta_y^3)] \end{aligned} \quad (89)$$

where for the forces and displacements a superscript denotes the node number and a subscript denotes the direction (z is the out-of-plane direction). As with the planar analysis case, a similar computation can be performed using the results of only one analysis. The nodes used for this case are illustrated in Figure 32(b).

In summary, for through-cracks in thin plates and shells there are two membrane and two bending fracture modes. The SIFs for the membrane modes correspond to those of plane stress modes I and II. For bending, the definition of the SIFs depends on the plate theory used. Usually Kirchhoff plate theory is more appropriate for thin shell FE analysis, because the zone of dominance is on the order of the crack length, whereas the zone of dominance is on the order of the plate thickness for Reissner theory. Expressions for extracting energy release rates from a FE analysis are given in Equation (89). These can be used with Equations (86) and (87) to compute SIFs.

3.01.3.9 Summary

A number of different techniques for extracting SIFs from FE results were presented in this section. Of these, the J -integral approach is the most accurate and should be used prefer-

entially. Unfortunately, the implementation of the method is the most involved of those shown, and is aided if one has access to the FE programs subroutines for shape functions and numerical integration (often inaccessible to users of a commercial FE program). Obviously, these capabilities can be replicated in a stand-alone post-processing program for computing SIFs, but often acceptably accurate results can be obtained using the MCCI approach that uses only nodal displacements and forces, which are standard outputs from most FEM programs.

The displacement correlation technique is the least accurate but is simple enough that it is readily amenable to hand calculations. Also, because it does not require additional terms for cases with crack-face tractions or body forces, it provides a simple "sanity" check to make sure that the more accurate techniques are formulated and being used properly.

This section also described how some of these extraction techniques are used for cases in which the cracking material is anisotropic, and also for cases in which the cracking structure can best be modeled with plate or shell elements.

3.01.4 PREDICTING CRACK TRAJECTORY AND ITS STABILITY

This section addresses the problems of predicting crack trajectory and its stability. In LEFM the T -stress plays an important role in these problems. Here the T -stress is first defined. Then theories based on first-order trajectory formulations, in which T -stress is ignored, are presented as baselines for later comparison. First-order trajectory stability formulations that require T -stress calculation are then discussed. The next two subsections present models for materials with fracture resistance orthotropy in 2D and 3D. These are logically followed by presentation of theories for crack trajectory with T -stress effects in such materials. These theories accommodate a characteristic length and both modes I and II dominance. Finally, techniques for accurate calculation of T -stress using the FEM are presented.

3.01.4.1 Linear Elastic Crack Kinking due to Mixed-mode Loading without T -stress: First-order Kinking Theory

The mixed-mode expressions for the 2D elastic stress field around a crack tip, Figure 33, are given to the first two terms (Williams,

1957) as

$$\begin{aligned}\sigma_r = & \frac{1}{\sqrt{2\pi r}} \cos \frac{\theta}{2} \left[K_I \left(1 + \sin^2 \frac{\theta}{2} \right) \right. \\ & \left. + \frac{3}{2} K_{II} \sin \theta - 2 K_{II} \tan \frac{\theta}{2} \right] \\ & + \frac{T}{2} (1 + \cos 2\theta)\end{aligned}\quad (90)$$

$$\begin{aligned}\sigma_\theta = & \frac{1}{\sqrt{2\pi r}} \cos \frac{\theta}{2} \left[K_I \cos^2 \frac{\theta}{2} - \frac{3}{2} K_{II} \sin \theta \right] \\ & + \frac{T}{2} (1 - \cos 2\theta)\end{aligned}\quad (91)$$

$$\begin{aligned}\sigma_{r\theta} = & \frac{1}{2\sqrt{2\pi r}} \cos \frac{\theta}{2} [K_I \sin \theta + K_{II} (3 \cos \theta - 1)] \\ & - \frac{T}{2} \sin 2\theta\end{aligned}\quad (92)$$

where K_I and K_{II} are the SIFs associated with modes I and II loading as illustrated in Figure 34. The T -stress is the constant component of the stress field, and oriented parallel to the crack tip as shown in Figure 33.

Most of the studies related to crack turning found in the literature focus on determining the kink angle that occurs when a crack is loaded with in-plane asymmetry. The leading stress

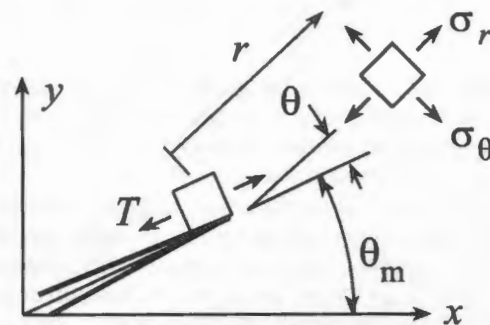


Figure 33 Crack-tip coordinate and stress notation.

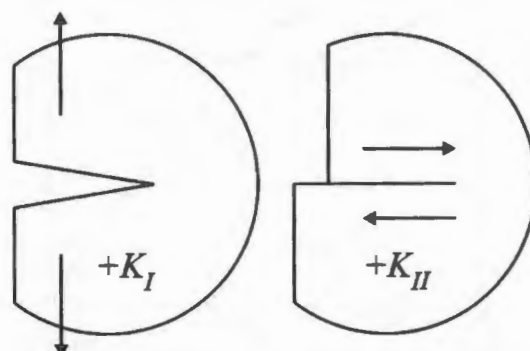


Figure 34 Illustration of crack-tip loading modes (shown with positive sense).

terms are singular in r , thus dominating crack-tip stresses in the elastic solution. Thus, with the tacit assumption that the mechanism by which the crack is directed occurs at or very close to the physical crack tip, the second- and higher-order terms are often neglected, even though they may be significant at some distance from the crack tip. In these first-order turning theories, the asymmetry is characterized exclusively in terms of the mode mixity, K_{II}/K_I . Second-order kinking theories, which assume a process zone size large enough for T -stress to affect the kink angle, are discussed in Section 3.01.4.5.

The classical first-order maximum tangential stress ($\sigma_{\theta\theta} \max$) theory, proposed by Erdogan and Sih (1963) for isotropic materials, asserts that the crack will grow in a direction normal to maximum tangential tensile stress. By differentiating the first term in Equation (91) with respect to theta and setting it to zero (equivalent to setting $\sigma_{r\theta}=0$), they obtained (shown somewhat rearranged):

$$\frac{K_{II}}{K_I} = \frac{-\sin \Delta\theta_c}{(3 \cos \Delta\theta_c - 1)} \quad (93)$$

or,

$$\Delta\theta_c = 2 \tan^{-1} \left(\frac{1 - \sqrt{1 + 8(K_{II}/K_I)^2}}{4(K_{II}/K_I)} \right) \quad (94)$$

where $\Delta\theta_c$ is the kink angle. This expression predicts straight crack growth unless $K_{II}=0$, as in asymmetric loading, or in the case of a crack with a perturbed trajectory.

Equation (94) is plotted in Figure 35, along with two other well-known first order linear elastic theories, the maximum energy release rate ($G(\theta)_{\max}$) theory proposed by Hussain *et al.* (1974), and the minimum strain energy density

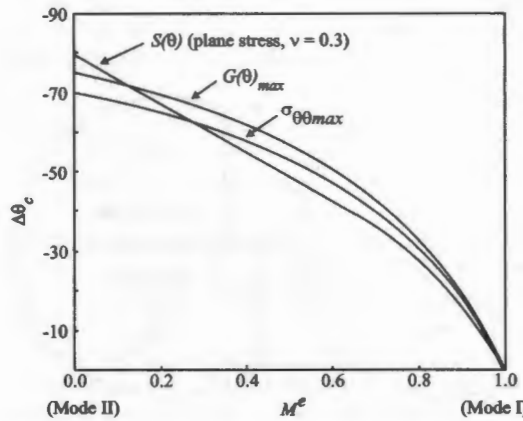


Figure 35 Comparison of first-order linear elastic crack kinking theories.

theory ($S(\theta)_{\min}$) proposed by Sih (1974). For convenience, the data is plotted using the mode mixity parameter:

$$M^e = \frac{2}{\pi} \tan^{-1} \left(\frac{K_I}{K_{II}} \right) \quad (95)$$

By assuming other quantities, such as maximum principal stress, maximum hoop strain and/or void growth, numerous first-order kinking criteria have been proposed (e.g., Maiti and Smith, 1983; Theocaris, 1989; Shirmohammadi, 1995).

For the most part, all these theories predict quite similar kink angles, particularly as $K_{II} \ll K_I$. Nevertheless, the data of many authors have been correlated with the various theories in an attempt to determine the most accurate. Noteworthy among the empirical studies in this respect is the very meticulous work of Maccagno and Knott (1989, 1991), who, unlike most authors, chose a specimen geometry with near zero T -stress in order to minimize higher-order effects. They also designed their specimens of sufficient thickness to ensure a plain strain state of stress near the crack tip. Their work included testing of plexiglass at room temperature, and various grades of steel at low temperature (-196°C, resulting in transgranular cleavage fracture), and showed that even for moderate amounts of ductility, the initial kink angle was well predicted by the maximum tangential stress theory of Erdogan and Sih. This was true even when the ductility was sufficiently high that they had to resort to an elastic-plastic failure criterion to correlate the fracture initiation loads. However, they cautioned that while this was true of the transgranular cleavage failure mode, it might not be true of other failure mechanisms.

Pook (1971), and Liu (1974) provided crack-kinking data for aluminum alloys that also correlate well with the maximum tangential stress theory, at least in the predominately mode I regime.

3.01.4.2 Linear Elastic Crack Path Stability in a T -stress Environment: First-order Crack-path Instability Theory

Notwithstanding the foregoing discussion of crack-kinking theories, the crack-turning problems encountered in many real structural applications are not really crack-kinking problems. In an average macroscopic sense, cracks typically initiate normal to the maximum tensile stress, and propagate in a rather smoothly curving fashion as the crack negotiates its way among the structural features of

the part. Since the first-order isotropic theories predict crack kinking for nonzero K_{II} , it would appear that the only way for a crack to propagate smoothly is for the crack to follow a path along which $K_{II}=0$. Since all the first-order isotropic theories agree exactly for this condition, the crack path is apparently independent of any first-order theory.

While it is true that at a sufficiently small scale the crack path is not smooth due to material inhomogeneities, microscopic failure phenomena, or fluctuations about a mean loading orientation, these anomalies may be considered random in nature, and may be viewed as perturbations to the crack path. Nevertheless, short of characterizing these perturbations and including them explicitly in a probabilistic analysis, it would appear that the best deterministic estimate of the crack path in an average sense would be the path for which $K_{II}=0$.

The above conclusion seems quite intuitive, and was suggested at least as early as Cotterell and Rice (1980), who further proved that for a crack propagating in pure mode I, the strain energy release rate is locally maximized for a straight crack extension. They started with an approximate kinked crack solution for infinitesimal kinks,

$$\begin{aligned} K_I &= C_{11}k_I + C_{12}k_{II} \\ K_{II} &= C_{21}k_I + C_{22}k_{II} \end{aligned} \quad (96)$$

where k_I and k_{II} are the stress intensities of the lead (unkinked) crack, K_I and K_{II} are the resulting stress intensities at the kink tip, and

$$\begin{aligned} C_{11} &= \frac{1}{4}[3\cos(\Delta\theta/2) + \cos(3\Delta\theta/2)] \\ C_{12} &= -\frac{3}{4}[\sin(\Delta\theta/2) + \sin(3\Delta\theta/2)] \\ C_{21} &= \frac{1}{4}[\sin(\Delta\theta/2) + \sin(3\Delta\theta/2)] \\ C_{22} &= \frac{1}{4}[\cos(\Delta\theta/2) + 3\cos(3\Delta\theta/2)] \end{aligned} \quad (97)$$

that was shown accurate to the second order in $\Delta\theta$. For small angles,

$$\begin{aligned} K_I &= C_{11}k_I = k_I[1 - \frac{3}{8}\Delta\theta^2] + O(\Delta\theta^3) \\ K_{II} &= C_{21}k_I = -\frac{\Delta\theta}{2}k_I + O(\Delta\theta^3) \end{aligned} \quad (98)$$

The potential energy release rate is (plane stress)

$$\begin{aligned} G &= \frac{1}{E}(K_I^2 + K_{II}^2) \\ &= \frac{1}{E}(1 - \frac{1}{2}\Delta\theta^2)K_I^2 + O(\Delta\theta^3) \end{aligned} \quad (99)$$

that is clearly maximized for $\Delta\theta=0$.

Cotterell and Rice then considered the future path of an (initially straight) crack propagating in pure mode I as shown in Figure 36, subject

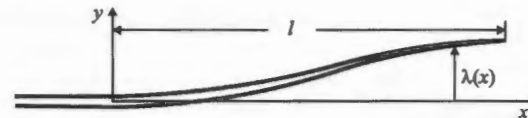


Figure 36 Schematic of a growing crack.

to a small perturbation in k_{II} as the crack reaches the origin of the local coordinate system indicated. They retained the T -stress term in their calculations to observe its influence on the crack path.

Based on a formulation of their own derivation that integrates the tractions due to the lead crack stress field over the developing crack path to obtain the SIFs at the crack tip, they obtained for K_{II} :

$$K_{II} = k_{II} + \frac{1}{2}\lambda'(l)k_I - \sqrt{\frac{2}{\pi}}T \int_0^l \frac{\lambda'(x)}{\sqrt{l-x}} dx \quad (100)$$

accurate to the first order in λ' , the slope of the extending crack. Cotterell and Rice gave evidence that this solution was accurate to within $\sim 5\%$ up until the slope of the extending crack exceeds 15° . Setting $K_{II}=0$ at the developing crack tip:

$$\theta_0 = \lambda'(l) - \frac{\beta}{\sqrt{\pi}} \int_0^l \left[\frac{\lambda'(x)}{\sqrt{l-x}} \right] dx \quad (101)$$

where

$$\begin{aligned} \theta_0 &= -2\frac{k_{II}}{k_I} \\ \beta &= 2\sqrt{2}\frac{T}{k_I} \end{aligned} \quad (102)$$

Note that the expression for the small perturbation angle, θ_0 , has been defined in such a way as to be in agreement with Equation (94) as K_{II} becomes small compared to K_I . Solving equation (101) for $\lambda(x)$ using the method of Laplace transforms, Cotterell and Rice obtained,

$$\lambda(x) = \frac{\theta_0}{\beta^2} \left[\exp(\beta^2 x) \operatorname{erfc}(-\beta\sqrt{x}) - 1 - 2\beta\sqrt{\frac{x}{\pi}} \right] \quad (103)$$

that is plotted in normalized format in Figure 37.

The primary conclusion drawn is that if $T>0$, the crack path diverges, if $T<0$, the crack path turns back toward a relatively straight trajectory after the initial perturbation. These behaviors are in qualitative agreement with test data, e.g., Leevens and Radon (1982).

The predicted rate of divergence is proportional to the perturbation and the square of the T -stress. A similar analysis was performed by Sumi *et al.* (1985), who included one additional higher-order term in the stress field expansion,

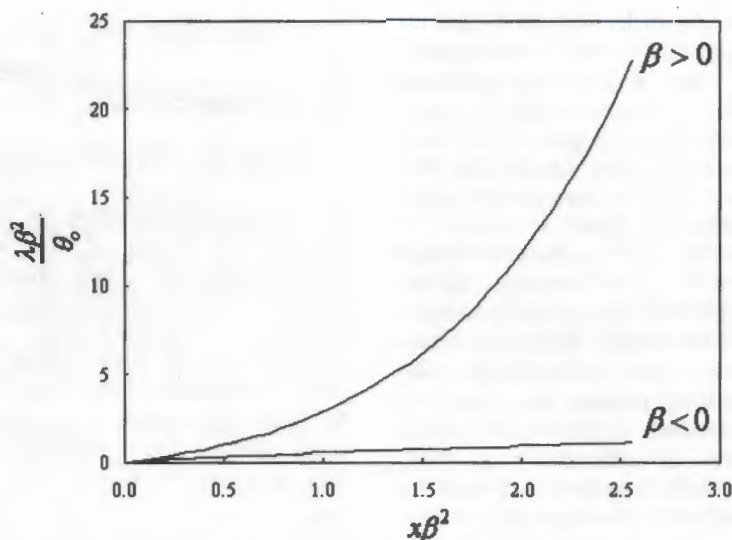


Figure 37 Normalized plot of the perturbed crack path of Cotterell and Rice (1980).

and who was able to obtain additional information about whether the crack was approaching a region of greater stability or instability.

First-order linear elastic crack kinking theory has been presented. First-order refers in this sense to the absence of the T -stress or higher-order crack-tip field parameters in the crack-kinking expression. This infers that the theory either assumes a process zone of negligible size, or allows a finite process zone, but excludes or neglects the presence of higher-order terms in the analysis. All first-order theories predict kinking for nonzero K_{II} , thus inferring that the crack path will be smooth only if $K_{II}=0$.

Crack-path instability theory has been presented in the case where the linear elastic crack-kinking theory is construed to admit the presence of T -stress, but (tacitly) with vanishing process zone size so that the kinking theory is first order ($K_{II}=0$). A divergent crack path is predicted in the presence of positive (tensile) T -stress, which is in qualitative agreement with observation. This behavior will be referred to hereafter as the “first-order crack-path instability” associated with the T -stress.

3.01.4.3 Fracture Resistance Orthotropy in 2D

In general, materials may exhibit elastic anisotropy as well as anisotropy in fracture resistance. Both forms of anisotropy can have significant effects on crack trajectory. Many materials, such as wrought metal products, are virtually isotropic elastically, but have a preferred direction of (mode I) crack propagation

resulting from the manner in which the material is processed. Often, as for rolled sheet or plate, the processing is of symmetric character, and the 2D relation describing the crack growth resistance as a function of orientation has two axes of symmetry. This special case is referred to hereafter as 2D fracture toughness orthotropy. For convenience, the orientation describing the crack angle in material coordinates is measured from the longitudinal grain direction, which corresponds to the rolling direction for rolled products. The crack growth resistance is maximum for growth across the rolling direction ($\theta=90^\circ$, or L-T) and minimum for growth parallel to the rolling direction ($\theta=0^\circ$, or T-L), e.g., Lemant and Pineau (1981). Materials produced by other processes, such as extrusion, and to a lesser extent forgings, would be expected to exhibit comparable symmetries, at least locally.

One can approximate the orthotropic crack growth resistance as a function of θ of the form (Chen, 1999):

$$K_p(\theta)^n \left(\frac{\cos^2 \theta}{K_p(0^\circ)^n} + \frac{\sin^2 \theta}{K_p(90^\circ)^n} \right) = 1 \quad (104)$$

where n is a constant exponent. For the present study, K_p is taken to represent the stress intensity at which the crack propagates. It has been proposed (Pettit *et al.*, 1997) that K_p is a material-dependent function of the orientation of the crack tip consistent with the regime of crack growth. Thus, for fatigue crack growth, K_p represents the stress intensity at which the crack propagates at a given rate; for

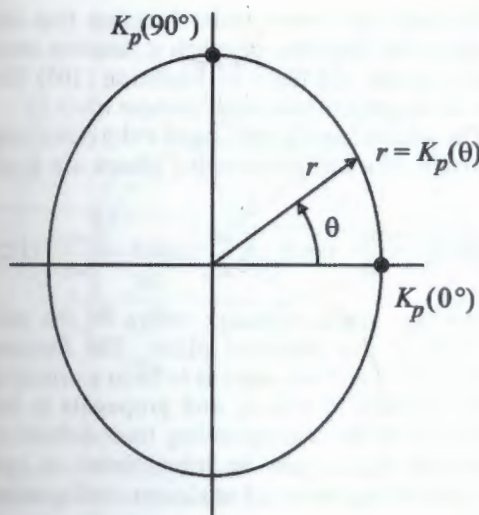


Figure 38 Assumed elliptical function describing crack growth resistance as a function of orientation for materials with fracture resistance orthotropy.

stable tearing, K_p represents the fracture toughness.

In the context of a maximum stress theory, Buczek and Herakovich (1985) suggested a fracture resistance orthotropy relation equivalent to setting $n = -1$. They deduced the form of the equation by requiring that the toughness function be independent of θ for isotropic materials, and that it possess the desired orthogonal symmetry, collocating to $K_p(0^\circ)$ and $K_p(90^\circ)$ values. Kfouri (1996) used the more familiar form of an ellipse ($n = 2$). Either case produces a nearly identical oblong shape in polar coordinates for fairly small orthotropy ratios, as illustrated in Figure 38. However, for severe values of orthotropy, positive exponents result in an unjustifiably spiked relationship, as illustrated in Figure 39, plotted in a normalized format given below. In the absence of data to show otherwise, the use of $n = -1$ is favored, or

$$K_p(\theta) = K_p(0^\circ) \cos^2 \theta + K_p(90^\circ) \sin^2 \theta \quad (105)$$

For the 2D problem we define the normalized crack growth resistance as:

$$\bar{K}(\theta) \equiv \frac{K_p(\theta)}{K_p(0^\circ)} \quad (106)$$

which varies between unity and \bar{K}_m , where \bar{K}_m is the fracture resistance orthotropy ratio defined by

$$\bar{K}_m \equiv \frac{K_p(90^\circ)}{K_p(0^\circ)} \quad (107)$$

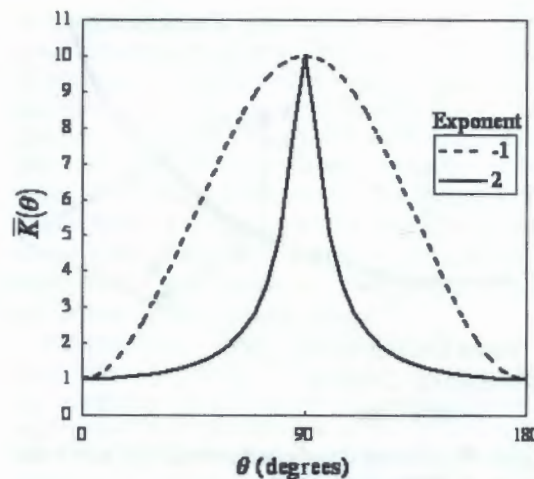


Figure 39 The orthotropic toughness function, $\bar{K}(\theta)$, evaluated for $\bar{K}_m = 0.1$.

One can rewrite Equation (104) in normalized form as

$$\bar{K}(\theta) = (\cos^2 \theta + \bar{K}_m \sin^2 \theta)^{-1/n} \quad (108)$$

or, for $n = -1$:

$$\bar{K}(\theta) = \cos^2 \theta + \bar{K}_m \sin^2 \theta \quad (109)$$

Unless otherwise specified, \bar{K} and \bar{K}_m will be assumed to apply to mode I dominated crack growth, and could thus be designated \bar{K}_I and \bar{K}_{Im} . For convenience, the modal subscripts will be omitted unless clarity requires them.

3.01.4.4 Fracture Resistance Orthotropy in 3D

In a 3D body a crack may be nonplanar, and oriented arbitrarily. At any point along the crack front in an orthotropic material, however, one can characterize the local orientation in terms of the tangent plane and the crack front normal vector within that plane, defined relative to the principal axes of the material.

For an orthotropic material such as a rolled or extruded plate, there are three orthogonal planes of symmetry. Within each of these planes there are thus two orthogonal axes of symmetry. This results in six principal fracture toughness values. The material is assumed to be homogeneous, thus the toughness for a given orientation relative to these principal planes is invariant with regard to translation.

Following the convention established for metals (Goode, 1972), the principal values of fracture toughness are written in a two-letter code ($i-j$) where the first letter refers to the principal axis normal to the crack plane, and the second subscript identifies the principal axis

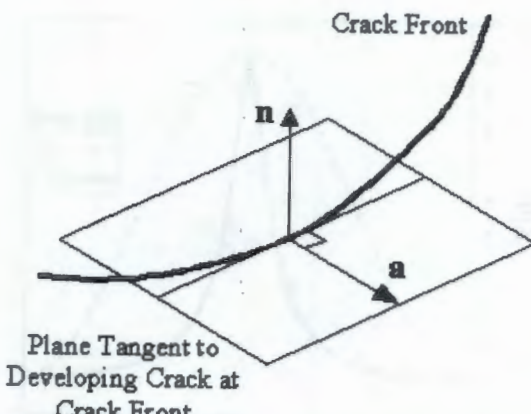


Figure 40 Geometry of crack orientation at a point on an arbitrary crack front.

corresponding to the direction of propagation. These designations have already been mentioned. The standard principal axes for rectangular products (plate, extrusion and forging) correspond to the longitudinal grain orientation (L), the long transverse grain orientation (T), and the short transverse grain orientation (S). Thus, a crack growing normal to the width in the rolling direction of a plate corresponds to the T-L orientation. The (mode I) fracture resistance in this direction we shall designate as K_{TL} . For convenience and generality, we will use numeric subscripts (1,2,3) in place of the metallurgical (L, T, S). The six principal fracture resistances are thus K_{12} , K_{21} , K_{23} , K_{32} , K_{13} , and K_{31} .

What is needed is a function to interpolate the fracture resistance for arbitrary orientations in terms of these principal values. As illustrated in Figure 40, a crack (or a point on an arbitrary crack front) may propagate in an arbitrary direction defined by unit vector

$$\mathbf{a} = a_1 \mathbf{i} + a_2 \mathbf{j} + a_3 \mathbf{k} \quad (110)$$

where \mathbf{i} , \mathbf{j} , and \mathbf{k} are unit vectors corresponding to the principal material axes x_1 , x_2 , and x_3 . Vector \mathbf{a} lies within a plane tangent to the developing crack surface at the crack front, which plane is uniquely described by its unit normal vector:

$$\mathbf{n} = n_1 \mathbf{i} + n_2 \mathbf{j} + n_3 \mathbf{k} \quad (111)$$

The crack orientation is uniquely defined by the direction cosines a_i and n_i . Following the work of Buczek and Herakovich, the interpolation function must

- (i) be independent of a_i and n_i for an isotropic material, and
- (ii) return the principal fracture resistances for cracks in the corresponding principal orientations.

We seek the lowest order function that can achieve this. Presumably such a function must revert to the 2D form of Equation (105) (for this development, we shall assume $n = -1$).

The angles (using right-hand rule) describing the trace of \mathbf{a} on the principal planes are given by

$$\tan(\theta_1) = \frac{a_3}{a_2} \quad \tan(\theta_2) = \frac{a_1}{a_3} \quad \tan(\theta_3) = \frac{a_2}{a_1} \quad (112)$$

where the angle subscript refers to the axis normal to the principal plane. The fracture resistance of a crack, were it to lie in a principal plane normal to axis x_k and propagate in the direction of the corresponding trace defined in Equation (112), can be interpolated in two dimensions in a manner analogous to Equation (105):

$$K_k(\theta_k) = K_{ki} \cos^2 \theta_k + K_{kj} \sin^2 \theta_k \quad (113)$$

Further observing the trigonometric identity:

$$\begin{aligned} \cos^2 \left(\tan^{-1} \frac{b}{c} \right) &= \frac{c^2}{b^2 + c^2} \\ \sin^2 \left(\tan^{-1} \frac{b}{c} \right) &= \frac{b^2}{b^2 + c^2} \end{aligned} \quad (114)$$

and the property of direction cosines

$$a_1^2 + a_2^2 + a_3^2 = 1 \quad (115)$$

one can combine Equations (113) and (114) to write

$$\begin{aligned} K_1(\mathbf{a}) &= \frac{1}{1 - a_1^2} (K_{12} a_2^2 + K_{13} a_3^2) \\ K_2(\mathbf{a}) &= \frac{1}{1 - a_2^2} (K_{23} a_3^2 + K_{21} a_1^2) \\ K_3(\mathbf{a}) &= \frac{1}{1 - a_3^2} (K_{31} a_1^2 + K_{32} a_2^2) \end{aligned} \quad (116)$$

In essence, these may be considered as the fracture resistance components of \mathbf{a} in the principal planes, as illustrated in Figure 41. Presumably, they must be summed in some weighted combination based on crack-plane normal \mathbf{n} to obtain the effective fracture resistance, $K_p(\mathbf{a}, \mathbf{n})$. Since the weight factors must sum to unity to satisfy the isotropic case, it seems reasonable to write

$$\begin{aligned} K_p(\mathbf{a}, \mathbf{n}) &= K_1 n_1^2 + K_2 n_2^2 + K_3 n_3^2 \\ &= \frac{n_1^2}{1 - a_1^2} (K_{12} a_2^2 + K_{13} a_3^2) \\ &\quad + \frac{n_2^2}{1 - a_2^2} (K_{23} a_3^2 + K_{21} a_1^2) \\ &\quad + \frac{n_3^2}{1 - a_3^2} (K_{31} a_1^2 + K_{32} a_2^2) \end{aligned} \quad (117)$$

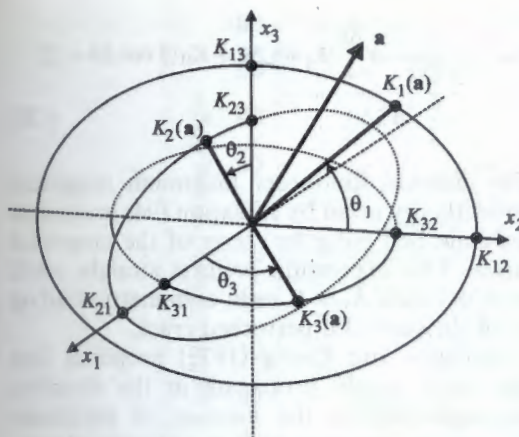


Figure 41 Principal orthotropic components of crack growth resistance for crack growth parallel to unit vector \mathbf{a} .

An inspection of Equation (117) shows that it satisfies the criteria previously outlined.

3.01.4.5 Crack-turning Theories with Process Zone Effects and Fracture Resistance Orthotropy

The purpose of this section is to develop practical approaches to simulate crack turning in 2D, including process zone effects and fracture resistance orthotropy. Two methods with regard to crack-path simulation beyond that presented in Section 3.01.4.1 are available: a second-order linear elastic approach which includes a single empirical process zone parameter (Finnie and Sait, 1973), and a fully elastic-plastic approach which directs the crack based on the crack-tip opening displacement (Sutton *et al.*, 2000; James, 1998). In order to be useful in practical problems, both methods have been extended to account for fracture toughness orthotropy, based on the 2D approach of Section 3.01.4.3. However, only the former method will be described in this chapter.

Both methods have been implemented into the FRANC2D or FRANC2D/L (2002) adaptive mesh, FE fracture simulation environment, building on the work of previous researchers (Pettit *et al.*, 1997). Therefore, it is appropriate to begin with a brief discussion of the piecewise, linear manner in which cracks are represented in such simulations.

3.01.4.5.1 Representation of a curvilinear crack by a series of segments

In Section 3.01.4.2, the statement was made that "the crack turning problems encountered

in many structural applications are not really crack kinking problems." From the first-order theoretical perspective, this meant that a "real" smoothly curving crack followed $K_{II}=0$ regardless of the kinking theory used, suggesting that the kinking theories are virtually irrelevant. With the exception of the initial kink angle when a crack initiates from a mixed-mode load state, and, provided that process zone effects and toughness anisotropy effects are absent, this is largely true.

Nevertheless, when simulating the crack path, it is typically convenient to represent the curved crack as a union of a series of linear segments, thus involving a series of kinks. In the FRANC2D environment, the need to kink reflects a limitation of the quadratic element type used, as well as to the fact that the small amount of mode II stress intensity detected at each step is used to determine the incremental path of the crack by virtue of some kinking theory. The program remeshes in the region of the crack tip for each step. Ideally, the path so determined should converge to the "true" crack path as the step size and element size is reduced.

For the isotropic case, following the $K_{II}=0$ criterion, a method was proposed by Stone and Babuška (1998) to model the crack path as a C^1 continuous (kink-free) series of polynomial segments. They implemented their approach in a p-element program using quadratic segments. Two of the three coefficients associated with the quadratic polynomial of each segment were defined to make the path C^1 continuous. The remaining coefficient was iterated to drive K_{II} at the tip of the crack extension to zero within some tolerance.

Stone and Babuška provided theoretical and numerical evidence to substantiate that this method indeed converges to an arbitrarily accurate approximation (limited by the accuracy of the stress intensity solution) of the true crack path, so long as the junctions between segments are at least C^1 continuous. Kinks, of course, are only C^0 continuous, and the theory could not prove convergence in this case. Nevertheless, Stone and Babuška performed a highly accurate analysis of a curvilinear crack spanning an arc of $\sim 27^\circ$, and compared the path with paths developed by various sequences of quadratic segments, and also by sequences of linear segments using the kinking criterion of Equation (93). As the step size was reduced, the kink angles also reduced, thus approaching a smooth crack path. While the curvilinear method was seen to converge more rapidly (with fewer segments) than the kinked crack approximation, it seems apparent from their results that if the kink

angles are below 10° for the propagating crack, the path is probably of sufficient accuracy for most engineering purposes. With adaptive mesh codes, such convergence is easily obtained, as observed by Wawrynek and Ingraffea (1987), and Knops (1994), among others.

This is not surprising in view of the results presented in Section 3.01.4.2. There it was shown that, in many respects, a slightly curved crack (limited to a threshold of 15° arc by Cotterell and Rice) can be represented to the first order in arc angle by a straight line with an infinitesimal kink at the tip, aligned with the tip of the true curved crack. Thus, one might expect that a slightly curved segment would be sufficiently well represented by a straight segment with an infinitesimal kink oriented tangent to the direction of the next segment (determined according to the criterion $K_{II}=0$). Note that for small K_{II}/K_I , Equation (94) predicts turning angles resulting in $K_{II}=0$ to the first order in θ , as can be verified by Equation (100).

The above discussion is based on first-order, isotropic crack-kinking theory, but at least provides support to the notion that for other crack-kinking theories, an assemblage of straight segments should converge to a correct theoretical crack path if, as the segment length is reduced, the discrete turning angles become small in regions of curvilinear growth. Of course, this restriction does not apply at the first kink of a crack loaded with mixed mode loading, where the physical fracture response is well represented by a kink.

3.01.4.5.2 Second-order, linear elastic, isotropic maximum stress kinking theory

The mixed mode expressions for the elastic stress field around a crack tip including the first two terms are

$$\sigma_r = \frac{1}{\sqrt{2\pi r}} \cos \frac{\Delta\theta}{2} \left[K_I \left(1 + \sin^2 \frac{\Delta\theta}{2} \right) + \frac{3}{2} K_{II} \sin \Delta\theta - 2K_{II} \tan \frac{\Delta\theta}{2} \right] + \frac{T}{2} (1 + \cos 2\Delta\theta) \quad (118)$$

$$\sigma_\theta = \frac{1}{\sqrt{2\pi r}} \cos \frac{\Delta\theta}{2} \left[K_I \cos^2 \frac{\Delta\theta}{2} - \frac{3}{2} K_{II} \sin \Delta\theta \right] + \frac{T}{2} (1 - \cos 2\Delta\theta) \quad (119)$$

$$\begin{aligned} \sigma_{r\theta} = & \frac{1}{2\sqrt{2\pi r}} \cos \frac{\Delta\theta}{2} [K_I \sin \Delta\theta + K_{II}(3 \cos \Delta\theta - 1)] \\ & - \frac{T}{2} \sin 2\Delta\theta \end{aligned} \quad (120)$$

The classical first-order maximum tangential stress theory given by Equation (94) maximizes only the first (singular) term of the tangential stress. This expression predicts straight crack growth unless $K_{II} \neq 0$, as in asymmetric loading or in the case of a perturbed crack.

Williams and Ewing (1972) proposed that the crack would propagate in the direction corresponding to the location of maximum tangential stress evaluated at a material-dependent finite distance, r_c , ahead of the crack tip, and included the second term in the crack-tip stress field expansion. Finnie and Saith (1973) corrected the formulation of Williams and Ewing for the angled crack problem, and Kosai *et al.* (1992) later derived a more general formulation of the same second-order theory by forcing the $\Delta\theta$ derivative of Equation (119) to zero at $r=r_c$ to obtain the implicit expression:

$$\begin{aligned} \frac{K_{II}}{K_I} = & \frac{-2 \sin(\Delta\theta_c/2)}{(3 \cos \Delta\theta_c - 1)} \\ & \left[\cos \frac{\Delta\theta_c}{2} - \frac{8}{3} \frac{T}{K_I} \sqrt{2\pi r_c} \cos \Delta\theta_c \right] \end{aligned} \quad (121)$$

Note that according to this expression, the crack may turn with sufficient T -stress even if $K_{II}=0$. In this case, Equation (121) yields $\Delta\theta_c > 0$ only if Finnie and Saith's inequality is satisfied.

$$r_c > r_o = \frac{9}{128\pi} \left(\frac{K_I}{T} \right)^2 \quad (122)$$

where, for $T > 0$, r_o represents the distance forward of the crack tip at which the angle of maximum tangential stress becomes nonzero. In Figure 42, Equation (121) is plotted in normalized format using the dimensionless parameter (defined to result in a bifurcation value of unity):

$$T \equiv \frac{8}{3} \frac{T}{K_I} \sqrt{2\pi r_c} = \frac{T}{|T|} \sqrt{\frac{r_c}{r_o}} \quad (123)$$

Equation (121) can be rewritten in terms of T :

$$T = \frac{\sin \Delta\theta_c + (K_{II}/K_I)(3 \cos \Delta\theta_c - 1)}{2 \sin(\Delta\theta_c/2) \cos \Delta\theta_c} \quad (124)$$

From Figure 42, straight crack growth is predicted only for the case where $K_{II}=0$, and $r_o > r_c$. As r_o approaches r_c , the predicted path becomes very sensitive to small amounts of K_{II} .

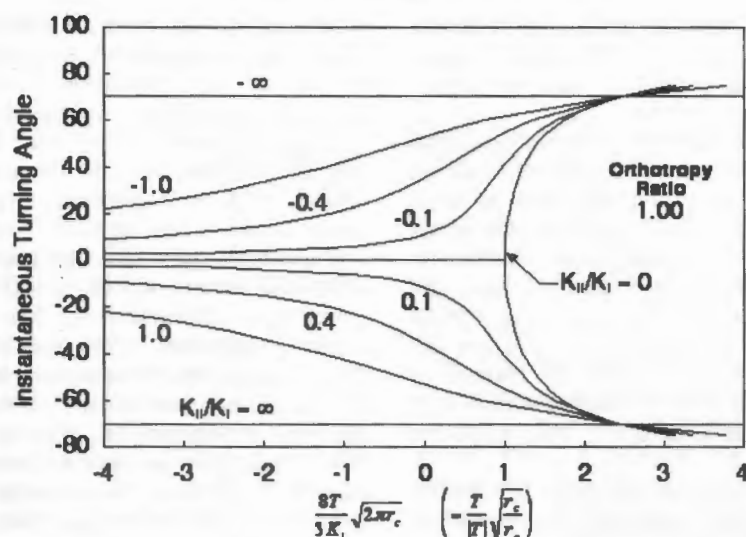


Figure 42 Normalized crack turning plot for isotropic material based on the formulation of Kosai *et al.* (1992).

As should be the case, with $T=0$ or $r_c=0$, the maximum tangential stress theory of Equation (124) reduces to the first order theory of Equation (93). As has been mentioned, Equation (93) can be derived either by maximizing σ_θ or by setting $\sigma_{r\theta}=0$.

In the case of finite T -stress, one might likewise consider enforcing $\sigma_{r\theta}=0$ to obtain

$$T_{(\sigma_{r\theta} \rightarrow 0)} = \frac{4}{3} \left(\frac{\sin \Delta\theta_c + (K_{II}/K_I)(3 \cos \Delta\theta_c - 1)}{2 \sin (\Delta\theta_c/2) \cos \Delta\theta_c} \right) \\ = \frac{4}{3} T \quad (125)$$

that indicates that the two criteria predict identical kink angles if one recognizes that the applicable characteristic lengths are related by

$$r_{c(\sigma_{r\theta} \rightarrow 0)} = \frac{16}{9} r_c \quad (126)$$

where the unsubscripted r_c is the characteristic length pertaining to the maximum tangential stress theory defined previously. Thus, the definition of the characteristic length may vary with the criterion used. Before formulating the extension to fracture orthotropy, a discussion with regard to the physical basis and determination of the characteristic length is in order.

3.01.4.5.3 The characteristic length, r_c , of the second-order maximum tangential stress theory

Irwin (1960), Dugdale (1960) and others gave approximate expressions for the size of plastic zone in front of a crack tip in elastic-plastic materials. Reasoning that r_c is related to some failure process, it seems probable that the characteristic length associated with the

maximum tangential stress crack-turning theory should be no larger than the inelastic zones identified.

Rice and Johnson (1969) discussed the role of various characteristic lengths associated with microscopic failure mechanisms in elastic-plastic materials, including the crack blunting radius and void spacing, in the context of plain strain fracture problems. As mentioned previously, the characteristic length associated with crack turning was proposed by Williams and Ewing. As an estimate of the characteristic length for PMMA (plexiglass), they referenced a previous work by Constable *et al.* (1970) that identified equivalent flaw sizes based on fatigue thresholds in polyvinyl chloride of the order of 0.064 mm (0.0025 in). Constable *et al.* conjectured that the equivalent flaw effect might be associated with crazing.

Using photoelastic methods to observe path instability of a nominally symmetric specimen, Ramulu and Kobayashi (1983) experimentally determined r_c for PMMA to be 1.27 mm (0.05 in). This was a considerably larger value than those obtained by prior authors, but Theocaris and Andrianopoulos (1982) independently obtained similar results. While the independent corroboration of r_c data from these authors would seem encouraging, the characteristic length estimate was more than an order of magnitude larger than the plane stress Irwin plastic zone size for this material. Further, based on the fracture toughness and critical T -stress for crack path instability in PMMA given by Selvarathinam and Goree (1998), Equation (122) would yield a value of $r_c = 2.54$ mm (0.1 in). While the cohesive, strain-softening nature of fracture in this

material could enlarge the process zone somewhat, these values of r_c would seem too large based on the scale of any known failure mechanism in that material.

Because imperfections or perturbations giving rise to small amounts of K_{II} can be found in any real cracked structure, the onset of path instability in nominally symmetric specimens would be expected to occur at an r_o value in excess of r_c . Note from Figure 42 that the predicted sensitivity even to very small amounts of K_{II} is substantial as one nears the bifurcation. The more sensitive the manner in which the onset of path instability is detected, the larger the overestimate of r_c that might be expected.

Also using photoelastic methods to observe the onset of path instability in symmetric specimens, Streit and Finnie (1980) determined r_c for 7075-T651 aluminum plate to be 0.254 mm (0.010 in). They described r_c as the distance at which void growth or crack initiation will occur, referencing Rice and Johnson and others. Using values of strength and toughness they provided, their value of r_c is ~ 0.7 times the size of the plane strain Irwin plastic zone radius (plane strain assumed based on their specimen configuration).

Kosai *et al.* (1992) later estimated r_c for 2024-T3 and 7075-T6 sheet to be 1.52 mm (0.06 in) based on the lengths of micro-crack branches observed along dynamic fracture surfaces of test specimens. This is considerably larger than the value given by Streit and Finnie for 7075-T651 plate, but the method of determination of r_c is completely different from previous methods, and the thickness of the material used would justify a plane stress assumption. In this case, the characteristic length estimate is about a third of the plane stress Irwin plastic zone size for 7075-T6, and more than an order of magnitude less than the plastic zone size of 2024-T3.

Pettit *et al.* (1997) found that severe path instability occurred consistently in 2024-T3 double cantilever beam specimens at values of r_o at least as high as 2.8 mm (0.11 in) (the specimen with the shortest crack, and lowest T -stress tested). To obtain an estimate of r_c , the turning radius was plotted as a function of r_o , and extrapolated to zero turning radius (a sharp kink), at critical value of $r_o = 1.27$ mm (0.05 in). This was subsequently used as a conservative estimate of r_c , though it tended to underestimate crack turning in crack-turning simulations. Chen (1999) used an r_c value of 2.29 mm (0.09 in) to obtain improved correlation with Pettit's results. A larger r_c would have further improved correlation, but there was concern that r_c was growing too large

compared to the $K-T$ dominant zone of the specimen. Also, spurious oscillation was observed in the predicted crack path, and increased with higher values of r_c .

The disagreement in the literature with regard to values of r_c for the various materials tested, and the apparent disparity between some of the values derived from test data and the assumed physical significance of r_c begs reconsideration of the significance of this parameter. Nevertheless, from the equivalence of Equation (126), one can realize that the characteristic length may not correspond to the actual size of any particular physical damage phenomenon, but that its use in the maximum tangential stress theory is simply a surrogate for something more complex than the theory describes. However, if the theory is even a decent surrogate, it would be expected that the r_c would be at least proportional in size to some phenomenological length scale.

3.01.4.5.4 Second-order maximum tangential stress theory for materials with fracture resistance orthotropy (mode I dominated)

Whereas the isotropic crack turning theory maximizes tangential stress, Buczek and Herakovich (1985) suggested that the crack path in anisotropic materials would follow the maximum of the ratio of the tangential stress to the crack growth resistance obtained by

$$\frac{d}{d(\Delta\theta)} \left(\frac{\sigma_\theta(\Delta\theta)}{\bar{K}(\theta + \Delta\theta)} \right) = 0 \quad (127)$$

Separating variables, one obtains

$$\frac{1}{\sigma_\theta(\Delta\theta)} \frac{d\sigma_\theta}{d\theta} = \frac{1}{\bar{K}(\theta + \Delta\theta)} \frac{d\bar{K}}{d\theta} \equiv \Psi \quad (128)$$

Ψ can be obtained in terms of \bar{K}_m using Equation (108):

$$\Psi(\theta + \Delta\theta_c) = \left(\frac{2}{n} \right) \frac{\beta \sin 2(\theta + \Delta\theta_c)}{1 + \beta \cos 2(\theta + \Delta\theta_c)} \\ \text{where } \beta = \frac{\bar{K}_m^n - 1}{\bar{K}_m^n + 1} \quad (129)$$

To simplify notation, the argument of Ψ will not be shown explicitly unless it differs from that given above or is required for clarity. Based on the discussion of Section 3.01.4.3, a value of $n = -1$ will be used. Defining Ψ_1 with reference to the mode I orthotropy ratio \bar{K}_{lm} ,

evaluating the left-hand side of Equation (128) with use of Equation (119), and solving for \bar{T} :

$$\bar{T} = \frac{\sin \Delta\theta_c + (K_{II}/K_I)(3 \cos \Delta\theta_c - 1) - 2\Psi_1[(K_{II}/K_I) \sin \Delta\theta_c - (1 + \cos \Delta\theta_c)/3]}{\sin(\Delta\theta_c/2)(2 \cos \Delta\theta_c - \Psi_1 \sin \Delta\theta_c)} \quad (130)$$

Note that for $K_{Im} = 1$, $\Psi_1 = 0$, and Equation (130) reverts to the isotropic form of Equation (124).

Equation (130) is plotted in Figure 43 for $K_{Im} = 1.6$ with various crack orientations, illustrating how the orthotropy influences the location and nature of the bifurcation. As would be expected, a crack propagating in the direction of least crack growth resistance requires a higher K_{II} or T -stress to alter its course. Conversely, a self-similar crack propagating along the direction of maximum crack growth resistance may turn in a compressive T -stress environment given sufficient fracture orthotropy.

One must take care when evaluating Equation (130) to obtain maxima, and not minima. The minima occur to the right of the bifurca-

$$\bar{T}_{II} = \frac{2 \cos \frac{\Delta\theta_c}{2} \left[\frac{K_I}{K_{II}} + 4\Psi_{II} \left((1 - 3 \cos \Delta\theta_c) - \frac{K_I}{K_{II}} \sin \Delta\theta_c \right) \right] - 2 \left(9 \sin \frac{3\Delta\theta_c}{2} + \sin \frac{\Delta\theta_c}{2} \right) + 6 \frac{K_I}{K_{II}} \cos \frac{3\Delta\theta_c}{2}}{3(2 \cos 2\Delta\theta_c - \Psi_{II} \sin 2\Delta\theta_c)} \quad (135)$$

tion line. In order to derive an expression for the value of \bar{T} where the bifurcation occurs, we examine the limiting case of Equation (130):

$$\lim_{\Delta\theta_c \rightarrow 0} \bar{T} = \frac{2}{\Delta\theta_c} \left(\frac{K_{II}}{K_I} + \frac{2}{3}\Psi_1(\theta + \Delta\theta_c) \right) \quad (131)$$

Note that the theory only predicts straight growth where \bar{T} is below the bifurcation value and

$$\frac{K_{II}}{K_I} = \left(\frac{K_{II}}{K_I} \right)_{crit} = -\frac{2}{3}\Psi_1(\theta) = -\frac{2}{3}\Psi_{Io} \quad (132)$$

where Ψ_{Io} is defined as Equation (129) evaluated at $\Delta\theta_c = 0$. If K_{II}/K_I exceeds this value, then $\Delta\theta_c < 0$. The bifurcation value of \bar{T} is obtained when we assume that Equation (129) is satisfied and continue with the limit, from which we obtain

$$\bar{T}_{crit} = 1 + \frac{4}{3} \left(\Psi_{Io}^2 + \frac{4\beta(\beta + \cos 2\theta)}{n(1 + \beta \cos 2\theta)^2} \right) \quad (133)$$

where β is as given in Equation (129).

3.01.4.5.5 Second-order maximum shear stress theory with fracture orthotropy (mode II dominated)

The above theory is mode I dominant, inasmuch as σ_θ is analogous to mode I stress intensity. However, it has been observed that under certain conditions the crack propagates in the direction of maximum $\sigma_{r\theta}$. Following a similar development to the maximum tangential stress theory, the second-order orthotropic maximum shear stress theory can be obtained by maximizing via

$$\frac{d}{d(\Delta\theta)} \left(\frac{\sigma_{r\theta}(\Delta\theta)}{K_{II}(\theta + \Delta\theta)} \right) = 0 \quad (134)$$

to obtain

$$\text{where } \Psi_{II} \text{ is evaluated in terms of the mode II fracture resistance orthotropy ratio, and}$$

$$\bar{T}_{II} \equiv \frac{8}{3} \frac{T}{K_{II}} \sqrt{2\pi r_c} \quad (136)$$

Selected plots of Equation (135) are shown in Figures 44 and 45. In this case, there is no bifurcation, but one must be careful to obtain the global maximum or minimum of the greatest absolute value of the ratio in brackets in Equation (135). For the maximum stress theory, transition from modes I to II dominated fracture may be postulated to occur when:

$$\max \left(\frac{\sigma_\theta(\Delta\theta)}{K_I(0) K_I(\theta + \Delta\theta)} \right) \leq \max \left| \frac{\sigma_{r\theta}(\Delta\theta)}{K_{II}(0) K_{II}(\theta + \Delta\theta)} \right| \quad (137)$$

3.01.4.5.6 Second-order linear elastic virtual kink theory

Consider a lead crack under plane stress conditions with a plastic zone as shown in

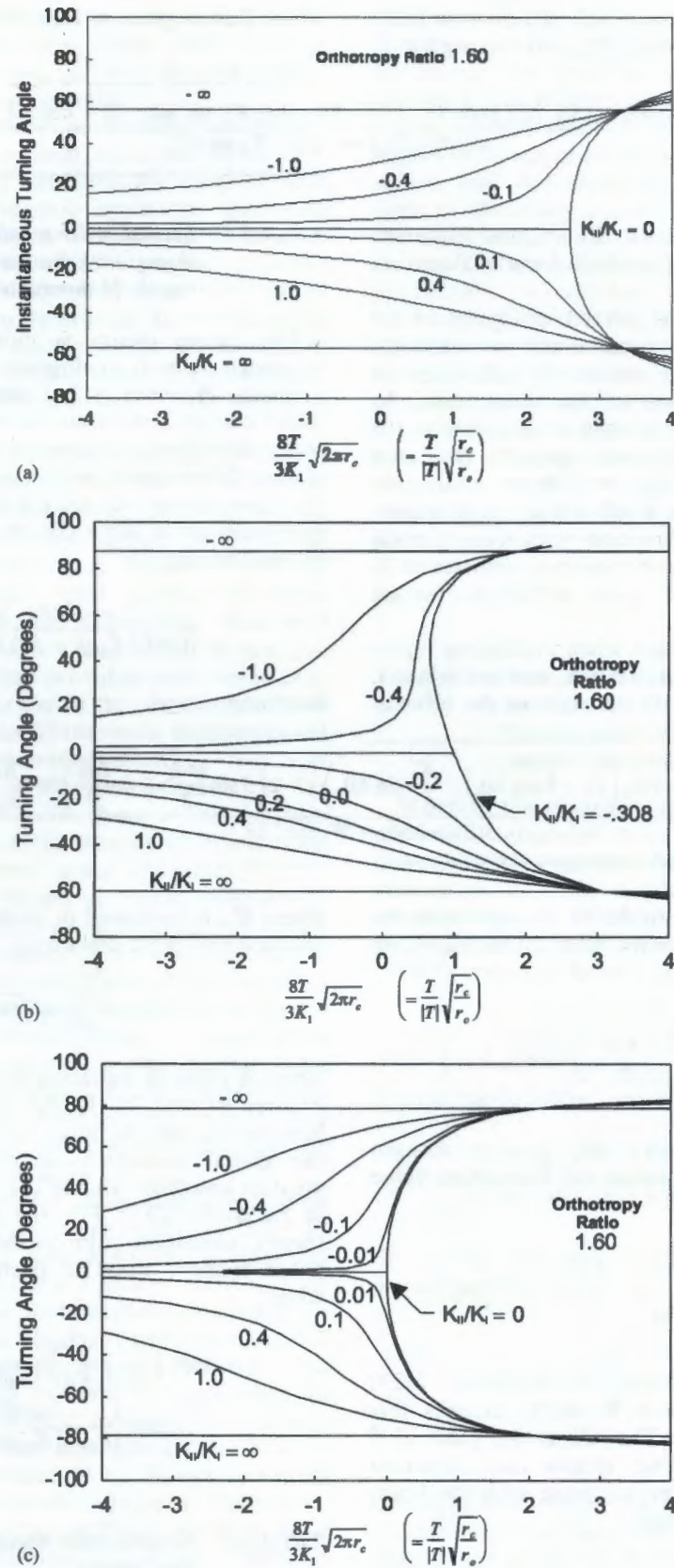


Figure 43 Normalized Crack turning plots for an elastically isotropic material with fracture orthotropy $K_m = 1.6$, $n = -1$, various crack orientations: (a) crack oriented at $\theta = 0^\circ$; (b) crack oriented at $\theta = 45^\circ$; and (c) crack oriented at $\theta = 90^\circ$.

Figure 43
theory

Figure 43 shows normalized crack turning plots for an elastically isotropic material with fracture orthotropy $K_m = 1.6$, $n = -1$, for various crack orientations. The plots illustrate the effect of crack orientation on crack turning behavior. The x-axis represents the normalized crack tip radius $\frac{8T}{3K_1} \sqrt{2\pi r_e}$ or $\left(\frac{T}{|T|} \sqrt{\frac{r_e}{r_o}} \right)$, and the y-axis represents the crack turning angle in degrees. The plots show curves for different crack orientation ratios K_u/K_i , including values such as $-\infty$, -1.0, -0.4, -0.1, 0.1, 0.4, 1.0, and $K_u/K_i = \infty$. The plots are labeled with "Orthotropy Ratio 1.60". The results show that the crack turning angle is significantly affected by the crack orientation ratio K_u/K_i , particularly for non-zero values.

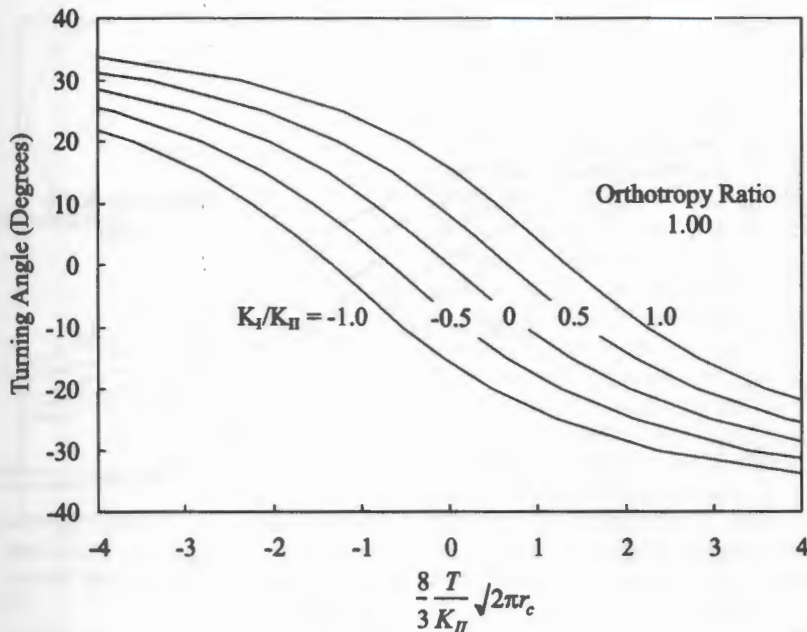


Figure 44 Predicted effect of T -stress on kink angle for mode II crack according to maximum shear stress theory, isotropic case.

Figure 46(a). Compared to an elastic crack, the plastic zone results in additional deformation that can be approximated by a virtual elastic crack kink as shown in Figure 46(b). For self-similar crack growth, Wells (1961), used the Irwin plastic zone correction as an approximation of the effective elastic kink length to obtain an estimate of the CTOD. While the appropriate choice of length may remain in question, it is not unreasonable to assert that for a given material and loading, there is a unique kink length, b_c , and orientation, θ_c , which will best simulate the deformation field as one moves away from the crack tip into the elastic region. One might even postulate that a crack kink so defined would provide a reasonable approximation of the future crack trajectory. For a crack propagating under steady-state conditions, b_c would be expected to assume a constant, material-dependent value analogous to r_c .

The direct implementation of such a criterion is problematic. Nevertheless, as linear elasticity is approached (as for so-called brittle materials, and also approximately for slow fatigue crack growth), the length of the virtual kink necessarily vanishes. In this limiting case, Cotterell and Rice (1980) concluded, based on a maximum energy release rate argument, that the crack propagates in pure mode I, which is equivalent to the criterion $K_{II}=0$. For a finite (virtual) kink in the presence of nonzero T -stress, setting $K_{II}=0$ does not generally result in maximizing strain energy release rate,

nor does it maximize K_I . Nevertheless, depending on the materials and loading conditions, cracks are observed experimentally to develop trajectories corresponding either to pure mode I or pure mode II cracking. Based on this evidence, an isotropic theory is proposed based on the concept that the virtual kink representing the process zone of an extending crack will develop in the direction of either pure mode I or pure mode II crack opening.

Isida and Nishino (1990) (see also Kfouri (1996)) give a solution for a crack in an infinite plate with a kink at one end subject to general in-plane loading. The SIFs at the kink tip, (uppercase) K_I and K_{II} , are expressed in terms of lead crack (lowercase) stress intensities and T as

$$\begin{aligned} K_I &= F_I^{(1)} k_I + F_I^{(3)} k_{II} - F_I^{(2)} T \sqrt{\pi a} \\ K_{II} &= F_{II}^{(1)} k_I + F_{II}^{(3)} k_{II} - F_{II}^{(2)} T \sqrt{\pi a} \end{aligned} \quad (138)$$

where a is the crack length, and $F_n^{(i)}$ are functions of the kink angle, $\Delta\theta$, and the normalized kink length, b/a , given in polynomial form by Isida and Nishino. The crack length parameter can be eliminated by normalizing in the form

$$\begin{aligned} \frac{K_I}{k_I} &= F_I^{(1)} + F_I^{(3)} \frac{k_{II}}{k_I} - \frac{F_I^{(2)}}{\sqrt{b/a}} \frac{3}{8\sqrt{2}} T_b \\ \frac{K_{II}}{k_I} &= F_{II}^{(1)} + F_{II}^{(3)} \frac{k_{II}}{k_I} - \frac{F_{II}^{(2)}}{\sqrt{b/a}} \frac{3}{8\sqrt{2}} T_b \end{aligned} \quad (139)$$

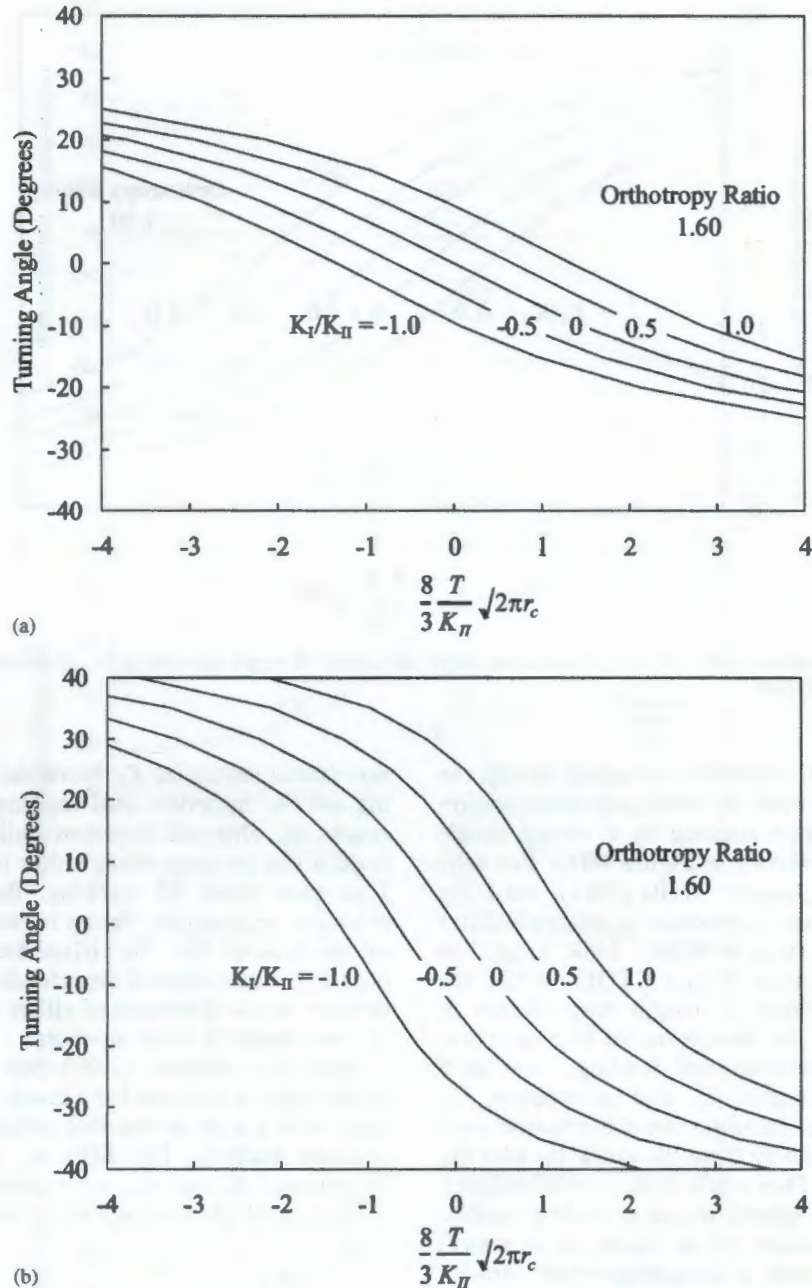


Figure 45 Predicted effect of T -stress on kink angle for mode II crack according to maximum shear stress theory, $K_{IIm} = 1.6$, $n = -1$: (a) crack oriented at $\theta = 0^\circ$ and (b) crack oriented at $\theta = 90^\circ$.

where $\sqrt{b/a}$ divides cleanly out of functions $F_n^{(2)}$, and \tilde{T}_b is defined with $b = b_c$ in a manner similar to Equation (124):

$$\tilde{T}_b \equiv \frac{8}{3} \frac{T}{K_I} \sqrt{2\pi b_c} \quad (140)$$

For mode I dominated growth, values of the crack propagation angle, θ_c , can be obtained by varying $\Delta\theta$ to enforce $K_{II}=0$ for various combinations of k_{II}/k_I and \tilde{T} , as presented in Figure 47. Also shown for comparison is the second-order maximum tangential stress theo-

ry of Equation (124) with its characteristic length, r_c . The two theories are fairly equivalent (though not identical) if one recognizes that the characteristic lengths differ at the bifurcation by a constant factor:

$$b_c = 2.21r_c \quad (141)$$

The corresponding mode II fracture behavior has not been evaluated, but could easily be developed in the same manner. Nevertheless, from a linear elastic perspective, there is no

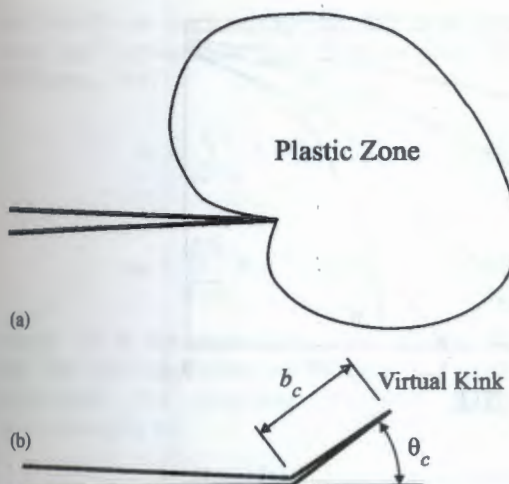


Figure 46 Crack-tip plastic zone deformation simulated by an effective virtual kink: (a) physical crack tip and plastic zone and (b) physical crack with virtual kink.

apparent advantage to this theory over the maximum stress theory, which is easier to implement, and has already been extended to include toughness orthotropy and modal transition.

3.01.4.6 Calculation of the T -stress

T -stress calculations have been performed by various authors. In one of the earliest studies, Larsson and Carlsson (1973) evaluated the T -stress using FEs. Later, Leeviers and Radon (1982) directly imposed the infinite series solution given by Williams (1957) in a variational approach to obtain estimates of K_I and T simultaneously. They gave estimates of the T -stress in the form of the dimensionless parameter:

$$B = \frac{T\sqrt{a}}{K_I} \quad (142)$$

Based on the convergence observed, Leeviers and Radon estimated the error in the B values they provided for various specimen geometries to be less than 3%. Sham (1991) used second-order weight functions and a work conjugate integral to calculate T -stresses in various specimen configurations. Fett (1997, 1998) introduced a Green's function approach to calculate T -stresses, and analyzed numerous configurations. A more approximate displacement correlation method was outlined by Al-Ani and Hancock (1991) that is nevertheless easy to implement in plate and shell codes, and has been utilized in various forms by other authors (Pettit *et al.*, 1997; Knops, 1994; Chen., 1999).

Cardew *et al.* (1985) and Kfouri (1986) computed the T -stress using a modified J -integral based on unpublished work of Eshelby, and also gave results for selected specimens based on FE analyses. Another type of path independent integral based on the Betti-Rayleigh reciprocal theorem has also been proposed by Stern *et al.* (1976) and also by Yuan and Yang (1998). It was shown to be mathematically equivalent to the J -integral method by Chen *et al.* (2001). By implementing the contour integral solution into a high polynomial order (p -version) FE program, Chen *et al.* obtained T -stresses that were claimed to be numerically exact to at least five significant figures. The numerical accuracy was verified by way of an exact benchmark solution (a crack tip and surrounding region with the exact boundary conditions applied corresponding to arbitrary combinations of K_I , K_{II} , and T) and a theoretical error relationship:

$$e_T = T_{FE} - T = \tilde{e}_T \frac{K_I}{\sqrt{r_1}} \quad (143)$$

where e_T is the error in the computed T -stress, r_1 is a characteristic dimension of the integration zone, and \tilde{e}_T is a coefficient related to the discretization error in the vicinity of the integration zone.

Note that Equation (143) predicts that the error in the computed T -stress is degraded as the size of the integration domain is reduced—a trend common to both integral methods described. Also, the integration must be performed about a straight segment at the crack tip. This means that when modeling a curvilinear crack, the integration radius cannot exceed the increment dimension, and as the step size is reduced, as required for path convergence, the accuracy of the T -stress solution will be simultaneously degraded.

Nevertheless, using the highly accurate solutions for simple geometries provided by Chen *et al.* as benchmarks, together with the error estimation parameter, it was found that much of the error in the contour integral results is of a systematic nature, and can be corrected *a posteriori* for a given rosette geometry. Following a brief review of the contour integral solution based on the Betti-Rayleigh reciprocal theorem (Chen 1999), an error correction scheme will be discussed, and correction parameters will be determined for the element type and rosette geometry used in FRANC2D.

3.01.4.6.1 Contour integral methods

The Betti-Rayleigh reciprocal theorem can be written for a 2D body bounded by a closed

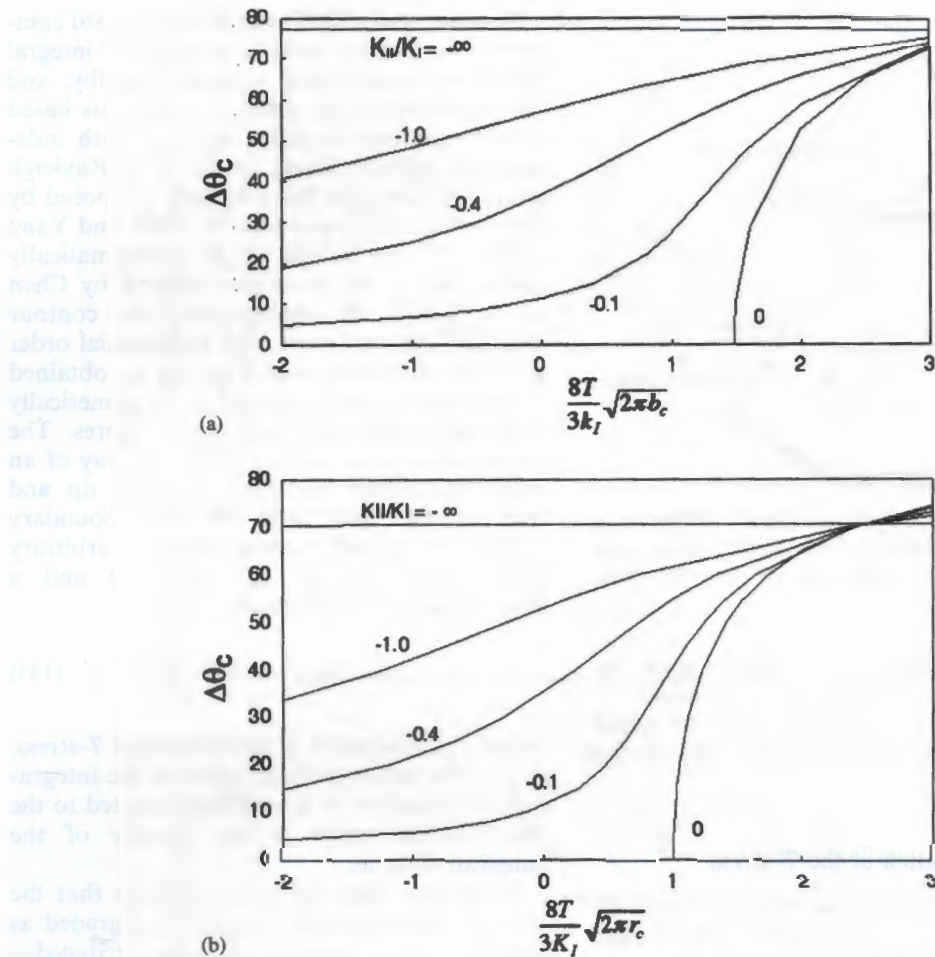


Figure 47 Comparison of mode I virtual kink theory with maximum tangential stress theory: (a) virtual kinked crack with pure mode I opening, $K_{II}=0$ and (b) second-order maximum tangential stress theory.

curve S without body forces as

$$\int_S (T_i^* u_i - T_i u_i^*) dS = 0 \quad (144)$$

where T_i represents a set of surface tractions with resulting surface displacements u_i , and T_i^* and u_i^* are an independent set of surface tractions and corresponding surface displacements, referred to as *auxiliary fields*. By evaluating the integral at a crack tip around the closed four-segment path shown in Figure 48, and recognizing that segments C_+ and C_- are traction free, path independence can be shown with regard to the other two segments:

$$\int_C (T_i^* u_i - T_i u_i^*) dC = \int_{C_e} (T_i^* u_i - T_i u_i^*) dC_e \quad (145)$$

By substituting $T_i = \sigma_{ij} n_j$ for each field, where n_j are components of the outward normal vector along the corresponding path segment,

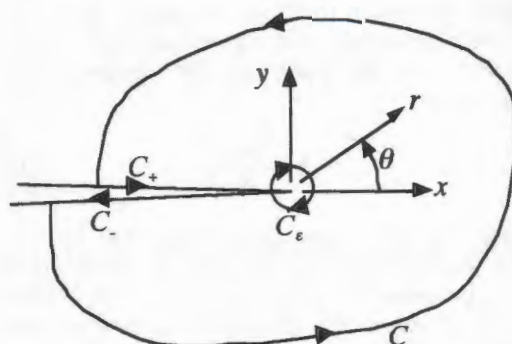


Figure 48 A closed contour around a crack tip.

we obtain

$$\begin{aligned} \int_C (\sigma_{ij}^* u_i - \sigma_{ij} u_i^*) n_j dC &= \int_{C_e} (\sigma_{ij}^* u_i - \sigma_{ij} u_i^*) n_j dC_e \end{aligned} \quad (146)$$

Defining ε as a characteristic dimension of path C_e , the right-hand side can be evaluated

analytically as $\varepsilon \rightarrow 0$ using the 2D crack-tip stress and displacement field solution given by (Williams, 1957)

$$\sigma_{ij} = \sum_{\lambda=-\infty}^{+\infty} A_{\lambda} r^{\lambda/2} f_{ij}^{\lambda}(\theta) \quad (147)$$

$$u_{ij} = \sum_{\lambda=-\infty}^{+\infty} B_{\lambda} r^{\lambda/2+1} g_{ij}^{\lambda}(\theta) \quad (148)$$

where $\lambda/2$ is the eigenvalue, and A_{λ} and B_{λ} are the corresponding coefficients for each eigenvalue. By choosing auxiliary fields corresponding to

$$\begin{aligned} \sigma_{ij}^* &\sim r^{-\lambda/2-2} \\ u_i^* &\sim r^{-\lambda/2-1} \end{aligned} \quad (149)$$

in Equation (146), coefficients of order $\lambda/2$ alone are obtained. T is of order $\lambda=0$, corresponding to auxiliary stresses and displacements in local Cartesian coordinates (see Figure 48) of

$$\begin{aligned} \sigma_{xx}^* &= \frac{\cos 2\theta + \cos 4\theta}{2\pi r^2} \\ \sigma_{yy}^* &= \frac{\cos 2\theta - \cos 4\theta}{2\pi r^2} \\ \sigma_{xy}^* &= \frac{\sin 4\theta}{2\pi r^2} \end{aligned} \quad (150)$$

$$\begin{aligned} u_x^* &= -\frac{\kappa \cos \theta + \cos 3\theta}{8\pi r G} \\ u_y^* &= \frac{\kappa \sin \theta - \sin 3\theta}{8\pi r G} \end{aligned} \quad (151)$$

where G is the shear modulus, $\kappa = (3-v)/(4+v)$ for plane stress, and $\kappa = (3-4v)$ for plane strain problems. The T -stress is then obtained for $\varepsilon \rightarrow 0$ as

$$T = \frac{8G}{\kappa+1} \int_{C_s} (\sigma_{ij}^* u_i - \sigma_{ij} u_i^*) n_j dC_s \quad (152)$$

By virtue of the path independence of Equation (146), an equivalent integral can be performed numerically using stresses and strains from the FE analysis (superscript FE):

$$T = \frac{8G}{\kappa+1} \int_C (\sigma_{ij}^* u_i^{\text{FE}} - \sigma_{ij}^{\text{FE}} u_i^*) n_j dC \quad (153)$$

or the equivalent domain integral (Chen, 1999)

$$T = \frac{8G}{\kappa+1} \iint_A (\sigma_{ij}^* u_i^{\text{FE}} - \sigma_{ij}^{\text{FE}} u_i^*) q_{ij} dA \quad (154)$$

where A is a domain surrounding the crack tip bounded by curves Γ_0 and Γ_1 , and function q is equal to unity on Γ_0 and zero on Γ_1 . For the FRANC2D implementation, the domain A is

the area comprising the outer ring of the crack tip rosette as illustrated in Figure 49. The integration zone radius, r_1 , also shown in Figure 49, is twice the internal radius of the domain for the FRANC2D implementation.

3.01.4.6.2 Error correction scheme

Equation (143) was derived by recognizing that the stress contribution of the singular terms in the stress field will converge far more slowly than the contribution of the nonsingular terms, leaving an error in the coefficients of all terms proportional to the coefficients of the singular terms. (In spite of this argument, K_{II} was found to have no pollution effect on the T -stress in numerical experiments.) The square root term in the denominator was included due to dimensional considerations, consistent with the form of Equations (118) through 120. Based on a similar convergence rate argument, terms of higher order than T are expected to contribute little error to the computed value of T .

Unlike the error estimation expression given in Chen (1999) and Chen *et al.* (2001), we have taken the liberty to write Equation (143) with no absolute value signs enforcing that the error measure always be positive. This represents an assertion that we now acknowledge—namely, that the sign and magnitude of \tilde{e}_T is (at least on an average basis) a characteristic of the rosette configuration. Thus, if the value of \tilde{e}_T were known for a given rosette configuration, the systematic error in a T -stress value calculated using that rosette could be estimated (and thus corrected) via Equation (143). The influence of

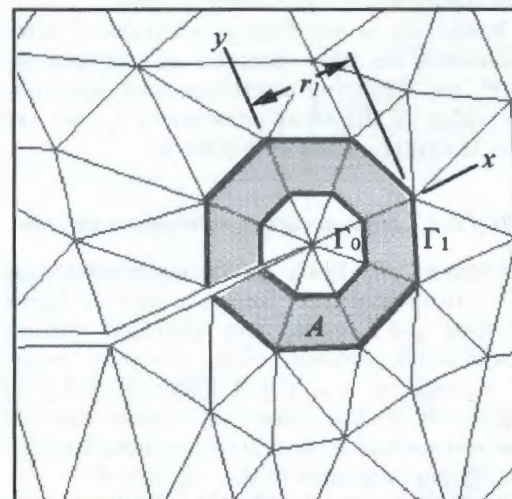


Figure 49 Rosette configuration (midside nodes not shown) and integration domain used in FRANC2D implementation.

scaling the rosette dimension is captured by way of the length parameter r_1 .

The veracity of this assertion can be supported by rewriting Equation (143) in the form of the relative error:

$$e_{T_{\text{rel}}} = \frac{e_T}{T} = \tilde{e}_T \frac{K_I}{T\sqrt{r_1}} \quad (155)$$

The assertion that the relative error in T -stress scales with the dimensionless parameter $K_I/T\sqrt{r_1}$ is supported by the observation that geometrically similar FE models that differ only in scale (which implies that the integration path is likewise scaled), should give numerically identical error fractions in the computed T -stress (or any other local stress measurement). In essence, the rosette may be considered as a FE model with imposed boundary conditions representing K_I and T . Recognizing the similarity of all K_I and T fields relative to a characteristic length $(K_I/T)^2$, one may therefore conclude that the combination of such a field with a rosette model of fixed geometry and scale relative to the field characteristic length will be similar (and thus have comparable relative error) to all other rosette/field combinations with the same relative scaling ratio.

Because \tilde{e}_T represents the discretization error in the vicinity of the integration zone, it should thus be relatively constant so long as the mesh geometry, or rosette, within the integration zone is geometrically similar for all problems. The mesh geometry outside of the integration zone is of secondary influence, and may change from problem to problem, thus its effect will be treated as a probabilistic source of error. Nevertheless, provided that the external mesh is reasonably proportioned, the error introduced should be relatively small.

Based on some highly accurate T -stress solutions, we now proceed to numerically verify the foregoing assertions, and determine the value of the error parameter, \tilde{e}_T , for the rosette configuration of Figure 49.

3.01.4.6.3 High-accuracy reference solutions

Chen *et al.* (1999, 2001) implemented the Betti reciprocal-type integral into a highly accurate p-FE code, and analyzed various model configurations. First, a square model of a crack tip was constructed as shown in Figure 50, with a numerically exact external traction distribution imposed representing arbitrary combinations of K_I , K_{II} , and T .

With this model, Chen showed that by increasing the polynomial order of the solution, the relative T -stress error could be reduced to about 10^{-6} with the rosette

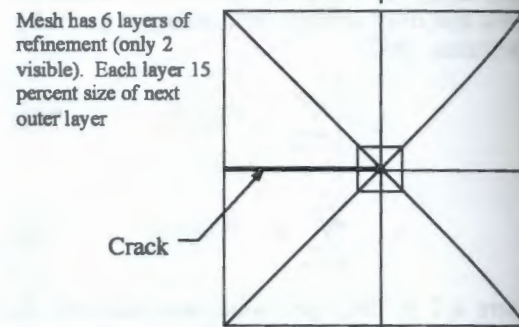


Figure 50 Rosette configuration used in p-element implementation, Chen (1999), Chen *et al.* (2001).

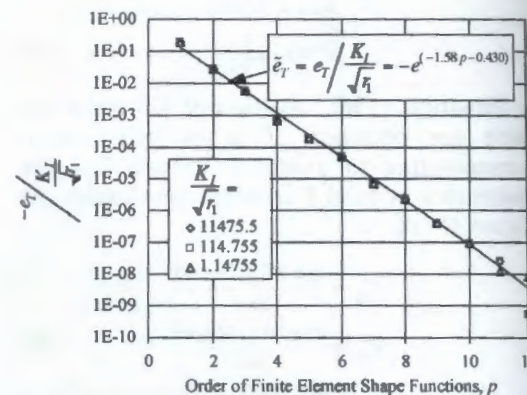


Figure 51 Accuracy assessment of T -stress computations using p-version FEM, Chen *et al.* (2001).

geometry used and an element shape function order, $p = 11$. Extremely accurate stress intensities were also obtained. The T -stress error data is re-plotted in Figure 51 in terms of \tilde{e}_T , showing that for the rosette of Figure 50, \tilde{e}_T is characteristically negative for all p values evaluated, and is a logarithmic function of p . It was also verified by varying load (K_I) and r_1 that \tilde{e}_T is constant for a given level of p . Having established the extremely tight accuracy of the rosette geometry at high values of p , Chen then embedded the same rosette geometry within the meshes of various test specimen geometries to obtain solutions estimated to be within five significant figures of accuracy. The specimen geometries are summarized in Figure 52, and the results tabulated in Table 6.

3.01.4.6.4 Calibration of the rosette geometry

Using the data of Table 6 as a type of calibration standard, the error parameter, \tilde{e}_T , was determined for the FRANC2D rosette configuration of Figure 49. To do this, FRANC2D models were created of the various specimen types shown in Figure 52 using the FRANC2D rosette configuration, and the T -

stresses Section were in to pro represent e_T , in t was the

where Table 6 try and seen th is char under

For paramo



(b)
Figure
geom

Speci
DCB
SEN
SEN
SEN

stresses were calculated using the methods of Section 3.01.4.6.1. A range of integration radii were included for each specimen configuration to provide more data points (each also representing a unique outer mesh). The error, e_T , in the as-calculated T -stress for each case was then determined by

$$e_T = T_{FE} - T_{ref} \quad (156)$$

where T_{ref} is the reference T -stress value from Table 6 corresponding to the specimen geometry and loading. As plotted in Figure 53, it is seen that the error for the FRANC2D rosettes is characteristically negative (the T -stress is underestimated by the FEM).

For each data point, a value of the error parameter was calculated by

$$\tilde{e}_T = \frac{T_{FE} - T_{ref}}{K_I / \sqrt{r_1}} \quad (157)$$

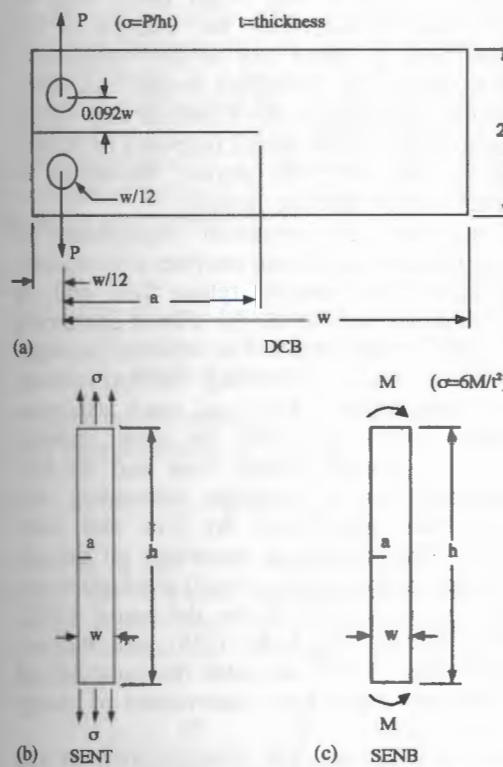


Figure 52 Summary of reference test specimen geometries (after Chen *et al.*, 2001).

As would be expected, the \tilde{e}_T values calculated in this way do not agree precisely, but vary according to some distribution function, and can be characterized in terms of mean and standard deviation values:

$$\tilde{e}_T = \tilde{e}_{T_M} \pm \tilde{e}_{T_{SD}} = -0.00825 \pm 0.00255 \quad (158)$$

A corrected estimate, T_{cor} , of the T -stress can then be calculated by solving Equation (143) for T , and employing the mean value of \tilde{e}_T :

$$T \approx T_{cor} = T_{FE} - \tilde{e}_{T_M} \frac{K_I}{\sqrt{r_1}} \quad (159)$$

The standard deviation of the remaining (random) error in T_{cor} can be estimated as

$$\text{Std. deviation} \approx \tilde{e}_{T_{SD}} \frac{K_I}{\sqrt{r_1}} \quad (160)$$

A plot of remaining error in the corrected data, $e_{T_{cor}}$ is shown with lines denoting 50% and 90% confidence levels is given in Figure 54. The average error (50% confidence level) of the corrected solution was about one-fifth of the original error—a significant improvement in accuracy obtained with negligible additional computation.

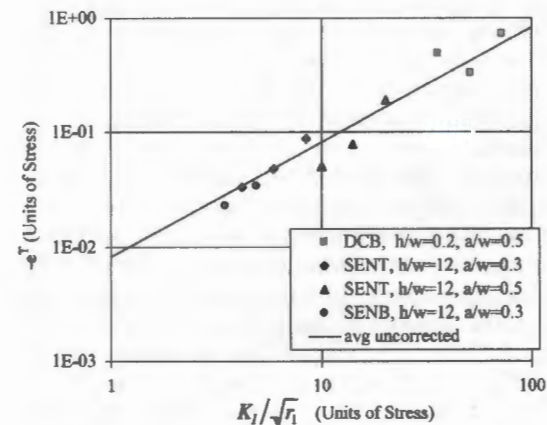


Figure 53 As-calculated error in T -stress using FRANC2D.

Table 6 High-accuracy solutions for selected test specimens.

Specimen description	$K_I / \sigma \sqrt{\pi a}$	T / σ	$B = T \sqrt{\pi a} / K_I$
DCB ($h/w = 0.2$, $a/w = 0.5$)	3.9225	11.5745	2.9508
SENT ($h/w = 12$, $a/w = 0.3$)	1.6598	-0.61033	-0.36771
SENT ($h/w = 12$, $a/w = 0.5$)	2.8246	-0.42168	-0.14929
SEN B ($h/w = 12$, $a/w = 0.3$)	1.1241	-0.079177	-0.070436

After Chen *et al.* (2001).

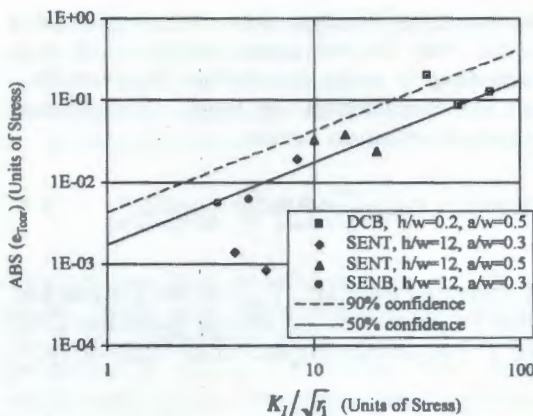


Figure 54 Corrected error in T -stress calculated by FRANC2D with upper bounds representing estimated error.

3.01.4.6.5 Other details of potential significance with regard to T -stress calculation

A few other observations arising in the course of the T -stress computation development effort include the following:

- The presence of K_{II} was not found to incur any numerical pollution into T .
- The singular elements at the center of the rosette shown in Figure 50 were intentionally omitted from the integration domain, requiring the use of a two-layer rosette configuration. If included, the singular elements resulted in additional scatter in the T -stress calculations, making error correction less effective. The reason for this is not known, but may have something to do with the Gauss integration algorithm as applied to singular elements. An alternate path, not chosen, would be to integrate throughout a single-stage rosette without singular elements, and to correct both T and the stress intensities obtained from the J -integral by correction methods similar to those presented above. In this regard, it was found that the systematic component of relative error in K_I was a constant for a given rosette configuration, and is independent of scale;
- Since the error in the T -stress depends on K_I , and not T , the relative error in T will of course be large if T is small compared to K_I . This is acceptable for the present crack turning application, because the influence of T is only significant as it becomes large compared to K_I .

3.01.4.7 Summary

This section summarized the principal theories for predicting 2D crack trajectory and its stability in a FE context. The roles of T -stress

and r_c in these theories were highlighted, and methods for accurate computation of T -stress were described. Direct extension of these theories to 3D crack shape prediction is still problematic. The next two Sections provide additional theoretical and implementation support for this difficult problem.

3.01.5 RATES OF ENERGY RELEASE RATE AND STABILITY OF 2D CRACK SYSTEMS

In some areas of fracture mechanics, higher order derivatives of energy release rate due to crack extension are required for prediction of the stability of a single crack, stability of multiple-crack systems, and the prediction of fatigue crack growth rate. In the case of multiple-crack systems, for example, the variation of energy release rate at one crack tip due to the growth of any other crack must be calculated to determine the strength of the interaction. Another use of the higher-order derivatives is for size effect models that relate nominal strength to the structure size. In the universal size effect model proposed by Bazant (1995), the first and second derivatives of energy release rate are needed.

Therefore, an important requirement of some fracture mechanics analyses is to evaluate accurately the energy release rate and its higher-order derivatives for a body containing multiple cracks subjected to arbitrary loadings, including crack-face loading, thermal loading, and body forces. A virtual crack extension method which provided the direct integral forms of energy release rate and its first derivative for a structure containing one crack was introduced by Lin and Abel (1988). This technique maintains all the advantages of the similar virtual crack extension techniques introduced by deLorenzi (1982, 1985), Haber and Koh (1985), and Barbero and Reddy (1990) and adds the capability of calculating higher-order derivatives of energy release rate.

In this section, the generalization of the analytical virtual crack extension method for LEFM presented by Lin and Abel (1988) is presented. Derivations are provided for the following situations: the general case of multiple-crack systems, the axisymmetric case, inclusion of crack-face and thermal loading, and evaluation of the second-order derivative of energy release rate. The salient feature of this method is that the energy release rate and its higher-order derivatives for multiple-crack systems are computed in a single analysis. In Section 3.01.5.1, the general formulation for

the rates of energy release rates for a multiple crack system is presented. In Section 3.01.5.2, several 2D numerical examples with exact solutions or with solutions available in the literature are solved to demonstrate the accuracy of the current method. These examples include: a pressurized crack in an infinite plane as an example of crack-face loading; a center-cracked infinite plane subjected to a remote stress, to show the evaluation of the second-order derivative of energy release rate; a circular crack subjected to symmetric point loads in an infinite 3D space, to illustrate an axisymmetric case; and a system of multiple, parallel-edge cracks subjected to thermal loading in a semi-infinite plane.

3.01.5.1 Formulation

In this section, the analytical expressions for rates of energy release rate for a multiple-cracked system under arbitrary loading conditions are derived. For all the developments reported herein, it is assumed that each crack tip will be surrounded by a uniform rosette of standard, quarter-point singular elements, as shown in Figure 55. A discussion of additional mesh perturbation of the nonsingular element layers is also presented.

3.01.5.1.1 General formulation for rates of energy release rate for multiply cracked systems

The potential energy Π of a cracked body with multiple cracks is given by

$$\Pi = \frac{1}{2}u^T Ku - u^T f \quad (161)$$

where u , K , and f are the nodal displacement vector, the structural stiffness matrix and the applied nodal force vector, respectively. The energy release rate at crack tip i can be expressed as

$$G_i = -\frac{\delta\Pi}{\delta a_i} = -\frac{1}{2}u^T \frac{\delta K}{\delta a_i} u + u^T \frac{\delta f}{\delta a_i} \quad (162)$$

where a_i is the length of crack i , and nonzero contributions to $\delta K/\delta a_i$ and $\delta f/\delta a_i$ occur only over elements adjacent to the crack tip. It is noted that whenever crack face, thermal and body force loadings are applied, the variations of loading must be taken into account to reflect the local load change on the crack face or in the crack-tip vicinity as a result of virtual crack extension.

The variation of G_i , Equation (162), with respect to the growth of any other crack,

j , is

$$\begin{aligned} \frac{\delta G_i}{\delta a_j} &= -u^T \frac{\delta K}{\delta a_i} \frac{\delta u}{\delta a_j} - \frac{1}{2}u^T \frac{\delta^2 K}{\delta a_i \delta a_j} u \\ &\quad + \frac{\delta u^T}{\delta a_j} \frac{\delta f}{\delta a_i} + u^T \frac{\delta^2 f}{\delta a_i \delta a_j} \end{aligned} \quad (163)$$

We assume that the elements influenced by each crack tip in a multiply cracked body comprise disjoint sets. Therefore, if $i \neq j$, then the second order variations of stiffness and loading with respect to two different crack extensions a_i and a_j vanish:

$$\frac{\delta^2 K}{\delta a_i \delta a_j} = \frac{\delta^2 f}{\delta a_i \delta a_j} = 0 \quad (164)$$

and, $\delta G_i/\delta a_j$ reduces to

$$\frac{\delta G_i}{\delta a_j} = -u^T \frac{\delta K}{\delta a_i} \frac{\delta u}{\delta a_j} + \frac{\delta u^T}{\delta a_j} \frac{\delta f}{\delta a_i} \quad (165)$$

The variation of the displacement can be obtained from the variation of the global equilibrium equation $Ku=f$ with respect to a_j :

$$\begin{aligned} \frac{\delta K}{\delta a_j} u + K \frac{\delta u}{\delta a_j} &= \frac{\delta f}{\delta a_j} \quad \text{or} \\ \frac{\delta u}{\delta a_j} &= K^{-1} \left(\frac{\delta f}{\delta a_j} - \frac{\delta K}{\delta a_j} u \right) \end{aligned} \quad (166)$$

By substituting Equation (166) into Equation (165), we obtain the final expression for $i \neq j$:

$$\begin{aligned} \frac{\delta G_i}{\delta a_j} &= -u^T \frac{\delta K}{\delta a_i} K^{-1} \left(\frac{\delta f}{\delta a_j} - \frac{\delta K}{\delta a_j} u \right) \\ &\quad + \left(\frac{\delta f}{\delta a_j} - \frac{\delta K}{\delta a_j} u \right)^T K^{-1 T} \frac{\delta f}{\delta a_i} \end{aligned} \quad (167)$$

For the case of $i=j$,

$$\frac{\delta G_i}{\delta a_i} = -u^T \frac{\delta K}{\delta a_i} \frac{\delta u}{\delta a_i} - \frac{1}{2}u^T \frac{\delta^2 K}{\delta a_i^2} u + \frac{\delta u^T}{\delta a_i} \frac{\delta f}{\delta a_i} + u^T \frac{\delta^2 f}{\delta a_i^2} \quad (168)$$

Making similar substitutions, this can be expressed as

$$\begin{aligned} \frac{\delta G_i}{\delta a_i} &= -u^T \frac{\delta K}{\delta a_i} K^{-1} \left(\frac{\delta f}{\delta a_i} - \frac{\delta K}{\delta a_i} u \right) - \frac{1}{2}u^T \frac{\delta^2 K}{\delta a_i^2} u \\ &\quad + \left(\frac{\delta f}{\delta a_i} - \frac{\delta K}{\delta a_i} u \right)^T K^{-1 T} \frac{\delta f}{\delta a_i} + u^T \frac{\delta^2 f}{\delta a_i^2} \end{aligned} \quad (169)$$

Element stiffness variations $\delta k/\delta a$ and $\delta^2 k/\delta a^2$ are assembled to produce the global stiffness variations $\delta K/\delta a$ and $\delta^2 K/\delta a^2$. From Lin and Abel (1988), element stiffness variations are

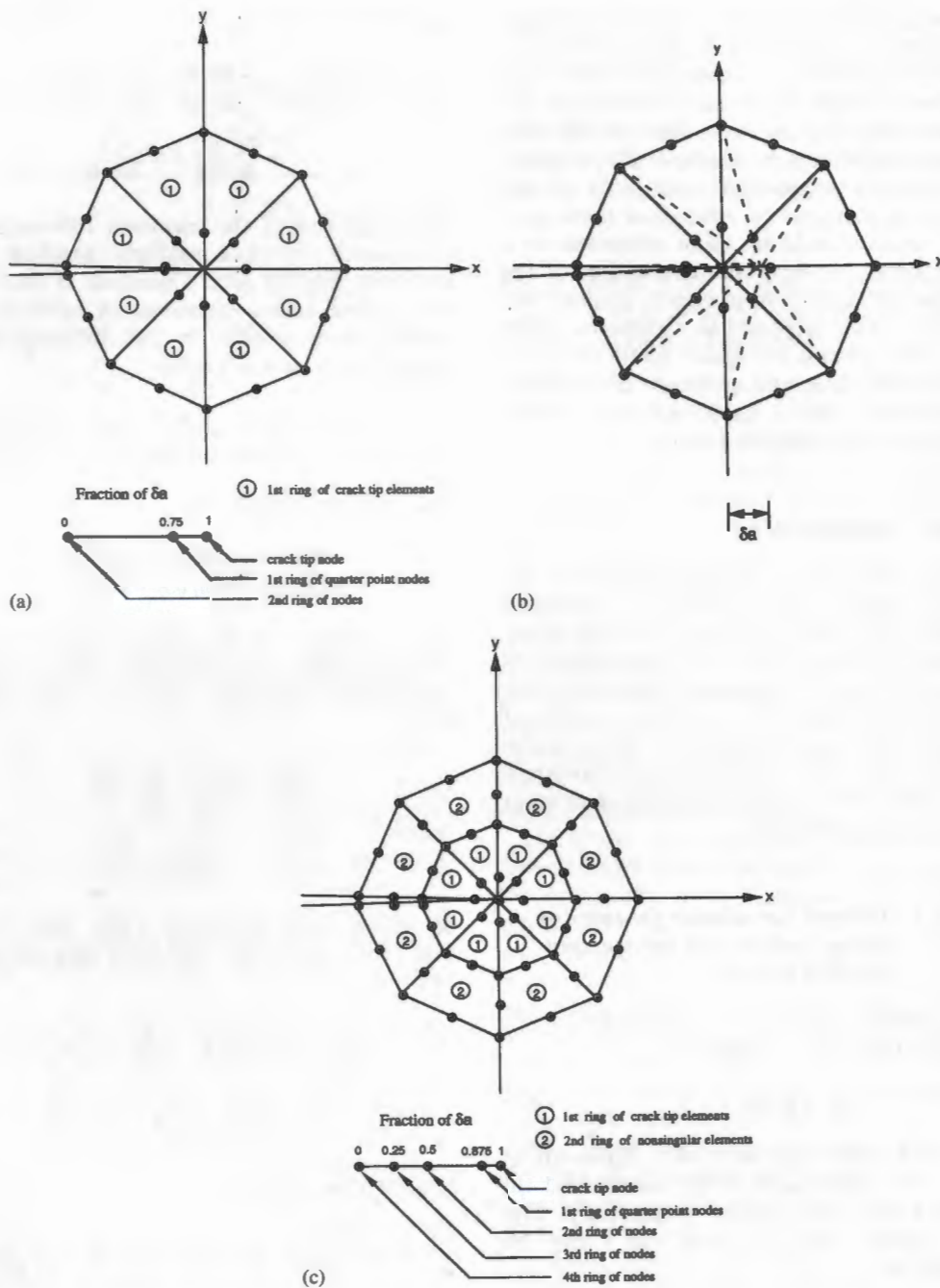


Figure 55 (a) Standard arrangement of rosette of single ring of quarter-point elements; (b) the perturbation of the first ring of crack-tip elements; and (c) the perturbation of the first and second ring of elements.

given by

$$\delta k = \int_V [\delta B^T D B + B^T D \delta B + \text{Tr}(\tilde{\epsilon}) B^T D B] dV \quad (170)$$

$$\begin{aligned} \delta^2 k = \int_V & [\delta^2 B^T D B + 2\delta B^T D \delta B \\ & + B^T D \delta^2 B + 2|\tilde{\epsilon}| B^T D B \\ & + 2\text{Tr}(\tilde{\epsilon})(\delta B^T D B + B^T D \delta B)] dV \quad (171) \end{aligned}$$

where $\tilde{\epsilon}$ is the virtual strain-like matrix, B is the strain-nodal displacement matrix, and D the elastic constitutive matrix. $\tilde{\epsilon}$ is defined as

$$\tilde{\epsilon} = J^{-1} \left\{ \frac{\partial N / \partial \xi^1}{\partial N / \partial \xi^2} \right\} \begin{bmatrix} \Delta_n^1 & \Delta_n^2 \end{bmatrix} = \begin{bmatrix} \tilde{\epsilon}_{11} & \tilde{\epsilon}_{12} \\ \tilde{\epsilon}_{21} & \tilde{\epsilon}_{22} \end{bmatrix} \quad (172)$$

where Δ 's are the geometry changes of the meshes due to virtual crack extension.

Equations
generalizati
Abel (1988)
crack tip.

Once G_i ,
puted, SIF a
a pure mode

$$\frac{\delta^2(K_I)_i}{\delta \sigma_i^2} =$$

where $H = 1$
 $H = E/(1 -$
Young's mo

The appl
mixed mod
ward by m
decomposit
mesh in the
et al., 1979;
procral the
representati
method (St
The genera
release rate
their rates
presented in

The desc
mented in
FRANC2D
dimensional
crack prop
1987). This
propagation
court, 1996)

3.01.5.1.2

The glob
are produc
variations, d

The elem
ciated with

Equations (167) and (169) are seen to be the generalization of Equation (2.21) in Lin and Abel (1988) that was developed for a single crack tip.

Once G_i , $\delta G_i/\delta a_i$, and $\delta^2 G_i/\delta a_i^2$ are computed, SIF and its higher-order derivatives for a pure mode I can be expressed by

$$(K_I)_i = \sqrt{G_i H} \quad (173)$$

$$\frac{\delta(K_I)_i}{\delta a_i} = \frac{1}{2} \frac{\delta G_i}{\delta a_i} \sqrt{\frac{H}{G_i}} \quad (174)$$

$$\frac{\delta^2(K_I)_i}{\delta a_i^2} = \frac{1}{2} \frac{\delta^2 G_i}{\delta a_i^2} \sqrt{\frac{H}{G_i}} - \frac{1}{4 G_i} \left(\frac{\delta G_i}{\delta a_i} \right)^2 \sqrt{\frac{H}{G_i}} \quad (175)$$

where $H = E$ for plane stress condition and $H = E/(1 - v^2)$ for plane strain condition. E is Young's modulus and v is Poisson's ratio.

The application of the proposed method to mixed mode fracture problems is straightforward by making use of Ishikawa's mode-decomposition technique with a symmetric mesh in the crack-tip neighborhood (Ishikawa *et al.*, 1979; Ishikawa, 1980), or Betti's reciprocal theorem and Yau's mutual energy representation for virtual crack extension method (Stern *et al.*, 1976; Yau *et al.*, 1980). The generalized forms of uncoupled energy release rate, mutual energy release rate and their rates for multiply cracked body are presented in Section 3.01.5.1.4.

The described formulation has been implemented in the fracture analysis code, FRANC2D (2002), a workstation-based two-dimensional FE based code for simulating crack propagation (Wawrynek and Ingraffea, 1987). This code performs automatic crack propagation in a variety of materials (Bittencourt, 1996).

3.01.5.1.2 Additional considerations for crack-face, thermal and body force loading

The global load variations, $\delta f/\delta a$ and $\delta^2 f/\delta a^2$, are produced by assembling the element load variations, $\delta f_e/\delta a$ and $\delta^2 f_e/\delta a^2$:

$$\frac{\delta f}{\delta a} = \sum_e \frac{\delta f_e}{\delta a} \quad (176)$$

$$\frac{\delta^2 f}{\delta a^2} = \sum_e \frac{\delta^2 f_e}{\delta a^2} \quad (177)$$

The elemental equivalent load variations associated with crack extension for a non-uniform

crack-face pressure, p , are given by

$$\delta f_e = \delta \int_s N^T p \, ds = \int_s [N^T \delta p + \text{Tr}(\tilde{\epsilon}) N^T p] \, ds \quad (178)$$

$$\begin{aligned} \delta^2 f_e &= \delta^2 \int_s N^T p \, ds \\ &= \int_s [N^T \delta^2 p + 2 \text{Tr}(\tilde{\epsilon}) N^T \delta p + 2|\tilde{\epsilon}| N^T p] \, ds \end{aligned} \quad (179)$$

where N are the shape functions.

If an arbitrary pressure distribution, p , is a function of x , then its variations with respect to crack extension for mode I are

$$p = p(x) \quad (180)$$

$$\frac{\delta p}{\delta a} = \frac{\partial p}{\partial x} \frac{\partial x}{\partial a} = \left[N_k \left(\frac{\partial p}{\partial x} \right)_k \right] \cdot \left[N_k \left(\frac{\partial x}{\partial a} \right)_k \right] \quad (181)$$

$$\frac{\delta^2 p}{\delta a^2} = \left[N_k \left(\frac{\partial^2 p}{\partial x^2} \right)_k \right] \cdot \left[N_k \left(\frac{\partial x}{\partial a} \right)_k \right]^2 \quad (182)$$

where p_k , $(\partial p/\partial x)_k$, and $(\partial^2 p/\partial x^2)_k$ are the nodal pressure value and its first and second derivatives with respect to the direction x at node k , respectively. The term $(\partial x/\partial a)_k$ represents the change of nodal coordinates at node k in the direction x due to the virtual crack extension, δa , as

$$\delta x_k = \left(\frac{\partial x}{\partial a} \right)_k \delta a \quad (183)$$

If the mesh perturbation due to virtual crack extension is considered for standard quarter-point crack-tip elements, the variation of nodal coordinates in the direction of x is $\delta x_C = \delta a$ at the crack-tip node and $\delta x_Q = 0.75\delta a$ at quarter-point nodes, Figure 55(a). The term $(\partial x/\partial a)_k$ will have a value of 1 for the degree-of-freedom in the x -direction at the crack-tip node, 0.75 at the quarter-point nodes, and zero otherwise. It is noted that the solution is independent of the magnitude of the virtual crack extension, δa . δa is usually taken as unity.

In the same manner, the variations of thermal loading for an isotropic material can be derived as

$$f_e = \int_V B^T D(\alpha \Delta T) \, dV \quad (184)$$

$$\begin{aligned} \delta f_e &= \int_V [\delta B^T D(\alpha \Delta T) + B^T D \delta(\alpha \Delta T) \\ &\quad + \text{Tr}(\tilde{\epsilon}) B^T D(\alpha \Delta T)] \, dV \end{aligned} \quad (185)$$

$$\begin{aligned}\delta^2 f_e = \int_V & [\delta^2 B^T D(\alpha \Delta T) + 2\delta B^T D\delta(\alpha \Delta T) \\ & + B^T D\delta^2(\alpha \Delta T) + 2\text{Tr}(\tilde{\epsilon})(\delta B^T D\alpha \Delta T) \\ & + B^T D\delta(\alpha \Delta T)] dV \quad (186)\end{aligned}$$

where ΔT is the temperature profile and α is the thermal expansion coefficient. If an arbitrary temperature profile, ΔT , is a function of x and y , then its variations with respect to crack extension for mode I are as follows:

$$\Delta T = \Delta T(x, y) \quad (187)$$

$$\begin{aligned}\frac{\delta \Delta T}{\delta a} &= \frac{\partial \Delta T}{\partial x} \frac{\partial x}{\partial a} + \frac{\partial \Delta T}{\partial y} \frac{\partial y}{\partial a} = \frac{\partial \Delta T}{\partial x} \frac{\partial x}{\partial a} \\ &= \left[N_k \left(\frac{\partial \Delta T}{\partial x} \right)_k \right] \cdot \left[N_k \left(\frac{\partial x}{\partial a} \right)_k \right] \quad (188)\end{aligned}$$

$$\frac{\delta^2 \Delta T}{\delta a^2} = \left[N_k \left(\frac{\partial^2 \Delta T}{\partial x^2} \right)_k \right] \cdot \left[N_k \left(\frac{\partial x}{\partial a} \right)_k \right]^2 \quad (189)$$

where ΔT_k , $(\partial \Delta T / \partial x)_k$, and $(\partial^2 \Delta T / \partial x^2)_k$ are the nodal temperature change and its first and second derivatives with respect to the direction x at node k , respectively. The derivation for body forces is similar to that of thermal loading and is not shown here. The derivations for the axisymmetric problem and the second derivative of energy release rate are given later in Sections 3.01.5.1.5 and 3.01.5.1.6, respectively.

3.01.5.1.3 Perturbation of nonsingular elements layers

In this section, the perturbation of additional nonsingular, eight-noded quadrilateral element layers is considered. It is expected that the use of a nonsingular element layer in the mesh perturbation will improve the solution accuracy for higher-order rates of energy release rate, because nonsingular elements contain additional higher-order terms lost to the crack-tip elements because of those quarter-point distortions. In the quarter-point crack-tip element, the stress field is expressed by the singular term (\sqrt{r}) and a constant term, while in a regular eight-noded quadrilateral element, it is represented by the constant term and linear term (r). By perturbing additional layers of nonsingular elements, the high-order terms can be included in the computation and the solution accuracy of the high-order variations of SIF is considerably enhanced. When only the first ring of crack-tip elements is perturbed as a result of virtual crack extension, δa , the crack-tip node is shifted to a new crack-tip location by δa , and the quarter points to

new quarter points by $0.75 \delta a$, Figure 55(b). If the second ring of non-singular, eight-noded elements along with the first ring of crack-tip elements is perturbed, the nodes in those elements have to be shifted to new locations. We selected the linear perturbation shown in Figure 55(c). Other perturbation schemes are possible but we have not investigated them. A similar procedure is used for three or more rings of elements. For three different mesh perturbations, three different load variations can be derived. Consider the constant crack-face pressure, p , for illustration. It is easily shown that only the first-order variations of equivalent nodal pressure loading have non-zero values for the virtual crack extension:

$$\begin{aligned}\delta f_e &= \delta \int N^T p dL = \delta \int N^T p J d\xi \\ &= \int N^T \delta p J d\xi + \int N^T p \delta J d\xi \\ &= \int N^T p \delta J d\xi = \int N^T p \tilde{\epsilon} J d\xi \quad (190)\end{aligned}$$

where $\delta p = 0$ for constant pressure;

$$\delta^2 f_e = \delta \int N^T p \delta J d\xi = \int N^T p \delta^2 J d\xi \quad (191)$$

where J and $\tilde{\epsilon}$ are constants for 1D Jacobian variations, δJ and $\delta^2 J$, are as follows:

$$\delta J = \tilde{\epsilon} J = J^{-1} \left(\sum_i \frac{\partial N_i}{\partial \xi} \Delta_i \right) J = \sum_i \frac{\partial N_i}{\partial \xi} \Delta_i \quad (192)$$

$$\delta^2 J = \delta \tilde{\epsilon} J + \tilde{\epsilon} \delta J = -\tilde{\epsilon}^2 J + \tilde{\epsilon}^2 J = 0 \quad (193)$$

where N_i are shape functions, and Δ_i are the virtual geometry changes of the meshes as a result of virtual crack extension, δa . Now, when only the first of ring of crack-tip elements is perturbed due to a unit virtual crack extension ($\delta a = 1.0$), Δ_i , δJ and load variation are

$$\Delta_i = [0 \ 0.75 \ 1]^T \quad (194)$$

$$\begin{aligned}\delta J &= \frac{\partial N_i}{\partial \xi} \Delta_i = [(\xi - 0.5) \ -2\xi \ (\xi + 0.5)] \begin{Bmatrix} 0 \\ 0.75 \\ 1 \end{Bmatrix} \\ &= \frac{1}{2}(1 - \xi) \quad (195)\end{aligned}$$

$$\begin{aligned}\delta f_e &= \int N^T p \delta J d\xi = \int N^T p \frac{1}{2}(1 - \xi) d\xi \\ &= p \left[\frac{1}{3} \ \frac{2}{3} \ 0 \right]^T \quad (196)\end{aligned}$$

When the first and second rings of elements are perturbed, Δ_i , δJ and load variations for each

ring are

$$\Delta_i = \begin{bmatrix} 0.5 & 0.875 & 1 \end{bmatrix}^T \quad (197)$$

$$\delta J = \frac{1}{4}(1 - \xi) \quad \text{for the first ring}$$

$$\Delta_i = \begin{bmatrix} 0 & 0.25 & 0.5 \end{bmatrix}^T \quad (198)$$

$$\delta J = \frac{1}{4} \quad \text{for the first ring}$$

$$\delta f_e = \int N^T p \frac{1}{4}(1 - \xi) d\xi$$

$$= p \begin{bmatrix} \frac{1}{6} & \frac{1}{3} & 0 \end{bmatrix}^T \quad \text{for the first ring} \quad (199)$$

$$\delta f_e = \int N^T p \frac{1}{4} d\xi = p \begin{bmatrix} \frac{1}{12} & \frac{1}{3} & \frac{1}{12} \end{bmatrix}^T$$

$$\text{for the second ring} \quad (200)$$

Along the crack face, the total load variation is obtained by adding Equations (199) and (200):

$$\delta f_e = p \begin{bmatrix} \frac{1}{12} & \frac{1}{3} & \frac{1}{4} & \frac{1}{3} & 0 \end{bmatrix}^T \quad (201)$$

Finally, when the 1st, 2nd, and 3rd rings of elements are perturbed, Δ_i , δJ and load variations for each ring are

$$\Delta_i = \begin{bmatrix} 0.75 & 0.9375 & 1 \end{bmatrix}^T \quad (202)$$

$$\delta J = \frac{1}{8}(1 - \xi) \quad \text{for the first ring}$$

$$\Delta_i = \begin{bmatrix} 0.5 & 0.625 & 0.75 \end{bmatrix}^T \quad (203)$$

$$\delta J = \frac{1}{8} \quad \text{for the second ring}$$

$$\Delta_i = \begin{bmatrix} 0 & 0.25 & 0.5 \end{bmatrix}^T, \quad (204)$$

$$\delta J = \frac{1}{4} \quad \text{for the third ring}$$

$$\delta f_e = \int N^T p \frac{1}{8}(1 - \xi) d\xi = p \begin{bmatrix} \frac{1}{12} & \frac{1}{6} & 0 \end{bmatrix}^T$$

$$\text{for the first ring} \quad (205)$$

$$\delta f_e = \int N^T p \frac{1}{8} d\xi = p \begin{bmatrix} \frac{1}{24} & \frac{1}{6} & \frac{1}{24} \end{bmatrix}^T$$

$$\text{for the second ring} \quad (206)$$

$$\delta f_e = \int N^T p \frac{1}{4} d\xi = p \begin{bmatrix} \frac{1}{12} & \frac{1}{3} & \frac{1}{12} \end{bmatrix}^T$$

$$\text{for the third ring} \quad (207)$$

Summing Equations (205)–(207) the total load variation along the crack face is

$$\delta f_e = p \begin{bmatrix} \frac{1}{12} & \frac{1}{3} & \frac{1}{8} & \frac{1}{6} & \frac{1}{8} & \frac{1}{6} & 0 \end{bmatrix}^T \quad (208)$$

3.01.5.1.4 Formulation for mixed-mode fracture problem

The mode decomposition technique developed by Ishikawa *et al.* (1979, 1980) can be used to solve the mixed-mode fracture problem. Ishikawa *et al.* have shown that the analytical crack-tip field parameters can be decomposed into modes I and II components through the use of a symmetric crack-tip mesh, with respect to the local crack-tip coordinate system. Thus, by decomposing nodal displacement vector and load vector, u and f , into modes I and II vectors, $u = u_I + u_{II}$ and $f = f_I + f_{II}$, uncoupled energy release rates at crack tip i are

$$G_i = (G_I)_i + (G_{II})_i \quad (209)$$

$$(G_I)_i = -\frac{1}{2}(u_I)^T \frac{\delta K}{\delta a_i} u_I + (u_I)^T \frac{\delta f_I}{\delta a_i} \quad (210)$$

$$(G_{II})_i = -\frac{1}{2}(u_{II})^T \frac{\delta K}{\delta a_i} u_{II} + (u_{II})^T \frac{\delta f_{II}}{\delta a_i} \quad (211)$$

in which subscripts I and II represent modes I and II components, respectively.

In the same manner, rates of uncoupled energy release rate are

$$\frac{\delta G_i}{\delta a_j} = \frac{\delta(G_I)_i}{\delta a_j} + \frac{\delta(G_{II})_i}{\delta a_j} \quad (212)$$

For $i \neq j$,

$$\frac{\delta(G_I)_i}{\delta a_j} = -(u_I)^T \frac{\delta K}{\delta a_i} K^{-1} \left(\frac{\delta f_I}{\delta a_j} - \frac{\delta K}{\delta a_j} u_I \right) + \left(\frac{\delta f_I}{\delta a_j} - \frac{\delta K}{\delta a_j} u_I \right)^T K^{-1T} \frac{\delta f_I}{\delta a_i} \quad (213)$$

$$\frac{\delta(G_{II})_i}{\delta a_j} = -(u_{II})^T \frac{\delta K}{\delta a_i} K^{-1} \left(\frac{\delta f_{II}}{\delta a_j} - \frac{\delta K}{\delta a_j} u_{II} \right) + \left(\frac{\delta f_{II}}{\delta a_j} - \frac{\delta K}{\delta a_j} u_{II} \right)^T K^{-1T} \frac{\delta f_{II}}{\delta a_i} \quad (214)$$

For $i = j$,

$$\frac{\delta(G_I)_i}{\delta a_i} = -(u_I)^T \frac{\delta K}{\delta a_i} K^{-1} \left(\frac{\delta f_I}{\delta a_i} - \frac{\delta K}{\delta a_i} u_I \right) - \frac{1}{2}(u_I)^T \frac{\delta^2 K}{\delta a_i^2} u_I + \left(\frac{\delta f_I}{\delta a_i} - \frac{\delta K}{\delta a_i} u_I \right)^T K^{-1T} \frac{\delta f_I}{\delta a_i} + u^T \frac{\delta^2 f_I}{\delta a_i^2} \quad (215)$$

$$\begin{aligned} \frac{\delta(G_{II})_i}{\delta a_i} = & - (u_{II})^T \frac{\delta K}{\delta a_i} K^{-1} \left(\frac{\delta f_{II}}{\delta a_i} - \frac{\delta K}{\delta a_i} u_{II} \right) \\ & - \frac{1}{2} (u_{II})^T \frac{\delta^2 K}{\delta a_i^2} u_{II} \\ & + \left(\frac{\delta f_{II}}{\delta a_i} - \frac{\delta K}{\delta a_i} u_{II} \right)^T K^{-1 T} \frac{\delta f_{II}}{\delta a_i} \\ & + u^T \frac{\delta^2 f_{II}}{\delta a_i^2} \end{aligned} \quad (216)$$

Here, it is noted that the mesh in the crack-tip neighborhood must be symmetric.

Another method for solving mixed-mode fracture problems is to use Betti's reciprocal theorem and Yau's mutual energy representation for the virtual crack extension method (Stern *et al.*, 1976; Yau *et al.*, 1980). Here, the generalized forms of mutual energy release rate and its derivative for a multiply cracked body are presented. The mutual energy release rate at crack tip i is

$$\begin{aligned} M_i^{(1, 2)} = & - \frac{\delta \Pi}{\delta a_i} = - \left(u^{(2)} \right)^T \frac{\delta K}{\delta a_i} u^{(1)} \\ & + \left(u^{(2)} \right)^T \frac{\delta f^{(1)}}{\delta a_i} + \left(u^{(1)} \right)^T \frac{\delta f^{(2)}}{\delta a_i} \end{aligned} \quad (217)$$

in which superscripts (1) and (2) represent any two sets of equilibrium states of the elastic body. The rates of mutual energy release rate are

For $i \neq j$,

$$\begin{aligned} \frac{\delta M_i^{(1, 2)}}{\delta a_j} = & - \left(\frac{\delta u^{(2)}}{\delta a_j} \right)^T \frac{\delta K}{\delta a_i} u^{(1)} - \left(u^{(2)} \right)^T \frac{\delta K}{\delta a_i} \frac{\delta u^{(1)}}{\delta a_j} \\ & + \left(\frac{\delta u^{(2)}}{\delta a_j} \right)^T \frac{\delta f^{(1)}}{\delta a_i} + \left(\frac{\delta u^{(1)}}{\delta a_j} \right)^T \frac{\delta f^{(2)}}{\delta a_i} \end{aligned} \quad (218)$$

For $i = j$,

$$\begin{aligned} \frac{\delta M_i^{(1, 2)}}{\delta a_i} = & - \left(\frac{\delta u^{(2)}}{\delta a_i} \right)^T \frac{\delta K}{\delta a_i} u^{(1)} - \left(u^{(2)} \right)^T \frac{\delta^2 K}{\delta a_i^2} u^{(1)} \\ & - \left(u^{(2)} \right)^T \frac{\delta K}{\delta a_i} \frac{\delta u^{(1)}}{\delta a_i} + \left(\frac{\delta u^{(2)}}{\delta a_i} \right)^T \frac{\delta f^{(1)}}{\delta a_i} \\ & + \left(u^{(2)} \right)^T \frac{\delta^2 f^{(1)}}{\delta a_i^2} + \left(\frac{\delta u^{(1)}}{\delta a_i} \right)^T \frac{\delta f^{(2)}}{\delta a_i} \\ & + \left(u^{(1)} \right)^T \frac{\delta^2 f^{(2)}}{\delta a_i^2} \end{aligned} \quad (219)$$

Displacement variations can be computed from the variation of global equilibrium equation:

$$\frac{\delta u^{(1)}}{\delta a_j} = K^{-1} \left(\frac{\delta f^{(1)}}{\delta a_j} - \frac{\delta K}{\delta a_j} u^{(1)} \right) \quad (220)$$

$$\frac{\delta u^{(2)}}{\delta a_j} = K^{-1} \left(\frac{\delta f^{(2)}}{\delta a_j} - \frac{\delta K}{\delta a_j} u^{(2)} \right) \quad (221)$$

Now, mutual energy release rate and its rates can be related to SIF and its rates by

$$M_i^{(1, 2a)} = 2\alpha \left(K_I^{(1)} \right)_i \quad (222)$$

$$M_i^{(1, 2b)} = 2\alpha \left(K_{II}^{(1)} \right)_i \quad (223)$$

$$\frac{\delta M_i^{(1, 2a)}}{\delta a_j} = 2\alpha \frac{\delta \left(K_I^{(1)} \right)_i}{\delta a_j} \quad (224)$$

$$\frac{\delta M_i^{(1, 2b)}}{\delta a_j} = 2\alpha \frac{\delta \left(K_{II}^{(1)} \right)_i}{\delta a_j} \quad (225)$$

in which superscript (1) represents equilibrium state of numerical solution, while (2a) and (2b) represent equilibrium states of analytical solutions for pure mode I and pure mode II for the used mesh, respectively.

3.01.5.1.5 Formulation for axisymmetric problem

Let

G_i	the energy release rate at crack i
a_i	the length of crack i
k	the element stiffness matrix
K	the structural stiffness matrix
f_e	the element load vector
u	the nodal displacement vector
p	the crack-face load distribution
$\tilde{\epsilon}$	the virtual strain-like matrix
N_k	the shape function at node k
r	the radius from z axis to a point in the cross-section
r_{ai}	the radius to the tip of the crack i
B	the strain-nodal displacement matrix
D	the elastic constitutive matrix
J	the jacobian matrix
ΔT	the temperature profile
α	the thermal expansion coefficient

The energy release rate at crack tip i can be expressed as

$$G_i = - \frac{\delta \pi}{\delta a_i r_{ai}} = - \frac{1}{2} u^T \frac{\delta K}{\delta a_i r_{ai}} u + u^T \frac{\delta f}{\delta a_i r_{ai}} \quad (226)$$

The variation of G_i of Equation (226) with respect to the growth of any other crack, j , is

$$\begin{aligned} \frac{\delta G_i}{\delta a_j r_{aj}} = & - u^T \frac{\delta K}{\delta a_i r_{ai}} \frac{\delta u}{\delta a_j r_{aj}} - \frac{1}{2} u^T \frac{\delta^2 K}{\delta a_i \delta a_j r_{ai} r_{aj}} u \\ & + \frac{\delta u^T}{\delta a_j r_{aj}} \frac{\delta f}{\delta a_i r_{ai}} + u^T \frac{\delta^2 f}{\delta a_i \delta a_j r_{ai} r_{aj}} u \end{aligned} \quad (227)$$

If $i \neq j$, then the second-order variations of stiffness and loading with respect to two different crack extensions a_i and a_j vanish:

$$\frac{\delta^2 K}{\delta a_i \delta a_j r_{ai} r_{aj}} = \frac{\delta^2 f}{\delta a_i \delta a_j r_{ai} r_{aj}} = 0 \quad (228)$$

Rewriting Equation (227), $\delta G_i / \delta a_j r_{aj}$ is

$$\frac{\delta G_i}{\delta a_j r_{aj}} = -u^T \frac{\delta K}{\delta a_i r_{ai}} \frac{\delta u}{\delta a_j r_{aj}} + \frac{\delta u^T}{\delta a_j r_{aj}} \frac{\delta f}{\delta a_i r_{ai}} \quad (229)$$

The variation of the displacement can be obtained from the variation of the global equilibrium equation $Ku = f$ with respect to $a_j r_{aj}$:

$$\begin{aligned} \frac{\delta K}{\delta a_j r_{aj}} u + K \frac{\delta u}{\delta a_j r_{aj}} &= \frac{\delta f}{\delta a_j r_{aj}} \quad \text{or} \quad \frac{\delta u}{\delta a_j r_{aj}} \\ &= K^{-1} \left(\frac{\delta f}{\delta a_j r_{aj}} - \frac{\delta K}{\delta a_j r_{aj}} u \right) \end{aligned} \quad (230)$$

By substituting Equation (230) into Equation (229), we obtain,

$$\begin{aligned} \frac{\delta G_i}{\delta a_j r_{aj}} &= -u^T \frac{\delta K}{\delta a_i r_{ai}} K^{-1} \left(\frac{\delta f}{\delta a_j r_{aj}} - \frac{\delta K}{\delta a_j r_{aj}} u \right) \\ &\quad + \left(\frac{\delta f}{\delta a_j r_{aj}} - \frac{\delta K}{\delta a_j r_{aj}} u \right)^T K^{-1 T} \frac{\delta f}{\delta a_i r_{ai}} \end{aligned} \quad (231)$$

For the case of $i = j$,

$$\begin{aligned} \frac{\delta G_i}{\delta a_i r_{ai}} &= -u^T \frac{\delta K}{\delta a_i r_{ai}} \frac{\delta u}{\delta a_i r_{ai}} - \frac{1}{2} u^T \left(\frac{\delta^2 K}{\delta a_i^2 r_{ai}^2} - \frac{\delta K}{\delta a_i^3 r_{ai}^3} \right) u \\ &\quad + \frac{\delta u^T}{\delta a_i r_{ai}} \frac{\delta f}{\delta a_i r_{ai}} + u^T \left(\frac{\delta^2 f}{\delta a_i^2 r_{ai}^2} - \frac{\delta f}{\delta a_i^3 r_{ai}^3} \right) \end{aligned} \quad (232)$$

where the overall stiffness variations $\delta K / \delta a_i$ and $\delta^2 K / \delta a_i^2$ are produced by assembling element stiffness variations $\delta k / \delta a_i$ and $\delta^2 k / \delta a_i^2$.

The element stiffness for axisymmetric problem and its variations are

$$k = \int B^T D B r dr dz = \int B^T D B r |J| d\xi d\eta \quad (233)$$

$$\begin{aligned} \delta k &= \delta \left[\int B^T D B r |J| d\xi d\eta \right] \\ &= \int [\delta B^T DB + B^T D \delta B + \text{Tr}(\tilde{\epsilon}) B^T DB] r |J| d\xi d\eta \\ &\quad + \int B^T D B \delta r |J| d\xi d\eta \end{aligned} \quad (234)$$

$$\begin{aligned} \delta^2 k &= \int [\delta^2 B^T DB + 2\delta B^T D \delta B + B^T D \delta^2 B] r |J| d\xi d\eta \\ &\quad + \int [2|\tilde{\epsilon}| B^T DB + 2\text{Tr}(\tilde{\epsilon})] \\ &\quad \times (\delta B^T DB + B^T D \delta B) r |J| d\xi d\eta \\ &\quad + 2 \int [\delta B^T DB + B^T D \delta B + \text{Tr}(\tilde{\epsilon}) B^T DB] \\ &\quad \times \delta r |J| d\xi d\eta \end{aligned} \quad (235)$$

where δr is the change of nodal coordinate as a result of virtual crack extension and expressed by

$$\delta r = \frac{\partial r}{\partial a} \delta a = \left[N_k \left(\frac{\partial r}{\partial a} \right)_k \right] \delta a$$

If the first ring of element surrounding the crack tip is used in the mesh perturbation, the term $(\partial r / \partial a)_k$ for mode I crack behavior will have a value of one for the degree of freedom in the x -direction at the crack-tip node, 0.75 at the quarter-point nodes and zero otherwise. In the case of nonuniform crack-face loading, the element load variations are given by

$$\begin{aligned} \delta f_e &= \delta \int N^T p r |J| d\xi \\ &= \int [N^T \delta p + \text{Tr}(\tilde{\epsilon}) N^T p] |J| d\xi \\ &\quad + \int N^T p \delta r |J| d\xi \end{aligned} \quad (236)$$

$$\begin{aligned} \delta^2 f_e &= \int [N^T \delta^2 p + 2\text{Tr}(\tilde{\epsilon}) N^T \delta p + 2|\tilde{\epsilon}| N^T p] r |J| d\xi \\ &\quad + 2 \int [N^T \delta p + N^T p \text{Tr}(\tilde{\epsilon})] \delta r |J| d\xi \end{aligned} \quad (237)$$

In the same manner, the variations of thermal loading are

$$\begin{aligned} \delta f_e &= \delta \int B^T D(\alpha \Delta T) r |J| d\xi d\eta \\ &= \int [\delta B^T D(\alpha \Delta T) + B^T D \delta(\alpha \Delta T) \\ &\quad + \text{Tr}(\tilde{\epsilon}) B^T D(\alpha \Delta T)] r |J| d\xi d\eta \\ &\quad + \int B^T D(\alpha \Delta T) \delta r |J| d\xi d\eta \end{aligned} \quad (238)$$

$$\begin{aligned} \delta^2 f_e &= \int [\delta^2 B^T D(\alpha \Delta T) + 2\delta B^T D \delta(\alpha \Delta T) \\ &\quad + B^T D \delta^2(\alpha \Delta T) r |J|] d\xi d\eta \\ &\quad + \int [2\text{Tr}(\tilde{\epsilon}) (\delta B^T D \alpha \Delta T + B^T D \delta(\alpha \Delta T))] \\ &\quad + 2|\tilde{\epsilon}| B^T D \delta(\alpha \Delta T) r |J| d\xi d\eta \\ &\quad + 2 \int [\delta B^T D(\alpha \Delta T) + B^T D \delta(\alpha \Delta T) \\ &\quad + \text{Tr}(\tilde{\epsilon}) B^T D(\alpha \Delta T) \delta r |J| d\xi d\eta] \end{aligned} \quad (239)$$

3.01.5.1.6 Derivations for the second-order derivative of energy release rate

Let

G_i	the energy release rate at crack i
a_i	the length of crack i
k	the element stiffness matrix
K	the structural stiffness matrix
f_e	the element load vector
u	the nodal displacement vector
p	the crack-face load distribution
$\tilde{\epsilon}$	the virtual strain-like matrix
N_k	the shape function at node k
B	the strain-nodal displacement matrix
D	the elastic constitutive matrix
J	the jacobian matrix
ΔT	the temperature profile
α	the thermal expansion coefficient

The energy release rate at crack tip i can be expressed as

$$G_i = -\frac{1}{2} u^T \frac{\delta K}{\delta a_i} u + u^T \frac{\delta f}{\delta a_i} \quad (240)$$

The variation of this with respect to the crack length, a_i , is

$$\begin{aligned} \frac{\delta G_i}{\delta a_i} &= -u^T \frac{\delta K}{\delta a_i} \frac{\delta u}{\delta a_i} - \frac{1}{2} u^T \frac{\delta^2 K}{\delta a_i^2} u \\ &\quad + \frac{\delta u^T}{\delta a_i} \frac{\delta f}{\delta a_i} + u^T \frac{\delta^2 f}{\delta a_i^2} \end{aligned} \quad (241)$$

The second variation of this with respect to the crack length, a_i , is

$$\begin{aligned} \frac{\delta^2 G_i}{\delta a_i^2} &= -\frac{1}{2} u^T \frac{\delta^3 K}{\delta a_i^3} u - 2u^T \frac{\delta^2 K}{\delta a_i^2} \frac{\delta u}{\delta a_i} \\ &\quad - u^T \frac{\delta K}{\delta a_i} \frac{\delta^2 u}{\delta a_i^2} - \frac{\delta u^T}{\delta a_i} \frac{\delta K}{\delta a_i} \frac{\delta u}{\delta a_i} \\ &\quad + \frac{\delta^2 u^T}{\delta a_i^2} \frac{\delta f}{\delta a_i} + 2 \frac{\delta u^T}{\delta a_i} \frac{\delta^2 f}{\delta a_i^2} + u^T \frac{\delta^3 f}{\delta a_i^3} \end{aligned} \quad (242)$$

where the variations of displacements are

$$\begin{aligned} \frac{\delta u}{\delta a_i} &= K^{-1} \left(\frac{\delta f}{\delta a_i} - \frac{\delta K}{\delta a_i} u \right) \quad \text{and} \\ \frac{\delta^2 u}{\delta a_i^2} &= K^{-1} \left(\frac{\delta^2 f}{\delta a_i^2} - \frac{\delta^2 K}{\delta a_i^2} u - 2 \frac{\delta K}{\delta a_i} \frac{\delta u}{\delta a_i} \right) \end{aligned} \quad (243)$$

and the element stiffness variations with respect to crack length are

$$\delta k = \int_v [\delta B^T DB + B^T D \delta B + \text{Tr}(\tilde{\epsilon}) B^T DB] dV \quad (244)$$

$$\begin{aligned} \delta^2 k &= \int_v [\delta^2 B^T DB + 2\delta B^T D \delta B \\ &\quad + B^T D \delta^2 B] dV \\ &\quad + \int_v [2|\tilde{\epsilon}| B^T DB + 2\text{Tr}(\tilde{\epsilon}) \\ &\quad \times (\delta B^T DB + B^T D \delta B)] dV \end{aligned} \quad (245)$$

$$\begin{aligned} \delta^3 k &= \int_v [\delta^3 B^T DB + 3\delta^2 B^T D \delta B \\ &\quad + 3\delta B^T D \delta^2 B + B^T D \delta^3 B] dV \\ &\quad + 3 \int_v [\delta^2 B^T DB + 2\delta B^T D \delta B \\ &\quad + B^T D \delta^2 B] \text{Tr}(\tilde{\epsilon}) dV \\ &\quad + \int_v [2|\tilde{\epsilon}|^2 B^T DB + 6|\tilde{\epsilon}| (\delta B^T DB \\ &\quad + B^T D \delta B) + 2|\tilde{\epsilon}| \text{Tr}(\tilde{\epsilon}) B^T DB] dV \end{aligned} \quad (246)$$

where

$$\delta^3 B = -6(\tilde{\epsilon})^3 B \quad (247)$$

Element load variations for a non-uniform crack-face loading are

$$\delta f_e = \delta \int_s N^T p ds = \int_s [N^T \delta p + \text{Tr}(\tilde{\epsilon}) N^T p] ds \quad (248)$$

$$\begin{aligned} \delta^2 f &= \delta^2 \int_s N^T p ds \\ &= \int_s [N^T \delta^2 p + 2\text{Tr}(\tilde{\epsilon}) N^T \delta p + 2|\tilde{\epsilon}| N^T p] ds \end{aligned} \quad (249)$$

$$\begin{aligned} \delta^3 f_e &= \int_s [N^T \delta^3 p + 6|\tilde{\epsilon}| N^T \delta p + 2|\tilde{\epsilon}|^2 N^T p \\ &\quad + \text{Tr}(\tilde{\epsilon}) (3N^T \delta^2 p + 2|\tilde{\epsilon}| N^T p)] ds \end{aligned} \quad (250)$$

If an arbitrary load distribution, p , is a function of x , then its variations with respect to crack extension for mode I (x -direction) are as follows:

$$\frac{\delta p}{\delta a} = \frac{\partial p}{\partial x} \frac{\partial x}{\partial a} = \left[N_k \left(\frac{\partial p}{\partial x} \right)_k \right] \cdot \left[N_k \left(\frac{\partial x}{\partial a} \right)_k \right] \quad (251)$$

$$\frac{\delta^2 p}{\delta a^2} = \left[N_k \left(\frac{\partial^2 p}{\partial x^2} \right)_k \right] \cdot \left[N_k \left(\frac{\partial x}{\partial a} \right)_k \right]^2 \quad (252)$$

$$\frac{\delta^3 p}{\delta a^3} = \left[N_k \left(\frac{\partial^3 p}{\partial x^3} \right)_k \right] \cdot \left[N_k \left(\frac{\partial x}{\partial a} \right)_k \right]^3 \quad (253)$$

where p_k , $(\partial p / \partial x)_k$, $(\partial^2 p / \partial x^2)_k$, and $(\partial^3 p / \partial x^3)_k$ are the nodal load value and its

first, second and third derivatives with respect to the direction x at node k .

In the same manner, the variations of thermal loading can be derived as described below:

$$(245) \quad f_e = \int_v B^T D(\alpha \Delta T) dV \quad (254)$$

$$(246) \quad \delta f_e = \int_v [\delta B^T D(\alpha \Delta T) + B^T D\delta(\alpha \Delta T) + \text{Tr}(\tilde{\varepsilon}) B^T D(\alpha \Delta T) dV] \quad (255)$$

$$(247) \quad \delta^2 f_e = \int_v [\delta^2 B^T D(\alpha \Delta T) + 2\delta B^T D\delta(\alpha \Delta T) + B^T D\delta^2(\alpha \Delta T) + 2\text{Tr}(\tilde{\varepsilon})(\delta B^T D\alpha \Delta T + B^T D\delta(\alpha \Delta T)) + 2|\tilde{\varepsilon}| B^T D\delta(\alpha \Delta T)] dV \quad (256)$$

$$(248) \quad \delta^3 f_e = \int_v [\delta^3 B^T D(\alpha \Delta T) + 3\delta^2 B^T D\delta(\alpha \Delta T) + 3\delta B^T D\delta^2(\alpha \Delta T) + B^T D\delta^3(\alpha \Delta T)] dV + 3 \int_v \delta^2 B^T D(\alpha \Delta T) + 2\delta B^T D\delta(\alpha \Delta T) + B^T D\delta^2(\alpha \Delta T) \text{Tr}(\tilde{\varepsilon}) dV + \int_v [2|\tilde{\varepsilon}|^2 B^T D(\alpha \Delta T) + 6|\tilde{\varepsilon}|(\delta B^T D(\alpha \Delta T) + B^T D\delta(\alpha \Delta T)) + 2|\tilde{\varepsilon}| \text{Tr}(\tilde{\varepsilon}) B^T D(\alpha \Delta T)] dV \quad (257)$$

If an arbitrary temperature profile ΔT is a function of x and y , then its variations with respect to crack extension for mode I are as follows:

$$(249) \quad \Delta T = \Delta T(x, y) \quad (258)$$

$$\frac{\delta \Delta T}{\delta a} = \frac{\partial \Delta T}{\partial x} \frac{\partial x}{\partial a} + \frac{\partial \Delta T}{\partial y} \frac{\partial y}{\partial a} = \frac{\partial \Delta T}{\partial x} \frac{\partial x}{\partial a} \\ = \left[N_k \left(\frac{\partial \Delta T}{\partial x} \right)_k \right] \cdot \left[N_k \left(\frac{\partial x}{\partial a} \right)_k \right] \quad (259)$$

$$(250) \quad \frac{\delta^2 \Delta T}{\delta a^2} = \left[N_k \left(\frac{\partial^2 \Delta T}{\partial x^2} \right)_k \right] \cdot \left[N_k \left(\frac{\partial x}{\partial a} \right)_k \right]^2 \quad (260)$$

$$(251) \quad \frac{\delta^3 \Delta T}{\delta a^3} = \left[N_k \left(\frac{\partial^3 \Delta T}{\partial x^3} \right)_k \right] \cdot \left[N_k \left(\frac{\partial x}{\partial a} \right)_k \right]^3 \quad (261)$$

where ΔT_k , $(\partial \Delta T / \partial x)_k$, $(\partial^2 \Delta T / \partial x^2)_k$, and $(\partial^3 \Delta T / \partial x^3)_k$ are the nodal temperature drop and its first, second and third derivatives with respect to the direction x at node k .

3.01.5.2 Numerical Examples

3.01.5.2.1 Example 1: a pressurized mode-I crack in an infinite plate

The first numerical example investigates a small, pressurized central crack in a large plate. As shown in Figure 56, the initial crack length to width ratio a/W is 0.01 to approximate a central crack in the infinite plate under a plane stress condition. Due to the symmetry in the problem, one-half of the plate was modeled with about 500 linear strain triangular elements including quarter-point elements at the crack tip, Figure 57(a). The exact K_I and $\delta K_I / \delta a$ solutions for mode I crack growth under uniform crack pressure, p , in an infinite plate can be expressed analytically as

$$(252) \quad K_I = p \sqrt{\pi a} \quad \frac{\delta K_I}{\delta a} = \frac{p}{2} \sqrt{\frac{\pi}{a}}$$

Table 7 compares the computed values of K_I and $\delta K_I / \delta a$ for various crack lengths with the exact solutions. The results are in good agreement with exact solutions, giving maximum errors for K_I and $\delta K_I / \delta a$ of 0.1% and 2%, respectively, for this mesh.

3.01.5.2.2 Example 2: a center-cracked infinite plate subjected to a uniform remote tensile stress

The next example considers the same geometry as that of the first example, but with a different loading condition. The infinite cracked plate is subjected to uniform remote tensile stress, σ_0 , instead of crack-face pressure. It should be noted that the $\delta f / \delta a$ and $\delta^2 f / \delta a^2$ terms are null for virtual crack extension under this loading. This model is analyzed to demonstrate the capability of the proposed method for evaluating the second derivative of

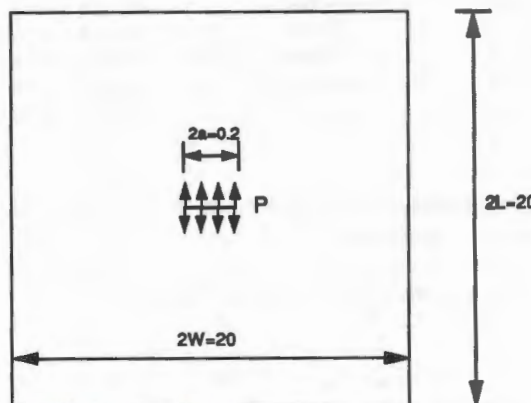


Figure 56 A pressurized central crack in a simulated infinite plate, Example 1.

Symmetry

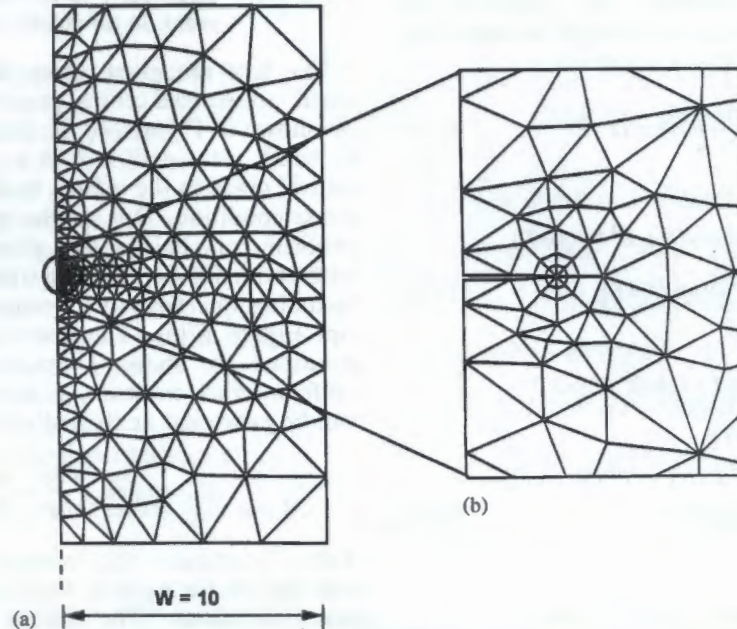


Figure 57 (a) FE mesh for Example 1 and (b) detail of crack-tip meshing.

Table 7 Comparison of computed with exact solutions for K_I and $\delta K_I/\delta a$, Example 1, $p = 1.0$, crack-tip element size = $a/8$.

a/W	$K_I \text{ MPa m}^{1/2}$ Exact	$K_I \text{ MPa m}^{1/2}$ Computed (error %)	$\delta K_I/\delta a \text{ MPa m}^{1/2} \text{ m}^{-1}$ Exact	$\delta K_I/\delta a \text{ MPa m}^{1/2} \text{ m}^{-1}$ Computed (error %)
0.010	0.5605	0.5600 (0.09)	2.802	2.759 (1.53)
0.011	0.5879	0.5876 (0.05)	2.672	2.642 (1.12)
0.012	0.6140	0.6134 (0.10)	2.558	2.536 (0.87)
0.013	0.6391	0.6385 (0.09)	2.458	2.409 (1.97)
0.014	0.6632	0.6630 (0.03)	2.369	2.320 (5.05)

Table 8 Comparison of computed with exact solutions for K_I and $\delta K_I/\delta a$, Example 2, $\sigma_0 = 1.0$, crack-tip element size = $a/8$.

a/W	$K_I \text{ MPa m}^{1/2}$ Exact	$K_I \text{ MPa m}^{1/2}$ Computed (error %)	$\delta K_I/\delta a \text{ MPa m}^{1/2} \text{ m}^{-1}$ Exact	$\delta K_I/\delta a \text{ MPa m}^{1/2} \text{ m}^{-1}$ Computed (error %)
0.010	0.5605	0.5610 (0.09)	2.802	2.739 (5.25)
0.011	0.5879	0.5884 (0.08)	2.672	2.617 (5.06)
0.012	0.6140	0.6145 (0.08)	2.558	2.561 (1.17)
0.013	0.6391	0.6395 (0.06)	2.458	2.404 (5.20)
0.014	0.6632	0.6627 (0.08)	2.369	2.313 (5.36)

energy release rate. The exact K_I , $\delta K_I/\delta a$, and $\delta K_I^2/\delta a^2$ solutions for a mode I crack under uniform remote tensile stress, σ_0 , in an infinite plate can be expressed analytically as:

$$K_I = \sigma_0 \sqrt{\pi a} \quad \frac{\delta K_I}{\delta a} = \frac{\sigma_0}{2} \sqrt{\frac{\pi}{a}} \quad (263)$$

$$\frac{\delta^2 K_I}{\delta a^2} = -\frac{\sigma_0}{4a} \sqrt{\frac{\pi}{a}}$$

Tables 8 and 9 show that the best computed solutions differ from the exact by $\sim 0.1\%$ for K_I , 2% for $\delta K_I/\delta a$, and 5–10% for $\delta K_I^2/\delta a^2$, respectively. Table 9 shows that the solution accuracy for $\delta K_I^2/\delta a^2$ is affected considerably by the number of rings of elements surrounding the crack tip that are involved in the mesh perturbation due to the virtual crack extension. When additional rings of surrounding elements from the crack tip are used in the perturbation,

Table 9 Comparison of computed with exact solutions for $\delta^2 K_I / \delta a^2$ for 3 different mesh perturbations, Example 2, $\sigma_0 = 1.0$, crack-tip element size = $a/8$.

a/W	Exact	1st ring (error %)	1st + 2nd rings (error %)	1st + 2nd + 3rd (error %)
0.010	-14.012	-52.373 (273.8)	-17.465 (24.6)	-15.044 (7.37)
0.011	-12.145	-58.599 (382.5)	-15.386 (26.7)	-11.637 (4.18)
0.012	-10.659	-40.801 (282.8)	-13.447 (26.2)	-11.915 (11.8)
0.013	-9.454	-46.023 (386.8)	-12.394 (31.1)	-9.881 (4.52)
0.014	-8.459	-25.607 (167.3)	-10.941 (29.3)	-8.911 (5.34)

Table 10 The computed values of K_I for various crack-tip element sizes in three different mesh perturbation schemes. Example 2, $\sigma_0 = 1.0$ (Exact value of $K_I = 0.5605$ for $a/W = 0.01$).

Element size	1st ring (error %)	1st + 2nd rings (error %)	1st + 2nd + 3rd (error %)
$a/8$	0.5625 (0.36)	0.5617 (0.21)	0.5610 (0.09)
$a/16$	0.5622 (0.30)	0.5613 (0.14)	0.5611 (0.11)
$a/32$	0.5620 (0.27)	0.5610 (0.09)	0.5607 (0.04)
$a/64$	0.5617 (0.21)	0.5608 (0.05)	0.5604 (0.02)
$a/128$	0.5616 (0.20)	0.5606 (0.02)	0.5602 (0.05)

Table 11 The computed values of $\delta K_I / \delta a$ for various crack-tip element sizes in three different mesh perturbation schemes. Example 2, $\sigma_0 = 1.0$ (exact value of $\delta K_I / \delta a = 2.802$ for $a/W = 0.01$).

Element size	1st ring (error %)	1st + 2nd rings (error %)	1st + 2nd + 3rd (error %)
$a/8$	2.698 (3.71)	2.745 (5.03)	2.739 (5.25)
$a/16$	2.618 (6.57)	2.744 (5.07)	2.741 (5.18)
$a/32$	2.501 (10.7)	2.736 (5.36)	2.747 (1.96)
$a/64$	2.250 (19.7)	2.732 (5.50)	2.747 (1.96)
$a/128$	1.788 (36.2)	2.732 (5.50)	2.765 (1.32)

Table 12 The computed values of $\delta^2 K_I / \delta a^2$ for various crack-tip element sizes in three different mesh perturbation schemes. Example 2, $\sigma_0 = 1.0$ (exact value of $\delta^2 K_I / \delta a^2 = -14.013$ for $a/W = 0.01$).

Element size	1st ring (error %)	1st + 2nd rings (error %)	1st + 2nd + 3rd (error %)
$a/8$	-52.373 (273.8)	-17.465 (24.6)	-15.044 (7.4)
$a/16$	-67.957 (384.9)	-18.990 (35.5)	-14.967 (6.8)
$a/32$	-225.25 (1507.4)	-29.614 (111.3)	-14.264 (1.8)
$a/64$	-856.94 (6015.3)	-79.044 (464.1)	-13.151 (6.2)
$a/128$	-3404.7 (24196.7)	-281.20 (1906.7)	-17.647 (25.9)

increasingly more accurate solutions for $\delta K_I^2 / \delta a^2$ are obtained. The effect of crack-tip element size on solution accuracy was also investigated. For Example 2 the crack-tip element size was decreased by repeatedly dividing the crack-tip element at the midpoint to create a new, regular 8-noded element, and a singular element. As the crack-tip element size gets small, the radii of the second and third rings are also decreased. Tables 10 and 11 show that as the crack-tip element size is decreased, the solutions for $\delta K_I / \delta a$ and $\delta K_I^2 / \delta a^2$ deteriorate, while the accuracy of the computed values of K_I is retained. This solution deterioration can be reduced by perturbing additional

rings of nonsingular elements surrounding the first ring of crack-tip elements. Hence, it is recommended based on these results that at least one ring of nonsingular elements for $\delta K_I / \delta a$ and two rings for $\delta K_I^2 / \delta a^2$ should be used in the mesh perturbation along with the first ring of crack-tip elements for a more accurate analysis.

However, adding additional rings alone does not guarantee uniform convergence as shown, e.g., in the last column of Table 12. This data indicates that if the crack tip elements get too small, insufficient information from the singular field, which this element only can reproduce, is available for an accurate solution.

3.01.5.2.3 Example 3: a circular crack under two symmetric point loads in an infinite space

The next problem considered is a circular crack subjected to two symmetric point loads in an infinite space. An analytical solution (Bonnet, 1994) for energy release rate G is:

$$G = \frac{(1-v^2)P^2\alpha(\kappa + \alpha^2)}{E(nh)^3(1+\alpha^2)^4} \quad \text{where}$$

$$\alpha = \frac{a}{h} \quad \text{and} \quad \kappa = \frac{2-v}{1-v} \quad (264)$$

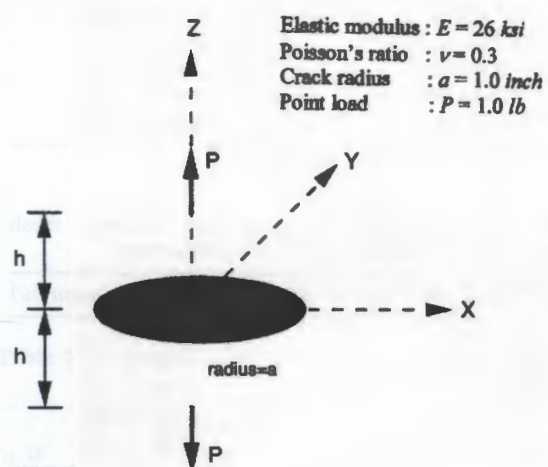


Figure 58 Circular crack subjected to two symmetric point loads in mode I, Example 3. 1 ksi = 6.984 MPa, 1 in = 25.4 mm, 1 lb = 4.45 N.

The crack is located in the xy plane and is loaded by two symmetric point forces, $\pm P$, applied at points $(0, 0, \pm h)$ as shown in Figure 58. It is interesting to note that the parameter $\alpha(a/h)$ governs the crack's stability.

$$\begin{aligned} \frac{dG}{d\alpha} &< 0 \quad (\alpha > \alpha_m) & \frac{dG}{d\alpha} &> 0 \quad (0 < \alpha < \alpha_m) \\ \frac{dG}{d\alpha} &= 0 \quad (\alpha = \alpha_m) \end{aligned} \quad (265)$$

with

$$\alpha_m^2 = \frac{\sqrt{16v^2 - 72v + 105} - 2v + 9}{2(2-v)} \quad (266)$$

Here, when $\alpha > \alpha_m$, the crack growth is stable, and unstable otherwise (Bonnet, 1994). For a Poisson's ratio, $v = 0.3$, the critical value α_m is ~ 5.276 .

The FE discretization for this problem is based on axisymmetric elements as shown in Figures 59(a) and (b). A boundary element solution due to Bonnet (Bonnet, 1994) is used as another reference solution. The computed values for K_I and $\delta K_I/\delta a$ are presented along with the exact solutions and the boundary element solution in Figures 60(a) and (b). The results agree well with the reference solutions. The present method gives a computed value of 5.297 for the bifurcation point, α_m , which differs by only 1% from the exact solution.

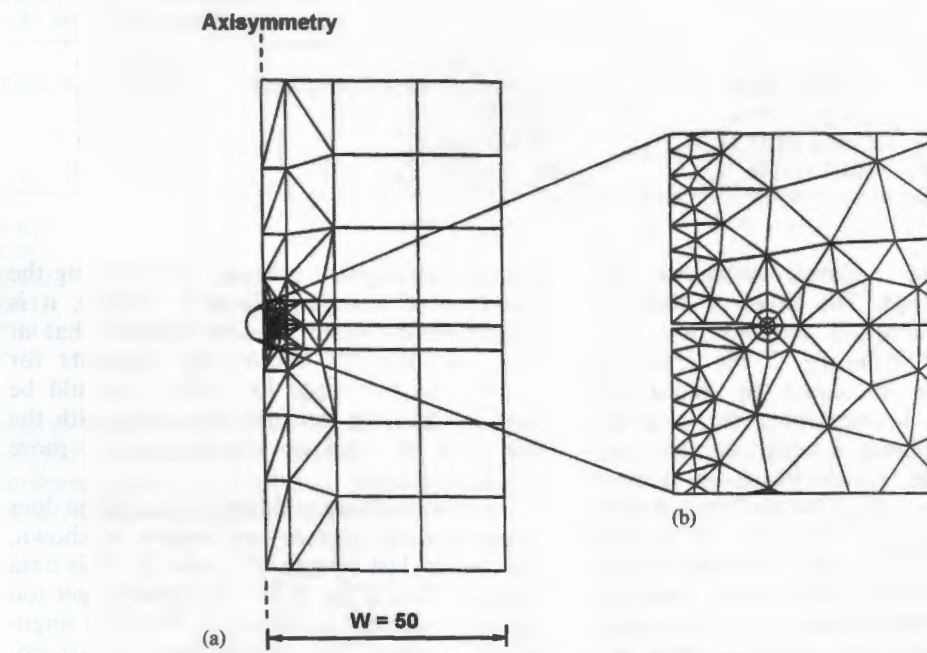


Figure 59 (a) FE mesh for Example 3 and (b) detail of crack-tip meshing.

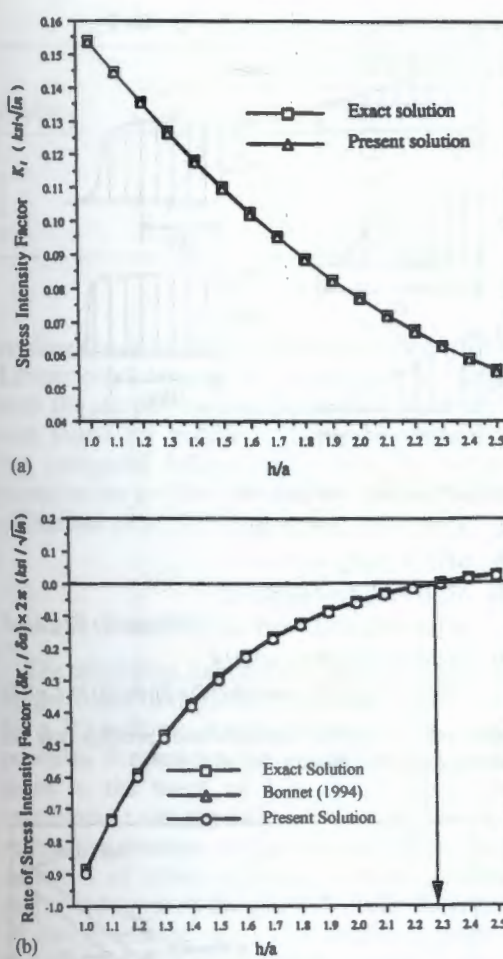


Figure 60 (a) Comparison between present and exact solution for stress intensity factor, Example 3; (b) Comparison between present, other numerical, and exact solution for rate of stress intensity factor, Example 3. $1 \text{ ksi}^{1/2} = 1.098 \text{ MPa m}^{1/2}$.

3.01.5.2.4 Example 4: a system of interacting parallel equidistant cracks in a semi-infinite plane

The example considered in this section is a system of thermally induced, equally spaced, parallel-edge cracks in a homogeneous, isotropic, elastic, semi-infinite plane, Figure 61. This problem has been studied by many researchers (Bazant and Ohtsubo, 1977; Bazant *et al.*, 1979; Bazant and Wahab, 1979; Nemat-Nasser, 1978; Nemat-Nasser *et al.*, 1978; Sumi *et al.*, 1980; Keer *et al.*, 1978; Nemat-Nasser *et al.*, 1980). Other problems of this kind include: shrinkage cracks in drying concrete and polymers, surface cracks in aging wood, thermal cracks in nuclear reactor fuel elements, and desiccation cracks in dried-up lake beds and deserts (Nemat-Nasser, 1978; Nemat-Nasser *et al.*, 1978; Sumi *et al.*, 1980). In this section, major attention is focused on showing

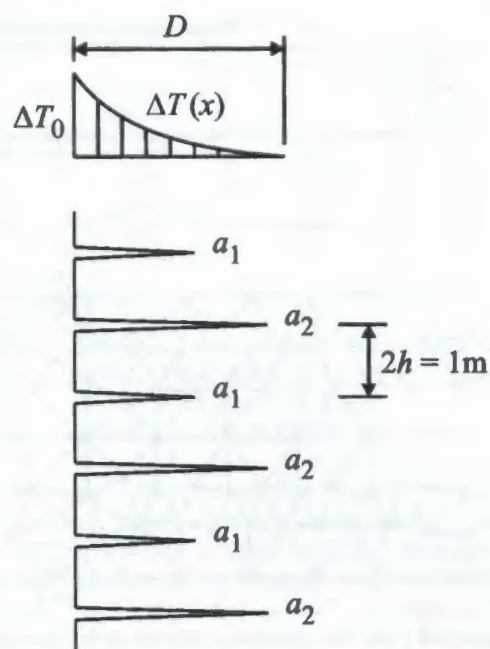


Figure 61 Thermally induced parallel edge cracks having a periodic pattern in a semi-infinite plane, Example 4.

the computational capacity of the proposed method for evaluating rates of SIFs of the system of multiple cracks under thermal loading.

First, the problem is briefly reviewed and later numerical results are presented. In this problem, the cracks are initially formed perpendicular to the free surface by cooling at the free surface. As the thermal gradient penetrates into the half-plane due to heat convection or conduction, the cracks start to grow. Quasi-static critical crack growth is assumed. That is, the cracks grow in such a manner that the SIF K_I remains at the critical value K_{IC} , but slowly enough that inertial effects are negligible. Here, the loading parameter is the cooling penetration depth, D , in which an appreciable temperature gradient has been formed in the half-plane. When crack spacing is larger than crack length, the cracks interact weakly and grow at an equal rate. As crack length becomes comparable to the spacing, interaction becomes significant. Finally, at the critical state, one crack arrests and the other cracks grow faster with increasing loading. This critical state of crack propagation bifurcation corresponds to vanishing diagonal terms in the matrix $\partial(K_I)_i / \partial a_j$ (Bazant and Ohtsubo, 1977; Bazant *et al.*, 1979; Bazant and Wahab, 1979; Nemat-Nasser, 1978; Nemat-Nasser *et al.*, 1979; Sumi *et al.*, 1980). Hence, for the determination of this critical state, rates of SIFs for the system should be accurately

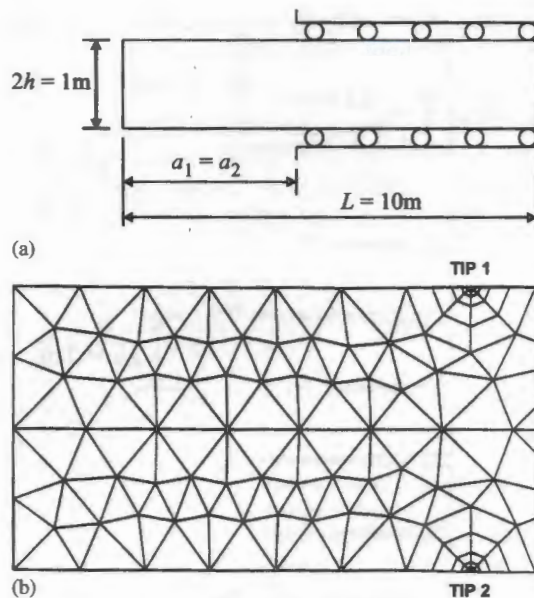
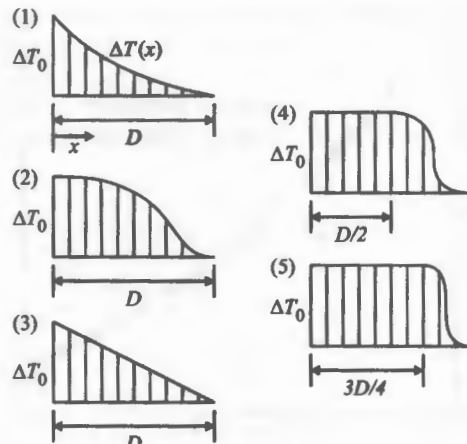


Figure 62 (a) The geometry of the strip between two independent edge cracks, Example 4 and (b) Detail of mesh around the crack tips in the strip.

calculated. In Bazant and Ohtsubo (1977), Bazant *et al.* (1979), and Bazant and Wahab (1979), the derivative matrix $\partial(K_I)_i/\partial a_j$ has been calculated using a finite difference approximation that requires two complete analyses. This technique is highly sensitive to the length of virtual crack extension Δa . In contrast, the present method calculates the solution for the rates of SIF analytically with a single analysis and, therefore, more objective solutions are obtained.

In this example, the bifurcation points are computed for various temperature profiles and compared with those of Bazant *et al.* (1979). As D increases, the corresponding value of crack length "a" is calculated such that $K_I^{(1)} = K_I^{(2)} = K_{IC}$. The computed a and D values are used to construct the equilibrium path which represents the equilibrium state for the system of cracks during crack growth. For a given a and D , on the equilibrium path, the matrix $\partial(K_I)_i/\partial a_j$ is analytically calculated, from which the bifurcation point can be determined. Figure 61 shows a model of an infinite number of parallel-edge cracks having a periodic pattern. The stability of this system can be represented by a set of two symmetric independent crack lengths, a_1 and a_2 , Figures 62(a) and (b). Initial spacing is $2h = 1\text{ m}$. The following material properties of typical graphite are used for the calculations: Young's modulus $E = 3.76 \times 10^4 \text{ MN m}^{-2}$; Thermal expansion coefficient $\alpha = 8 \times 10^{-6} \text{ }^\circ\text{C}^{-1}$; Poisson's ratio $\nu = 0.305$; Critical stress intensity factor



- (1) $\Delta T(x) = \Delta T_0 \cdot \text{erfc}(x\sqrt{3}/D)$
- (2) $\Delta T(x) = \Delta T_0 \cdot \cos\pi(x/D)$
- (3) $\Delta T(x) = \Delta T_0(1 - x/D)$
- (4) $\Delta T(x) = \Delta T_0$ for $0 \leq x \leq D/2$
 $\Delta T(x) = \Delta T_0 / 2 \cdot [1 + \cos\pi(2x/D - 1)]$ for $D/2 \leq x \leq D$
- (5) $\Delta T(x) = \Delta T_0$ for $0 \leq x \leq 3D/4$
 $\Delta T(x) = \Delta T_0 / 2 \cdot [1 + \cos\pi(4x/D - 3)]$ for $3D/4 \leq x \leq D$

Figure 63 Various temperature profiles use in Example 4, after Bazant *et al.* (1979).

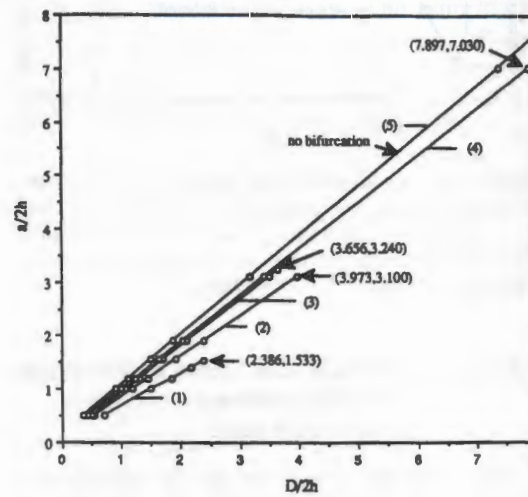


Figure 64 Predicted equilibrium paths and bifurcation points for the temperature profiles shown in Figure 63, Example 4.

$K_{IC} = 2.94 \text{ MN m}^{-3/2}$. Initial surface temperature drop ΔT_0 is taken as 100°C and fixed during the crack growth. Figure 63 shows five different temperature profiles used in this example. These are the same as those used by Bazant *et al.* (1979).

In Figure 64, the equilibrium paths and bifurcation points for various temperature profiles are presented. It is shown that the location of bifurcation $a/2h$ and a/D ratios are strongly influenced by the steepness of the

Table 13 Critical states of crack arrest for various temperature profiles, Example 4.

Profile	Results from Bazant (1979)			Results of present method		
	$a/2h$	$D/2h$	a/D	$a/2h$	$D/2h$	a/D
1	1.53	2.342	0.651	1.53	2.386	0.642
2	3.07	3.907	0.787	3.10	3.973	0.780
3	3.20	3.594	0.891	3.24	3.656	0.886
4	6.97	7.806	0.893	7.03	7.897	0.890

cooling front in the given temperature profile. Longer crack lengths for the same D are found with the steeper cooling front, with no bifurcation found for profile 5. Table 13 shows that the computed bifurcation points for various temperature profiles are within $\sim 2\%$ of those of Bazant *et al.* (1979).

3.01.5.3 Summary

The analytical expressions are presented for higher-order derivatives of energy release rates for a 2D multiply cracked system. This section provides derivations for the following extensions to the work of Lin and Abel (1988): extension to the general case of multiple-crack systems, extension to the axisymmetric case, inclusion of crack-face and thermal loading, and evaluation of the second-order derivative of energy release rate. The salient feature of this method is that the energy release rate and its higher-order derivatives for multiple-crack systems are computed in a single analysis. The present formulation has been implemented and tested in FRANC2D (2002). It is demonstrated through several 2D numerical examples that the proposed method gives very accurate results for higher-order derivatives of energy release rates for single or multiple cracks. It is also shown that the number of rings of elements surrounding the crack tip that are involved in the mesh perturbation due to the virtual crack extension has an effect on the solution accuracy for higher-order derivatives of energy release rate. When more rings of surrounding elements from the crack tip are used in the perturbation, more accurate solutions for the higher-order derivatives of energy release rate are obtained. The maximum computed errors were $\sim 0.2\%$ for energy release rate, 2–3% for its first derivative and 5–10% for its second derivative between the simulated solutions and the true infinite medium solutions for the mesh density used in the examples.

Extension of this approach to calculation of energy release rate and its derivatives to 3D cracks is described in the next section.

3.01.6 RATES OF ENERGY RELEASE RATE FOR AND STABILITY OF A 3D PLANAR CRACK OF ARBITRARY SHAPE

The derivatives of energy release rates are important parameters in some fracture mechanics problems. In Section 3.01.5, equations for the prediction of stability and arrest of a single crack, and the growth pattern of a system of interacting cracks were presented. Another important LEFM problem is shape prediction (Bui and Van, 1979; Sousa, 1992; Nguyen, 1980, 1994) and stability analysis (Rice, 1985; Gao and Rice, 1986a, 1986b, 1987, 1989; Nguyen, 1980, 1994; Nguyen *et al.*, 1990); of an evolving 3D crack.

For example, the first-order variation of energy release rate, and thus the second variation of potential energy with respect to local crack extension, is required to study the stability of a planar crack of arbitrary shape. The second variation can be used to predict the shape of a propagating crack, using a concept of maximization of total energy released as a crack propagates in brittle fracture. Also, the second variation is necessary to investigate configurational stability versus small deviations from the fundamental shape of an evolving crack front in fatigue crack propagation. Therefore, an important requirement of some fracture mechanics analyses is to evaluate accurately the energy release rates and their higher-order derivatives for a body containing a 3D planar crack of arbitrary shape, subjected to arbitrary loadings, including crack-face loading, thermal loading and body forces.

There have been several numerical methods for calculating the derivatives of energy release rates. DeKoning and Lof (1984) calculated the derivatives of crack-opening displacement and stress intensity factor due to virtual crack-front perturbations for a 3D planar crack of arbitrary shape, based on FEs and stiffness derivative technique. In their approach, finite perturbations of FE meshes are applied to approximate the stiffness derivative by subtracting two stiffness matrices. Meade and Keer (1984a, 1984b) analyzed the half-plane

crack with a slightly wavy crack front subjected to mode I loading using asymptotic expansion and presented the first-order variation of SIF due to variation in crack geometry. Rice (1985) developed, using 3D weight function theory, a linear perturbation scheme for calculating the first-order variation in SIF and crack opening displacement due to small changes in 3D planar crack geometry. Nguyen *et al.* (1990) introduced an explicit expression for the matrix of the second derivatives of energy with respect to the crack lengths in terms of path-independent integrals. Destyunder *et al.* (1983) introduced a geometrical Lagrangian description to derive the expression for the energy release rates in terms of Lagrangian variables. Bonnet (1994) extended the concepts of shape differentiation of Destyunder *et al.* to develop a Galerkin-type symmetric boundary integral equation formulation for the energy release rates and their rates around an arbitrary shaped crack.

In this section, the variational formulation for the derivatives of energy release rates presented in Section 3.01.5 is extended to the problems of a 3D crack with an arbitrarily curved front. The method provides the direct integral forms of stiffness derivatives, and thus there is no need for the analyst to specify a finite length of virtual crack extension. The salient feature of this method is that the energy release rates and their higher derivatives for 3D cracks of arbitrary shape can be computed in a single analysis. Furthermore, the generalized formulation for the 3D crack problem has a couple of new features. First, the method considers the interaction between virtual crack extensions at different positions along the crack front, because the areas perturbed due to crack extensions at adjacent positions on the front are overlapped. The additional term representing the interaction between virtual crack extensions is explicitly derived and included in the formulation for the second variations of element stiffness. Second, it is shown that a local curvature on the curved crack front must be taken into account to properly calculate the derivatives of energy release rate. The general formula for the derivatives of energy release rates around an arbitrarily curved front is provided.

In Section 3.01.6.1, the explicit expressions for energy release rate and its rates are derived for a 3D crack with arbitrarily curved front under arbitrary loading. The details of the general formulation are described, including the issues of interaction between virtual crack extensions and the effect of local crack front curvature on the solution. In Section 3.01.6.2, several 3D numerical examples with exact

solutions or with solutions available in the literature are solved to demonstrate the accuracy of the current method. These examples include an embedded penny-shaped crack in a large cylinder under remote uniform tensile loading, a semi-circular surface crack in a half-circular cylinder under remote uniform tensile loading, a center-cracked plate under remote uniform tensile loading, and a single-edge-cracked plate under remote uniform tensile loading.

3.01.6.1 Formulation

In this section, the explicit expressions for energy release rate and its rates are derived for a 3D crack with curved front under arbitrary loading. For all the developments reported herein, it is assumed that the crack front will be surrounded by a uniform set of 15-noded wedge elements or 20-noded brick elements with quarter-point nodes, like those described in Section 3.01.2, and as shown in Figure 65.

The potential energy Π of a 3D solid is given by:

$$\Pi = \frac{1}{2}u^T Ku - u^T f \quad (267)$$

where u , K , and f are the nodal displacement vector, the structural stiffness matrix and the applied nodal force vector, respectively. The potential energy change due to a virtual crack front perturbation along the arbitrary crack front can be written as,

$$\begin{aligned} -\delta\Pi &= \int_{\text{Crack Front}} G(s) \delta a(s) ds \\ &= -\frac{1}{2}u^T \delta K u + u^T \delta f \end{aligned} \quad (268)$$

where $\delta\Pi$ is the variation in potential energy for a virtual crack extension, $\delta a(s)$ is the local crack front advance in a direction normal to the original crack front and a function of distance s along the crack front, $G(s)$ is the local energy release rate due to $\delta a(s)$, ds denotes an increment of arc length along the crack front, and δK and δf are variations of the structural stiffness matrix and load vector due to virtual crack-front advance, respectively.

According to deLorenzi (1982), it is possible to define both local and average values of energy release rate along the crack front. The average energy release rate can be found by advancing all node points on the crack front a distance and dividing the total released energy by the area of the virtual crack extension. The local energy release rate can be evaluated by advancing one node at a time and calculating

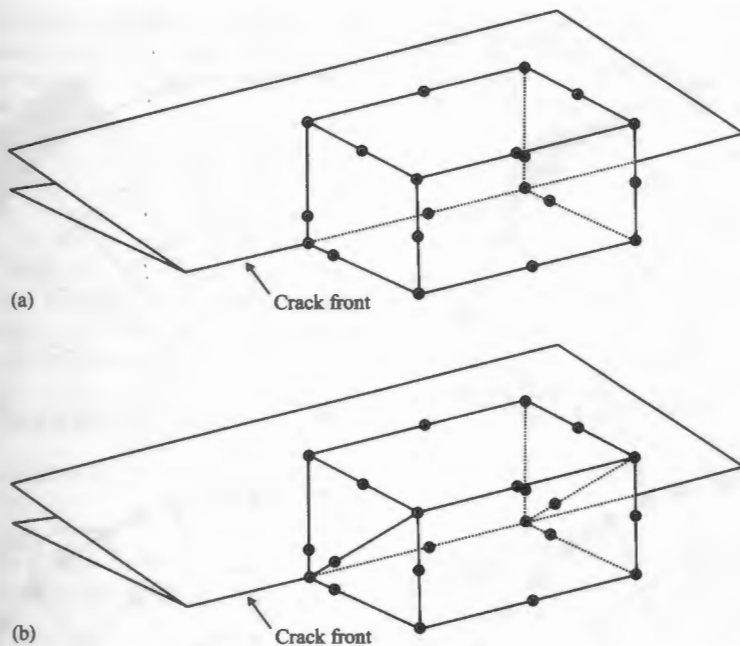


Figure 65 (a) 20-noded brick element with quarter-point nodes and (b) 15-noded wedge element with quarter-point nodes.

the area of the virtual crack extension from the FE interpolation functions, Figure 66.

To calculate the local energy release rate along the crack front, various types of virtual crack extensions are possible, as shown in Figure 67. Banks-Sills (1991) showed that most accurate results are obtained if $\delta a(s)$ varies linearly with crack front arc length for the crack extension (see Figure 67(a)). In this study, linear virtual crack extension is used. An area perturbed due to virtual crack extension at a point i along the front can be written as:

$$\delta A_i = \int_0^{L_i} \delta a(s) ds = \delta a_i l_i \quad (269)$$

where δA_i is a perturbed area, δa_i is the magnitude of virtual crack extension, L_i is the length of the crack front segment, and l_i is an effective width of the perturbed area. It seems reasonable to assume that for small enough segments of crack front, the variation of $G(s)$ may be neglected within each crack front segment. Thus, Equation (267) can be rewritten as:

$$\begin{aligned} -\delta \Pi &= \int_{\text{Crack Front Segment}} G(s) \delta a(s) ds \\ &= G_{\text{Average}} \int_{\text{Crack Front Segment}} \delta a(s) ds \\ &= G_{\text{Average}} \cdot \delta A \\ &= G_{\text{Average}} \cdot \delta a \cdot l \end{aligned} \quad (270)$$

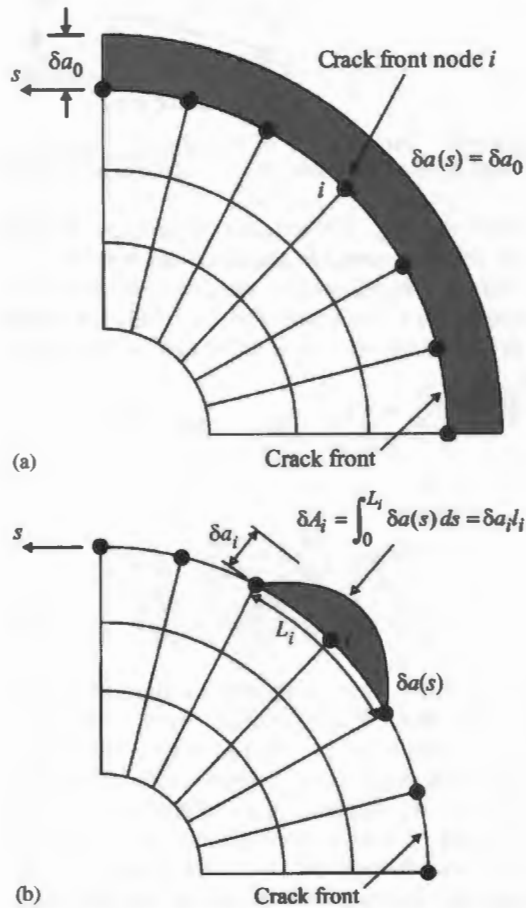


Figure 66 (a) Virtual crack extension for the definition of average energy release rate and (b) virtual crack extension for definition of local energy release rate.

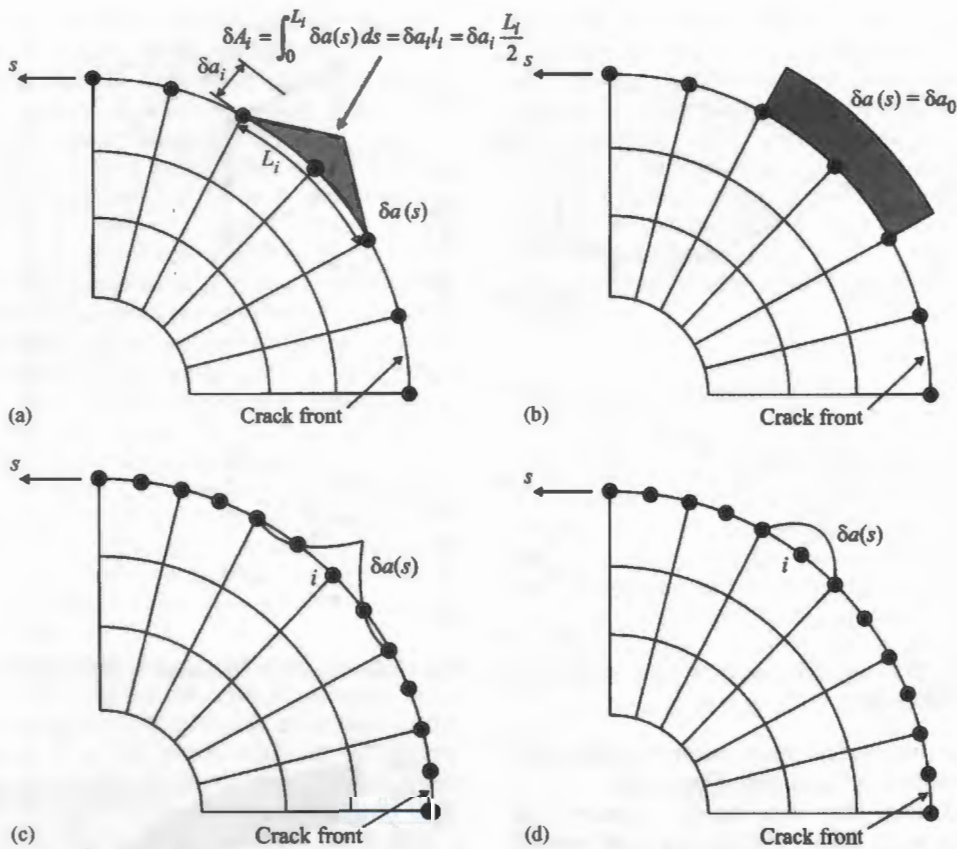


Figure 67 Various types of virtual crack front perturbations: (a) linear; (b) constant; (c) quadratic spanning 2 elements; and (d) quadratic over one element at midside node.

where G_{Average} is the average energy release rate within a small segment of crack front.

Thus, a local energy release rate due to a virtual crack front perturbation, δA_i , at a point i on the arbitrary crack front can be expressed as

$$G_i = -\frac{\delta \Pi}{\delta A_i} = -\frac{\delta \Pi}{\delta a_i l_i} \quad (271)$$

$$\begin{aligned} G_i &= -\frac{\delta \Pi}{\delta A_i} = -\frac{\delta \Pi}{\delta a_i l_i} \\ &= \frac{1}{l_i} \left(-\frac{1}{2} u^T \frac{\delta K}{\delta a_i} u + u^T \frac{\delta f}{\delta a_i} \right) \end{aligned} \quad (272)$$

It is noted that nonzero contributions to $\delta K/\delta a_i$ and $\delta f/\delta a_i$ occur only over elements perturbed by virtual crack extension. Whenever crack-face, thermal and body-force loadings are applied, the variations of loading must be taken into account to reflect the local load change on the crack face or in the crack-tip vicinity as a result of virtual crack extension.

The second-order variation of potential energy with respect to the virtual crack extensions at different points, i and j , on the

arbitrary crack front is

$$\begin{aligned} -\frac{\delta^2 \Pi_i}{\delta a_i \delta a_j} &= -u^T \frac{\delta K}{\delta a_i} \frac{\delta u}{\delta a_j} - \frac{1}{2} u^T \frac{\delta^2 K}{\delta a_i \delta a_j} u \\ &\quad + \frac{\delta u^T}{\delta a_j} \frac{\delta f}{\delta a_i} + u^T \frac{\delta^2 f}{\delta a_i \delta a_j} \end{aligned} \quad (273)$$

The variation of the displacement is obtained from the variation of the global equilibrium equation $Ku = f$ with respect to a_j ,

$$\begin{aligned} \frac{\delta K}{\delta a_j} u + K \frac{\delta u}{\delta a_j} &= \frac{\delta f}{\delta a_j} \quad \text{or} \\ \frac{\delta u}{\delta a_j} &= K^{-1} \left(\frac{\delta f}{\delta a_j} - \frac{\delta K}{\delta a_j} u \right) \end{aligned} \quad (274)$$

By substituting Equation (274) into Equation (273), we obtain the final expression:

$$\begin{aligned} -\frac{\delta^2 \Pi}{\delta a_i \delta a_j} &= -\frac{1}{2} u^T \frac{\delta^2 K}{\delta a_i \delta a_j} u + u^T \frac{\delta^2 f}{\delta a_i \delta a_j} \\ &\quad - u^T \frac{\delta K}{\delta a_i} K^{-1} \left(\frac{\delta f}{\delta a_j} - \frac{\delta K}{\delta a_j} u \right) \\ &\quad + \left(\frac{\delta f}{\delta a_j} - \frac{\delta K}{\delta a_j} u \right)^T K^{-1 T} \frac{\delta f}{\delta a_i} \end{aligned} \quad (275)$$

3.01.6.1.1 First-order derivatives of energy release rates for a crack with arbitrarily curved front

Now, energy release rates and their derivatives for a crack with arbitrarily curved front are derived. Consider a segment of curved crack front with a local radius $R(s)$ on the crack front, Figure 68. It is assumed that for small enough segments of crack front, the variation of $R(s)$ is neglected within each crack-front segment. The area of a circular sector containing the crack-front segment is

$$A_i = \frac{1}{2}R_i^2\theta_i = \frac{1}{2}a_i^2\theta \quad \text{where } a_i = R_i \quad (276)$$

and its variation due to a small change in radius is given by

$$\delta A_i = \frac{1}{2}R_i\theta_i \delta R_i = \delta R_i l_i = \delta a_i l_i \quad \text{for linear perturbation in Figure 67(a)} \quad (277)$$

$$l_i = \frac{1}{2}R_i\theta_i \quad (278)$$

where A_i is the area of a circular sector influenced by virtual crack-front perturbation at crack-front node i , R_i is a local radius of curvature at crack-front node i , δA_i is the

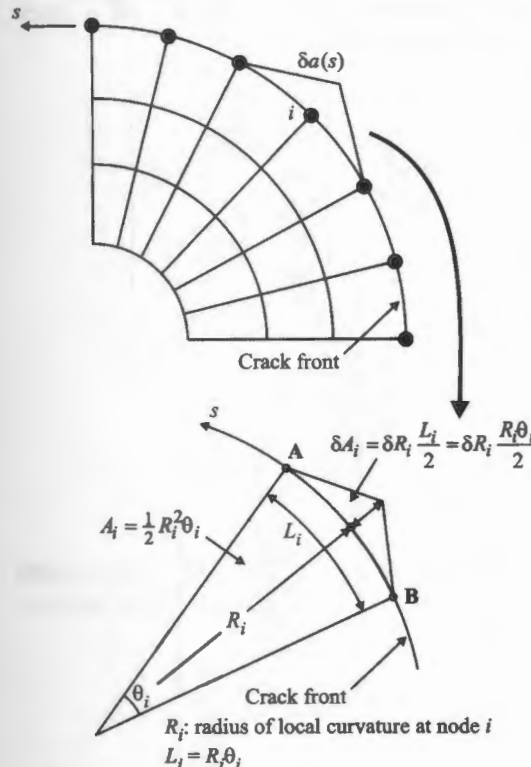


Figure 68 Virtual crack extension on a curved crack-front segment.

variation of the area A_i due to virtual crack-front perturbation, δR_i is the variation of radius and θ_i is the angle of the circular sector.

Thus, energy release rate is given by

$$G_i = -\frac{\delta\Pi}{\delta A_i} = -\frac{\delta\Pi}{\delta R_i} \frac{2}{R_i \theta_i} = -\frac{\delta\Pi}{\delta R_i} \frac{1}{l_i} \quad (279)$$

The rate of energy release is:

$$\begin{aligned} \frac{\delta G_i}{\delta R_j} &= -\frac{\delta^2\Pi}{\delta R_i \delta R_j} \frac{2}{R_i \theta_i} + \frac{\delta\Pi}{\delta R_i} \frac{2}{R_i^2 \theta_i} \frac{\delta R_i}{\delta R_j} \\ &= -\frac{\delta^2\Pi}{\delta R_i \delta R_j} \frac{1}{l_i} - \frac{G_i}{R_i} \frac{\delta R_i}{\delta R_j} \end{aligned} \quad (280)$$

where it is clearly shown that a local curvature on a curved crack front plays an important role in the calculation of rates of energy release rate:

$$\begin{aligned} \frac{\delta G_i}{\delta a_j} l_i &= -\frac{\delta^2\Pi}{\delta a_i \delta a_j} - \frac{G_i l_i}{R_i} \frac{\delta R_i}{\delta R_j} \\ &= -\frac{\delta^2\Pi}{\delta a_i \delta a_j} - \frac{G_i l_i}{R_i} \delta_{ij} \end{aligned} \quad (281)$$

where $\delta R_i/\delta R_j$ is replaced by Kronecker delta δ_{ij} which is 1 for $i=j$ and zero for $i \neq j$. Thus, the explicit forms of energy release rates and their rates for the general case of a planar crack with an arbitrarily curved front are given by

$$G_i l_i = -\frac{\delta\Pi}{\delta a_i} = -\frac{1}{2} u^T \frac{\delta K}{\delta a_i} u + u^T \frac{\delta f}{\delta a_i} \quad (282)$$

$$\begin{aligned} \frac{\delta G_i}{\delta a_j} l_i &= -\frac{1}{2} u^T \frac{\delta^2 K}{\delta a_i \delta a_j} u + u^T \frac{\delta^2 f}{\delta a_i \delta a_j} \\ &\quad - u^T \frac{\delta K}{\delta a_i} K^{-1} \left(\frac{\delta f}{\delta a_j} - \frac{\delta K}{\delta a_j} u \right) \\ &\quad + \left(\frac{\delta f}{\delta a_j} - \frac{\delta K}{\delta a_j} u \right)^T K^{-1 T} \frac{\delta f}{\delta a_i} \\ &\quad + \left(\frac{1}{2} u^T \frac{\delta K}{\delta a_i} u - u^T \frac{\delta f}{\delta a_i} \right) \frac{\delta_{ij}}{R_i} \end{aligned} \quad (283)$$

3.01.6.1.2 Derivations of stiffness derivatives for 3D FEs

This section provides derivations for stiffness variations of 3D FEs. Firstly, a strain-like

matrix, $\tilde{\epsilon}$, for the 3D problem is defined as

$$\begin{aligned}\tilde{\epsilon} &= J^{-1} \left\{ \begin{array}{l} \frac{\partial N}{\partial \xi^1} \\ \frac{\partial N}{\partial \xi^2} \\ \frac{\partial N}{\partial \xi^3} \end{array} \right\} \left[\Delta_n^1 \quad \Delta_n^2 \quad \Delta_n^3 \right] \\ &= \left[\begin{array}{ccc} J_{11} & J_{12} & J_{13} \\ J_{21} & J_{22} & J_{23} \\ J_{31} & J_{32} & J_{33} \end{array} \right]^{-1} \left\{ \begin{array}{l} \frac{\partial N}{\partial \xi^1} \\ \frac{\partial N}{\partial \xi^2} \\ \frac{\partial N}{\partial \xi^3} \end{array} \right\} \left[\Delta_n^1 \quad \Delta_n^2 \quad \Delta_n^3 \right] \quad (284)\end{aligned}$$

$$\tilde{\epsilon} = \begin{bmatrix} \tilde{\epsilon}_{11} & \tilde{\epsilon}_{12} & \tilde{\epsilon}_{13} \\ \tilde{\epsilon}_{21} & \tilde{\epsilon}_{22} & \tilde{\epsilon}_{23} \\ \tilde{\epsilon}_{31} & \tilde{\epsilon}_{32} & \tilde{\epsilon}_{33} \end{bmatrix} = \begin{bmatrix} [\tilde{\epsilon}_1] \\ [\tilde{\epsilon}_2] \\ [\tilde{\epsilon}_3] \end{bmatrix} \quad (285)$$

where Δ_n are nodal values of the infinitesimal mesh perturbations Δ . $\tilde{\epsilon}$ is a strain-like matrix created by the geometry changes of the meshes Δ 's on the unstrained structure, Figure 69. The strain-displacement matrix, B , for a 3D problem is

$$B = \begin{bmatrix} \frac{\partial N}{\partial x^1} & & & \\ & \frac{\partial N}{\partial x^2} & \frac{\partial N}{\partial x^3} & \\ & & \frac{\partial N}{\partial x^1} & \\ \frac{\partial N}{\partial x^2} & \frac{\partial N}{\partial x^1} & & \\ & \frac{\partial N}{\partial x^3} & \frac{\partial N}{\partial x^2} & \\ & & \frac{\partial N}{\partial x^1} & \end{bmatrix} \quad (286)$$

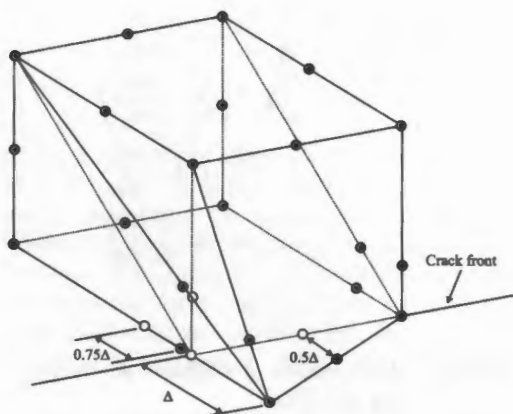


Figure 69 Mesh perturbation, Δ , in 15-noded wedge elements.

The first-order variation of B due to virtual crack extension, δa_i , at a point i on a crack front is defined as

$$\frac{\delta B}{\delta a_i} = - \left[\begin{bmatrix} [\tilde{\epsilon}_1] \\ [\tilde{\epsilon}_2] \\ [\tilde{\epsilon}_3] \end{bmatrix} \quad \begin{bmatrix} [\tilde{\epsilon}_1] \\ [\tilde{\epsilon}_2] \\ [\tilde{\epsilon}_3] \end{bmatrix} \quad \begin{bmatrix} [\tilde{\epsilon}_1] \\ [\tilde{\epsilon}_2] \\ [\tilde{\epsilon}_3] \end{bmatrix} \right] \left[\begin{array}{l} \frac{\partial N}{\partial x^1} \\ \frac{\partial N}{\partial x^2} \\ \frac{\partial N}{\partial x^3} \end{array} \right] \quad (287)$$

$$\begin{bmatrix} \frac{\partial N}{\partial x^1} \\ \frac{\partial N}{\partial x^2} \\ \frac{\partial N}{\partial x^3} \end{bmatrix}$$

where $[\tilde{\epsilon}_1]$, $[\tilde{\epsilon}_2]$, and $[\tilde{\epsilon}_3]$ are the component matrices of $[\tilde{\epsilon}]$ defined by

$$\tilde{\epsilon} = \left\{ \begin{array}{l} [\tilde{\epsilon}_1] \\ [\tilde{\epsilon}_2] \\ [\tilde{\epsilon}_3] \end{array} \right\} \quad (288)$$

The second-order variation of B due to virtual crack extension, δa_i , at a point i on a crack front is written as

$$\frac{\delta^2 B}{\delta a_i^2} = - \left[\begin{bmatrix} [\tilde{\epsilon}'_1] \\ [\tilde{\epsilon}'_2] \\ [\tilde{\epsilon}'_3] \end{bmatrix} \quad \begin{bmatrix} [\tilde{\epsilon}'_1] \\ [\tilde{\epsilon}'_2] \\ [\tilde{\epsilon}'_3] \end{bmatrix} \quad \begin{bmatrix} [\tilde{\epsilon}'_1] \\ [\tilde{\epsilon}'_2] \\ [\tilde{\epsilon}'_3] \end{bmatrix} \right] \left[\begin{array}{l} \frac{\partial N}{\partial x^1} \\ \frac{\partial N}{\partial x^2} \\ \frac{\partial N}{\partial x^3} \end{array} \right] \quad (289)$$

$$\begin{bmatrix} \frac{\partial N}{\partial x^1} \\ \frac{\partial N}{\partial x^2} \\ \frac{\partial N}{\partial x^3} \end{bmatrix}$$

in which $[\tilde{\varepsilon}_1'']$, $[\tilde{\varepsilon}_2'']$, and $[\tilde{\varepsilon}_3'']$ are the component matrices of $[\tilde{\varepsilon}'']$ defined by

$$\begin{aligned} \tilde{\varepsilon}'' &= 2\tilde{\varepsilon}^2 = \left\{ \begin{array}{c} [\tilde{\varepsilon}_1''] \\ [\tilde{\varepsilon}_2''] \\ [\tilde{\varepsilon}_3''] \end{array} \right\} \\ &= 2 \begin{bmatrix} \tilde{\varepsilon}_{11} & \tilde{\varepsilon}_{12} & \tilde{\varepsilon}_{13} \\ \tilde{\varepsilon}_{21} & \tilde{\varepsilon}_{22} & \tilde{\varepsilon}_{23} \\ \tilde{\varepsilon}_{31} & \tilde{\varepsilon}_{32} & \tilde{\varepsilon}_{33} \end{bmatrix} \cdot \begin{bmatrix} \tilde{\varepsilon}_{11} & \tilde{\varepsilon}_{12} & \tilde{\varepsilon}_{13} \\ \tilde{\varepsilon}_{21} & \tilde{\varepsilon}_{22} & \tilde{\varepsilon}_{23} \\ \tilde{\varepsilon}_{31} & \tilde{\varepsilon}_{32} & \tilde{\varepsilon}_{33} \end{bmatrix} \quad (290) \end{aligned}$$

To derive the expression for the second-order variation of B due to two different virtual crack extensions, δa_i and δa_j , one can use the relationship:

$$\frac{\delta e_i}{\delta a_j} = \varepsilon_{ij} = -\varepsilon_j \varepsilon_i \quad (291)$$

which yields an expression similar to Equation (289) for $\delta^2 B / \delta a_i \delta a_j$

$$\frac{\delta^2 B}{\delta a_i \delta a_j} = - \begin{bmatrix} [\tilde{\varepsilon}_1''] & & & \\ & [\tilde{\varepsilon}_2''] & & \\ & & [\tilde{\varepsilon}_3''] & \\ \hline [\tilde{\varepsilon}_2''] & [\tilde{\varepsilon}_1''] & & \\ [\tilde{\varepsilon}_3''] & & [\tilde{\varepsilon}_2''] & \\ & & & [\tilde{\varepsilon}_1''] \\ \hline [\tilde{\varepsilon}_3''] & & & [\tilde{\varepsilon}_2''] \end{bmatrix} \begin{bmatrix} \frac{\partial N}{\partial x^1} \\ \frac{\partial N}{\partial x^2} \\ \frac{\partial N}{\partial x^3} \\ \hline \frac{\partial N}{\partial x^1} \\ \frac{\partial N}{\partial x^2} \\ \frac{\partial N}{\partial x^3} \\ \hline \frac{\partial N}{\partial x^1} \\ \frac{\partial N}{\partial x^2} \\ \frac{\partial N}{\partial x^3} \end{bmatrix} \quad (292)$$

in which $[\tilde{\varepsilon}_1'']$, $[\tilde{\varepsilon}_2'']$, and $[\tilde{\varepsilon}_3'']$ are the component matrices of $[\tilde{\varepsilon}'']$ defined by

$$\tilde{\varepsilon}'' = \left\{ \begin{array}{c} [\tilde{\varepsilon}_1''] \\ [\tilde{\varepsilon}_2''] \\ [\tilde{\varepsilon}_3''] \end{array} \right\} = [\varepsilon_j] [\varepsilon_i] + [\varepsilon_i] [\varepsilon_j] \quad (293)$$

The first- and second-order variations of $|J|$ with respect to virtual crack extension, δa_i , at a

point i on the crack front are defined as

$$\frac{\delta |J|}{\delta a_i} = \text{Tr}(\tilde{\varepsilon}) |J| \quad (294)$$

$$\frac{\delta^2 |J|}{\delta a_i^2} = (\text{Tr}^2(\tilde{\varepsilon}) - \text{Tr}(\tilde{\varepsilon}^2)) |J| \quad (295)$$

The second-order variation of $|J|$ with respect to two different virtual crack extensions, δa_i and δa_j , is written as

$$\frac{\delta^2 |J|}{\delta a_i \delta a_j} = (\text{Tr}(\tilde{\varepsilon}_i) \text{Tr}(\tilde{\varepsilon}_j) - \text{Tr}(\tilde{\varepsilon}_i \tilde{\varepsilon}_j)) |J| \quad (296)$$

The first- and second-order variations of element stiffness matrix are written as

$$\frac{\delta k}{\delta a_i} = \int_v \left[\frac{\delta B^T}{\delta a_i} DB + B^T D \frac{\delta B}{\delta a_i} + \text{Tr}(\tilde{\varepsilon}) B^T DB \right] dV \quad (297)$$

$$\begin{aligned} \frac{\delta^2 k}{\delta a_i^2} &= \int_v \left[\frac{\delta^2 B^T}{\delta a_i^2} DB + 2 \frac{\delta B^T}{\delta a_i} D \frac{\delta B}{\delta a_i} + B^T D \frac{\delta^2 B}{\delta a_i^2} \right. \\ &\quad + (\text{Tr}^2(\tilde{\varepsilon}) - \text{Tr}(\tilde{\varepsilon}^2)) B^T DB \\ &\quad \left. + 2 \text{Tr}(\tilde{\varepsilon}) \left(\frac{\delta B^T}{\delta a_i} DB + B^T D \frac{\delta B}{\delta a_i} \right) \right] dV \quad (298) \end{aligned}$$

The second-order variation of element stiffness, $\delta^2 k / \delta a_i \delta a_j$, with respect to two different virtual crack extensions, δa_i and δa_j , is written as:

$$\begin{aligned} \frac{\delta^2 k}{\delta a_i \delta a_j} &:= \int_v \left[\frac{\delta^2 B^T}{\delta a_i \delta a_j} L B + \frac{\delta B^T}{\delta a_i} L \frac{\delta B}{\delta a_j} \right. \\ &\quad + \frac{\delta B^T}{\delta a_j} D \frac{\delta B}{\delta a_i} + B^T D \frac{\delta^2 B}{\delta a_i \delta a_j} \\ &\quad + (\text{Tr}(\tilde{\varepsilon}_i) \text{Tr}(\tilde{\varepsilon}_j) - \text{Tr}(\tilde{\varepsilon}_i \tilde{\varepsilon}_j)) B^T DB \\ &\quad \left. + \text{Tr}(\tilde{\varepsilon}_i) \left(\frac{\delta B^T}{\delta a_j} DB + B^T D \frac{\delta B}{\delta a_j} \right) \right. \\ &\quad \left. + \text{Tr}(\tilde{\varepsilon}_j) \left(\frac{\delta B^T}{\delta a_i} DB + B^T D \frac{\delta B}{\delta a_i} \right) \right] dV \quad (299) \end{aligned}$$

In the case of a system of 2D multiple cracks, Section 3.01.5, the elements influenced by each crack tip comprised disjoint sets and thus the second-order variations of stiffness and loading with respect to two different crack extensions a_i and a_j vanished. On the contrary, in the 3D case, the second-order stiffness derivatives due to two different crack extensions on the crack front are not necessarily zero, because areas perturbed due to different crack extensions along the crack front may be overlapped, Figure 70, and then the interaction between crack-front perturbations should be taken into account. For the linear virtual crack extension

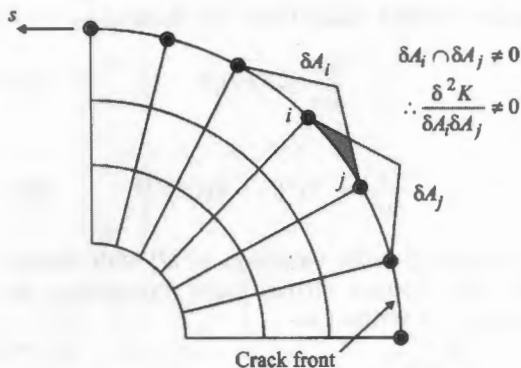


Figure 70 Interaction between crack-front perturbations.

along the crack front, the elements influenced by virtual crack extension at one point are also affected by the extensions at adjacent points. The shadowed portion in Figure 70 represents the crack-front perturbation area simultaneously affected by virtual crack extensions at two neighboring positions. Therefore, for the linear virtual crack-front perturbation in Figure 67(a), the second-order variations of element stiffness are

$$\frac{\delta^2 k}{\delta a_i \delta a_j} \neq 0 \quad \frac{\delta^2 f}{\delta a_i \delta a_j} \neq 0 \quad \text{for } j = i - 1, i, \text{ or } i + 1 \quad (300)$$

$$\frac{\delta^2 k}{\delta a_i \delta a_j} = 0 \quad \frac{\delta^2 f}{\delta a_i \delta a_j} = 0 \quad \text{otherwise} \quad (301)$$

Element stiffness variations, $\delta k / \delta a_i$, $\delta^2 k / \delta a_i^2$, and $\delta^2 k / \delta a_i \delta a_j$ are assembled to produce the global stiffness variations $\delta K / \delta a_i$, $\delta^2 K / \delta a_i^2$, and $\delta^2 K / \delta a_i \delta a_j$, respectively.

3.01.6.1.3 Crack-face, thermal and body-force loadings in 3D

The elemental equivalent load variations associated with crack extension for a nonuniform crack-face pressure, p , are given by

$$f_e = \int_s N^T p \, ds \quad (302)$$

$$\frac{\delta f_e}{\delta a_i} = \int_s \left[N^T \frac{\delta p}{\delta a_i} + \text{Tr}(\tilde{\varepsilon}) N^T p \right] \, ds \quad (303)$$

$$\begin{aligned} \frac{\delta^2 f_e}{\delta a_i^2} &= \int_s \left[N^T \frac{\delta^2 p}{\delta a_i^2} + 2\text{Tr}(\tilde{\varepsilon}) N^T \frac{\delta p}{\delta a_i} \right. \\ &\quad \left. + (\text{Tr}^2(\tilde{\varepsilon}) - \text{Tr}(\tilde{\varepsilon}^2)) N^T p \right] \, ds \end{aligned} \quad (304)$$

$$\begin{aligned} \frac{\delta^2 f_e}{\delta a_i \delta a_j} &= \int_s \left[N^T \frac{\delta^2 p}{\delta a_i \delta a_j} + \text{Tr}(\tilde{\varepsilon}_i) N^T \frac{\delta p}{\delta a_j} \right. \\ &\quad \left. + \text{Tr}(\tilde{\varepsilon}_j) N^T \frac{\delta p}{\delta a_i} + (\text{Tr}(\tilde{\varepsilon}_i) \text{Tr}(\tilde{\varepsilon}_j) \right. \\ &\quad \left. - \text{Tr}(\tilde{\varepsilon}_j \tilde{\varepsilon}_i)) N^T p \right] \, ds \end{aligned} \quad (305)$$

where N is the shape function matrix and ds is an unit crack-face area.

In the same manner, the variations of thermal loading for an isotropic material can be derived as:

$$f_e = \int_v B^T D(\alpha \Delta T) \, dV \quad (306)$$

$$\begin{aligned} \frac{\delta f_e}{\delta a_i} &= \int_v \left[\frac{\delta B^T}{\delta a_i} D(\alpha \Delta T) + B^T D \frac{\delta(\alpha \Delta T)}{\delta a_i} \right. \\ &\quad \left. + \text{Tr}(\tilde{\varepsilon}) B^T D(\alpha \Delta T) \right] \, dV \end{aligned} \quad (307)$$

$$\begin{aligned} \frac{\delta^2 f_e}{\delta a_i^2} &= \int_v \left[\frac{\delta^2 B^T}{\delta a_i^2} D(\alpha \Delta T) + 2 \frac{\delta B^T}{\delta a_i} D \frac{\delta(\alpha \Delta T)}{\delta a_i} \right. \\ &\quad \left. + B^T D \frac{\delta^2(\alpha \Delta T)}{\delta a_i^2} + 2 \text{Tr}(\tilde{\varepsilon}) \right. \\ &\quad \times \left(\frac{\delta B^T}{\delta a_i} D \alpha \Delta T + B^T D \frac{\delta(\alpha \Delta T)}{\delta a_i} \right) \\ &\quad \left. + (\text{Tr}^2(\tilde{\varepsilon}) - \text{Tr}(\tilde{\varepsilon}^2)) B^T D \frac{\delta(\alpha \Delta T)}{\delta a_i} \right] \, dV \end{aligned} \quad (308)$$

$$\begin{aligned} \frac{\delta^2 f_e}{\delta a_i \delta a_j} &= \int_v \left[\frac{\delta^2 B^T}{\delta a_i \delta a_j} D(\alpha \Delta T) + \frac{\delta B^T}{\delta a_i} D \frac{\delta(\alpha \Delta T)}{\delta a_j} \right. \\ &\quad \left. + \frac{\delta B^T}{\delta a_j} D \frac{\delta(\alpha \Delta T)}{\delta a_i} + B^T D \frac{\delta^2(\alpha \Delta T)}{\delta a_i \delta a_j} \right. \\ &\quad \left. + (\text{Tr}(\tilde{\varepsilon}_i) \text{Tr}(\tilde{\varepsilon}_j) - \text{Tr}(\tilde{\varepsilon}_j \tilde{\varepsilon}_i)) B^T D(\alpha \Delta T) \right. \\ &\quad \left. + \text{Tr}(\tilde{\varepsilon}_i) \left(\frac{\delta B^T}{\delta a_j} D(\alpha \Delta T) + B^T D \frac{\delta(\alpha \Delta T)}{\delta a_j} \right) \right. \\ &\quad \left. + \text{Tr}(\tilde{\varepsilon}_j) \left(\frac{\delta B^T}{\delta a_i} D(\alpha \Delta T) \right. \right. \\ &\quad \left. \left. + B^T D \frac{\delta(\alpha \Delta T)}{\delta a_i} \right) \right] \, dV \end{aligned} \quad (309)$$

3.01.6.1.4 Mixed-mode fracture problem

The crack-tip field parameters (displacements, stresses, strains, and tractions) within the symmetric region in the crack-tip neighborhood along the straight crack front can be separated into mode I, II, and III components. Nodal displacement vector and load vector, u and f are decomposed into mode I, II,

and III as:

$$\begin{aligned}\{u\} &= \{u^I\} + \{u^{II}\} + \{u^{III}\} \\ &= \frac{1}{2} \begin{Bmatrix} u_1 + u'_1 \\ u_2 - u'_2 \\ u_3 + u'_3 \end{Bmatrix} + \frac{1}{2} \begin{Bmatrix} u_1 - u'_1 \\ u_2 + u'_2 \\ 0 \end{Bmatrix} \\ &\quad + \frac{1}{2} \begin{Bmatrix} 0 \\ 0 \\ u_3 - u'_3 \end{Bmatrix} \end{aligned}\quad (310)$$

$$\begin{aligned}\{f\} &= \{f^I\} + \{f^{II}\} + \{f^{III}\} \\ &= \frac{1}{2} \begin{Bmatrix} f_1 + f'_1 \\ f_2 - f'_2 \\ f_3 + f'_3 \end{Bmatrix} + \frac{1}{2} \begin{Bmatrix} f_1 - f'_1 \\ f_2 + f'_2 \\ 0 \end{Bmatrix} \\ &\quad + \frac{1}{2} \begin{Bmatrix} 0 \\ 0 \\ f_3 - f'_3 \end{Bmatrix} \end{aligned}\quad (311)$$

where

$$u'_i(x_1, x_2, x_3) = u_i(x_1, -x_2, x_3) \quad (312)$$

$$f'_i(x_1, x_2, x_3) = f_i(x_1, -x_2, x_3) \quad (313)$$

The total energy release rate, under mixed-mode loading at any point along a 3D crack front for unit crack extension, is given by:

$$G_i = (G_I)_i + (G_{II})_i + (G_{III})_i \quad (314)$$

By decomposing the computed displacement and loading fields into mode I, II, and III components, one may evaluate energy release rate components G_I , G_{II} , and G_{III} , as:

$$(G_I)_i = -\frac{1}{2}(u_I)^T \frac{\delta K}{\delta a_i} u_I + (u_I)^T \frac{\delta f_I}{\delta a_i} \quad (315)$$

$$(G_{II})_i = -\frac{1}{2}(u_{II})^T \frac{\delta K}{\delta a_i} u_{II} + (u_{II})^T \frac{\delta f_{II}}{\delta a_i} \quad (316)$$

$$(G_{III})_i = -\frac{1}{2}(u_{III})^T \frac{\delta K}{\delta a_i} u_{III} + (u_{III})^T \frac{\delta f_{III}}{\delta a_i} \quad (317)$$

For an arbitrarily shaped crack front, it is not straightforward to use the mode-decomposition technique. In this case, a point-by-point co-ordinate transformation from a global Cartesian co-ordinate system to the local crack-front co-ordinate system can be performed prior to the calculation of energy release rate and its derivatives (Nikishkov and Atluri, 1987). After the transformation, the crack front is straight and the mode decomposition technique can be applied.

3.01.6.2 Numerical Examples

In this section, a series of numerical examples is presented and compared with results existing in the literature to demonstrate the accuracy of the proposed method.

3.01.6.2.1 Example 5: embedded penny-shaped crack in a large cylinder under a remote uniform tensile loading normal to the crack plane

The first example is a penny-shaped crack of radius $a = 1.0$ in a large cylindrical body subjected to a remote tensile load perpendicular to the crack surface. A large cylinder with $R/a = 20$ and $H/a = 20$ simulates the infinite domain, Figure 71(a). Figure 71(b) shows nodes defined on the crack front. Due to the symmetry in the problem, only 1/8 of the cracked cylinder was considered. The mesh used for the penny-shaped crack is shown in Figure 71(c). The FE mesh consists of 432 elements and 3263 nodes. The detail of the mesh around the crack front is shown in Figure 71(d). The quarter-point 15-noded wedge elements were employed to model the singularity around the crack front. Young's modulus E was taken to be unity, and Poisson's ratio 0.3. The exact K_I and $\delta K_I/\delta a$ solutions for mode I crack growth under uniform stress in an infinite domain can be expressed analytically (Sneddon, 1946) as:

$$K_I = 2\sigma \sqrt{\frac{a}{\pi}} \quad (318)$$

$$\frac{\delta K_I}{\delta a} = \frac{\sigma}{\sqrt{\pi a}} \quad (319)$$

It is noted that the virtual crack extension is given in the direction normal to the crack front such that it produces self-similar crack growth. For $R/a = 20$, the present virtual crack extension method gives $K_I = 1.1302$ for all θ , which is in excellent agreement with the exact solution of 1.1284 by Equation (318), giving an error of 0.16% for this mesh.

Table 14 lists the values of rates of stress intensity factor computed with the present virtual crack extension method. The sums of the rows in Table 14 represent the rate of stress intensity factor at all nodes along the crack front, due to a uniform extension of an entire crack front. The theoretical value of $\delta K_I/\delta a$ by Equation (319) for the axisymmetric case is 0.5642 for all θ . The difference between the computed and theoretical $\delta K_I/\delta a$ values is about 4%. To demonstrate the accuracy of the present method, the SIFs K_i^{Elliptic} for several

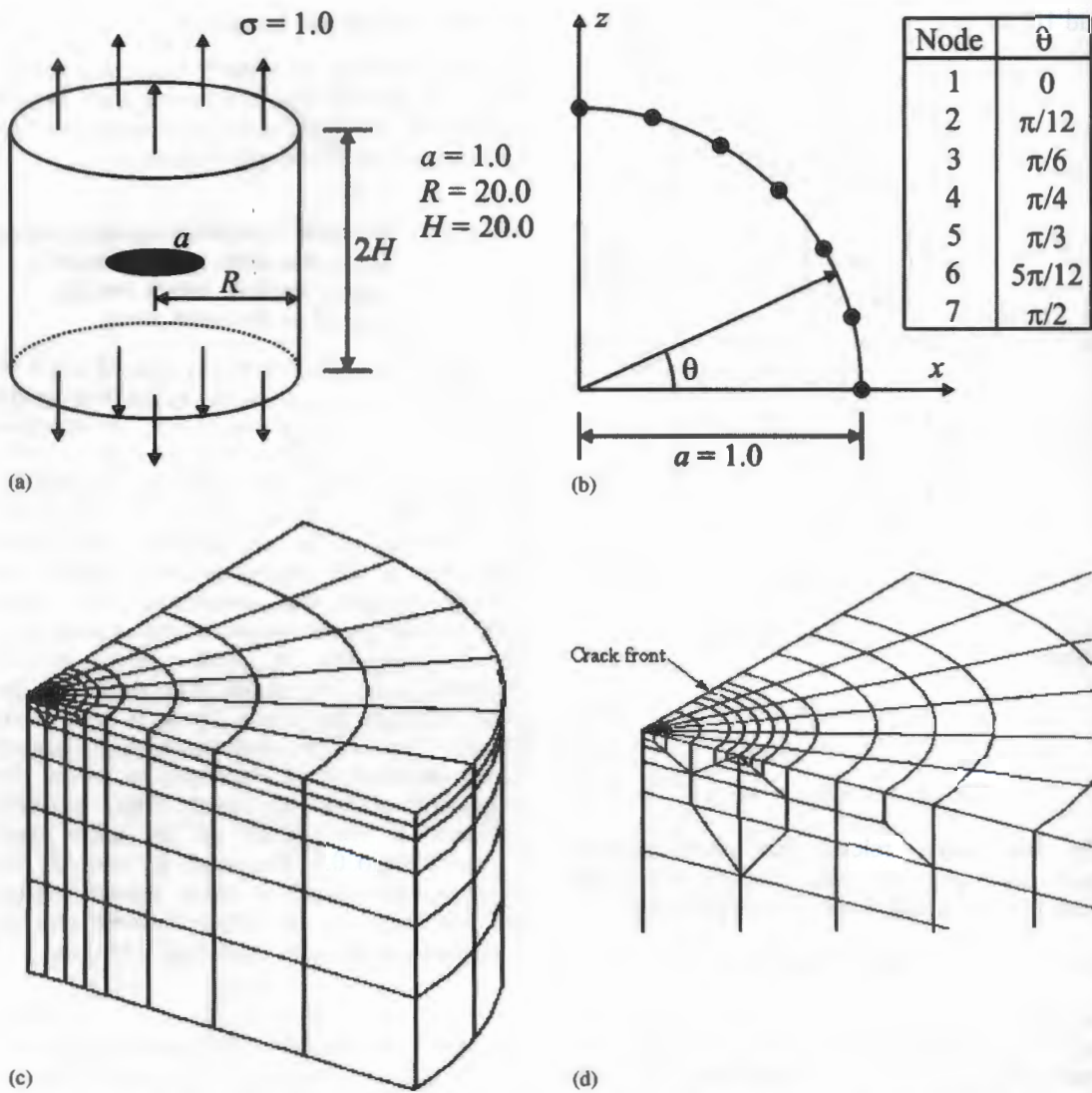


Figure 71 (a) Embedded penny-shaped crack in a large cylinder subjected to uniform remote tensile loading, Example 5; (b) nodes around crack front; (c) mesh configuration; and (d) detail of mesh around crack front.

Table 14 The computed values of first order derivatives of SIFs, Example 5 (exact value of $\delta K_I / \delta a = 0.5642$ for axisymmetric case).

Node	j:1	2	3	4	5	6	7	Row sum
i:1	-1.9232	1.4975	0.4725	0.2064	0.1347	0.1040	0.0487	0.5406
2	0.7487	-1.6870	0.8519	0.3036	0.1552	0.1161	0.0520	0.5406
3	0.2362	0.8519	-1.8558	0.8007	0.2850	0.1552	0.0674	0.5406
4	0.1032	0.3036	0.8007	-1.8745	0.8007	0.3036	0.1032	0.5406
5	0.0674	0.1552	0.2850	0.8007	-1.8558	0.8519	0.2362	0.5406
6	0.0520	0.1161	0.1552	0.3036	0.8519	-1.6870	0.7487	0.5406
7	0.0487	0.1040	0.1347	0.2064	0.4725	1.4975	-1.9232	0.5406

elliptical cracks are approximated, based on the known values of the SIFs K_i^{Circle} and their rates $\partial K_i^{\text{Circle}} / \partial a_j$ for the current penny-shaped crack front, and using the linear relation, Figure 72:

$$K_i^{\text{Ellipse}} = K_i^{\text{Circle}} + \frac{\partial K_i^{\text{Circle}}}{\partial a_j} \delta a_j \quad (320)$$

Comparison of the extrapolated SIFs with a reference solution (Irwin, 1962) is given in

Table 15. Close agreement with the reference solution was obtained.

3.01.6.2.2 Example 6: semi-circular surface crack in a half-cylinder under a remote uniform tensile loading normal to the crack plane

A half-cylinder containing a semi-circular surface crack subjected to a remote uniform tensile loading normal to the crack plane is shown in Figure 73. The mesh used is the same as that for the penny-shaped crack in Example 5 and the only change occurs in the boundary conditions of the two vertical surfaces intercepting the crack surface that were previously supported by rollers. The flat face becomes free for the half-cylinder problem. Table 16 shows the comparison of the SIF calculated by the present method with the reference solution by Newman and Raju (1981), where the SIF was normalized by $K_0 = 2\sigma\sqrt{a/\pi}$ for a penny-shaped embedded crack. As illustrated in Figure 74, good agreement was obtained at all locations along the crack front.

Table 17 lists the calculated SIF derivatives for a semi-circular surface crack. Since there have been no published values for derivatives of the SIF, verification with other reference solutions is not straightforward. One way to

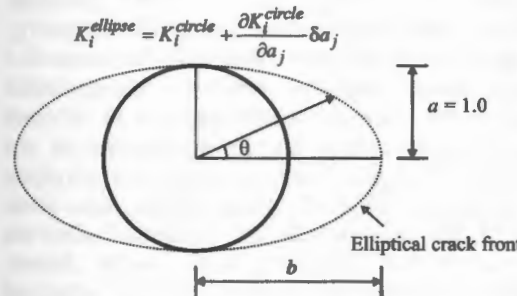


Figure 72 Approximation of SIF around an elliptical crack front based on known values of SIF and its derivative for a penny-shaped crack front, Example 5.

Table 15 SIFs extrapolated to an elliptical crack and compared with reference solution (Irwin, 1962). Example 5 ($b/a = 1.2, 1.4$).

θ	$b/a = 1.2$			$b/a = 1.4$		
	Exact	Predicted	Error %	Exact	Predicted	Error %
0	1.1214	1.1092	-1.09	1.1049	1.0591	-4.14
$\pi/12$	1.1328	1.1239	-0.78	1.1362	1.1047	-2.77
$\pi/6$	1.1594	1.1575	-0.16	1.1974	1.1941	-0.28
$\pi/4$	1.1880	1.1912	0.27	1.2495	1.2624	1.03
$\pi/3$	1.2104	1.2145	0.34	1.2834	1.2957	0.96
$5\pi/12$	1.2239	1.2266	0.22	1.3016	1.3073	0.44
$\pi/2$	1.2284	1.2302	0.15	1.3073	1.3097	0.18

evaluate the accuracy of the proposed method for $\delta K_I/\delta a$ is to compare results to semi-elliptical surface cracks, based on the known values of the SIFs and their rates on the current semi-circular crack front, Figure 75. In Table 18, the results for $b/a = 1.2$ and 1.4 are presented. In all cases, the maximum difference between the extrapolated value and the reference solution is less than 3%.

3.01.6.2.3 Example 7: a center-cracked plate subjected to a remote uniform tensile loading normal to the crack plane

The next numerical example investigates a center-cracked plate subjected to a remote uniform tensile loading, $\sigma = 1.0$, perpendicular to the crack surface, Figure 76(a). The present analysis is carried out on specimens of the following dimensions: (a) $W = H = 20.0$, $t = 4.0$, $a = 1.0$ (b) $W = H = 20.0$, $t = 4.0$, $a = 8.0$. Using the symmetry in the problem, only 1/8 of the plate was considered. The FE mesh consists of 432 elements and 3,263 nodes

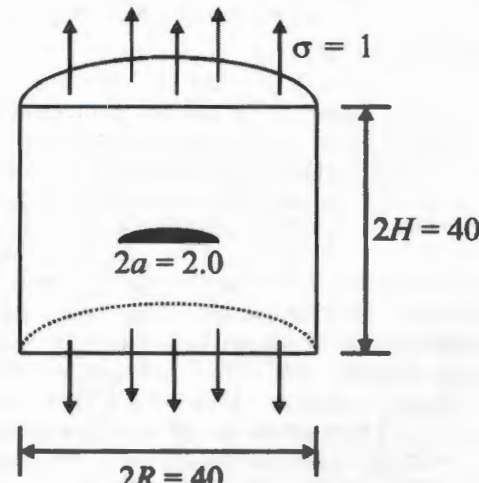


Figure 73 Half-penny-shaped surface crack under uniform remote tensile loading, Example 6.

Table 16 Comparison of the calculated values of SIFs with reference solutions (Newman *et al.*, 1981) for semi-circular surface crack. Example 6. ($K_0 = 2\sigma\sqrt{a/\pi}$ for penny-shaped crack).

Node	1	2	3	4	5	6	7
θ	0	$\pi/12$	$\pi/6$	$\pi/4$	$\pi/3$	$5\pi/12$	$\pi/2$
$K_I(\theta)/K_0$	1.1569	1.1171	1.0753	1.0546	1.0434	1.0379	1.0360
K_{REF}/K_0	1.1463	1.0990	1.0675	1.0504	1.0432	1.0414	1.0413
Error (%)	-0.92	-1.65	-0.73	-0.40	-0.03	0.33	0.51

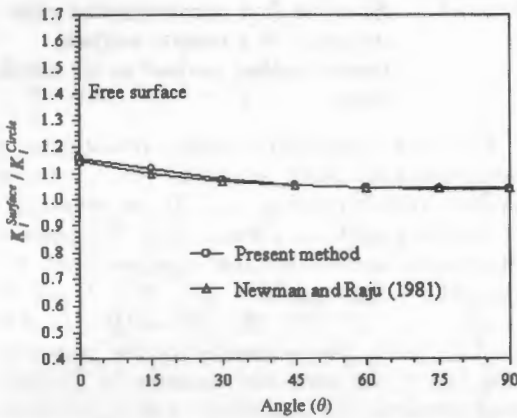


Figure 74 Comparison of the predicted values of SIF with reference solution, where $K_I^{\text{circle}} = 2\sigma\sqrt{a/\pi}$, Example 6.

for case (a), Figure 76(b), and 516 elements and 3,681 nodes for case (b). The quarter-point 15-noded wedge elements were employed to model the singularity around the crack front, Figure 76(d). The crack-tip element size was taken to be 1/8 of crack length a . It is noted that the result for $v = 0.0$ is identical to the 2D solution with the same Poisson's ratio and thus comparison of the results with reference solutions is possible. For $W/a = 20.0$ and $v = 0.0$, the present analysis gave $G = 3.1757$ and $\delta G/\delta a = 3.1518$, which are in excellent agreement with the reference values for a 2D crack (Isida, 1971), Tables 19 and 21. For $W/a = 2.5$, W being the same as before, the value computed for G by the present method is 37.367, which again is in correspondence with the value of 37.167 obtained using solutions of Ishida, Table 20.

The distribution of energy release rates along the crack front is shown in Figure 77 for different Poisson's ratios and the following geometries (a) $W = H = 20.0$, $t = 4.0$, $a = 1.0$ (b) $W = H = 20.0$, $t = 4.0$, $a = 8.0$. The local energy release rate around the crack front is normalized by K_I^2/E in which K_I is the reference SIF for a 2D crack. Figure 77 shows that, as one approaches the free surface, the energy release rate value decreases. This boundary layer effect was observed by Hartmann and Sih (1970). The

thickness of this layer is given by:

$$\frac{\varepsilon}{t} = \frac{1}{4 + 16t/a} \quad (321)$$

This is an approximate measure of the region within which the surface effects are significant (Narayana, 1994). The boundary layer thickness ε/t is 0.0147 and 0.08333 for the cases (a) $t/a = 4.0$ and (b) $t/a = 0.5$, respectively. In order to show this reduction for the case (a) $t/a = 4.0$, a much finer mesh near the free surface would be required. In the case of $t/a = 0.5$, the boundary layer effect is clearly illustrated in Figure 77(b).

3.01.6.3 Summary

In this section, the analytical virtual crack extension method introduced by Lin and Abel (1988) is generalized to a 3D crack problem. The general derivations are given for energy release rates and their higher derivatives of a 3D planar crack of arbitrary shape under arbitrary loading conditions. The present method maintains all the advantages of the similar virtual crack extension techniques (deLorenzi [38] 1982, 1985; Haber and Koh, 1985; Barbero and Reddy, 1990) and adds the capability of calculating higher-order derivatives of energy release rate for a 3D crack of arbitrary shape. The method provides the direct integral forms of stiffness derivatives for 3D FEs, and thus there is no need for the analyst to specify a finite length of virtual crack extension. The salient feature of this method is that the energy release rates and their higher derivatives for 3D cracks of arbitrary shape can be computed in a single analysis. Furthermore, this generalized formulation for the 3D crack problem has a couple of new features. First, the present method considers the interaction between virtual crack extensions at different positions along the crack front, because the areas perturbed due to crack extensions at adjacent positions on the front are overlapped. The additional term representing the interaction between virtual crack extensions is explicitly derived and included

Node
i:1
2
3
4
5
6
7



Figure 75 Semi-elliptical crack front

in the following section. Local curvatures and derivatives of energy release rates are provided.

Several solution methods have been presented in the literature. The accuracy of the method is about 0.2% for the first derivative and the density of the mesh can be imposed to the analyst. The following section illustrates the crack configuration and propagation in 3D.

The Section 3.01 even further extends the crack growth prediction. The crack tip is based on the energy

Table 17 The computed rates of SIFs for semi-circular surface crack. Example 6.

Node	j:1	2	3	4	5	6	7	Row sum
i:1	-1.9937	1.5874	0.5424	0.2207	0.1431	0.1107	0.0518	0.6625
2	0.8220	-1.8550	0.9243	0.3473	0.1774	0.1322	0.0593	0.6074
3	0.2918	0.9601	-2.0768	0.8409	0.3171	0.1771	0.0774	0.5876
4	0.1210	0.3679	0.8574	-2.0487	0.8301	0.3317	0.1148	0.5742
5	0.0794	0.1899	0.3268	0.8390	-1.9972	0.8792	0.2526	0.5696
6	0.0617	0.1423	0.1835	0.3370	0.8839	-1.8053	0.7639	0.5669
7	0.0579	0.1278	0.1606	0.2337	0.5086	1.5302	-2.0526	0.5661

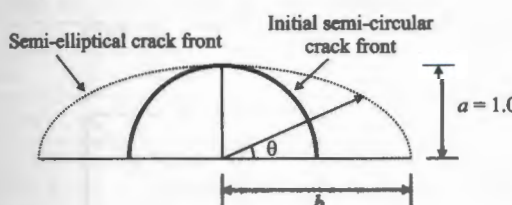


Figure 75 Approximation of SIF around a semi-elliptical crack front based on known values of stress intensity factor and its derivative for a semi-circular crack front, Example 6.

in the formulation for the second variations of element stiffness. Secondly, it is shown that a local curvature on the curved crack front must be taken into account to properly calculate the derivatives of energy release rate. The general formula for the derivatives of energy release rates around an arbitrarily curved front is provided.

Several 3D numerical examples with exact solutions or with solutions available in the literature are solved to demonstrate the accuracy of the current method. It was shown that the maximum computed errors were about 0.2% for energy release rate, and 2–4% for its first derivative between the simulated solutions and the reference solutions for the mesh density used in the examples. Accuracy can be improved with mesh refinement according to the guidelines provided herein. The proposed method has immediate application to the following related problems: the shape prediction and stability analysis of an evolving 3D crack front in fatigue or brittle fracture; configurational stability in fatigue crack propagation prediction; investigation of bifurcation in brittle fracture.

The variational methodology described in Sections 3.01.5 and 3.01.6 can be applied to even further generalizations of the LEFM crack growth problem. These include:

(i) non-collinear growth of 2D cracks. Section 3.01.4 presented various techniques for predicting the trajectory and stability of a 2D crack. One could take an alternative approach based on the principle of minimum potential energy to discover the trajectory of a noncol-

linear 2D crack or trajectories of a system of interacting noncollinear cracks. The methods described in Section 3.01.5 would be used to calculate the energy release rates and their derivatives necessary for such an approach. Some work on this problem is reported in Hwang *et al.* (1998) and Hwang *et al.* (2001)

(ii) noncoplanar growth of a 3D crack. Again, one could take an approach based on the principle of minimum potential energy to discover the shape of such a crack. The methods described in Section 3.01.6 would be used to calculate the energy release rates and their derivatives necessary for this problem.

3.01.7 PRACTICAL APPLICATIONS OF THE FE METHOD FOR LEFM

The previous sections of this chapter presented a number of example problems illustrating particular aspects of the FE method in LEFM. In this section, many of these aspects are integrated in a series of three practical problems from common engineering practice. The first problem employs the 2D, plane stress FEM to compute accurate stress intensity versus crack-length histories for crack growth in a lug. This would be a necessary computation for predicting fatigue crack growth rate, crack trajectories, and crack instability. The second problem uses a shell FE model to simulate curvilinear fatigue crack growth in a pressurized aircraft fuselage section. Again, such a simulation would be useful for making damage tolerance and residual strength predictions. The final problem involves 3D solid FE analysis of a spiral-bevel, power transmission gear. Here the issue is accurate prediction of fatigue crack shape: a fractured tooth is a less serious event than a fractured gear.

3.01.7.1 Computing Stress Intensity Factor Histories in a Lug

The objective of this example is to illustrate the process of using a FE program to compute SIF histories accurately, so that they can be

Table 18 Comparison of the extrapolated values of SIFs with reference solutions (Newman *et al.*, 1981). Example 6 ($b/a = 1.2, 1.4$).

θ	$b/a = 1.2$			$b/a = 1.3$		
	Exact	Predicted	Error %	Exact	Predicted	Error %
0	1.3030	1.2981	0.38	1.3015	1.2824	1.47
$\pi/12$	1.2537	1.2530	0.06	1.2584	1.2435	1.18
$\pi/6$	1.2466	1.2459	0.06	1.2698	1.2663	0.28
$\pi/4$	1.2607	1.2606	0.01	1.2992	1.3007	-0.12
$\pi/3$	1.2788	1.2741	0.37	1.3256	1.3215	0.31
$5\pi/12$	1.2919	1.2812	0.83	1.3423	1.3295	0.95
$\pi/2$	1.2966	1.2833	1.03	1.3479	1.3313	1.23

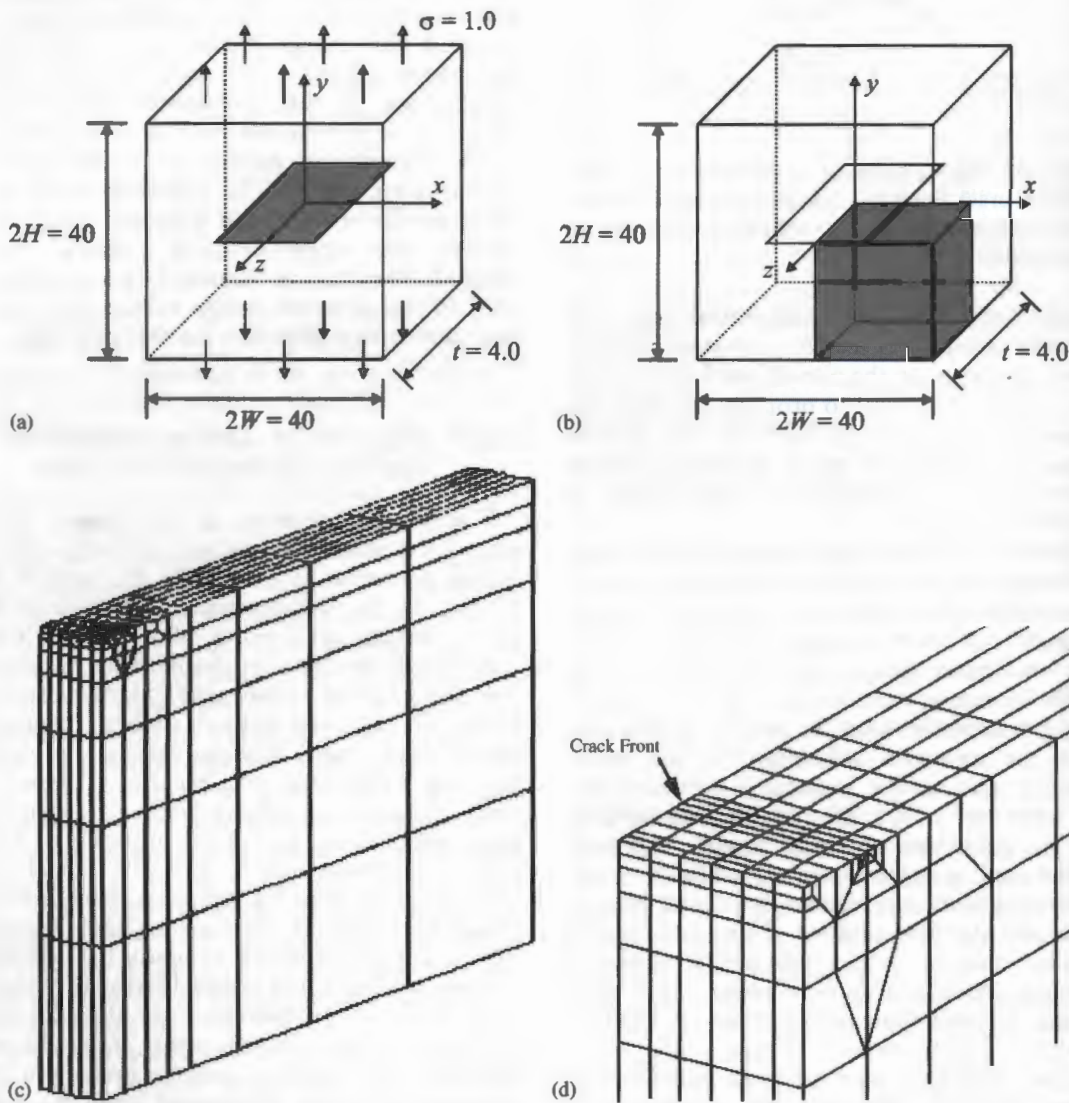


Figure 76 (a) Center-cracked plate under remote tensile loading, Example 7; (b) octant of problem (shaded) for FE analysis; (c) mesh; and (d) detail of mesh around crack front.

used for fatigue crack growth rate (FCGR) and life predictions.

The example is a relatively common structural detail, modeled as a plane stress problem, as shown in Figure 78. This figure shows a

simple lug under nonsymmetric loading. A contact-fit pin is inserted in the hole, and the pin load, P , is distributed to the hole by way of an elastic contact analysis. A crack is initiated from a location of high tensile stress

Table 1

z/t	Node
$v = 0.0$	
$v = 0.15$	
$v = 0.3$	
$v = 0.4$	

Table 2

z/t	Node
$v = 0.0$	
$v = 0.1$	
$v = 0.3$	
$v = 0.4$	

Table 2

z/t	Node
$v = 0.0$	
$v = 0.1$	
$v = 0.3$	
$v = 0.4$	

conce
allow
FRA
is use
Fig
prob
fit pi
quad
elem
the pi
thick
const
contac
repre
show
acros
norm
sion c
Fig
shape
from
o'clo
nono
of th
majo
confi

Fig
shape
from
o'clo
nono
of th
majo
confi

Table 19 The computed values of energy release rates along the crack front for various Poisson's ratios. Example 7 ($W=H=20.0$, $t=4.0$, $a=1.0$, 2D reference solution of $G=3.1681$ for $\nu=0.0$).

z/t	0.5000	0.4167	0.3333	0.2500	0.1667	0.0833	0.0000
<i>Node</i>	1	2	3	4	5	6	7
$\nu=0.0$	3.1757	3.1757	3.1757	3.1757	3.1757	3.1757	3.1757
$\nu=0.15$	3.2020	3.2128	3.1692	3.1393	3.1226	3.1144	3.1119
$\nu=0.3$	3.1718	3.2308	3.1337	3.0573	3.0106	2.9862	2.9786
$\nu=0.4$	3.0983	3.2253	3.0903	2.9733	2.8991	2.8594	2.8470

Table 20 The computed values of energy release rates along the crack front for various Poisson's ratios. Example 7 ($W=H=20.0$, $t=4.0$, $a=8.0$, 2D reference solution of $G=37.136$ for $\nu=0.0$).

z/t	0.5000	0.4167	0.3333	0.2500	0.1667	0.0833	0.0000
<i>Node</i>	1	2	3	4	5	6	7
$\nu=0.0$	37.367	37.367	37.367	37.367	37.367	37.367	37.367
$\nu=0.15$	35.661	36.926	37.418	37.576	37.639	37.665	37.672
$\nu=0.3$	32.738	36.009	37.387	37.865	38.071	38.160	38.186
$\nu=0.4$	29.857	34.992	37.291	38.120	38.490	38.655	38.703

Table 21 The computed values of first-order derivatives of energy release rates, Example 7 ($W=H=20.0$, $t=4.0$, $a=1.0$, 2D reference solution of $\delta G/\delta a=3.2114$ for $\nu=0.0$).

<i>Node</i>	<i>j:1</i>	2	3	4	5	6	7	Row sum
<i>i:1</i>	-5.9948	5.2121	1.9936	0.8648	0.5150	0.3858	0.1752	3.1518
2	2.6060	-5.8639	3.4901	1.3916	0.7550	0.5320	0.2409	3.1518
3	0.9968	3.4901	-7.1247	3.2745	1.3442	0.8252	0.3458	3.1518
4	0.4324	1.3916	3.2745	-7.247	3.2858	1.4534	0.5610	3.1518
5	0.2575	0.7550	1.3442	3.2858	-7.1528	3.5640	1.0982	3.1518
6	0.1929	0.5320	0.8252	1.4534	3.5640	-6.4154	2.9997	3.1518
7	0.1752	0.4818	0.6915	1.1219	2.1963	5.9993	-7.5143	3.1518

concentration along the lug bore, and then allowed to propagate in mixed mode. FRANC2D (Cornell Fracture Group, 2002) is used as a FE solver.

Figure 79 shows the initial FE model for this problem. The lug and its frictionless, contact-fit pin are both steel and are modeled with quadratic-order triangular and quadrilateral elements. The elastic contact problem between the pin and the lug is solved. Six-noded, zero-thickness interface elements with nonlinear constitutive capability are inserted around the contact surface. The constitutive model used to represent the normal contact conditions is shown in Figure 80. No tension is allowed across the contact, and a high compressive normal stiffness is assigned to minimize intrusion of the pin into the lug.

Figure 81 presents the uncracked, deformed shape and shows that separation of the pin from the lug has occurred from about the 8 o'clock to the 2 o'clock positions, while nonoverlapping contact occurs along the rest of the contact. Figure 82 shows contours of major principal stress for the initial, uncracked configuration. This solution involved about

9,200 DOF, and, with an error tolerance of 0.0005 on both equilibrium and displacement change between time steps, required about 5,200 time steps and 2.5 min on a PC running Windows 2000 on a 1 GHz Pentium III processor. This figure indicates two locations of high stress concentration around the lug bore, as expected. A slightly higher concentration occurs in the lower left quadrant, at about the 8 o'clock position, and a short crack (1.7 mm, 0.067 in) is initiated at the location of highest circumferential tensile stress near this point. Growth of this crack is then simulated by:

(i) Computing K_I and K_{II} using the equivalent domain formulation of the elastic J-Integral: see Section 3.01.3.5;

(ii) Calculating the direction of crack growth using the maximum circumferential tensile stress theory, see Section 3.01.4.1;

(iii) Extending the crack by 1.9 mm (0.075 in) in this direction;

(iv) Resolving the FE problem, including the nonlinear contact between lug and pin;

(v) Repeating steps 1-4 until the crack has extended about 64 mm (2.5 in) at which point

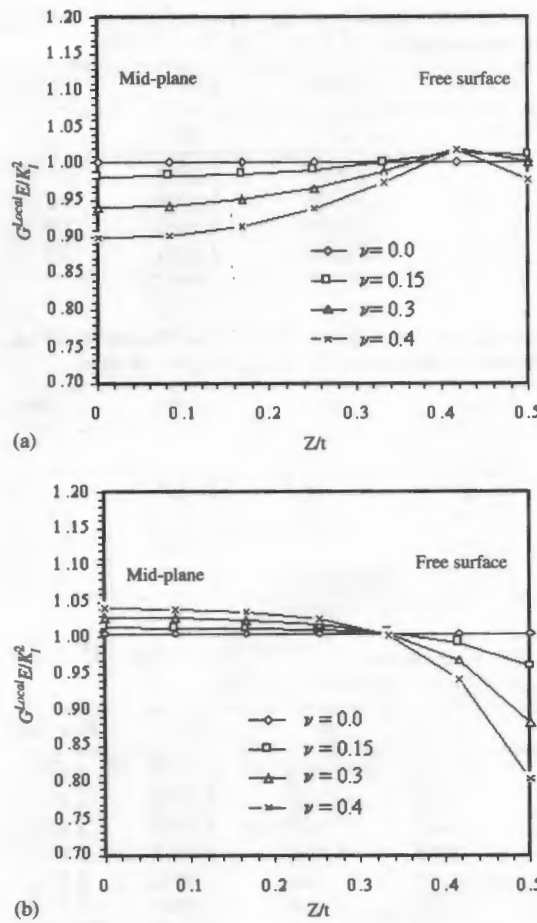


Figure 77 (a) Normalized local energy release rate along the half-crack front for various Poisson ratios with $a = 1.0$, $W = H = 20.0$, and $t = 4.0$, Example 7; (b) Normalized local energy release rate along the half-crack front for various Poisson ratios with $a = 8.0$, $W = H = 20.0$, and $t = 4.0$.

fatigue life or residual strength limits are likely to have been reached.

Experience has shown that the treatment shown in this example, a rosette of eight six-noded triangular elements immediately surrounding the tip, quarter-point versions of these elements, and element size ranging from a few to as much as 25% of crack length, will produce very accurate values of stress intensity factors.

Figure 83 shows the corresponding amplified displaced shape, while Figure 84 shows the resulting stress intensity factor histories. Figure 83 shows that the crack trajectory is not quite radial, and is responding to the asymmetrical loading and geometry. The trajectory is dictated here by the maximum circumferential tensile stress theory that requires that K_{II} remain zero along the crack path. With a FE model that discretizes the trajectory into finite, straight segments, there

will always be residual, nonzero values of K_{II} computed at each crack-tip location. If the segments are short enough, these residuals should be small compared to the K_I values. Figure 85 shows that the values of K_{II} are oscillating around zero, and are indeed small, in this case never reaching more than 3.5% of K_I . The highest values usually occur early in the trajectory while the FE model is adjusting to the stress field that is evolving as a result of crack growth, as shown in Figure 85. A key practical issue suggested here is the length of crack growth increment. This length should be sufficiently short to accurately discretize a curvilinear trajectory and provide enough data points for the accurate integration required for FCGR calculations, while not being so short that excessive computation times accrue. Here 32 increments were used. The number of DOFs grew to nearly 1.4×10^4 at the last increment, and a total of about 2 h of computing time was required.

A FE code with fracture mechanics features can be thought of as a general SIF calculator. As such it can be used to attack practically interesting variants of problems. For example, it is possible that two fatigue cracks might initiate in this lug problem, one from each of the locations of initially high stress concentration. This possibility is also simulated here, under the assumptions that the cracks initiate simultaneously, and that they have equal rates of growth. The resulting trajectories under these simplifying assumptions are shown in Figure 86. The corresponding mode I SIF histories are given in Figure 87. This figure shows that, even if initiation were simultaneous, rate of growth would not be equal; the left crack would have higher growth rate. However, even under these simplifying assumptions, Figure 87 also shows that the growth rate of the left crack would be higher than it would be if it were the only crack to occur.

3.01.7.2 Predicting Fatigue Crack Life and Trajectory in an Aircraft Fuselage Section

Simulations of curvilinear crack growth in a generic narrow body fuselage panel were performed in Potyondy *et al.* (1995) and Chen *et al.* (1997). The predicted crack trajectories were compared with the measured values from a full-scale pressurization test. This problem demonstrates the applicability of the SIF calculation techniques for shell structures, Section 3.01.3, and the

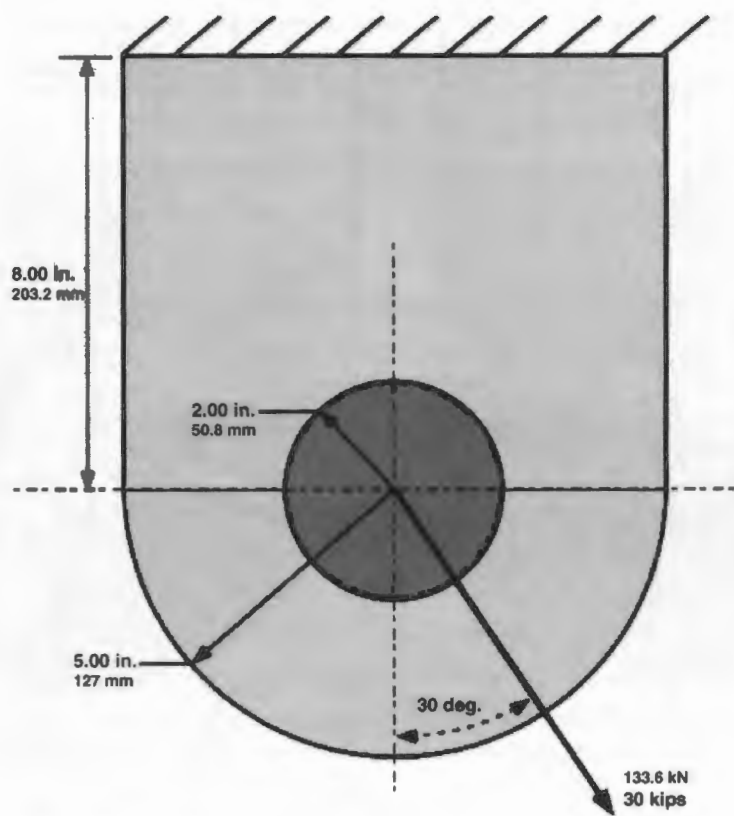


Figure 78 A lug under unsymmetrical load. Lug and pin are both steel, $E = 200 \text{ GPa}$ ($2.9 \times 10^4 \text{ ksi}$), $\nu = 0.30$, and frictionless, contact-fit of the pin in the lug is assumed. Thickness is 25.4 mm (1.00 in.).

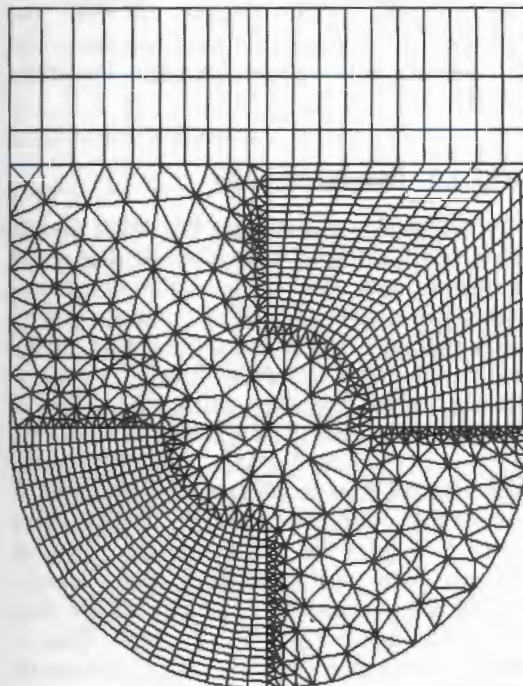


Figure 79 Initial FE mesh for lug problem.

direction criteria developed in Section 3.01.4 for predicting curvilinear crack growth in fuselage structures.

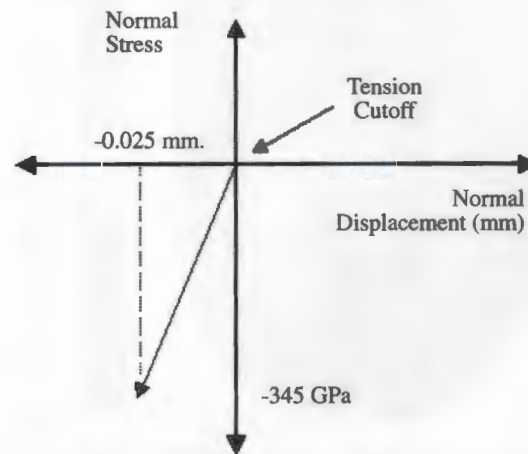


Figure 80 Constitutive model for normal stress-displacement on the pin/lug contact surface.

3.01.7.2.1 Description of experiment

A narrow body fuselage panel with tear straps, stringers, stringer clips, and frames was tested by the Boeing Commercial Airplane Group. Skins and tear straps were made of 0.036 in (0.91 mm) thick, 2024-T3 clad aluminum alloy. Stringers, frames, and stringer clips were made of 7075-T6 clad aluminum alloy. The tear straps were hotbonded to the skins at

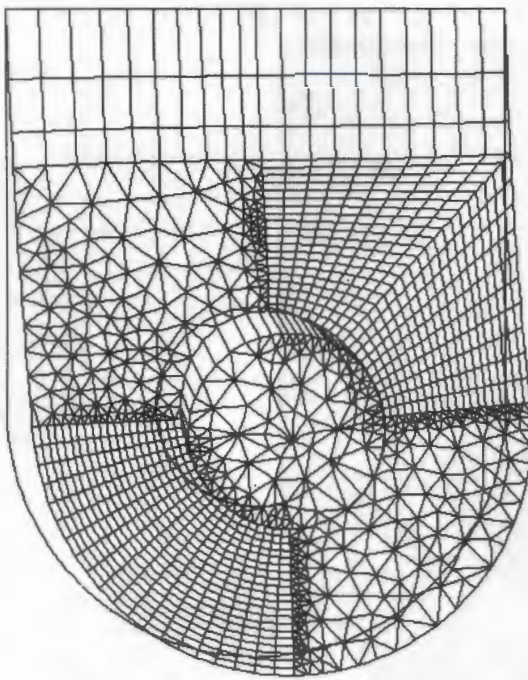


Figure 81 Deformed shape of uncracked configuration of lug. Displacement amplification factor is 225.

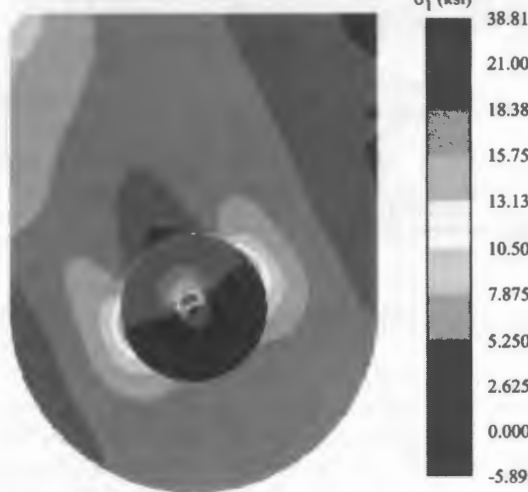


Figure 82 Contours of major principal stress in lug in uncracked condition. $1 \text{ ksi} = 6.984 \text{ MPa}$.

midbay and at each frame station. The structural features of the test panel are shown in Figure 88. More information about panel dimensions can be found in Gruber *et al.* (1996).

The panel had a 5.0 in (127 mm) initial saw cut in the T-L orientation centered on the midbay tear strap and just above the stringer tear strap. The saw cut went completely through both the skin and midbay tear strap. The panel was inserted into a test fixture with a

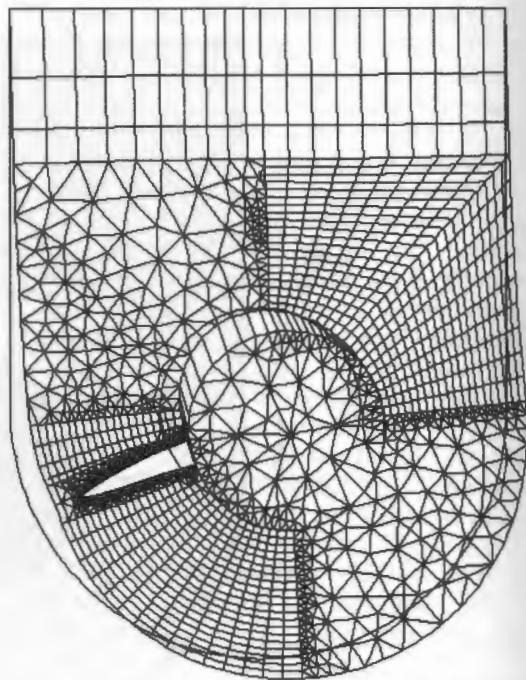
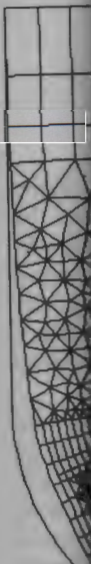


Figure 83 Final deformed shape of single cracked configuration of lug. Displacement amplification factor is 150.

radius of curvature of 74 in (1880 mm) to match narrow body airplanes. A cyclic pressure of 7.8 psi (53.63 kPa) was applied to propagate the crack. During the test, the positions of the crack tips were recorded. The detailed test data can be found in Potyondy (1993).

3.01.7.2.2 Numerical model

In this study, a 4-stringer-bay wide and 2-frame-bay long panel was analyzed. The entire curvilinear crack growth simulation consists of more than 20 in (508 mm) of crack extension. All structural components including skins, stringers, and frames were modeled by quadrilateral shell elements using the STAGS (Rankin *et al.*, 1997) and FRANC3D (Cornell Fracture Group, 2002) codes. Each node of the shell element has six degrees of freedom. A typical FE mesh used in the simulation is shown in Figure 89. Geometrically nonlinear analyses were performed. For this example, only internal pressure on the skin of the shell model was applied to the structure. Thus, a simple numerical model using symmetric boundary conditions imposed on all the boundary edges was used to simulate a cylinder-like fuselage structure. Uniform axial expansion was allowed at one longitudinal end. On this boundary edge, an axial force equal to $(PR/2)L$ was assigned where P is the applied



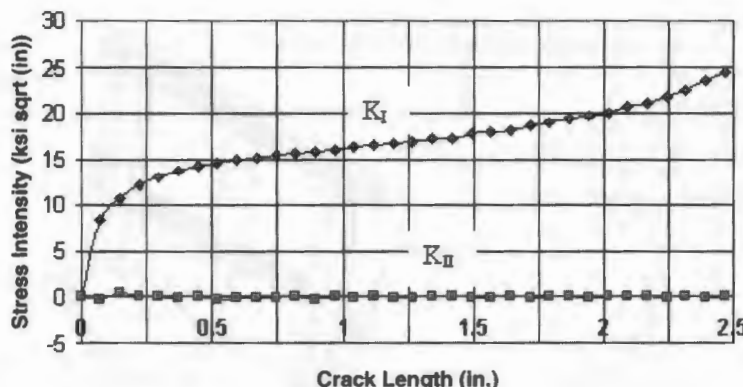


Figure 84 Computed SIF histories in lug. Single crack case. 1 in = 25.4 mm, 1 ksi $\text{in}^{1/2}$ = 1.098 MPa $\text{m}^{1/2}$.

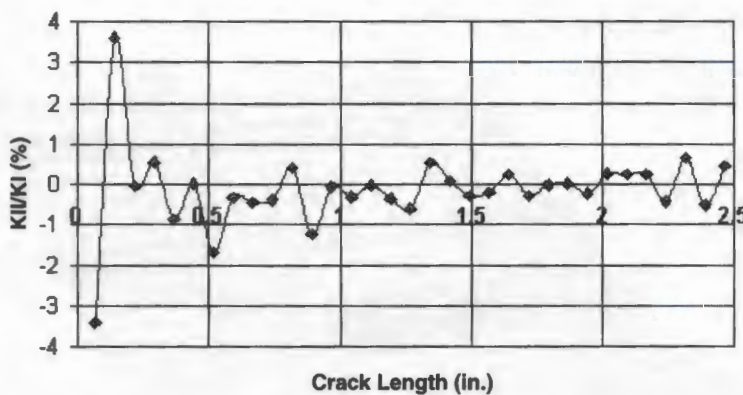


Figure 85 History of computed ratio of SIFs for lug problem. Single crack case. 1 in = 25.4 mm.

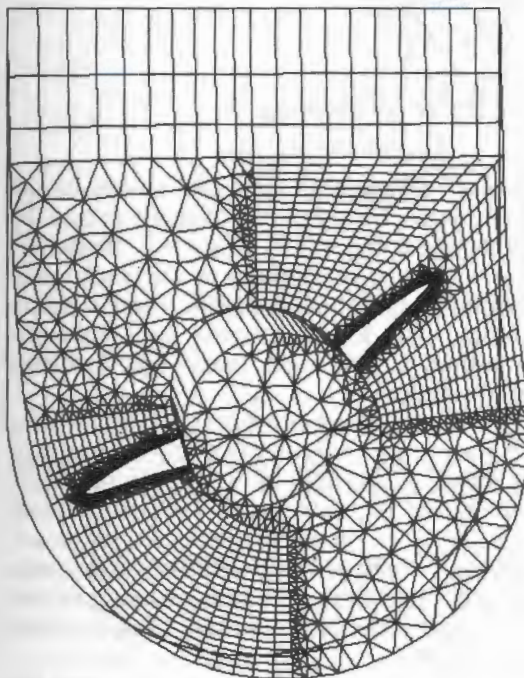


Figure 86 Final deformed shape of multiply cracked lug configuration. Displacement amplification factor is 100.

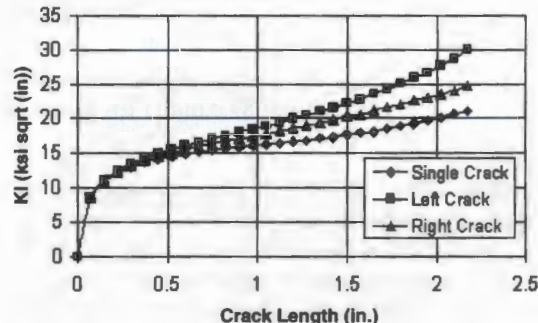


Figure 87 Comparison of SIF histories for single- and multiple-crack cases for lug problem. 1 in = 25.4 mm, 1 ksi $\text{in}^{1/2}$ = 1.098 MPa $\text{m}^{1/2}$.

pressure, R is the radius of the panel, and L is the arc-length of the edge.

3.01.7.2.3 Fracture parameter evaluation

Deformation and stress fields near the crack tip were used to compute fracture parameters for the crack growth simulations. The modified crack closure integral method, Section 3.01.3.8, was used to compute the membrane and

Material: Skin and tear strap, 2024-T3 clad, $E=10,500$ ksi, $v=0.33$;
stringer and frame, 7075-T6 clad, $E=10,700$ ksi, $v=0.33$;

Radius: 74 inches
Skin: 0.036 in. thick
Tear strap: 0.036 in. thick
Stringer: 0.028-in.-thick bat section
9.25-in. spacing
Frame: 0.040-in.-thick Z-section
20-in spacing

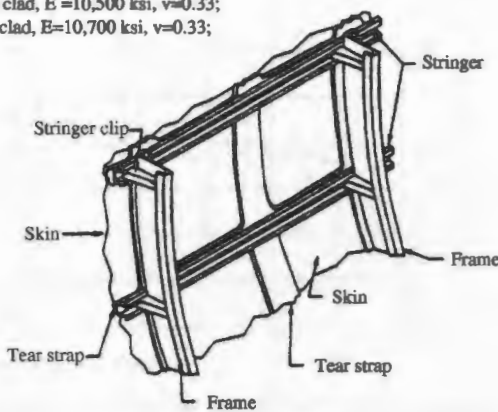


Figure 88 Structural features of a narrow body fuselage panel, modified after Gruber *et al.* (1996).

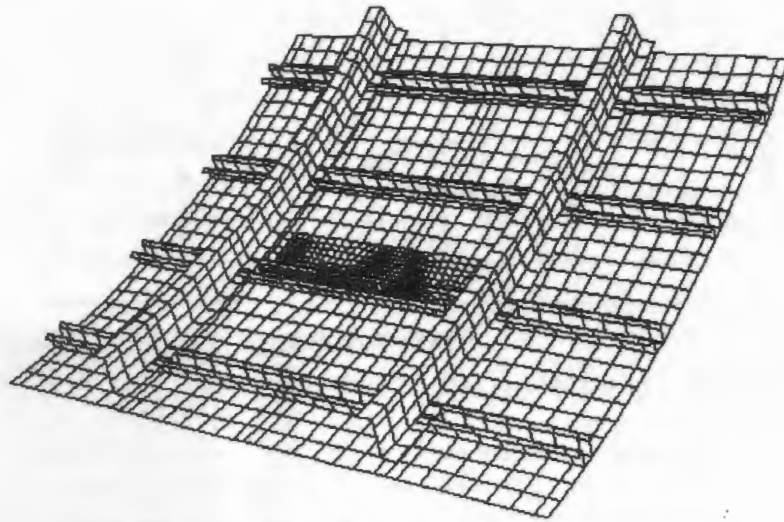


Figure 89 Initial FE model for the narrow body fuselage panel.

bending SIFs, K_I , K_{II} , k_1 , k_2 . Crack growth directional criteria for isotropic and orthotropic media from Section 3.01.4 were used to predict the propagation angle in this thin shell structure. The equivalent domain integral method for T -stress developed in Section 3.01.4.6 is only valid for 2D problems. The derivation of its counterpart for shell structures subjected to large displacements and rotations is not yet available. Instead, a simple displacement correlation method was used to evaluate the T -stress (Sutton *et al.*, 1997).

3.01.7.2.4 Results of crack growth simulation

The effect of T -stress and r_c on crack trajectory prediction was studied first. Figure 90 plots the predicted crack trajectories with $r_c=0$ in and $r_c=0.09$ in (2.29 mm) as well as the experimental measurements. Figure 91

shows the computed deformed shapes during curvilinear crack growth. Bulging caused by the applied pressure is observed. Moreover, severe flapping is predicted as the crack turns. Figure 92 shows the computed stress intensity factors and T -stress versus the half-crack extension at the right crack tip. Predicted results suggest:

(i) The T -stress has a very mild influence on the early crack trajectory prediction because of its small magnitude. However, as the crack approaches the tear strap, T -stress increases and plays an important role in the crack turning prediction. For the case with $r_c=0.09$ in (2.29 mm), a sharp turning caused by T -stress is predicted as the crack approaches the tear strap.

(ii) The computed fracture parameters for $r_c=0$ in and $r_c=0.09$ in (2.29 mm) are comparable at the early stage of curvilinear crack growth. However, sharp turning as the crack

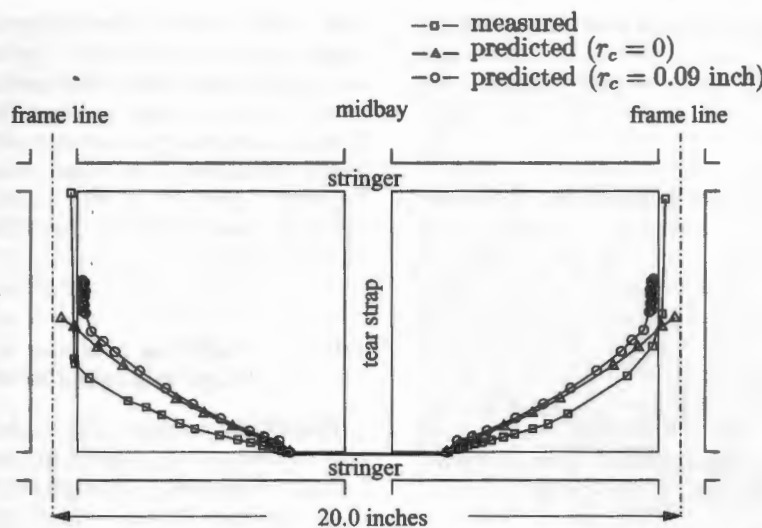


Figure 90 Comparisons between predicted and measured crack trajectories, with isotropic directional criterion and with various magnitudes of r_c . 1 in = 25.4 mm.

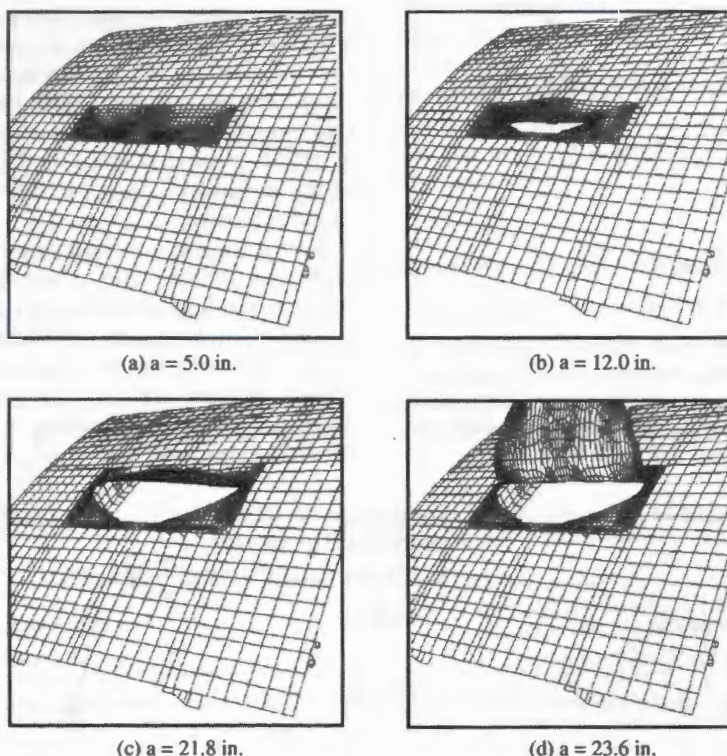


Figure 91 Computed deformed shapes during curvilinear crack growth for the isotropic case with $r_c = 0.09$ in. Magnification factor = 2.0. 1 in = 25.4 mm.

approaches the tear strap alters the deformation and stress fields. This drastically changes the computed values of fracture parameters.

(iii) Predicted crack paths from both numerical simulations at the right and left crack tips are almost symmetric about the midbay, but the measured crack paths are not. This observation gives a preliminary indication of

the experimental scatter that might occur in the panel test.

The predicted crack growth trajectories depicted in Figure 90 are comparable to the experimental measurements, but with some discrepancy. The disagreement during early stages of crack growth might be related to the fracture toughness orthotropy of the fuselage

skins. Therefore, additional analyses, using the orthotropic directional criterion were also performed. From coupon test results, the fracture toughness for this material and thickness was $\sim 100 \text{ ksi in}^{1/2}$ ($109.8 \text{ MPa m}^{1/2}$) in the L direction and $105\text{--}120 \text{ ksi in}^{1/2}$ ($115.3\text{--}131.8 \text{ MPa m}^{1/2}$) in the T direction (Potyondy, 1993). Thus, the fracture toughness was assumed to be 10% higher in the T than in the L direction. The predicted crack trajectories with $r_c = 0.09 \text{ in}$ (2.29 mm) are compared with those from the isotropic prediction and experimental measurements in Figure 93. During early stages of crack growth, the predicted trajectories for the orthotropic case agree better with the experimental measurements than the isotropic case. Crack-growth simula-

tion with fracture orthotropy also predicts crack turning as the crack approaches the tear strap. However, when the crack grows further into the tear strap region, the inclusion of fracture orthotropy adversely alters the crack-path prediction and does not predict the flapping observed in the panel test. Several possible reasons for this are discussed in Chen *et al.* (2002).

3.01.7.3 Predicting Evolution of 3D Crack Shape in a Spiral Bevel Gear

Predicting evolving crack shapes is important in determining the failure mode of a gear. Cracks propagating through the rim may result in catastrophic failure, whereas the gear may remain intact if one tooth fails and this may allow for early detection of failure.

Tooth-bending fatigue failure in spiral bevel gears was investigated using the boundary element method in Spievak *et al.* (2001). That effort was significant in developing a method for predicting 3D, nonproportional, fatigue crack growth incorporating moving loads. In this example, the problem studied by Spievak *et al.* is approached with the FEM, using many of the techniques described in previous sections of this chapter.

For accurate mixed-mode SIF calculation with the FEM, the equivalent domain J -integral method described in Section 3.01.3.5 is used. Crack trajectory predictions are made using the maximum circumferential stress theory, Section 3.01.4.1. Fatigue crack growth rates are determined using a modified Paris model accounting for crack closure (Spievak

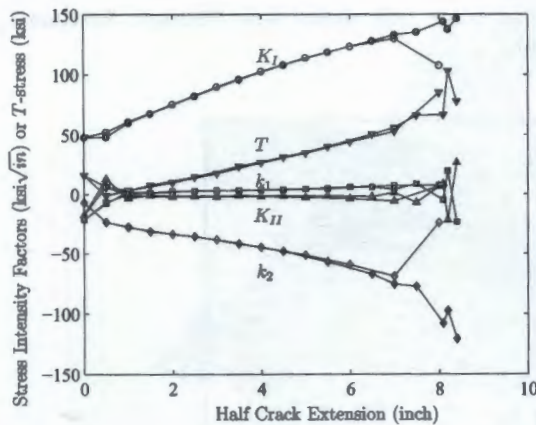


Figure 92 Computed stress intensity factors and T -stress versus half crack extension. The hollow and solid markers denote the computed fracture parameters for the isotropic case with $r_c=0 \text{ in}$ and $r_c=0.09 \text{ in}$, respectively. 1 in = 25.4 mm.

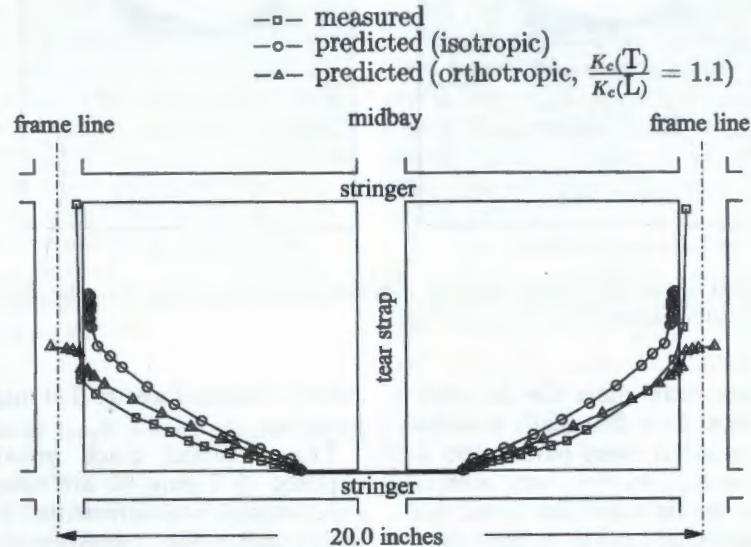


Figure 93 Comparisons between predicted and measured crack trajectories for isotropic and orthotropic cases with $r_c = 0.09 \text{ in}$. 1 in = 25.4 mm.

predicts the tear s further usion of te crack-dict the Several in Chen

Crack

impor- f a gear. ay result ear may his may

ral bevel boundary 1). That method fatigue oads. In Spievak ng many sections

culation main J- 3.01.3.5 re made l stress growth ed Paris Spievak

et al., 2001). Moving loads along the face of a tooth are taken into account by discretizing the loading into a number of steps that create a nonproportional load history on a crack. Solution time for each load step is substantially decreased by employing parallel FEM analysis.

The FRANC3D (Cornell Fracture Group, 2002) simulation system is used for this example. The method used to simulate crack growth in a gear is composed of the following steps:

- (i) Create initial geometry model of the spiral bevel pinion.
- (ii) Specify boundary conditions and material properties on the geometry model.
- (iii) Initiate a crack by locally modifying the geometry model.
- (iv) Create a surface mesh composed of triangular elements.
- (v) Create a 3D solid mesh of the model composed of tetrahedral.
- (vi) Calculate the magnitude and location of the nodal contact loads for each load step on the loaded elements.
- (vii) Using the mesh and geometry models, and load files for each step of loading, run analysis on a parallel PC-cluster. As a result of these analyses, SIF values at each discrete crack front point and displacement and stress values for each load step are calculated.
- (viii) Calculate the amount of crack extension at each discrete crack front point as a result of all steps of nonproportional moving load.
- (ix) Determine new crack front by piecewise least squares fit of the propagated points

corresponding to each discrete crack front point.

(x) Remesh surface locally and repeat steps 5–10.

3.01.7.3.1 Modeling of moving tooth loads

Contact in a spiral bevel gear occurs in 3D following a path along the tooth surface, starting from the fillet of the toe to the top of the heel. In analyzing the spiral bevel gear, it is assumed that the contact between the gear and its pinion follows Hertz theory of elastic contact. Hertzian contact holds as long as the significant dimensions of the contact area are small compared to the dimensions of each body and to the relative radii of curvature of surfaces. Hertz theory assumes that surfaces are continuous and nonconforming, strains are small, each solid can be considered as an elastic half-space, and surfaces are frictionless. Under these assumptions, only normal pressure acts between two bodies due to Hertz contact producing normal displacements of the surfaces. Hertzian contact assumptions are relaxed in Ural *et al.* (2002), wherein actual contact analysis is performed between the gear and its pinion.

3.01.7.3.2 Parallel FE analyses

A parallel-PC cluster was used for the FE analyses in the crack growth simulations, step 7, above. The hardware consists of 32 2-way Pentium III processors at 733 MHz running in a Windows environment. Table 22 presents

Table 22 Characteristics of FE simulation of crack growth in spiral bevel gear.

Item	Characteristic
Computer power	32 node Pentium III PC-cluster, 733 MHz
Number of unknowns	2.65×10^5 – 3.95×10^5
Solution time per load cycle	53–88 min (212–352 s/load step)
Typical time for one crack step	~4–6 h ^a

^a1–1.5 h solution time plus 3–4.5 h post-processing and remeshing.

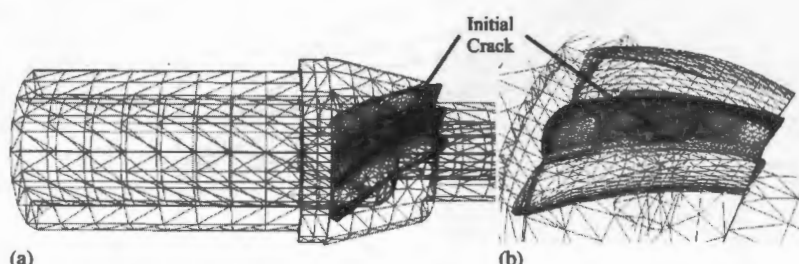


Figure 94 A spiral bevel pinion model with surface FE mesh: (a) whole pinion and (b) close up view of pinion teeth. Note the location of the initial crack in the middle tooth.

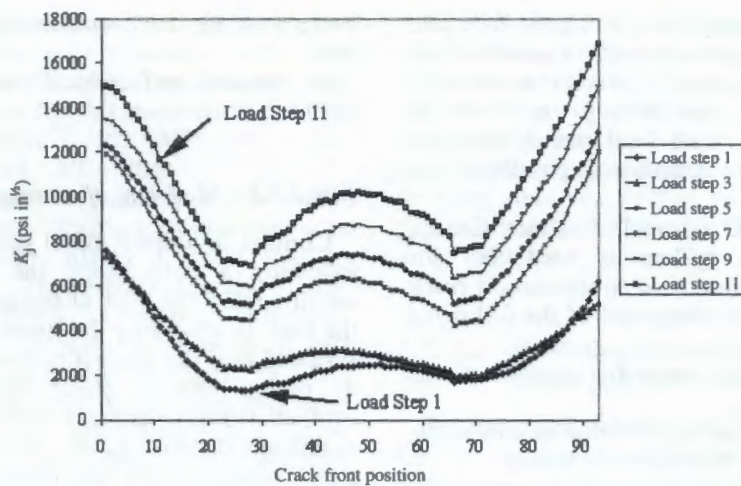


Figure 95 Initial mode I SIF distribution for load steps one through eleven. $1 \text{ ksi in}^{1/2} = 1.098 \text{ MPa m}^{1/2}$.

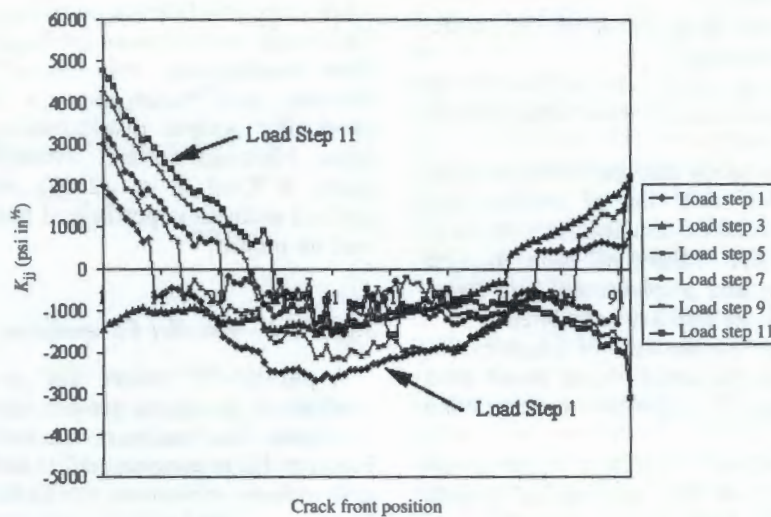


Figure 96 Initial mode II SIF distribution for load steps one through eleven. $1 \text{ ksi in}^{1/2} = 1.098 \text{ MPa m}^{1/2}$.

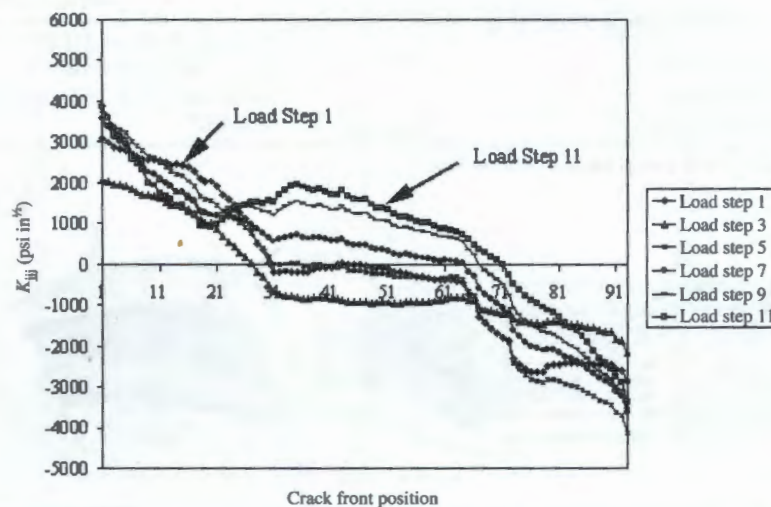


Figure 97 Initial mode III SIF distribution for load steps one through eleven. $1 \text{ ksi in}^{1/2} = 1.098 \text{ MPa m}^{1/2}$.

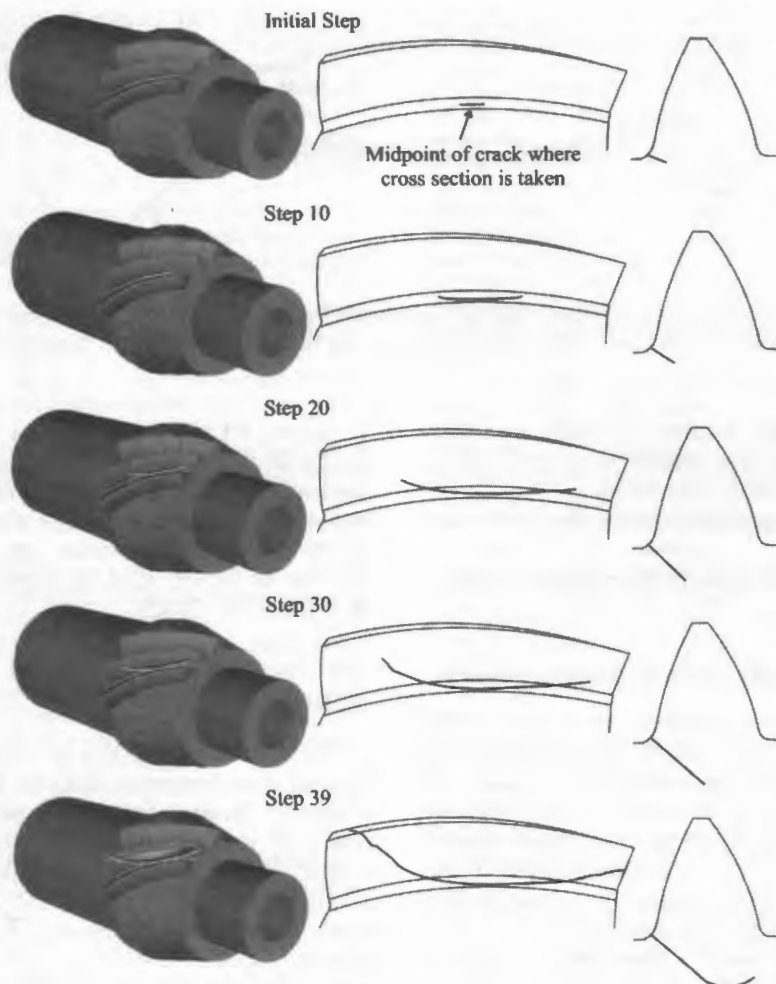


Figure 98 Crack trajectory predictions by FEM on tooth surface and tooth cross-section.

some typical timing results for this example problem.

3.01.7.3.3 Determining new crack front

Crack extension due to one nonproportional load cycle, step 8 above, is computed using the approach developed in Spievak *et al.* (2001). As previously mentioned, a modified Paris model that accounts for crack closure effects is used. A crack is assumed to advance when its maximum SIF is large enough to overcome closure and is larger than the maximum SIF of the previous load step. Thereafter, for every point along the crack front:

(i) Calculate the angle of crack growth corresponding to each load step using maximum circumferential stress theory, Section 3.01.4.1.

(ii) Calculate the final coordinates of the crack front and trajectory angles by approximating the contributions from each load step by a straight line.



Figure 99 Close-up view of the crack tooth after the last step of crack growth. Note the elliptical contact area for load step 14.

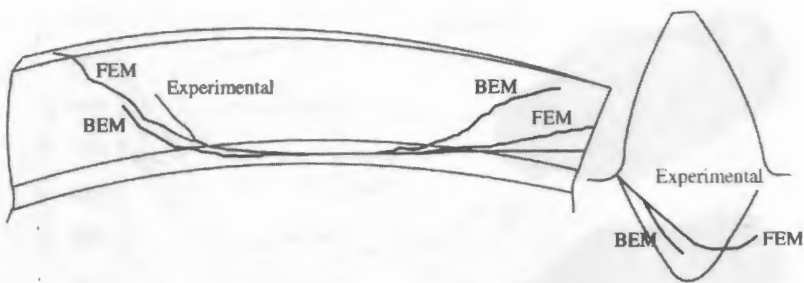


Figure 100 Comparison between crack trajectory predicted by the FEM and BEM (Spievak *et al.*, 2001) and observed in an experiment, on the tooth surface (left), and tooth cross-section at the midpoint of crack (right).

- (iii) Determine number of cycles necessary to have a reasonable amount of crack advance compared to pinion's geometry.
- (iv) Update geometry using the new crack front points.
- (v) Repeat for each crack extension step.

3.01.7.3.4 Results of crack growth simulation

Analyses were performed on a spiral bevel pinion for 39 crack growth steps, Figure 94. One crack growth step consists of 15 static FE analyses in order to simulate moving loads on the pinion tooth. After the 39th crack growth step, the analysis was stopped because it was concluded that propagating the crack further would not provide additional insights.

Figures 95, 96, and 97 show modes I, II, and III SIFs for the initial crack configuration for the first 11 load steps. Load steps 1–4 correspond to double tooth contact, load steps 5–11 correspond to single tooth contact, and load steps 12–15 again correspond to double tooth contact. Since a crack is not assumed to advance when its maximum SIF is smaller than the maximum SIF of the previous load step, only the first 11 steps practically contribute to crack growth calculations. In these figures, crack-front position corresponds to the points near the crack front at which SIF values are evaluated. In the initial step of crack-growth simulations, the crack front was discretized into 93 points at which SIF values were calculated.

Figure 98 shows the crack trajectory predictions on the tooth surface and cross-section of the tooth for several crack growth steps, including the initial and final configuration of the crack. Figure 99 is a close-up view of the last step of crack growth from the toe end of the tooth. This figure also shows the elliptical contact area for load step 14. Crack trajectory comparisons in Figure 100 show that, on the tooth surface, crack trajectory predicted by FEM is close to the experimental result.

However, FEM results show a steeper propagation angle at midcrack than that observed. In contrast, on the toe end FEM results exhibit a less steep propagation angle than the experiment. These discrepancies can be due to a number of factors that are further investigated in Ural *et al.* (2002).

ACKNOWLEDGMENTS

The authors would like to acknowledge their present and former colleagues in the Cornell Fracture Group for their contributions to much of the work reported here: Dr. Bruce Carter, Dr. Richard Pettit (Section 3.01.4), Dr. Changyu Hwang (Sections 3.01.5 and 3.01.6), Prof. Chuin-Shan Chen and Dr. David Pottydony (Section 3.01.7.2), Lisa Spievak and Ani Ural (Section 3.01.7.3). We also gratefully acknowledge the financial support of the United States National Science Foundation (Grants EIA 9726388, KDI 9873214, ITR 0085969), the NASA Langley Research Center (Grants NAG-1-02001, NAG-1-2069, NAG-1-2013), the NASA Glenn Research Center (Grant NAG-3-1993), and the Cornell University Theory Center.

3.01.8 REFERENCES

- A. Al-Ani and J. W. Hancock, 1991, J-dominance of short cracks in tension and bending. *J. Mech. Phys. Solids*, **39**(1), 23–43.
- S. N. Atluri, A. S. Kobayashi and M. Nakagaki, 1975, An assumed displacement hybrid finite element model for linear elastic fracture mechanics. *Int. J. Fract.*, **11**, 257–271.
- L. Banks-Sills, 1988, Use of three-dimensional finite elements in linear elastic fracture mechanics. *Anal. Num. Exp. Aspects Fract. Processes, ASME-AMD*, **91**, 89–97.
- L. Banks-Sills, 1991, Application of the finite element method to linear elastic fracture mechanics. *Appl. Mech. Rev.*, **44**, 447–461.
- L. Banks-Sills and Y. Bortman, 1984, Reappraisal of the quarter-point quadrilateral element in linear fracture mechanics. *Int. J. Fract.*, **25**, 169–180.

- L. Banks-Sills and Y. Bortman, 1987, Quarter-point singular elements revisited. *Int. J. Fract.*, **34**, R63–R69.
- L. Banks-Sills and O. Einav, 1987, On singular, nine-noded, distorted, isoparametric elements in linear elastic fracture mechanics. *Comp. Struct.*, **27**, 445–449.
- L. Banks-Sills and D. Sherman, 1989, On quarter-point three-dimensional finite elements in elastic fracture mechanics. *Int. J. Fract.*, **41**, 177–196.
- L. Banks-Sills and D. Sherman, 1992, On the computation of stress intensity factors for three-dimensional geometries by means of the stiffness derivative and J -integral methods. *Int. J. Fract.*, **53**, 1–20.
- E. J. Barbero and J. N. Reddy, 1990, The jacobian derivative method for three-dimensional fracture mechanics. *Comm. Appl. Num. Meth.*, **6**, 507–518.
- R. S. Barsoum, 1976, On the use of isoparametric finite elements in linear fracture mechanics. *Int. J. Num. Meth. Eng.*, **10**, 25–37.
- R. S. Barsoum, 1977, Triangular quarter-point elements as elastic and perfectly-plastic crack tip elements. *Int. J. Num. Meth. Eng.*, **11**, 85–98.
- Z. P. Bazant, 1995, Scaling theories for quasibrittle fracture: recent advances and new directions. In: "Proceedings of FRAMCOS-2, Zurich, 1995," ed. F. H. Wittmann, AEDIFICATIO Publishers, Freiburg, Germany, pp. 515–534.
- Z. P. Bazant and H. Ohtsubo, 1977, Stability conditions for propagation of a system of cracks in a brittle solid. *Mech. Res. Commun.*, **4**(5), 353–366.
- Z. P. Bazant, H. Ohtsubo and K. Aho, 1979, Stability and post-critical growth of a system of cooling or shrinkage cracks. *Int. J. Fract.*, **15**(5), 443–456.
- Z. P. Bazant and A. B. Wahab, 1979, Instability and spacing of cooling or shrinkage cracks. *J. Eng. Mech. Division, ASCE*, **105**(EM5), 873–889.
- S. F. Benzley, 1974, Representations of singularities with isoparametric finite elements. *Int. J. Num. Meth. Eng.*, **8**, 537–545.
- T. Bittencourt, P. Wawrzynek, J. Sousa and A. Ingraffea, 1996, Quasi-automatic simulation of crack propagation for 2D LEFM problems. *Eng. Fract. Mech.*, **55**(2), 321–334.
- M. Bonnet, 1994, Shape differentiation and boundary integral equations: application to energy methods in fracture mechanics. In: "Proceedings of Boundary Element Method XVI, Southampton, 1994," Computational Mechanics Publications, Southampton, UK, pp. 373–380.
- M. B. Buczek and C. T. Herakovich, 1985, A normal stress criterion for crack extension direction in orthotropic composite materials. *J. Composite Mater.*, **19**, 544–553.
- B. Budiansky and J. Rice, 1973, Conservation laws and energy release rates. *J. Appl. Mech.*, **40**, 201–203.
- H. D. Bui, 1983, Associated path independent J -integral for separating mixed modes. *J. Mech. Phys. Solids*, **31**, 439–448.
- H. D. Bui and K. D. Van, 1979, Généralisation de la théorie de la rupture de Griffith. *J. de Mécanique Appliquée*, **3**(2), 205–225.
- E. Byskov, 1970, The calculation of stress intensity factors using the finite element method with cracked elements. *Int. J. Fract.*, **6**, 159–167.
- G. E. Cardew, M. R. Goldthorpe, I. C. Howard and A. P. Kfouri, 1985, "Fundamentals of Deformation and Fracture: Eshelby Memorial Symposium," eds. B. A. Bilby, K. J. Miller and J. R. Willis, Cambridge University Press, Cambridge, UK, pp. 465–476.
- J. Červenka and V. E. Saouma, 1997, Numerical evaluation of 3D SIF for arbitrary finite element meshes. *Eng. Fract. Mech.*, **57**, 541–563.
- S. K. Chan, I. S. Tuba and W. K. Wilson, 1970, On the finite element method in linear fracture mechanics. *Eng. Fract. Mech.*, **2**, 1–17.
- C.-S. Chen, 1999, Crack growth simulation and residual strength prediction in thin shell structures. Ph.D. dissertation, Cornell University, Ithaca, New York.
- C.-S. Chen, R. Krause, R. G. Pettit, L. Banks-Sills and A. R. Ingraffea, 2001, Numerical assessment of T -stress computation using a P-version finite element method. *Int. J. Fract.*, **107**(2), 177–199.
- C.-S. Chen, P. A. Wawrzynek and A. R. Ingraffea, 1997, Methodology for fatigue crack growth and residual strength prediction with applications to aircraft fuselages. *Comp. Mech.*, **19**, 527–532.
- C.-S. Chen, P. A. Wawrzynek and A. R. Ingraffea, 2002, Prediction of residual strength and curvilinear crack growth in aircraft fuselages. *AIAA J.*, accepted for publication.
- G. P. Cherepanov, 1967, Crack propagation in continuous media. *USSR J. Appl. Math. Mech.*, Translation, **31**, 504.
- I. Constable, J. G. Williams and L. E. Culver, 1970, Notch root radii effects in the fatigue of polymers. *Int. J. Fract. Mech.*, **6**(3), 279–285.
- Cornell Fracture Group, 2002, FRANC2D and FRANC3-D, <http://www.cfg.cornell.edu>
- B. Cotterell and J. R. Rice, 1980, Slightly curved or kinked cracks. *Int. J. Fract.*, **16**, 155–169.
- A. U. DeKoning and C. J. Lof, 1984, K-distributions extrapolated on the basis of stress intensity rates. In: "Proceedings of the 3rd International Conference on Numerical Methods in Fracture Mechanics, Swansea, 1984," eds. A. R. Luxmoore and D. R. J. Owen, Pineridge Press, Swansea, UK, pp. 195–203.
- H. G. deLorenzi, 1982, On the energy release rate and the J -integral for 3-D crack configurations. *Int. J. Fract.*, **19**, 183–193.
- H. G. deLorenzi, 1985, Energy release rate calculations by the finite element method. *Eng. Fract. Mech.*, **21**, 129–143.
- D. L. Destyunder, M. Diaoua and S. Lescure, 1983, Quelques remarques sur la mécanique de la rupture élastique. *J. Mécanique Théorique et Appliquée*, **2**, 113–135.
- D. S. Dugdale, 1960, Yielding in steel sheets containing slits. *J. Mech. Phys. Solids*, **8**, 100–104.
- F. Erdogan and G. C. Sih, 1963, On the extension of plates under plane loading and transverse shear. *J. Basic Eng., ASME*, **85D**(4), 519–527.
- T. Fett, 1997, A Green's function for T -stresses in an edge-cracked rectangular plate. *Eng. Fract. Mech.*, **57**, 365–373.
- T. Fett, 1998, "A Compendium of T -stress Solutions." Institut für Materialforschung, Karlsruhe, Germany, Report FZKA 6057.
- I. Finnie and A. Saith, 1973, A note on the angled crack problem and the directional stability of cracks. *Int. J. Fract.*, **9**, 484–486.
- C. E. Freese and D. M. Tracey, 1976, The natural triangle versus collapsed quadrilateral for elastic crack analysis. *Int. J. Fract.*, **12**, 767–770.
- H. Gao and J. R. Rice, 1986a, Shear stress intensity factors for a planar crack with slightly curved front. *J. Appl. Mech.*, **53**, 774–778.
- H. Gao and J. R. Rice, 1986b, Somewhat circular tensile cracks. *Int. J. Fract.*, **33**, 155–174.
- H. Gao and J. R. Rice, 1987, Nearly circular connections of elastic half spaces. *J. Appl. Mech.*, **54**, 627–634.
- H. Gao and J. R. Rice, 1989, A first-order perturbation analysis of crack trapping by arrays of obstacles. *J. Appl. Mech.*, **56**, 828–836.
- R. J. Goode, 1972, Identification of fracture plane orientation. *Mater. Res. Stand. (MIRSA)*, **ASTM**, **12**, 9 (see also ASTM E1823).
- B. Gross, J. E. Srawley and W. F. Brown, Jr., 1964, "Stress Intensity Factors for a Single-edge-notch Tension

- Specimen by Boundary Collocation of a Stress Function." NASA, Technical Note D-2395 NASA Lewis Research Center, Cleveland, OH.
- M. L. Gruber, C. J. Mazur, K. E. Wilkins and R. E. Worden, 1996, "Investigation of Fuselage Structure Subject to Widespread Fatigue Damage." Technical Report DOT/FAA/AR95/47, Federal Aviation Administration, Washington DC.
- R. B. Haber and M. K. Koh, 1985, Explicit expressions for energy-release rates using virtual crack extensions. *Int. J. Num. Meth. Eng.*, 21, 278-301.
- R. J. Hartranft and G. Sih, 1968, Effect of plate thickness on the bending stress distribution around through cracks. *J. Math. Phys.*, 47, 276-291.
- R. J. Hartranft and G. C. Sih, 1970, An approximate three-dimensional theory of plates with application to crack problems. *Int. J. Eng. Sci.*, 8(8), 711-729.
- T. K. Hellen, 1975, On the method of virtual crack extension. *Int. J. Num. Meth. Eng.*, 9, 187-207.
- R. D. Henshell and K. G. Shaw, 1975, Crack tip finite elements are unnecessary. *Int. J. Num. Meth. Eng.*, 9, 495-507.
- H. D. Hibbit, 1977, Some properties of singular isoparametric elements. *Int. J. Num. Meth. Eng.*, 11, 180-184.
- A. Hoenig, 1982, Near-tip behavior of a crack in a plane anisotropic elastic body. *Eng. Fract. Mech.*, 16, 393-403.
- C. Y. Hui and A. T. Zehnder, 1993, A theory for the fracture of thin plates subjected to bending and twisting moments. *Int. J. Fract.*, 61, 211-229.
- M. A. Hussain, L. F. Coffin and K. A. Zaleski, 1981, Three-dimensional singular elements. *Comp. Struct.*, 13, 595-599.
- M. A. Hussain, S. L. Pu and J. H. Underwood, 1974, Strain energy release rate for a crack under combined mode I and mode II. In: "Fracture Analysis, ASTM STP 560," ASTM, Philadelphia, PA, pp. 2-28.
- C. G. Hwang, P. A. Warzynek, A. K. Tayebi and A. R. Ingraffea, 1998, On the virtual crack extension method for calculating rates of energy release rate. *Eng. Fract. Mech.*, 59(4), 521-542.
- C. G. Hwang, P. A. Wawrzynek and A. R. Ingraffea, 2001, On the virtual crack extension method for calculating the derivatives of energy release rates for a 3D planar crack of arbitrary shape under mode I loading. *Eng. Fract. Mech.*, 68(7), 925-947.
- A. R. Ingraffea and C. Manu, 1980, Stress-intensity factor computations in three dimensions. *Int. J. Num. Meth. Eng.*, 15, 1427-1445.
- G. R. Irwin, 1957, Analysis of stresses and strains near the end of a crack traversing a plate. *J. Appl. Mech.*, 24, 361-364.
- G. R. Irwin, 1960, Plastic zone near a crack and fracture toughness. In: "Proceedings of the 7th Sagamore Ordnance Materials Conference on Mechanics & Metals Behavior of Sheet Materials, Racquette Lake, NY, 1960," Syracuse University, New York, pp. 463-478.
- G. R. Irwin, 1962, Crack extension force for a part-through crack in a plate. *Trans. ASME. Ser. E, J. Appl. Mech.*, 29, 651-654.
- H. Ishikawa, 1980, A finite element analysis of stress intensity factors for combined tensile and shear loading by only a virtual crack extension. *Int. J. Fract.*, 16, 243-246.
- H. Ishikawa, H. Kitagawa and H. Okamura, 1979, J -integral of a mixed mode crack and its application. In: "Proceedings of the 3rd International Conference on Mechanical Behavior of Materials, Cambridge, England, 1979," eds. K. J. Miller and R. F. Smith, Pergamon, Oxford, London, pp. 447-455.
- M. Isida, 1971, Effect of width and length on stress intensity factors of internally cracked plates under various boundary conditions. *Int. J. Fract.*, 7(3), 301-316.
- M. Isida and T. Nishino, 1990, Formulae of stress intensity factors at the tips of kinked cracks under various loadings. *Eng. Fract. Mech.*, 36(5), 697-711.
- M. James, 1998, A plane stress finite element model for elastic plastic mode i/ii crack growth. Ph.D. dissertation, Kansas State University.
- P. F. Joseph and F. Erdogan, 1989, Surface crack problems in plates. *Int. J. Fract.*, 41, 105-131.
- L. M. Keer, S. Nemat-Nasser and K. S. Parthas, 1978, Unstable growth of thermally induced interacting cracks in brittle solids: further results. *Int. J. Solids Struct.*, 15, 111-126.
- A. P. Kfouri, 1986, Some evaluations of the elastic T-term using Eshelby's method. *Int. J. Fract.*, 30, 301-315.
- A. P. Kfouri, 1996, Crack extension under mixed-mode loading in an anisotropic mode-asymmetric material in respect of resistance to fracture. *Fatigue Fract. Eng. Mater. Struct.*, 19(1), 27-38.
- H. A. J. Knops, 1994, Numerical simulation of crack growth in pressurized fuselages. Ph.D. thesis, Delft University of Technology.
- J. K. Knowles and N. M. Wang, 1960, On bending of an elastic plate containing a crack. *J. Math. Phys.*, 39, 223-236.
- R. W. J. Koers, 1989, Use of modified standard 20-node isoparametric brick elements for representing stress/strain fields at a crack tip for elastic and perfectly plastic material. *Int. J. Fract.*, 40, 79-110.
- K. Koppenhoefer, A. S. Gullerund, C. Ruggieri, R. H. Dodds and B. E. Healy, 1994, "WARP3-D: Dynamic Nonlinear Analysis of Solids Using a Preconditioned Conjugate Gradient Software Architecture." Report number UILU-ENG-94-2017, Department of Civil Engineering, University of Illinois at Urbana-Champaign, Urbana, IL.
- M. Kosai, A. S. Kobayashi and M. Ramulu, 1992, Tear straps in aircraft fuselage. In: "Proceedings of International Workshop on Structural Integrity of Aging Airplanes, Atlanta, 1992," ed. S. Atluri, Atlanta Technology Publications, Atlanta, GA, pp. 443-457.
- S. G. Larsson and A. J. Carlsson, 1973, Influence of non-singular stress terms and specimen geometry on small-scale yielding at crack tips in elastic-plastic materials. *J. Mech. Phys. Solids*, 21, 263-277.
- P. S. Leevers and J. C. Radon, 1982, Inherent stress biaxiality in various fracture specimen geometries. *Int. J. Fract.*, 19, 311-325.
- F. Lemaitre and A. Pineau, 1981, Mixed mode fracture of a brittle orthotropic material—example of strongly textured zinc sheets. *Eng. Fract. Mech.*, 14, 91-105.
- F. Z. Li, C. F. Shih and A. Needleman, 1985, A comparison of methods for calculating energy release rates. *Eng. Fract. Mech.*, 21, 405-421.
- S. C. Lin and J. F. Abel, 1988, A variational approach for a new direct-integration form of the virtual crack extension methods. *Int. J. Fract.*, 28, 217-235.
- S. C. Liu, 1974, Crack growth and failure of aluminium plate under in-plane shear. *AIAA J.*, 12, 180-185.
- T. M. Maccagno and J. F. Knott, 1989, The fracture behaviour of PMMA in mixed modes I and II. *Eng. Fract. Mech.*, 34(1), 65-86.
- T. M. Maccagno and J. F. Knott, 1991, The low-temperature brittle fracture behaviour of steel in mixed modes I and II. *Eng. Fract. Mech.*, 38(2/3), 111-128.
- S. K. Maiti and R. A. Smith, 1983, Comparison of criteria for mixed-mode brittle fracture based on the preinstability stress-strain field: Part I. Slit and elliptical cracks under uniaxial tensile loading. *Int. J. Fract.*, 23, 281-293.
- C. Manu, 1983, Quarter-point elements for curved crack fronts. *Comp. Struct.*, 17, 227-231.
- C. Manu, 1985, Complete quadratic isoparametric finite elements in fracture mechanics analysis. *Int. J. Num. Meth. Eng.*, 21, 1547-1553.

- K. P. Meade and L. M. Keer, 1984a, On the problem of a pair of point forces applied to the faces of a semi-infinite plane crack. *J. Elasticity*, **14**, 3–14.
- K. P. Meade and L. M. Keer, 1984b, Stress intensity factors for semi-infinite plane crack with a wavy front. *J. Elasticity*, **14**, 79–92.
- B. Moran and C. F. Shih, 1987, A general treatment of crack tip contour integrals. *Int. J. Fract.*, **35**, 295–310.
- K. B. Narayana, 1994, A general procedure for modified crack closure integral in 3-D problems with cracks. *Eng. Fract. Mech.*, **48**, 167–176.
- S. Nemat-Nasser, 1978, Stability of a system of interacting cracks. *Lett. Appl. Eng. Sci.*, **16**, 277–285.
- S. Nemat-Nasser, L. M. Keer and K. S. Parihar, 1978, Unstable growth of thermally induced interacting cracks in brittle solids. *Int. J. Solids Struct.*, **14**, 409–430.
- S. Nemat-Nasser, Y. Sumi and L. M. Keer, 1980, Unstable growth of tension cracks in brittle solids: stable and unstable bifurcations, snap-through, and imperfection sensitivity. *Int. J. Solids Struct.*, **16**, 1017–1035.
- J. C. Newman, Jr. and I. S. Raju, 1981, "Stress Intensity Factors Equations for Cracks in Three-dimensional Finite Bodies." NASA Technical Memorandum 83200, NASA Langley Research Center, Hampton, VA, pp. 1–49.
- Q. S. Nguyen, 1980, Normal dissipativity and energy criteria in fracture. In: "Proceedings of IUTAM Symposium on Variational Methods in the Mechanics of Solids, Oxford, 1980," ed. S. Nemat-Nasser, Pergamon, pp. 254–259.
- S. Nguyen, 1994, Bifurcation and stability in dissipative media (plasticity, friction, fracture). *Appl. Mech. Rev.*, **47**(1), part 1, 1–31.
- Q. S. Nguyen, C. Stolz and G. Debruyne, 1990, Energy methods in fracture mechanics: stability, bifurcation and second variations. *Eur. J. Mech., A/Solids*, **9**(2), 157–173.
- G. P. Nikishkov and S. N. Atluri, 1987, Calculation of fracture mechanics parameters for an arbitrary three-dimensional crack, by the 'equivalent domain integral' method. *Int. J. Num. Meth. Eng.*, **24**, 1801–1827.
- S. G. Papaioannou, P. D. Hilton and R. A. Lucas, 1974, A finite element method for calculating stress intensity factors and its application to composites. *Eng. Fract. Mech.*, **6**, 807–823.
- D. M. Parks, 1974, Stiffness derivative finite element technique for determination of crack-tip stress intensity factors. *Int. J. Fract.*, **10**, 487–502.
- R. G. Pettit, J. C. Newman and M. S. Domack, 1997, Crack turning damage tolerance approach for integrally stiffened structure. In: "Proceedings of the 19th Symposium of the International Committee on Aeronautical Fatigue, Vol. II, 1997, Edinburgh, Scotland," eds. R. Cook and P. Poole, EMAS Publishing, pp. 819–830.
- L. P. Pook, 1971, The effect of crack angle on fracture toughness. *Eng. Fract. Mech.*, **3**, 205–218.
- D.O. Potyondy, 1993, A methodology for simulation of curvilinear crack growth in pressurized shells. Ph.D. thesis, Cornell University, Ithaca, New York.
- D. O. Potyondy, P. A. Wawrzynek and A. R. Ingraffea, 1995, Discrete crack growth analysis methodology for through cracks in pressurized fuselage structures. *Int. J. Num. Meth. Eng.*, **38**, 1611–1633.
- I. S. Raju, 1987, Calculation of strain-energy release rate with high order and singular finite elements. *Eng. Fract. Mech.*, **28**, 251–274.
- T. S. Ramamurthy, T. Krishnamurthy, K. Badari Narayana, K. Vijayakumar and B. Dattaguru, 1986, Modified crack closure integral method with quarter point elements. *Mech. Res. Commun.*, **13**, 179–186.
- M. Ramulu and A. Kobayashi, 1983, Dynamic crack curving—a photoelastic evaluation. *Exp. Mech.*, **23**, 1–9.
- C. C. Rankin, F. A. Brogan, W. A. Loden and H. D. Cabiness, 1997, "STAGS User Manual Version 2.4."
- Lockheed Martin Missiles & Space Co., Advanced Technology Center, Palo, Alta, CA.
- E. Reissner, 1947, On bending of elastic plates, *Quarterly of Applied Math.*, **5**, 55–68.
- J. R. Rice, 1968, A path-independent integral and the approximate analysis of strain concentrations by notches and cracks. *J. Appl. Mech.*, **35**, 379–386.
- J. R. Rice, 1985, First-order variation in elastic fields due to variation in location of a planar crack front. *J. Appl. Mech.*, **52**, 571–579.
- J. R. Rice and M. A. Johnson, 1969, The role of large crack tip geometry changes in plain strain fracture. In: "Inelastic Behavior of Solids," McGraw-Hill, New York, pp. 641–690.
- E. R. Rybicki and M. F. Kanninen, 1977, A finite element calculation of stress intensity factors by a modified crack closure integral. *Eng. Fract. Mech.*, **9**, 931–938.
- A. S. Selvarathinam and J. G. Goree, 1998, T-stress based fracture model for cracks in isotropic materials. *Eng. Fract. Mech.*, **60**(5/6), 543–561.
- T.-L. Sham, 1991, The determination of the elastic T-term using higher order weight functions. *Int. J. Fract.*, **48**, 81–102.
- C. F. Shih, H. G. Delorenzi and M. D. German, 1976, Crack extension modeling with singular quadratic isoparametric elements. *Int. J. Fract.*, **1**, 647–651.
- M. Shirmohamadi, 1995, Stable crack growth trajectories and fracture due to interacting cracks, Ph. D. dissertation, University of California at Berkeley.
- G. C. Sih, P. C. Paris and G. R. Irwin, 1965, On cracks in rectilinearly anisotropic bodies. *Int. J. Fract. Mech.*, **1**, 189–203.
- G. C. Sih, 1974, Strain-energy-density factor applied to mixed-mode crack problems. *Int. J. Fract.*, **10**, 305–321.
- R. Singh, B. Carter, P. Wawrzynek and A. Ingraffea, 1998, Universal crack closure integral for SIF estimation. *Eng. Fract. Mech.*, **60**, 133–146.
- N. Sneddon, 1946, The distribution of stress in the neighborhood of a crack in an elastic solid. *Proc. Roy. Soc. London, Ser. A*, **187**, 229–250.
- V. E. Saouma and D. Schwemmer, 1984, Numerical evaluation of the quarter-point crack tip element. *Int. J. Num. Meth. Eng.*, **20**, 1629–1641.
- J. Sousa, 1992, Three-dimensional simulation of near-wellbore phenomena related to hydraulic fracturing from a perforated wellbore. Ph.D. thesis, Cornell University, Ithaca, New York.
- L. Spievak, D. Lewicki, P. Wawrzynek and A. Ingraffea, 2001, Simulating fatigue crack growth in spiral bevel gears. *Eng. Fract. Mech.*, **68**(1), 53–76.
- M. Stern, E. B. Becker and R. S. Dunham, 1976, A contour integral computation of mixed-mode stress intensity factors. *Int. J. Fract.*, **12**, 359–368.
- T. J. Stone and I. Babuška, 1998, A numerical method with *a posteriori* error estimation for determining the path taken by a propagating crack. *Comp. Meth. Appl. Mech. Eng.*, **160**, 245–271.
- R. Streit and I. Finnie, 1980, An experimental investigation of crack-path directional stability. *Exp. Mech.*, **20**, 17–23.
- Y. Sumi, S. Nemat-Nasser and L. M. Keer, 1980, A new combined analytical and finite-element solution method for stability analysis of the growth of interacting tension cracks in brittle solids. *Int. J. Eng. Sci.*, **18**, 211–224.
- Y. Sumi, S. Nemat-Nasser and L. M. Keer, 1985, On crack path instability in a finite body. *Eng. Fract. Mech.*, **22**, 759–771.
- M.A. Sutton, X. Deng, F. Ma, J. C. Newman and M. James, 2000, Development and application of a COD-based mixed-mode fracture criterion. *Int. J. Solids Struct.*, in press.
- M. A. Sutton, W. Zhao, M. L. Boone, A. P. Reynolds and D. S. Dawicke, 1997, Prediction of crack growth

- direction for mode I/II loading using small-scale yielding and void initiation/growth concepts. *Int. J. Fract.*, **83**, 275–290.
- B. A. Szabó and I. Babuška, 1991, "Finite Element Analysis," Wiley, New York.
- P. S. Theocaris, 1989, Variation on the theme of fracture criteria. *Eng. Fract. Mech.*, **33**, 205–214.
- P. S. Theocaris and N. P. Andrianopoulos, 1982, A modified strain energy density criterion applied to crack propagation. *J. Appl. Mech.*, **49**(1), 81–86.
- S. Timoshenko and S. Woinowsky-Krieger, 1959, "Theory of Plates and Shells," McGraw-Hill, New York.
- P. Tong, T. H. H. Pian and S. J. Lasry, 1973, A hybrid element approach to crack problems in plane elasticity. *Int. J. Num. Meth. Eng.*, **7**, 1031–1036.
- D. M. Tracey, 1971, Finite elements for determination of crack tip elastic stress intensity Factors. *Eng. Fract. Mech.*, **3**, 255–256.
- D. M. Tracey, 1977, Discussion of "On the use of isoparametric finite elements in linear fracture mechanics," by R. S. Barsoum. *Int. J. Num. Meth. Eng.*, **11**, 401–402.
- A. Ural, A. R. Ingraffea, P. Wawrzynek and D. Lewicki, 2002, "Simulating Fatigue Crack Growth in Spiral Bevel Gears," NASA technical report, in press.
- M. J. Viz, D. O. Potyondy, A. T. Zehnder, C. C. Rankin and E. Riks, 1995, Computation of membrane and bending stress intensity factors for thin, cracked plates. *Int. J. Fract.*, **72**, 21–38.
- N. M. Wang, 1970, Twisting of an elastic plate containing a crack. *Int. J. Fract. Mech.*, **6**, 367–378.
- P. A. Wawrzynek and A. R. Ingraffea, 1987, Interactive finite-element analysis of fracture processes: an integrated approach. *Theor. Appl. Fract. Mech.*, **8**, 137–150.
- A. A. Wells, 1961, Unstable crack propagation in metals: cleavage and fast fracture. In: "Proceedings of the Crack Propagation Symposium, 1961, Cranfield," College of Aeronautics, Cranfield, UK, vol. 1, paper 84.
- M. L. Williams, 1957, On the stress distribution at the base of a stationary crack. *ASME Trans., J. Appl. Mech.*, **24**, 109–114.
- M. L. Williams, 1961, The bending stress distribution at the base of a stationary crack. *ASME Trans., J. Appl. Mech.*, **28**, 78–82.
- M. L. Williams and P. D. Ewing, 1972, Fracture under complex stress—the angled crack problem. *Int. J. Fract. Mech.*, **8**, 441–446.
- J. F. Yau, S. S. Wang and H. T. Corten, 1980, A mixed-mode crack analysis of isotropic solids using conservation laws of elasticity. *J. Appl. Mech.*, **47**, 335–341.
- L. A. Ying, 1982, A note on the singularity and the strain energy of singular elements. *Int. J. Num. Meth. Eng.*, **18**, 31–39.
- F. G. Yuan and S. Yang, 1998, The application of fracture mechanics to stitched warpkit fabric composites. In: "Proceedings of the 39th AIAA/ASME/ASCE/AHS/ASC Structures, Structural Dynamics, and Materials Conference, Long Beach, CA, April 1998." AIAA paper #98-2025 Reston, VA.